

UNIVERSITY OF NOVA GORICA
GRADUATE SCHOOL

**GPS for Weather
and
Space Weather Studies**

DISSERTATION

Andreja Sušnik

Supervisor: doc.dr. Klemen Bergant

Nova Gorica, 2013

UNIVERZA V NOVI GORICI
FAKULTETA ZA PODIPLOMSKI ŠTUDIJ

Uporaba sistema globalnega določanja lege za raziskave vremena in vesoljskega vremena

DISERTACIJA

Andreja Sušnik

Mentor: doc.dr. Klemen Bergant

Nova Gorica, 2013

to darko

Acknowledgments

First, I would like to thank my advisers doc.dr. Klemen Bergant and prof.dr. Samo Stanič for providing me with guidance, continuous support, and constructive ideas during my Ph.D. studies. Great thanks goes to members of the Centre for Atmospheric Research and Laboratory for Astroparticle Physics for all the help with problems, in particular thanks go to dr. Fei Gao and dr. Tingyao He for all the help and assistance not only during the measurements but also outside the office, when help was needed the most. Many thanks goes to Neva Pristov at Slovenian Environmental Agency and dr. R. Prieto-Cerdeira at European Space Agency for kindly providing the data used in the scope of dissertation.

There are no words that can describe my gratitude to prof.dr. Martin O'Loughlin, let me add only that I will be infinitely thankful in all space-time dimensions. Special thanks go to Maja Wagner, Tea Stibilj Nemec, Erika Gojkovič, Irena Lipičar, Adrijana Pisk, Bojan Korečič, Saeede Nafoshe, Đorđe Stevanović, and all other colleagues and friends for keeping me human and sane during the last four years, whether going for lunch or drinks with me.

Last but not least, I would like to thank my mom and dad for all the support, understanding and encouragements during my study years. I would not be here without you. The same thanks also go to my entire family, my aunts, sisters and uncle.

Abstract

The Global Positioning System (GPS) was designed to provide the position of any object anywhere on the Earth's surface in all weather conditions using a constellation of dedicated GPS satellites. When the GPS signals originating from satellites transverse the Earth's atmosphere, they experience delays due to atmospheric refraction. This delay presents one of the major obstacles for precise positioning and navigation and there have been many research efforts dedicated to the elimination of this source of inaccuracy. In contrast to the primary use of GPS as a positioning tool, in the past two decades ionospheric scientists, meteorologists and environmentalists started to measure GPS signal delay and use it to infer atmospheric profiles of temperature, pressure, humidity and electron density.

The aim of this dissertation was to study atmospheric properties using combined remote sensing techniques and in-situ measurements. The main remote sensing tools used in the scope of this dissertation were GPS monitors, radiosondes, Raman lidar and ground based meteorological stations measuring temperature, pressure and humidity. As a part of this dissertation, two dedicated GPS monitors were deployed at two University of Nova Gorica campuses, Rožna Dolina and Ajdovščina, together with co-located meteorological stations.

Different methods for estimation of the integrated water vapor from GPS monitor data have been tested and validated. In particular, GPS Inferred Positioning System-Orbit Analysis and Simulation Software (GIPSY-OASIS II) version 6.1.2, data processing strategies and analysis using data from GPS monitor stationed in Ljubljana, Slovenia were undertaken and compared with water vapor values calculated from the co-located radiosonde measurements in order to identify possible errors in the analysis. As a part of water vapor estimation from GPS-signal delay, the validation of weighted "mean temperature" (T_m) parametrization was performed for the first time in the Slovenian region, and the simple linear regression model of Bevis *et al.* (1992) was expanded to include, in addition to ground temperature measurements, also pressure and humidity data. Here, the analysis was performed using data from the meteorological station located in Ljubljana, Slovenia and the results were compared to the values from co-located radiosonde measurements. Even though different parametrizations clearly influence the final value of T_m , a comparison between these parametrizations shows that the water vapor estimate is not so sensitive to the value of T_m and therefore resulting in only small discrepancy. In the case of the University of Nova Gorica GPS monitors, preliminary results of water vapor estimation are presented and discussed. In both campaigns, the Raman lidar, stationed at Otlica, Slovenia, was used to measure the water vapor mixing ratio. This measurement was initially intended for verification of water vapor content, which was found not to be feasible due to limited lidar detection range. As a result, only Raman lidar based mixing ratio profiles up to altitudes of about 2 km are presented.

The second part of the dissertation presents a statistical analysis of GPS ionospheric scintillation occurrences in the equatorial region using data from the GSV4004 ionospheric monitor located in Douala, Cameroon, with a data span from March 2004 to February 2005. Here the variations of ionospheric scintillations with local time, season and spatial distribution are analyzed and discussed. The scintillation activity in the equatorial region appears to be seasonally governed, with maximum occurrence during the equinox months (March, April;

September, October), while minimum occurrence was found to be in the solstice months (June; December). Results also show that scintillations are predominantly a post-sunset event, commencing in pre-midnight hours.

The final chapter presents a study of the performance of GPS devices in the Pierre Auger Observatory, which is located close to Malargüe in Province Mendoza, Argentina. In Pierre Auger, GPS devices are being used only for the precise timing of cosmic-ray arrivals to individual detectors of the surface detector (SD) array, while the position of each SD station is determined by geodetic surveys during their deployment. The motivation for this operation strategy was to improve timing accuracy from the nominal >10 ns in navigation mode to <10 ns in position-hold mode. As a result of our study we established considerable inaccuracies in SD positions obtained by the surveys, which were directly translated into large absolute time offsets between the true time and the surface-detector time-keeping system.

PACS (2010): 42.25.Fx, 42.25.Gy, 42.68.Wt, 91.10.Fc, 91.10.Jf, 91.10.pa, 92.05.Fg, 92.60.-e, 93.30.Ge, 93.30.Jg, 93.30.Bz, 94.20.Bb

Keywords: electromagnetic waves, propagation, Earth's atmosphere, ionosphere, troposphere, Global Positioning System (GPS), GPS accuracy, Raman lidar, atmospheric water vapor, atmospheric delays of GPS signals, water vapor mixing ratio, ionospheric scintillations, cosmic rays, GPS as timing standard, topography

Povzetek

Glavni namen vzpostavitve Globalnega Navigacijskega Sistema (GPS) je bilo določanje lege poljubnega objekta na Zemeljskem površju s pomočjo satelitov ne glede na vremenske pogoje. Ko signal GPS potuje od satelita do sprejemnika na površini Zemlje, zaradi atmosfere refrakcije utрпи časovni zamik, ki se odraža v nenatančnosti pridobljenih koordinat in predstavlja eno izmed večjih omejitev za uporabo sistema GPS n.pr. v geodeziji in navigaciji. V preteklosti je bilo opravljenih že veliko raziskav namenjenih odstranitvi, šele v zadnjem obdobju pa so ga raziskovalci s področja ionosfere, meteorologije in okoljevarstva pričeli izkoriščati za daljinsko pridobivanje informacij o lastnostih Zemljine atmosfere kot so temperatura, tlak, vodna para ter gostota elektronske plazme v ionosferi. Njihovo prizadevanje je stimuliralo raziskave predstavljene v tej doktorski nalogi.

Glavni cilj doktorske naloge je bil študij atmosferskih lastnosti s pomočjo daljinskega zaznavanja in neposrednih meritev. Glavna raziskovalna orodja, uporabljena v raziskavah so bila sprejemniki GPS, Ramanski lidar, meteorološke radiosonde in talne meteorološke postaje. Del naloge zajema tudi razvoj in validacijo programskih orodij za analizo podatkov o vsebnosti vodne pare pridobljenih s pomočjo uporabe sistema GPS.

V okviru doktorske naloge smo testirali in potrdili različne metode za določitev vsebnosti vodne pare s pomočjo uporabe sistema GPS. Z uporabo podatkov, merjenih s sprejemnikom GPS v Ljubljani, smo testirali različne strategije v programskem okolju GPS Inferred Positioning System-Orbit Analysis and Simulation Software (GIPSY-OASIS II) verzija 6.1.2, in pridobljene rezultate primerjali z vsebnostjo vodne pare izračunane iz profilov temperature, pritiska ter vlage, izmerjenih s pomočjo meteoroloških radiosond. Kot del določanja vsebnosti vodne pare iz zamika signala GPS, smo izvedli validacijo parametra povprečne temperature (T_m) za območje Slovenije, pri čemer je bil enostavni linearni regresijski model (Bevis *et al.* (1992)) razširjen tako, da poleg temperature pri tleh, vsebuje tudi tlak in vlažnost, ki jih je izmerila talna meteorološka postaja Agencije Republike Slovenije za okolje (ARSO). Pridobljene rezultate smo primerjali z vrednostimi T_m izračunanimi iz meteoroloških radiosond. Kljub temu da so rezultati analize pokazali, da različne parametrizacije srednje temperature T_m vplivajo na njeno končno vrednost, nam je njihova primerjava pokazala, da je njen vpliv na končno vrednost vodne pare manj poudarjen. V primeru sprejemnikov GPS, pridobljenih na Univerzi v Novi Gorici, smo izvedli preliminarne meritve vodne pare, pri čemer so bili rezultati primerjani tako s sprejemnikom GPS v Ljubljani, kot tudi z meteorološkimi radiosondami. Med meritvami smo uporabljali tudi stacionaren Ramanski lidar na observatoriju na Otlici, z namenom validacije vrednosti vsebnosti vodne pare pridobljene s sprejemniki GPS.

Drugi del doktorske naloge zajema tudi študijo ionosferskih fluktuacij na signalih sistema GPS. Podatki so bili izmerjeni s pomočjo ionosferskega monitorja GSV4004 lociranega pri nizkih zemljepisnih širinah v kraju Douala v Kamerunu in se nanašajo na obdobje med marcem 2004 in februarjem 2005. Ugotovili smo, da je pojav ionosferskih fluktuacij pri nizkih zemljepisnih širinah sezonski pojav z okrepljenim pojavljanjem v mesecih enakonočja (marec, april; september, oktober) in z minimalnim pojavljanjem v mesecih junij in december. Opazili smo tudi dnevne cikle pojavljanja fluktuacij z značilnim večernim maksimumom, ki

je tipično nastopal pred polnočjo.

Poleg raziskav uporabe GPS sistema v atmosferski znanosti kot zadnjo študijo predstavljamo tudi uporabo postaj GPS znotraj Observatorija Pierre Auger, ki je postavljen v "Pampi Amarili" blizu kraja Malargüe v Argentini. Znotraj Observatorija Pierre Auger se postaje GPS uporabljajo za časovno označevanje detekcije kozmičnih žarkov v sklopu talnih detektorjev (SD) observatorija, sama pozicija talnih detektorjev pa je pridobljena s pomočjo geodetskih meritev. Glavni razlog za tako uporabo GPS sprejemnikov je bila potreba po izjemni natančnosti meritve časa prihoda kozmičnih žarkov, ki je bila v tem primeru manjša od 10 ns, in s tem boljša, kot če bi GPS hkrati uporabljali tudi za določanje pozicije detektorjev. Na podlagi večjega števila izvedenih meritev in analiz smo ugotovili, da so bile geodetske meritve ob namestitvi SD pogosto nenatančne, kar neposredno vpliva na pojav večjih časovnih zamikov med pravim časom in časom, ki ga vodijo talni detektorji.

Stvarni vrstilec, PACS (2010): 42.25.Fx, 42.25.Gy, 42.68.Wt, 91.10.Fc, 91.10.Jf, 91.10.pa, 92.05.Fg, 92.60.-e, 93.30.Ge, 93.30.Jg, 93.30.Bz, 94.20.Bb

Ključne besede: elektromagnetni valovi, propagacija elektromagnetnih valov, atmosfera, ionosfera, troposfera, Globalni Navigacijski Sistem (GPS), natančnost GPS, Ramanski lidar, atmosferska vodna para, atmosferski zamiki signalov GPS, mešalno razmerje vodne pare, ionosferske fluktuacije, kozmični žarki, GPS kot časovni standard, topografija

Contents

List of Figures	xxi
List of Tables	xxiii
List of Symbols	xxv
1 Introduction	1
1.1 Background	1
1.2 State of the art	3
1.3 Aims and Objectives of the thesis	6
1.4 Structure of the thesis	7
2 Overview of GPS and Raman LIDAR	9
2.1 Global Positioning System	9
2.1.1 GPS System Architecture	10
2.1.2 GPS Signal Structure and Modernization	12
2.1.3 GPS Observables	17
2.1.4 Positioning modes	21
2.1.5 GPS errors and biases	22
2.1.6 GPS monitors at the University of Nova Gorica	25
2.2 LIDAR System	27
2.2.1 Basic LIDAR setup	28
2.2.2 Elastic LIDAR equation	30
2.3 Summary	33
3 Atmospheric effects on EM wave propagation	35
3.1 Earth's atmosphere	35
3.1.1 Neutral Atmosphere	37
3.1.2 Ionosphere	43
3.2 Propagation of electromagnetic waves in atmosphere	49
3.2.1 Ionospheric delay	51
3.2.2 Tropospheric delay	58
3.2.3 Light scattering in the lower atmosphere	69
3.3 Summary	73
4 Water vapor estimation	75
4.1 Introduction	75
4.2 Methodology	76
4.2.1 GPS Inferred Positioning System-Orbit Analysis and Simulation Software (GPSY-OASIS II)	76
4.2.2 Processing strategy	77
4.3 From GPS wet delay to IWV	78
4.3.1 Validation of T_m parameter	80

4.3.2	Error analysis	83
4.4	Water vapor measurements at UNG	88
4.4.1	Water vapor mixing ratio measurements	89
4.4.2	GPS measurements	91
4.5	Conclusions	95
5	Ionospheric scintillations	97
5.1	Introduction	97
5.2	Methodology	97
5.2.1	Data selection	97
5.2.2	Ionospheric pierce-point calculation	99
5.3	Results and discussion	100
5.3.1	Amplitude scintillations	101
5.3.2	Phase scintillations	104
5.3.3	Spatial distribution of scintillation occurrence	105
5.4	Summary	106
6	The use of GPS in the Pierre Auger Observatory	117
6.1	Introduction	117
6.1.1	The Pierre Auger Observatory	118
6.2	Topography of the SD array	119
6.2.1	Difference to the digital elevation map	120
6.2.2	Array test with different GPS position acquisition mode	122
6.2.3	Positions of SD Stations: Dilution of Precision Corrections	137
6.3	Conclusions	143
7	Conclusions and Future work	145
7.1	Conclusions	145
7.2	Future work	146
	Bibliography	149
A	Atmospheric properties	161
B	Detection systems and their technical details	163
B.1	GPS monitors at University of Nova Gorica	163
B.2	Raman lidar at Otlica Observatory	164
B.3	GPS Auger Motorola Oncore UT+ specifications	166
C	RINEX data format	167

List of Figures

2.1	Evolution of GPS signals from Block I through Block III (GPS III) satellites. Shown on the figure are the normalized power spectral densities of the signals in decibels, where the bandwidths spanned between the first spectral nulls of the P(Y)-code and L5 signals are each 20.46 MHz [5].	12
2.2	Spectral contents of the L2 broadcast (left side) and of the L1 broadcast (right side) from Block IIR(M) GPS satellites.	13
2.3	L2C code structure containing same CM but different CL (20 ms) segments in the CL period [64].	14
2.4	L5 signal modulation [2, 67].	15
2.5	Example of a pseudorange measurement [60].	18
2.6	From left to right: a) single differencing geometry, b) double differencing geometry and c) triple differencing geometry illustration.	19
2.7	An example of multipath effect [60], where the signal is reflected due to the water surface causing antenna to receive signal via two different paths.	24
2.8	Geographical positions of the two GPS units in Ajdovščina and Rožna Dolina [85].	26
2.9	Schematic diagram of monitors setup at University of Nova Gorica. 1 – receiver (OEM4 – G3 GPSCard in ProPak – G2plus enclosure); 2 – GPS antenna (GPS – 533 model); 3 – RF cable; 4 – 12 V power adapter cable; 5 – optional AC adapter or aircraft power conditioner; 6 – null modem data cable; 7 – data communications equipment (PC unit with LINUX system) (adapted according to [83]).	26
2.10	Recording setup at Rožna Dolina campus (left) and antenna setup at Ajdovščina campus (right).	27
2.11	Azimuth (left) and elevation (right) plots for satellite with PRN 10 on 25 June 2012 obtained with the receiver stationed at Rožna Dolina.	28
2.12	Sky-plot (left) for satellite with PRN 10 on 25 June 2012 and the visibility plot (right) for all satellites in view on 25 June 2012 at Rožna Dolina.	28
2.13	Principles of lidar system: emitted laser light scatters in all directions on particles and molecules in the atmosphere. Higher concentrations of aerosols and molecules results in more intensive scattering and more backscattered light reaches the lidars receiver. It has to be taken into consideration that the power density of irradiance decreases with the square of distance from the scatter [87].	29
2.14	Photo of Raman lidar at Otlica Observatory during the August campaign measurements (photo by Robert Bremec, August 2012).	30
2.15	Example of photon-counting lidar data (left) from Raman lidar N ₂ (red) and H ₂ O (blue) channel before (left) and after range correction (right). The measurement was performed on 24 August 2012.	32
3.1	Schematic diagram of the Earth’s atmosphere showing the different domains. The dark solid curves show atmospheric temperature profiles for solar maximum and minimum conditions [93].	36

3.2	Temperature and pressure profiles obtained from radiosonde measurement in Ljubljana, Slovenia on 12 October 2011 (left) and on 1 February 2011 (right).	39
3.3	Pressure profiles obtained from radiosonde measurement in Ljubljana, Slovenia on 12 October 2011 (left) and on 1 February 2011 (right). Blue line presents the actual/measured pressure, while the red line corresponds to fitting function of Eq. (3.4).	40
3.4	Mixing ratio profiles measured with Raman lidar, located at Otlica Observatory, Slovenia, on 12 October 2011 (left) and on 24 August 2011 (right).	42
3.5	Ionospheric profiles for mid-latitude ionosphere [25].	44
3.6	International Quiet Solar Year (IQSY) daytime atmospheric composition based on mass spectrometer measurements [91].	45
3.7	Schematic presentation of equatorial fountain that gives rise to the equatorial anomaly [104], where Fountain process is indicated with $\mathbf{E} \times \mathbf{B}$, \mathbf{B} indicates the magnetic field, g gravity, ∇_p pressure gradients, \mathbf{V} neutral wind and \mathbf{E} electric field.	47
3.8	Schematic figure showing the extend of aurora oval around the north pole [116].	48
3.9	The amount of attenuation of an EM wave traveling through the atmosphere as a function of its wavelength, where atmospheric windows are colored in light blue (adapted from [118]).	50
3.10	Schematic diagram showing the curved/bended signal path (denoted by L) and geometric straight-line signal path (denoted as G) between receiver/user U and satellite S (adapted from [1]).	51
3.11	The propagation path length of a signal through the ionosphere increases with the zenith angle ζ . The increased path length is accounted for in terms of a multiplier of the zenith delay called as obliquity factor [1]. R_E —average radius of the Earth, h_I — mean ionospheric height, IPP — ionospheric pierce point, ζ and ζ' — zenith angles of the satellite.	53
3.12	The schematic figure presenting geometry of ionospheric scintillation. Irregularities in the ionosphere introduce phase shifts that become amplitude perturbations as the wave propagates into the regions below the ionosphere [105, 119].	56
3.13	Global occurrence pattern for scintillations at 1.5 GHz during both sunspot maximum and minimum. The figure shows three major scintillation regions: magnetic equator at post-sunset, night-side auroral oval, and the polar cap (including the day-side cusp) at all times of the day [25, 103, 106].	57
3.14	Measured scintillation indices at two different locations. The first two at the top are display S_4 and σ_ϕ measured in Douala, Cameroon (equatorial region), while the two bottom ones show measured S_4 and σ_ϕ measured at Ny-Ålesund, Svalbard.	59
3.15	Comparison between Saastamonian (blue) and Hopfield (red) model for calculation of tropospheric delays for the period of 7 years (2005 – 2011). From top to bottom – ZTD (total delay in zenith direction), ZHD (dry delay in zenith direction) and ZWD (wet delay in zenith direction).	64
3.16	Comparison between Saastamonian (blue) and Hopfield (red) model for calculation of tropospheric delays for the year 2010. From top to bottom – ZTD (total delay in zenith direction), ZHD (dry delay in zenith direction) and ZWD (wet delay in zenith direction).	65

3.17 Bending of the ray in the neutral atmosphere. It can be noticed that the outgoing (vacuum) elevation angle α is smaller than the initial elevation angle α_0 [128, 130]. 68

3.18 Scattering behaviors for three different types of atmospheric particles [8], where (a) presents atmospheric dust and smoke particles, (b) atmospheric molecules and (c) large water droplets. 70

3.19 Example of Rayleigh scattering in the atmosphere at sunset where one can see different variations in colors (from blue to reddish orange color at horizon). This variation in colors is caused either by variations of concentrations of fine atmospheric dust or tiny droplets in the atmosphere which contribute to variations in atmospheric clarity [8]. Photo by Darko Veberič. 71

3.20 Schematic description of Rayleigh and two types of Raman scattering [132], where ν_i is the frequency of the incoming photon, ν_s is the frequency of the scattered/outgoing photon and ν_0 represents the frequency shift in different types of scattering. 72

4.1 Schematic presentation of typical GPS data processing flow for obtaining IWV from GPS observations. 77

4.2 Calculated weighted mean temperature (T_m) using Eq. (4.5), where the profile of partial pressure of water vapor and temperature were taken from radiosonde measurements performed by ARSO in Ljubljana, Slovenia in a 7 year period (2005 – 2011), together with surface temperature (T_s), pressure (p) and relative humidity (RH %) at the time of radiosonde launch. It can be clearly noticed that T_m has similar seasonal variation as T_s , with pronounced maximum in the summer time and minimum in the winter time. It can be also noted that some seasonal variation is present also in pressure and humidity time series. 79

4.3 Mean weighted temperature of the atmosphere displayed as a function of surface temperature with linear regression gradient and RMS of 3.32 K (left) and histogram distribution of residuals (observed T_m minus predicted T_m) (right). 81

4.4 Top – annual distribution of mean weighted temperature (T_m) using different parametrizations. On the left side comparison between T_m using Eq. (4.5) (black line) and T_m from Eq. (4.10) (blue line) is shown, while on the right side comparison between T_m using Eq. (4.11) (red line) and T_m from Eq. (4.5) is shown. Bottom – corresponding scatter plots where y -axis in both plots is T_m from radiosonde, while x -axis is T_m using Eqs. (4.10) and (4.11), respectively. 82

4.5 Mean weighted temperature of the atmosphere displayed as a function of surface temperature, humidity and pressure with RMS of 2.91 K (left) and histogram distribution of residuals (observed \hat{T}_m minus predicted T_m) (right). . . 83

4.6 Top – annual distribution of mean weighted temperature (T_m) using different parametrizations. On the left side a comparison between T_m using Eq. (4.5) (black line) and T_m from Eq. (4.11) (red line) is shown, while on the right a comparison between T_m using Eq. (4.12) (green line) and T_m from Eq. (4.5) is shown. Bottom – corresponding scatter plots where y -axis in both plots is T_m from radiosonde, while the x -axis is T_m using Eqs. (4.11) (left) and (4.12) (right), respectively. 84

4.7	On the left side calculated κ is presented, using the three different equations, where the blue line denotes κ obtained with Eq. (4.11), the red line stands for κ calculated with Eq. (4.10) and the dashed black is κ obtained with Eq. (4.4). On the right side calculated κ is presented, using Eqs. (4.11) (blue line) and (4.10) (red line).	85
4.8	Top–scatter plots presenting the correlation between the IWV from radiosonde profiles and the IWV from GPS ZWD, where I, II, III, IV denote different models (Table 4.2). Bottom–the corresponding histogram distributions of residuals.	87
4.9	Histogram showing distributions of residuals after applying the linear correction to the data set, where the numbers I, II, III, IV refer to different models (Table 4.3).	87
4.10	Top–scatter plots presenting the correlation between the IWV from radiosonde profiles and IWV from GPS ZWD (second usage of GIPSY-OASIS software), where I, II, III, IV denote different models (Table 4.4). Bottom–corresponding histogram distributions of residuals.	88
4.11	IWV, where black dots represent IWV from radiosonde, red dots the IWV using first GIPSY setup and T_m from radiosonde profiles, green dots are denoting the second GIPSY run with T_m from radiosonde and the black triangles are the IWV from the second GIPSY run with T_m from surface pressure, temperature and humidity data, for a period of 6 months (from 1 January 2010 to 1 July 2010).	89
4.12	Water vapor mixing ratio measured with Raman lidar at Otlica Observatory on 12 October 2011 as a result of consecutive 3.5 h sampling from 20:00 CET (left), and on 8 August 2012 as a result of consecutive 5.5 h sampling from 22:42 CET. The mixing ratio is plotted up to the height until error exceeds 50% of the value.	90
4.13	Water vapor mixing ratio measured with the Raman lidar at Otlica Observatory on 8 August 2012 as a result of consecutive 6 hours and 45 minutes sampling starting at 20:53 CET. Two layers of water vapor can be seen at ~ 1 km and between ~ 1.2 to ~ 1.4 km above the lidar site.	91
4.14	Horizontal displacement of the radiosonde along the ascend path on 12 October 2011. The blue line denotes the path of the radiosonde launched from Otlica Observatory (948 m a.s.l.) and the red line presents the path of the radiosonde launched from Potoče (111 m a.s.l.). Note, the right plot is presenting zoom of the left figure up to the altitude of 50 km.	92
4.15	From top to bottom–IWV calculated from GPS delay (blue dots denotes Ljubljana receiver and red dots receiver located in Rožna Dolina), radiosonde (black dots present radiosonde launched in Ljubljana and black triangle radiosonde launched at Potoče and at Otlica Observatory, respectively); ground pressure, temperature and corresponding humidity measurements (where blue line presents station in Ljubljana and red line station in Rožna Dolina), between 11 October and 20 October 2011.	93

4.16	From top to bottom—IWV calculated from GPS delay (blue dots denotes Ljubljana receiver and red dots receiver located in Ajdovščina) and IWV calculated from radiosonde in Ljubljana; ground pressure, temperature and corresponding humidity measurements (where blue line presents station in Ljubljana and red line station in Ajdovščina, between 1 August and 31 August 2012.	94
5.1	Geographical location of Douala, Cameroon.	99
5.2	Geometry of ionospheric pierce point calculation.	100
5.3	C is earth-fixed-centered coordinate system (left) and C' is local coordinate system, tangential to the Earth's surface at the geographical position \vec{g}	101
5.4	Top – Percentage of occurrence of S_4 for threshold I between 13 March 2004 and 29 February 2005. Middle – Percentage of occurrence of S_4 for threshold II between 13 March 2004 and 29 February 2005. Bottom – Percentage of occurrence of S_4 for threshold III between 13 March 2004 and 29 February 2005. The percentage of occurrence of S_4 was calculated as the ratio between the number of minutes with S_4 in a given threshold and the total number of minutes within one day. Note, white "spots" are data gaps and not indication that there was no scintillation activity.	102
5.5	Top – Percentage of occurrence of σ_ϕ for threshold I between 13 March 2004 and 29 February 2005. Middle – Percentage of occurrence of σ_ϕ for threshold II between 13 March 2004 and 29 February 2005. Bottom – Percentage of occurrence of σ_ϕ for threshold III between 13 March 2004 and 29 February 2005. The percentage of occurrence of σ_ϕ was calculated as the ratio between the number of minutes with σ_ϕ in a given threshold and the total number of minutes within one day. Note, white "spots" are data gaps and not indication that there was no scintillation activity..	103
5.6	Histogram presenting percentage of occurrence of S_4 for threshold I between 13 March 2004 and 29 February 2005. Note, white "spots" are data gaps and not indication that there was no scintillation activity.	104
5.7	Percentage of occurrence of S_4 for all three thresholds presented with different colors (light blue \mapsto I, red \mapsto II and brown \mapsto III) throughout the whole day. For description of details in the figure, please see text.	107
5.8	Percentage of occurrence of σ_ϕ for all three thresholds presented with different colors (light blue \mapsto I, red \mapsto II and brown \mapsto III) throughout the whole day. For description of details in the figure, please see text.	108
5.9	Percentage of occurrence of S_4 for all three thresholds presented with different colors (light blue \mapsto I, red \mapsto II and brown \mapsto III) between 17:00 and 00:00 UT hours. For description of details in the figure, please see text.	109
5.10	Percentage of occurrence of σ_ϕ for all three thresholds presented with different colors (light blue \mapsto I, red \mapsto II and brown \mapsto III) between 17:00 and 00:00 UT hours. For description of details in the figure, please see text.	110
5.11	Histograms presenting the number of satellites observing S_4 for threshold I within one month for more than one minute. Each month is denoted with number (i.e. 3 \mapsto March 2004, 4 \mapsto April 2004, 5 \mapsto May 2004, 6 \mapsto June 2004, 7 \mapsto July 2004, 8 \mapsto August 2004, 9 \mapsto September 2004, 10 \mapsto October 2004, 11 \mapsto November 2004, 12 \mapsto December 2004, 1 \mapsto January 2005 and 2 \mapsto February 2005).	111

5.12	Histograms presenting the number of satellites observing σ_ϕ for threshold I within one month for more than one minute. Each month is denoted with number (i.e. 3 \mapsto March 2004, 4 \mapsto April 2004, 5 \mapsto May 2004, 6 \mapsto June 2004, 7 \mapsto July 2004, 8 \mapsto August 2004, 9 \mapsto September 2004, 10 \mapsto October 2004, 11 \mapsto November 2004, 12 \mapsto December 2004, 1 \mapsto January 2005 and 2 \mapsto February 2005).	112
5.13	Histograms presenting the number of satellites observing S_4 for threshold II within one month for more than one minute. Each month is denoted with number (i.e. 3 \mapsto March 2004, 4 \mapsto April 2004, 5 \mapsto May 2004, 6 \mapsto June 2004, 7 \mapsto July 2004, 8 \mapsto August 2004, 9 \mapsto September 2004, 10 \mapsto October 2004, 11 \mapsto November 2004, 12 \mapsto December 2004, 1 \mapsto January 2005 and 2 \mapsto February 2005).	113
5.14	Histograms presenting the number of satellites observing σ_ϕ for threshold II within one month for more than one minute. Each month is denoted with number (i.e. 3 \mapsto March 2004, 4 \mapsto April 2004, 5 \mapsto May 2004, 6 \mapsto June 2004, 7 \mapsto July 2004, 8 \mapsto August 2004, 9 \mapsto September 2004, 10 \mapsto October 2004, 11 \mapsto November 2004, 12 \mapsto December 2004, 1 \mapsto January 2005 and 2 \mapsto February 2005).	114
5.15	Left column – geographical distribution of the percentage of occurrence of S_4 on (from top to bottom) 4 April 2004, 15 June 2004, 29 September 2004 and 19 December 2004 for threshold I. Right column – corresponding sky-plots presenting S_4 for all satellites in view over Douala, Cameroon.	115
5.16	Left column – geographical distribution of the percentage of occurrence of σ_ϕ on (from top to bottom) 4 April 2004, 15 June 2004, 29 September 2004 and 19 December 2004 for threshold I. Right column – corresponding sky-plots presenting σ_ϕ for all satellites in view over Douala, Cameroon.	116
6.1	Location and structure of the Pierre Auger Observatory. Black dots show all theoretical positions of surface detector stations where the active ones (in the year 2012) are indicated with red circles, blue lines indicate the field of view of the fluorescence telescopes, located in four buildings on the perimeter of the surface detector (names marked in blue color).	118
6.2	The Pierre Auger Observatory surface detector, with marked components (left), motherboard of GPS receiver Oncore UT+ (right).	119
6.3	2D layout of the SD unit triangles in array-local Cartesian coordinates (left) and color-coded WGS84 altitude (height above the ellipsoid) of the SD stations in UTM easting/northing coordinates (right).	120
6.4	3D layout of the SD unit triangles from the Auger database (left) and the corresponding elevations from the digital elevation model [161] (right) in geographic coordinates.	121
6.5	The 3D difference between the station elevations from the Auger database and the digital elevation model.	121
6.6	The difference between the station elevations and the digital model map in color code (top) and the corresponding histogram (bottom), in the Auger database (left) and after the GPS measurement campaign (right). In the right plot the stations with GPS receivers still running in position hold mode are removed, i.e. resulting in more holes than in the left plot, see Section 6.2.2.	122

6.7	The difference between the elevation values from database and the navigate mode run, this time with a lighter color coding (left). x and y values are the 2D coordinates of the PampaAmarilla coordinate system. A larger view of the two interesting parts of the array, including the station ID numbers (right): close to Loma Amarilla (top) and close to Los Morados (bottom).	123
6.8	2D (horizontal) differences between the database entries and the navigate mode run. The green circle denotes a radius of 10 m (left). The same for elevation difference with green-indicated bounds of ± 15 m outside (right). . . .	123
6.9	Navigate mode measurement campaigns A, B and C in December 2009, and D in March 2010 as extracted from the Motorola UT+ log files. Blue points show the fluctuations of height h around the mean $\langle h \rangle$ for station with ID 137. Red points correspond to the Central Data Acquisition System (CDAS) initialization values taken from the survey database and sent to the station during the regular operation in the position–hold mode.	124
6.10	Distribution of total number of position measurements per station for all campaigns A–D (left). Total number of position measurements by station ID (right).	125
6.11	Distribution of time differences between consecutive GPS position measurements for all campaigns A–D for several randomly selected stations.	126
6.12	Fluctuations of height h around the mean $\langle h \rangle$ between the 24 and the 29 December 2009 (C) for several randomly selected stations.	127
6.13	Fluctuations of height h around the mean $\langle h \rangle$ between the 24 and the 29 December 2009 (C) for all 15 randomly selected stations from Fig. 6.12 plotted on the same graph (different colors for different stations).	128
6.14	Fluctuations of height h around the mean $\langle h \rangle$ between the 24 and the 29 December 2009 (campaign C) for the station with ID 1581 with color-coded days (left), and the same data but with a UTC-day wrapped time axis in UTC hours (right) in order to expose more clearly the obvious repeating of the drift patterns in each of the days. The consecutive shifts come from the difference of the solar and sidereal time (~ 4 min/day).	128
6.15	Correlation between easting, $e - \langle e \rangle$, and northing, $n - \langle n \rangle$, during the 24 and 29 December 2009 (campaign C) for the station with ID 1581. Color coding corresponds to the different days (in UTC time).	129
6.16	Trajectories of all visible GPS satellites (in zenith and azimuthal angles in a polar diagram) above Nova Gorica, for two consecutive days, 13 (larger red dots) and 14 (smaller blue dots) February 2011. Note that between these two days the travel pattern almost did not change. The exclusion zone towards the North (the GPS receiver in Nova Gorica is at 45.94°N , 13.64°E geographical location) is due to the 55° tilt of the GPS orbits, i.e. satellites do not fly over the North/South caps. In Malargüe the Southern exclusion zone should be smaller, with distance to the zenith point more like $\sim 25^\circ$ (and not $\sim 12^\circ$ like in Nova Gorica).	130
6.17	Distributions of northing, easting, and height related standard deviations σ_n , σ_e and σ_h over the stations. The average standard deviations taken over all the stations are 249, 154, and 494 cm, respectively.	131
6.18	Correlation time τ in the case of a station with ID 1581.	131
6.19	Distribution of northing, easting and height correlation time (left) and spread of the mean $\sigma_{\langle n \rangle}$, $\sigma_{\langle e \rangle}$, and $\sigma_{\langle h \rangle}$ (right) among the stations.	132

6.20	Systematic difference of the horizontal part of the position means of the stations, $\langle e \rangle_2 - \langle e \rangle_1$ and $\langle n \rangle_2 - \langle n \rangle_1$, where the indices refer to the consecutive measurement campaigns resulting in plots for the difference between the campaigns B–A, C–B, and D–C.	134
6.21	Systematic difference of the mean vertical position of the stations, $\langle h \rangle_2 - \langle h \rangle_1$, where the indices refer to the consecutive measurement campaigns resulting in plots for the difference between the campaigns B–A, C–B, and D–C.	134
6.22	Systematic difference of the mean vertical position of the stations, $\langle h \rangle_D - \langle h \rangle_C$, for the campaigns D–C (left). Outline of the SD array in the same scale, superimposed on the satellite image map, and given for easier identification of the elevated stations above (left).	135
6.23	Mean of the northing and easting positions, $\langle n \rangle$ and $\langle e \rangle$, from the campaigns A–D relative to the most frequent positions, n_{pms} and e_{pms} , from the log files for years 2009 and 2010.	135
6.24	Distribution of differences $n_{\text{pms}} - \langle n \rangle$, $e_{\text{pms}} - \langle e \rangle$, and $h_{\text{pms}} - \langle h \rangle$ over the stations.	136
6.25	Map of height differences $h_{\text{pms}} - \langle h \rangle$. Size of a circle is proportional to the absolute difference where for the touching circles this amounts to 20 m. Stations with $h_{\text{pms}} - \langle h \rangle \leq -5$ m are shown in red color and stations with $h_{\text{pms}} - \langle h \rangle > 5$ m in blue color. The rest is depicted in green. The horizontal positions of the stations are easting and northing subtracted by the corresponding values for the Malargüe coordinate system origin.	137
6.26	Map of horizontal differences ($e_{\text{pms}} - \langle e \rangle$, $n_{\text{pms}} - \langle n \rangle$). Size of an arrow is proportional to the square-root of the shift (in order to emphasize small deviations) where the largest arrows correspond to ~ 20 m of horizontal distance. Stations with shifts larger than 10 m are shown in red color and the rest is depicted in blue. The horizontal positions of the stations are easting and northing subtracted by the corresponding values for the Malargüe coordinate system origin. Note the locally ordered structure of shifts that are probably related to the surveying campaigns.	138
6.27	Time-line of the five measurement campaigns A–E, illustrated with the changing of the northing component n of station with ID 137.	139
6.28	Number of available position measurements per each station ID. In blue numbers for previous four measurement campaigns A–D and in red numbers for all five campaigns A–E.	139
6.29	Illustration of the origin of dilution of precision (DOP). <i>Left</i> : Good constellation of tracked satellites. <i>Right</i> : Bad constellation with close-by satellite directions, effectively reducing the number of degrees of freedom. Image taken from [60].	139
6.30	Measurement of height h for station with ID 1581 during one whole day (6 Feb 2012) of the last measurement campaign E (top). Vertical dilution of precision (VDOP) in units of pseudo-range error σ for the same time period (middle). Number of observed GPS satellites during this time period (bottom).	140
6.31	Difference between all station means for horizontal positions (n and e) for two consequent measurement-campaign pairs, using normal, unweighted averaging (top). The weighted means are the weights depend on instantaneous values of the HDOP parameter (bottom).	142

6.32	Difference between all station means of vertical positions (h) for two consequent measurement-campaign pairs, using normal, unweighted averaging (top). The same, but this time with the weighted means where the weights depend on instantaneous values of the VDOP parameter (bottom).	142
B.1	GPS receiver system functional diagram. 1–enclosure; 2–GPSCard; 3–RF section; 4–digital section; 5–controls; 6–RF-IF sections; 7–signal processor; 8–clock; 9–22-BIT CPU; 10–system I/O; 11–AGC; 12–clock; 13–VCTCXO; 14–optional LNA power; 15–power supply; 17–RF and power; 18–data and signal processing; 19–COM1; 20–COM2; 21–COM3; 22–input timing signal; 23–output timing signal; 24–USB communication [83].	164
B.2	Raman lidar setup at Otlica Observatory. M1–mirror; BS1, BS2–beam splitter; IF–Interference filter; PMT–photomultiplier tube; HV–high voltage power supply [89].	164
C.1	Standard naming convention for RINEX data files [172,173]	167

List of Tables

2.1	Overview of GPS satellite generations launched, where each Block presents different generation [2,4,52].	10
2.2	Summary of GPS signal characteristics [2].	16
2.3	GPS data differencing methods [73].	19
3.1	Composition of pure dry air up to 25 km [90]. It can be noticed that two main constituents are nitrogen (78.09%) and oxygen (20.95%).	37
3.2	Variable constituents of air [96–98].	37
3.3	Layers of daytime mid-latitude ionosphere [25], with corresponding major components and their main ionization processes.	44
3.4	Some empirical values of refractivity coefficients [18,125]. Values that are used in the scope of dissertation are presented with bold text.	61
3.5	Coefficients of the hydrostatic mapping function in NMF [53,126].	67
3.6	Coefficients of the wet mapping function in NMF [53,126].	67
3.7	Values of the parameters c_0 , c_{10} , c_{11} and ϕ , needed for the determination of the coefficient c in Eq. (3.68) for the hydrostatic mapping function in VMF1 [131].	69
3.8	Values of the parameters c_0 , c_{10} , c_{11} and ϕ , needed for the determination of the coefficient c in Eq. (3.68) for the total mapping function in VMF1 [131].	69
3.9	Cross section of Rayleigh and Raman scattering of N_2 and H_2O [89].	73
4.1	Different JPL’s Precise Orbit and Clock products with information about their latency, 3D RMS accuracy and product availability [136].	76
4.2	Description of the regression models (denoted with different roman numbers) presented in Fig. 4.8 together with their statistical information.	85
4.3	Description of the regression models (denoted with different roman numbers) presented in Fig 4.9 together with their statistical information. StdDev’ denotes standard deviation after the new estimate of IWV (Eq. (4.14)) where parameters a and b were obtained by linearly fitting the IWV_{rad} vs. IWV_{gps}	86
4.4	Description of the regression models (denoted with different roman numbers) presented in Fig. 4.10 together with their statistical information. StdDev-New denotes standard deviation after the second GIPSY run.	88
5.1	Division of the scintillations according to the value of S_4 with denoted roman number used in text.	98
A.1	Temperature, pressure and density (dry air and water vapor) variations with height according to U.S. Standard Atmosphere, 1976 [95].	161
B.1	General specification parameters of NovAtel antenna (model ANT-C2GA-TW-N) [83].	163
B.2	Specification parameters of the Raman lidar system [89].	165
B.3	Oncore technical characteristics for UT model [158].	166

List of Symbols

α_0	initial elevation angle.....	68
α	elevation angle.....	64
$\langle \epsilon \rangle$	background average dielectric permittivity.....	55
$\langle x \rangle$	estimate of the mean.....	130
$\langle \rangle$	average.....	58
β	stands for coefficients a, b, c	66
dg	line segment along the geometrical path G	50
dp	differential change in pressure.....	38
dz	differential change in height.....	38
$\Delta \nabla L$	double difference observation for carrier phase.....	20
$\Delta \nabla P$	double difference observation for pseudorange.....	20
$\Delta \nu_{\text{vib}}$	Raman wavenumber shift.....	72
$\delta \Phi^s(j)$	uncalibrated phase delays in the satellite.....	18
$\delta \Phi_r(j)$	uncalibrated phase delays in the receiver.....	18
δ_{iono}	ionospheric effects.....	17
δ_{trop}	tropospheric effects.....	17
ΔE	energy difference.....	72
ΔL	single difference observation for carrier phase.....	19
ΔL	total delay.....	51
ΔP	single difference observation for pseudorange.....	20
δt^s	satellite clock error.....	17
δt_r	receiver clock error.....	17
$\Delta \phi$	variation of the optical path length.....	55
ϵ	dielectric permittivity.....	55
λ	wavelength.....	49
B	magnetic field.....	47

\mathbf{E}	electric field	47
\mathbf{V}	neutral wind	47
∇_p	pressure gradients	47
ν_0	frequency shift	72
ν_g	group velocity	52
ν_i	frequency of the incoming photon	72
ν_p	phase velocity	52
ν_s	frequency of the scattered/outgoing photon	72
$\partial\Delta\nabla L$	triple difference observation for carrier phase	20
$\partial\Delta\nabla P$	triple difference observation for pseudorange	20
ϕ	latitude	62
Ψ	parameter that specifies the Northern or Southern hemisphere	69
ρ_r^s	geometric range between the receiver r at the reception time and satellite s at the emission time	17
ρ	density of air	38
ρ_d	density of dry air	41
ρ_m	the density of moist air	61
ρ_v	density of water vapor	41
h	hour	57
m	meter	59
σ_ϕ	phase scintillation index	58
σ_e	standard deviation for easting	129
σ_h	standard deviation for height	129
σ_n	standard deviation for northing	129
σ_x	unbiased estimate for the standard deviation	130
$\sqrt{\quad}$	square root	58
τ	correlation time	131
L1C	GPS signal at frequency 1575.42 MHz	16
L1	GPS signal at frequency 1575.42 MHz	12

L2C	GPS signal at frequency 1227.60 MHz	11
L2	GPS signal at frequency 1227.60 MHz	12
L5	GPS signal at frequency 1176.45 MHz	11
M	military signal at frequency L1 and L2	11
a.s.l.	above sea level	42
RH	relative humidity	42
bs	bits per second	13
dBW	decibel watt	15
dB	decibel	13
ms	millisecond	13
cm ³	cubic centimeters	45
cm	centimeter	43
eV	electron volt	118
g/cm ²	gram per square centimeter	43
hPa	hecto pascal	63
km ²	square kilometre	118
km	kilometer	35
K	Kelvin	35
m/s	meter per second	48
Pa	Pascal	60
W	watt	119
ε_{mul}	error due to the multipath	17
ε_{rx}	error due to the receiver noise	17
ζ	zenith angle	53
°	degrees	42
<i>i</i>	in form of subscript represents either dry or wet component	66
a_i, b_i, c_i	mapping parameters	66
<i>c</i>	speed of light	52
c_2, c_3, c_4, c_5	frequency independent coefficients	52

$d_F = \sqrt{\lambda(z - L/2)}$	first Fresnel zone	56
e	vapor pressure	41
e_s	saturation vapor pressure (pure phase)	42
f	frequency of the signal	52
f	the frequency of the incident wave	55
f_{p0}	plasma frequency corresponding to the N_0	55
G	geometrical path between satellite (S) and user(S)	50
g	gravitational acceleration	38
H	orthometric height of the antenna	62
h	Planck's constant (6.626×10^{-34} kg m ² /s)	72
h	height	62
$H = RT/gM$	scale height	38
h_d	height above the antenna at which the $N_{d0}(h_d) = 0$	62
h_1	mean ionospheric height	53
H_s	height above sea level	66
I	signal intensity	58
$k_0 = 2\pi/\lambda$	free-space wavenumber	55
L	minimum electrical path length	51
L_r^s	carrier phase observation between satellite s and receiver r	18
M	molar mass of air	38
m	general mapping function	64
M_d	molecular weight of the dry air	41
m_d	dry component mapping function	64
m_d	mass of dry air	41
m_{vs}	the mass of water vapor the sample would have had if it were saturated	41
M_v	molecular weight of the water vapor	41
m_v	mass of water vapor	41
m_w	wet component mapping function	64
N	refractivity	60

n	refractive index	51
N_0	background electron density	55
N_{d0}	dry refractivity at the surface	62
N_d	dry refractivity	60
N_T	fluctuations of the total electron content	55
N_w	wet refractivity	60
n_e	electron density	52
N_j	carrier phase ambiguity at frequency band j	18
$n_r^s(j)$	integer ambiguity of satellite s , receiver r and frequency band j	18
p_d	pressure of dry air	41
P_{\max}	power level of the third peak down from the maximum excursion of the scintillations	58
P_{\min}	power level of the third peak up from the maximum excursion of the scintillations	58
p_s	surface pressure	63
P_r^s	pseudorange observation between satellite s and receiver r	17
R	gas constant	38
r^s	satellite position vector	18
R_d	specific gas constant for dry air	41
R_E	average radius of the Earth	53
R_v	specific gas constant for water vapor	41
r_e	classical electron radius	55
r_r	receiver position vector	18
S_4	ionospheric amplitude scintillation index	58
SI	ionospheric amplitude scintillation index	58
T	temperature	38
t	time from January 0.0	66
T_0	adopted phase	66
T_m	weighted mean temperature	75

T_s	surface temperature	62
w	mixing ratio	41
z	height of the upper boundary of the irregular layer L	56
Z_d	compressibility factor of dry air	61
Z_w	compressibility factor of water vapor	61

CHAPTER 1

Introduction

What has been one scientist's "noise" is another scientist's "signal".

— Martin Morre-Ede (1986)

1.1 Background

The Global Positioning System (GPS) was developed by the Department of Defense (DoD) of the United States in 1973 and became fully operational in 1995 [1–4]. The main purpose of GPS is to provide location and time information in all weather conditions, anywhere on or near the Earth, where there is an unobstructed line of sight to four or more satellites [1]. The satellite constellation nominally consists of 24 satellites arranged in 6 orbital planes with 4 satellites per plane [1, 2]. These satellites operate in near circular orbits at a height of $\sim 20\,200$ km with inclination angle of 55° and a period of approximately 12 hours sidereal [2, 4]. One of the main objectives behind the development of the GPS system was to replace the Navy Navigation Satellite System, also known as Transit. Transit was a pioneering achievement of the Applied Physics Laboratory of the John Hopkins University. The development of the concept for the Transit system started in 1959 and the final system became operational in 1964 [1]. Similar systems and satellite-based augmentations are being developed and deployed by different governments, international consortia and commercial interests. For instance, the Soviet Union developed similar system called Globalnaya Navigatsionnaya Sputnikovaya Sistema (GLONASS) in the late 1980s [2, 5], while China is developing regional satellite navigation system called BeiDou Navigation Satellite System. BeiDou 3 consists of two separate satellite constellations – a limited test system that has been operating since 2000, when they launched two GEO (where GEO stands for geosynchronous equatorial orbit) satellite and a full-scale global navigation system that is currently under construction [5]. A more promising system currently under development is the European system GALILEO, which was conceived as a joint public-private enterprise under civilian control, to be financed and managed by the European Commission (EC), the European Space Agency (ESA) and industry. The first two of four operational satellites were launched on 21 October 2011, to validate the system, followed by a second launch on 12 October 2012. Full completion of the 30-satellite system is expected by 2019 [1, 6]¹. The generic name for these systems is Global Navigation Satellite System (GNSS) [1]. Although GPS was primarily developed for military use, there are many civil applications of GPS such as land transportation and maritime uses, precise time dissemination, high-precision (millimeter-to-centimeter level) positioning and consumer products.

¹beside those there are also Quasi-Zenith Satellite System (QZSS), developed by the government of Japan; Indian Regional Navigation Satellite System (IRNSS) and augmentation systems (satellite-based, ground-based and aircraft-based).

In all applications, the distance between GPS satellites and receivers is determined either by pseudorange (measuring the time of flight of the time-tagged radio signals that propagate from satellites to receivers) or by phase measurements [1–4]. Both approaches are affected by the presence of the Earth’s atmosphere, which increases the optical path length between satellite and receiver and thus also the corresponding time of travel of the GPS signal. When electromagnetic waves (EM), such as GPS signals, propagate through the Earth’s atmosphere, they “suffer” not only bending but also retardation, due to the different refractivity indices of each layer. Refraction, described by *Snell’s law* [7], occurs in the atmosphere when an EM wave passes at an angle through atmospheric layers with different speed of propagation, e.g. having varying humidity, electron density, temperature, pressure, etc. These variations influence the optical density of the atmospheric layers, which in turn causes a bending and retardation of the EM wave while passing from one layer to another [8,9]. One of the key tasks of geodetic GPS processing software is therefore to “correct” the ranges between the satellite and the receiver or in other words to remove the effects of the Earth’s atmosphere, thereby reducing all optical path lengths to straight-line path lengths [10].

In particular, solar flares and coronal mass ejection (CMEs) can induce geomagnetic storms that can make the Earth’s ionosphere unstable, causing rapid changes and spatial gradients in plasma density distribution which can strongly effect the radio wave propagation between space and Earth [11–13]. The free electrons of the ionosphere, which extends from about 60 km up to about 1000 km above the Earth’s surface, effect the propagation of radio waves. At frequencies above approximately 30 MHz, radio waves pass through the ionosphere but suffers from dispersion [3]. The ionosphere is normally well ordered with slow and predictable changes however, particularly during geomagnetic storms (even more pronounced during a solar maximum), rapid changes and strong gradients over distance can ultimately degrade GPS ranging measurements to the extent that users can lose signals [14–16]. Furthermore, small-scale structures in the ionosphere can cause scintillation of the signal. Scintillations are rapid changes in the amplitude and phase of the signal. Amplitude scintillations, that cause rapid changes in the signal-to-noise ratio, can lead to loss of carrier tracking in all receivers. Phase scintillation, that sufficiently disturbs the carrier phase causes the receiver phase tracking loop to lose lock thus impacting the reception of the important navigation data message which includes the satellite ephemerides. The code tracking loop, that measures range to the satellite, is fairly robust to phase scintillation and usually remains locked [17].

While ionospheric effects on GPS signals can be, to first order, compensated with given measurements on two different frequencies, this cannot be done in the case of delays caused by the neutral atmosphere. In the case of a delay caused by the neutral atmosphere, no dispersion effects are present and elimination is therefore not possible [1–4]. The neutral atmosphere is a mixture of dry gases and water vapor. Water vapor is unique in this mixture because it is the only constituent which possesses a dipole moment contribution to its refractivity, which is 20 times larger than non-dipole component throughout most of the troposphere [3,10,18]. As a consequence it is common to treat the dipole component of the water vapor refractivity separately from the non-dipole components of refractivities in the atmosphere. These two components are know as the “wet” and “hydrostatic” (sometimes referred to us as the “dry”) delays. Both of them are smallest in the zenith direction and increase approximately inversely with the sine of the elevation angle [3]. While the

dry delay (which presents 90% of the tropospheric error) can be very well modeled and determined by surface pressure, temperature and/or height of the station (depending on the model) this is not the case for wet delay. Although the wet delay is always much smaller than the dry one, it is usually far more variable due to the irregular distribution of water vapor in the atmosphere and is thus more difficult to remove [1–3,10].

As opposed to geodesicists, whose interest is to estimate ionospheric and tropospheric delay and then “eliminate” them, thus increasing the accuracy of the measurements. Ionospheric scientists, meteorologists and environmentalists use this additional information about water vapor and electron density/scintillation in the atmosphere as an input in weather forecasting, climate studies, hazard predictions and early warning systems [10].

1.2 State of the art

Electromagnetic waves provide powerful tools for observing and measuring certain properties of the Earth’s atmosphere. Quantitative measurements, which greatly extend direct sensory observations, are made by radar, by satellite sensors and by many other instruments [10]. Over the last 100 years various traditional techniques have been applied by different countries worldwide to monitor atmospheric properties. A brief overview of some of them is provided below.

In the past in-situ measurements using direct sensors, such as radiosondes, were the only way to measure water vapor in the atmosphere. A radiosonde is a balloon-borne instrument (also called weather balloon), with radio transmitting capabilities, which is capable of in-situ measurements of humidity, pressure, air temperature, wind speed and wind direction as a function of height [3]. In the 1940s a global radiosonde network had been established and in 1991 more than 1000 radiosonde had been installed by 92 countries [10]. With knowledge of temperature, pressure and humidity at specific heights, one can then, among the others calculate the amount of water vapor (i.e. water vapor profile) and further the integrated water vapor (IWV). One of the major disadvantages of radiosondes is that the data quality is variable in the upper troposphere and poor in the stratosphere and with quality of observations poor at very high and low humidities. Second, their very sparse launches (not more than 4 times per day) is another important disadvantage. Although radiosondes can be launched in any type of weather and can under ideal conditions provide temperature measurements accurately to about 0.5 K, severe thunderstorms and heavy precipitation can lead to system failures [10]. Furthermore, differences in instruments used by different countries make data interpolation difficult [19].

On the other hand, LIDARs (**L**ight **D**etection **A**nd **R**anging) can be very useful for detailed local studies of atmospheric properties such as aerosol content, mixing ratio profiles, temperature profiles, etc (depending on the system). The LIDAR is an active remote sensing technique that operates in a similar way to sonar and radar systems [20–23]. A pulse of laser light is emitted into the atmosphere where a portion of light is scattered by molecules and aerosols. The amount of return due to the backscatter from the molecules and aerosols is then collected by a receiver and measured versus time. With knowledge of the speed of light, the time is then converted into altitude. The number of photons counted for each altitude bin is then proportional to the concentration of the investigated constituent (i.e. the amount of water vapor, dust particles etc., depending on the user selected wavelength) at that alti-

tude [20–24]. Using LIDAR measurements one can get high-quality data with high vertical and temporal resolution, however measurements are limited in daytime and in cloudy conditions (especially in the case of our Raman LIDAR system). Furthermore, the systems are very expensive and usually require highly skilled operators. Beside the radiosonde and LIDAR there are numerous other observation tools used for water vapor measurements, such as ground-based water vapor radiometers and instruments mounted on special aircraft [10].

In the past, most of the information gathered worldwide concerning properties of the ionosphere has come through the direct measurements of quantities by radio soundings. For more than half a century, sounding the ionosphere with ionosondes has been the most important technique, which is in principle high frequency (HF) radar that records the time of travel of a transmitted HF signal as a measure of its ionospheric reflection height. By sweeping in frequency (typically from 0.5 to 20 MHz), an ionosonde obtains a measurement of the ionospheric height as a function of frequency [25, 26]. However one of the major disadvantages of the ground-based ionosonde technique is that it is essentially restricted to observations of the bottomside of the ionosphere [26].

Since GPS became fully operational, it has produced an unprecedented high accuracy and great flexibility with a tremendous contribution to navigation, positioning, timing and scientific questions related to precise positioning on the Earth’s surface. Furthermore, because it gives highly precise, continuous, all-weather and real-time measurements, with signals that travels through the Earth’s atmosphere, additional scientific applications have been explored by scientists [3, 27, 28]. Ground-based, aircraft based and GPS receivers on Low Earth Orbit (LEO) satellites can receive refracted signals that travel through the Earth’s atmosphere. These refracted signals can then be used to estimate characteristics of the Earth’s atmosphere [27].

In general the use of GPS in atmospheric studies can be divided into two major groups: space born GPS Meteorology and ground based GPS Meteorology [3, 29]. Here, the GPS or GNSS Meteorology refers to the use of the effects of the Earth’s atmosphere on the propagation of GPS signals in order to derive atmospheric parameters such as the ionospheric Total Electron Content (TEC), tropospheric temperature, pressure and water vapor content, which could be used in ionospheric science and meteorological applications [3, 10].

Space born GPS meteorology

LEO satellites are equipped with a GPS receiver and are being used to “track” the signals of rising or setting GPS satellites behind the Earth’s limb. GPS satellites send navigation signals, which pass through successively deeper layers of the Earth’s atmosphere and are received by LEO satellites. These signals are bent and retarded, due to the atmospheric constituents, causing a delay in the arrival at the LEO satellite. This delay is measured and can be inverted to give vertical profiles of refractivity, temperature, pressure and humidity within the neutral atmosphere and electron density in the ionosphere. This general technique is known as atmospheric *radio occultation* [10, 27, 30]. The development of this technique dates to the early 1960s when Mariners 3 and Mariners 4, viewed from Earth, passed behind Mars. One of the first demonstration experiments, called GPS/MET, to limb probe the Earth’s atmosphere was carried out in the early 1990s by a group led by the University Corporation for Atmospheric Research (UCAR), where they converted a low cost geodetic ground receiver to fly in space on a satellite to acquire occultation

data [10, 27, 29–31]. Since then several other atmospheric sounding missions have been launched aboard LEO satellites: CHAMP (CHALLENGING Minisatellite Payload) was a German small satellite mission for geoscientific and atmospheric research and applications, managed by GFZ German Research Centre for Geosciences, which is no longer active but data are available [32], GRACE (Gravity Recovery and Climate Experiment), COSMIC (Constellation Observing System for Meteorology, Ionosphere and Climate) and MetOp. MetOp is a series of polar orbiting meteorological satellites operated by the EUMESAT (EUROPEAN organization for the exploitation of METeorological SATellites). Although that the MetOp satellites are primarily used for providing the data to support operational meteorology, environmental and climate monitoring, they also carry on board the GRAS (GNSS Receiver for Atmospheric Sounding) instruments, specifically designed in Europe for radio occultation measurements [33]. These kind atmospheric missions provide more than 5000 occultation data with daily global coverage [10].

Ground-based GPS meteorology

Just as space-based GPS measurements are capable of determining temperature, pressure, water vapor profiles and ionospheric electron density, ground-based GPS measurements take advantage of the frequency signals collected by a GPS receiver at a fixed point on the ground. By using existing continuously operating stations, the observations of the wet delay on the signal can then be used for quantifying the water vapor along the path between the satellite and the receiver. Furthermore, using the dispersive nature of the ionosphere, the delay caused by the ionosphere can then be inverted into TEC along the signal path [28, 34–36]. While both methods are discussed and presented in detail in Chapters 3 and 4, here we give a brief overview of the development and current status of the ground based GPS meteorology.

The potential use of ground-based GPS receivers for atmospheric research, in particularly for remote sensing of water vapor, was introduced by Bevis *et al.* (1992, 1994) [3, 28, 35]. They proposed a method where, with given surface temperature and pressure readings at the GPS receiver, the retrieved zenith wet delay can be transformed with very little additional uncertainty into an estimate of the integrated water vapor above the receiver [3]. Based on the approach suggested in [3, 28, 35], experiments were conducted in 1993-1994 that demonstrated the use of GPS data for the continuous monitoring of IWV from ground-based stations. One of them was the GPS/STORM (Storm-Scale Observations Regional Measurement Program) [34, 37, 38] experiment, performed at sites in Colorado, Kansas and Oklahoma using 6 receivers over a 1 month period. The experiment compared water vapor measurements obtained with GPS to water vapor radiometer measurements (WVR) and demonstrated the validity of the method [34, 37, 38]. The second experiment, conducted by the National Oceanic and Atmospheric Administration (NOAA) and the University NAVSTAR Consortium (UNAVCO), was the GPS-Winter Icing and Storms Project experiment (GPS-WISP94) [37, 38]. The main purpose of the GPS-WISP94 experiment was to investigate the scientific and engineering (hardware and software configurations, data acquisition parameters etc.) issues involved in developing an operational GPS IWV system [38]. The two experiments lead to development of the NOAA GPS Integrated Precipitable Water Vapor (GPS-IPW) network [38]. Since then a number of research project were carried out using continuous GPS networks for the monitoring of Earth's atmosphere. On a global scale one such network is IGS (International GNSS Service), which coordinates many applications not only

for accurate positioning but also for remote sensing [39]. Officially established in January 1994, the IGS operates as a voluntary, non-commercial confederation involving more than 200 institutions world-wide, providing users with precision GPS satellite orbit and clock corrections and other products such as tropospheric zenith path delays and ionospheric TEC grids [40]. In Europe the development of such networks dates back to 1996, when several research projects were carried out over a ten-years period, like WAVEFRONT (GPS Water Vapour Experiment For Regional Operational Network Trials, 1996-1999), NEW-BALTIC (Numerical Studies of the Energy and Water Cycle of the BALTIC Region), MAGIC (Meteorological Applications of GPS Integrated Column Water Vapor Measurements in the Western Mediterranean, 1998-2001), TOUGH (Towards Operational Use of GPS Humidity Measurements in Meteorology, 2003-2006) and the COST Action 716 (where COST is the French acronym for European cooperation in the field of scientific and technical research, 1998-2004) [41–47]. At the same time national and international surveying and research organizations started to invest in continuously operating ground-based GPS networks [41], not only for support in GPS meteorology but also for geodetic applications. Based on the main conclusions from these projects, proposal was made for the E-GVAP-I project with main objective to move from test phase to an operational GNSS observing system producing near-real-time tropospheric delays and IWV, useful in operational numerical weather prediction models [41, 47]. E-GVAP-I started in 2005 as a common part of the European network of National Meteorological Services (EUMETNET), and was officially closed in 2009, when E-GVAP-II started and will run until the end of 2013 [48]. For the moment the E-GVAP network consists of more than 1500 GNSS sites. Mainly in Europe, but recently processing and distribution of global GNSS data has started, since many E-GVAP members run global NWP models. For the same reason E-GVAP welcomes collaboration with both European and non European institutions, in order to density the GNSS meteorological observing network [48]. These kind of ground-based networks not only provide data for meteorological purposes but, because they store raw (RINEX format) GPS data, benefits also other scientific fields like ionospheric monitoring [49], monitoring surface motion [50] and many more. Furthermore, because Earth's atmosphere "produces" noise terms in GPS positioning, these kind of meteorological observing networks and models contain useful information which can in future help geodesists to determine positions faster and more precisely. This kind of cooperation between different fields of science leads to sharing of GPS site facilities therefore helping to reduce costs. The use of ground-based GPS receivers it is now very well established and the estimation of IWV has consistently been shown to be accurate to 1-2 kg/m² [51].

1.3 Aims and Objectives of the thesis

This thesis summarises an attempt to introduce GPS techniques into the research efforts at the University of Nova Gorica. The main aim of the PhD research was therefore to investigate potential benefits of using GPS techniques in different existing research areas at the University of Nova Gorica, such as precise timing of cosmic ray arrivals, ionospheric physics, tropospheric remote sensing.

Specific objectives of the presented PhD research were:

- to set up a ground based GPS monitoring system at the University of Nova Gorica as a widely applicable atmospheric research tool,

- to investigate capabilities of the GPS system for remote sensing of water vapor in SW part of Slovenia as a complementary tool to the existing Raman lidar located at Otlica, Slovenia,
- to investigate potential future use of the GPS system for detection of ionospheric scintillations by analysing data obtained by a similar system located in Douala, Cameroon, and
- to improve the positioning of surface detectors at the Pierre Auger Observatory, Pampa Amarilla, Argentina, and through that to improve the precise-timing of cosmic ray arrivals to the surface.

1.4 Structure of the thesis

In general, the thesis can be divided in two major parts – theoretical and practical. While the theoretical part of the thesis is outlined in Chapter 2 and Chapter 3, the experimental work is described in Chapters 4, 5 and 6. Chapter 7 provides a summary of thesis together with some prospects and recommendations for future work.

In Chapter 2 a description of the Global Positioning System is given, its signal structure, observables and some errors and biases that are not described in following Chapters. Moreover, beside GPS, a short description of the Raman Lidar technique is given, together with some data examples.

The first part of Chapter 3 deals with a description of the Earth's atmosphere, its structure and properties, such as chemical composition, pressure, temperature and electron density variations together with some examples. The second part of Chapter 3 gives a detailed introduction to the propagation of electromagnetic waves in the atmosphere together with a description of the effects of the atmosphere on electromagnetic waves.

Chapter 4 describes the methods for obtaining the wet delay from GPS signals and the subsequent retrieval of integrated water vapor from the wet delay. First a validation of the “mean weighted temperature” (which is an important parameter in estimating IWV from GPS wet delay) is given in detail together with experimental results. Furthermore, results of the first water vapor estimates using GPS monitors located in Ajdovščina and Rožna Dolina, Slovenia are presented, where the obtained results were compared with results obtained from GPS monitor located in Ljubljana, Slovenia.

While the measurements of atmospheric water vapor at mid-latitude region where presented in Chapter 4, Chapter 5 shows the results of the measurement of ionospheric scintillation effects on GPS signals in the equatorial region (Douala, Cameroon).

Beside numerous GPS applications in atmospheric science, GPS also plays important role in other scientific fields. One of those is precise-timing of cosmic ray arrivals at the surface detectors in the Pierre Auger Observatory. Chapter 6 presents the results of a study in which we wanted to revise and correct the station positions using several different methods.

Overview of GPS and Raman LIDAR

Contents

2.1 Global Positioning System	9
2.1.1 GPS System Architecture	10
2.1.2 GPS Signal Structure and Modernization	12
2.1.3 GPS Observables	17
2.1.4 Positioning modes	21
2.1.4.1 Precise Point Positioning (PPP)	21
2.1.5 GPS errors and biases	22
2.1.6 GPS monitors at the University of Nova Gorica	25
2.2 LIDAR System	27
2.2.1 Basic LIDAR setup	28
2.2.2 Elastic LIDAR equation	30
2.2.2.1 Raman LIDAR equation	31
2.3 Summary	33

In this chapter a short theoretical introduction on two remote sensing techniques used during the research work is given, together with the description on the detection systems developed and deployed at the University of Nova Gorica with some examples of data. In the first part the basics of Global Positioning System are presented, by looking at its architecture, signal structure and some of its errors and biases. The second part of chapter introduces basic lidar setup, its technical details and techniques for data retrieval and analysis.

2.1 Global Positioning System

The Global Positioning System has been developed by the Department of Defense (DoD) of the United States since 1973. The main purpose of GPS is to provide location and time information in all weather conditions, anywhere on or near the Earth, where there is an unobstructed line of sight to four or more satellites [1, 2, 53, 54]. One of the main objectives behind the development of the GPS system, was to replace the Navy Navigation Satellite System, also known as Transit. Transit was a pioneering achievement of the Applied Physics Laboratory of the John Hopkins University. The concept development of the Transit system started in 1959 and final system became operational in 1964 [1].

Block	Launch period	No. of satellite launched	No. of satellites in orbit
Block I	22 February 1978–9 October 1985	11	0
Block II	14 February 1989–1 October 1990	9	0
Block IIA	26 November 1990–6 November 1997	19	9
Block IIR	17 January 1997–6 November 2004	13	12
Block IIR(M)	26 September 2005–17 August 2009	8	8
Block IIF	28 May 2010–	4	4
Block III (GPS III)	under development		

Table 2.1: Overview of GPS satellite generations launched, where each Block presents different generation [2,4,52].

2.1.1 GPS System Architecture

The GPS system consist of three major segments [1,2,54,55]: the *Space Segment*, the *Control Segments* and the *User Segment*. The Space Segment comprises the satellites, their developing, manufacturing and launching. The baseline constellation comprises of 24 operational satellites fielded in nearly circular orbits with a radius of 26,559.7 km [1,2,5]. The satellites are arranged in six orbital planes with inclination angle of 55° with respect to the equatorial plane [1,2,5]. Additionally, in each orbital plane there is a spare satellite slot, primarily used for satellites in reserve [1]. General overview of GPS system development since its first satellite launch up to present time is presented in Table 2.1, where for each generation of GPS satellites (know as Block's) the launch period, number of satellites launches (including failed) and current number of satellites (in the time of this writing) in service is given.

The first satellite in system was launched on 22 February 1978 in generation of GPS satellites know as Block I. Block I presented a series of 11 satellites, which were mainly used to demonstrate the feasibility of GPS [1,4]. In contrast to next generations of satellites, Block I satellites had inclination angle, with respect to the equator, 63° . The inclination angle was in later generations changed to 55° [1,2,4]. The next generation of GPS satellites that followed Block I, was Block II, which presented first full scale operational satellites developed by Rockwell International [4,52]. Block II satellites had increase in navigation message data storage capability of 14 days. This storage capability was later increased in next generation, called Block IIA ("A" stands for advanced version), to 180 days [1,2,4,52]. Additionally to the increased navigation data storage, Block IIA satellites also have the Selective Availability (which was deactivated on 2 May 2000 in accordance with Presidential decree) and Anti-Spoof (A-S) capabilities [4,52]. The last satellite launch was on 6 November 1997 and currently there are 9 satellites still in operational use (Table 2.1). Generation that followed Block IIA satellites is Block IIR ("R" stand for replenishment). They are backward compatible with Block II/IIA, which means that the changes are transparent to users. In addition to the expected higher accuracy, Block IIR satellites have the capability of operating autonomously for at least 180 days without ground corrections or accuracy degradation [4].

Although that the first generations of GPS satellites where primarily designed and developed for military applications, GPS system has provided significant benefits to a wide variety of civil applications due to its flexibility and worldwide applicability. Direct result of

these benefits was, that in January 1999, U.S. Vice President Al Gore announced GPS modernization, which extended GPS capabilities even further [56]. One of the main components of this modernization is that two new navigation signals, denoted as L2C and L5, became available for civil use. The first GPS satellite with L2C signal, was launched on 26 September 2005 within the Block IIR(M) (“M” stand for modernized) generation of GPS satellites, while L5 signal within Block IIF (“F” stands for follow on) on 28 May 2010 [2, 52]. Additionally to the development of two new civil signals, a new military signal, called M code was also developed [5].

Currently under development by Lockheed Martin, is the Block III series (in some literature also know as GPS III generation), which will provide more powerful signals in addition to enhanced signal reliability, accuracy and integrity, which will support precision, navigation and timing services [57–59]. The Block III generation of satellites will replace aging GPS satellites while improving capability to meet the evolving demands of commercial, civilian and military users worldwide. Additionally Block III satellites will also provide increased accuracy and anti-jamming power while enhancing the spacecrafts design life and adding a new civil signal designed to be interoperable with other international global navigation satellite systems (for instance GALILEO) [1, 2, 59]. One of the key improvements will be the fourth civilian GPS signal (L1C), designed to enable interoperability between GPS and international satellite navigation systems such as GLONASS and GALILEO [57]. The first and second Block III satellites are on schedule for launch availability in 2014 and 2015, respectively [59]

In the time of this writing there are 33 operational satellites placed in orbits, which includes 9 Block IIA, 12 Block IIR, 8 Block IIR(M) and 4 Block IIF satellites. These satellites are monitored and controlled by ground network known as the *Control Segment*. Control Segment includes a master control station, located at Schriever Air Force Base in Colorado, a global set of monitor stations (currently there are 16 monitor station located at various places on Earth), an alternate master control station (located at Vandenberg Air Force Base in California) and 12 command and control antennas [1, 2, 5, 57]. At the same time as the signal modernization was underway, also the control segment went through two major transitions. The first major transition was the addition of a number of new monitor station within program know as Legacy Accuracy Improvement Initiative (L-AII) [2, 5, 57]. The L-AII, completed in 2008, expanded the number of monitoring sites from previously 6 to currently 16 [57]. The second major upgrade of the control segment, completed in 2007, was the upgrade of the master control station in policy referred to as the Architecture Evolution Plan (AEP) [5, 57]. AEP consisted of upgrading a legacy system based upon an IBM mainframe computer to a system based upon distributed Sun workstation configuration [5]. The next modernization step in upgrading the control segment started in 2008, when the US Air Force awarded a contract to Raytheon Company for development of the Next Generation Operational Control System (OCX) [5, 57]. OCX will add many new capabilities to the GPS control segment, including the ability to fully control the modernized civil signals (L2C, L5, and L1C) [57].

The third segment, know as *User Segment*, consists of numerous antennas and receivers providing positioning, velocity and precise timing to commercial and scientific users [1, 2, 54, 55]. Beside the military use of GPS system, there are growing civil applications of GPS, such us: navigation, geodesy, timing, surveying, surveillance, aviation, agriculture, cadastr, etc. Three different scientific areas of use of the GPS are presented and discussed in following

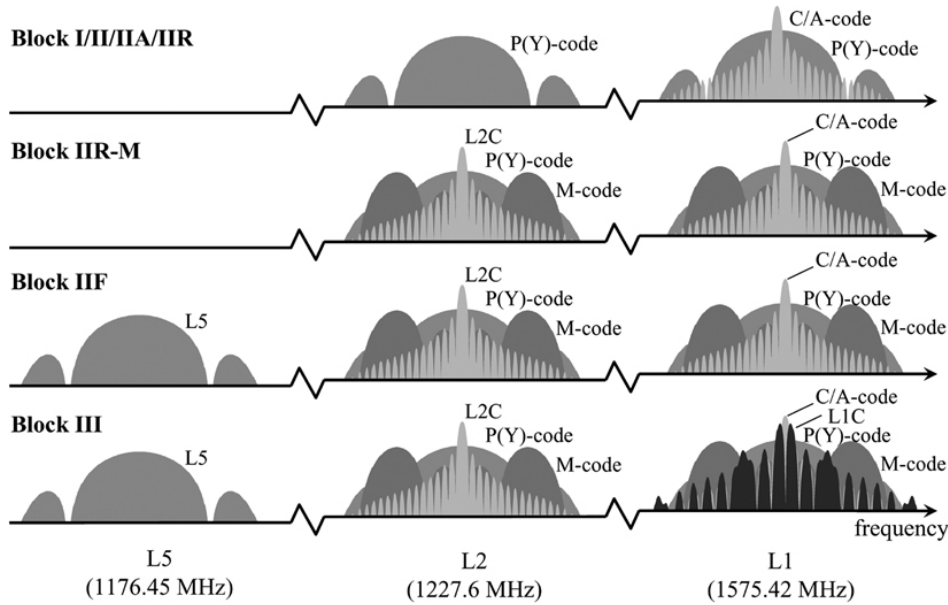


Figure 2.1: Evolution of GPS signals from Block I through Block III (GPS III) satellites. Shown on the figure are the normalized power spectral densities of the signals in decibels, where the bandwidths spanned between the first spectral nulls of the P(Y)-code and L5 signals are each 20.46 MHz [5].

chapters.

2.1.2 GPS Signal Structure and Modernization

L1 and L2 signal

Schematic presentation of the GPS signal modernization from Block I through Block III (GPS III) generations of satellites is shown in Fig. 2.1. As can be seen from Fig. 2.1, the Block I through Block IIR satellites broadcast signals using two frequencies in the L-band (L1 and L2), where the center frequencies are $L1=1575.42$ MHz, and $L2=1227.60$ MHz, with corresponding carrier wavelengths of 19 cm and 24 cm [1, 2, 53, 60, 60–62], respectively. The two ranging codes, known as coarse acquisition (or C/A code) and precision (encrypted) code (or P(Y) code), represent a family of binary codes commonly known as PRN codes (*pseudo-random noise*). While the C/A code is modulated only on L1 frequency, the P(Y) code is modulated onto both, L1 and L2 frequency [1], with a biphasic modulation (carrier phase is shifted by 180° when the code value changes from zero to one or from one to zero) [60]. The C/A code has a 1.023 MHz chip rate which is repeated every 1 millisecond, with the wavelength ~ 300 m [1, 53]. The precision P code is an extremely long PRN sequence with 10.23 MHz chip rate and has a 7 day period. This period is unique for each satellite, i.e. a GPS satellite is identified by its unique 1-week segment of P code. For example, a GPS satellite with an ID of PRN 20 refers to a GPS satellite that is assigned the 20th week segment of the PRN P code [60]. The wavelength of the P code is ~ 30 m. The smaller wavelength results in greater precision in the range measurements than C/A code, thus the P code is the principal military navigation ranging code [1, 53]. The Y code is used in place of the P code whenever the

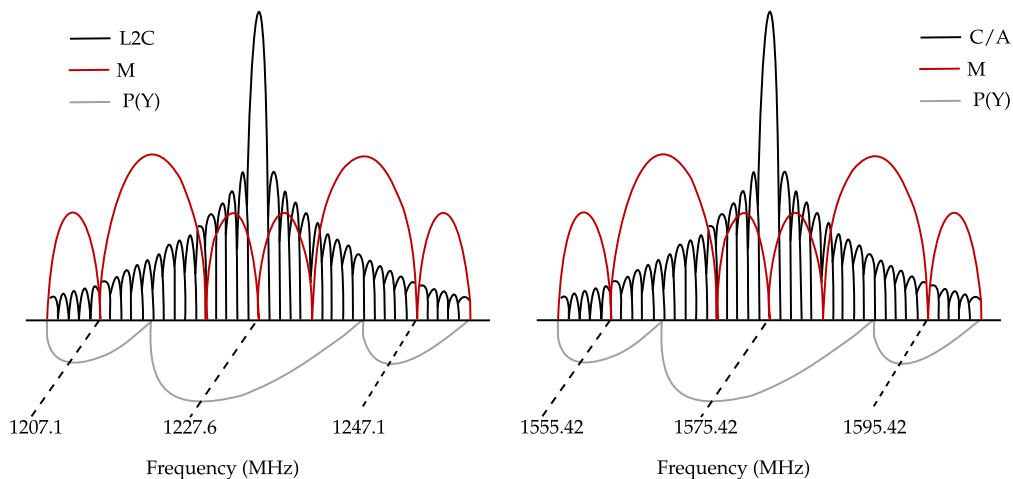


Figure 2.2: Spectral contents of the L2 broadcast (left side) and of the L1 broadcast (right side) from Block IIR(M) GPS satellites.

anti-spoofing (A/S) mode of operation is activated [53]. Navigation data are binary-coded messages consisting of data about the satellite health status, ephemeris (satellite position and velocity), clock biases and an almanac giving reduced-precision ephemeris data on all satellites in the constellation. The navigation message is transmitted at 50 bps, with a bit duration of 20 ms while the essential ephemeris and clock parameters are repeated each thirty seconds [1].

L2 civil signal (L2C) and M code

The Block IIR-M satellites introduced two new signals on L2 frequency – a new civil signal (referred to us as L2C) and a new military signal on both L1 and L2 frequency (referred to us as M code) [1, 2, 5]. Both signals have advanced designs that include a dataless signal component and forward error correction of the navigation data which enables robust tracking and data demodulation by user equipment [5]. When a White House press release announced that a new civil signal will be added to the GPS L2 frequency, many expected that will replace the C/A code, however the modern design of L2C signal structure better meets 21st century capabilities and requirements [63]. There were two primary requirements that drove the design of L2C signal. First requirement was that the signal must serve the current large and growing population of not only dual-frequency civil users but also applications that are adding value to society (i.e. scientific projects to monitor volcanoes, earthquakes; cadastral and land survey, etc.), where the most important objective was to eliminate the need for the marginal and fragile semi-codeless tracking technique by placing a civil code on the L frequency. Although a C/A code replica would meet this requirement, L2C enhances performance by having no data on one of its codes (civil long), which improves threshold tracking performance by 3 dB and provides “full-wavelength” carrier measurements without the 180° phase ambiguity inherent in GPS signals which carry data. The second key objective was to make L2 valuable for a host of single-frequency GPS applications which was up to then served only by the L1 C/A signal. Here, the primary need was to eliminate the unacceptable 21 dB crosscorrelation performance of the C/A code, which

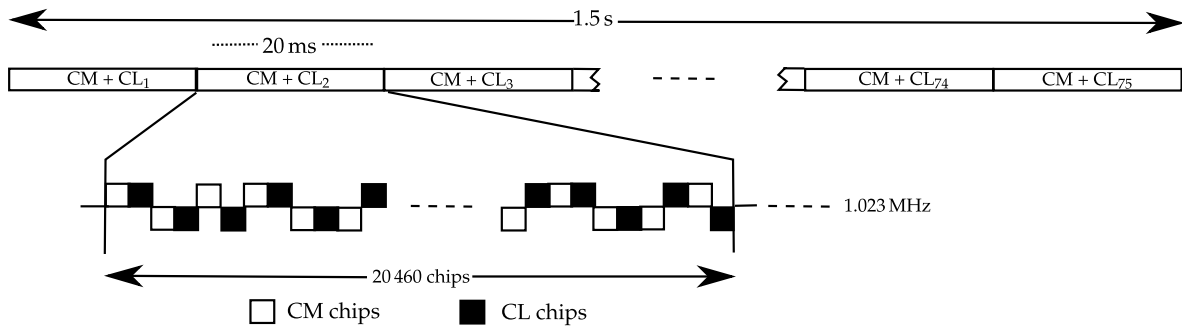


Figure 2.3: L2C code structure containing same CM but different CL (20 ms) segments in the CL period [64].

allows a strong GPS signal to interfere with weak GPS signals. The L2C signal achieves this by having a worst-case crosscorrelation performance of 45 dB (which is over 251 times better). Furthermore, L2C lowers the data demodulation threshold, making it possible to read the message when barely tracking the signal [63].

The schematic presentation of the spectral contents of the L1 and L2 frequency broadcast from Block IIR(M) satellites is presented in Fig. 2.2. As can be seen from Fig. 2.2, the L2C signal has a similar power spectrum as the C/A, however L2C is very different from C/A code in many other ways [2]. The L2C signal contains two ranging codes of different length, know as civil moderate (CM) and civil long (CL) [63,64]. The CM code is moderate length code, which repeats every 20 ms, contains 10 230 chips and is modulated with message data, while the CL code has a period of 1.5 s containing 767 250 chips [63,65]. Furthermore, the CM code is modulo-2 added to the data (i.e. it modulates the data), and the resultant sequence of chips is time multiplexed with the CL code on a chip-by-chip basis [64,65]. The individual CM and CL codes are locked at 511.5 kHz, while the composite L2C code has a frequency of 1.023 MHz (the same as the C/A code). Code boundaries of CM and CL are aligned, and each CL period contains exactly 75 CM periods. This time-multiplexed L2C sequence modulates the L2 carrier [64,65]. The civil navigation (CNAV) data, that includes satellite ephemerides, system time, satellite clock behaviour, etc. is a 25 bits per second data stream where a half rate convolution encoder is employed to transmit the data at 50 symbols per second [65]. Consequence of that is that each data symbol matches the CM period of 20 milliseconds (see Fig. 2.3) [64]. Because the L2C signal has to “share” L2 frequency with the M code and the legacy P(Y) code (see Fig. 2.2), is limited to a single bi-phase signal component, unlike than two signal in quadrature [64,65]. Due to its novel structure, L2C signal offers advantages in applications such as indoor positioning, ionospheric elimination (when combined with L1 measurements), improved tracking performance, etc.

The primary requirement for design of the M code, was to provide better jamming resistance than the Y code signal, primarily through enabling transmission at much higher power whiteout interference with C/A code or Y code receivers. Additionally, the M code signal also needed to be compatible with jamming prevention against enemy use of GPS, has to coexist with current signals on L1 and L2, and not interfering with current or future civilian or military user equipment [66]. The M code uses direct-sequence spread-spectrum (DSSS) modulation with a 5.115 MHz chipping rate and a spread-spectrum symbol that is two cycles of a 10.23 MHz square wave. This type of modulation is referred to as binary offset

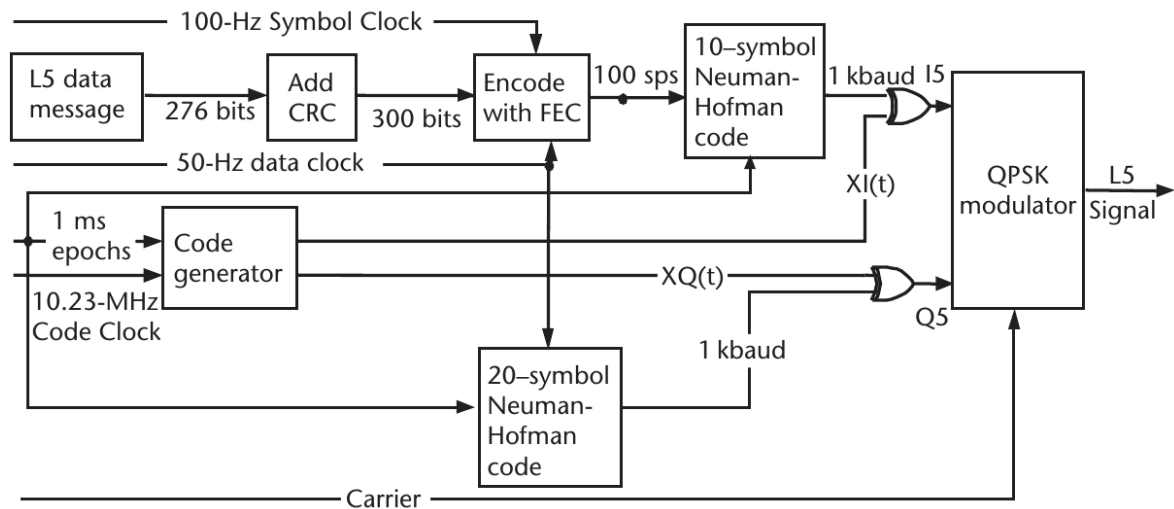


Figure 2.4: L5 signal modulation [2,67].

carrier (BOC) [5]. The BOC modulation uses a 10.23 MHz square wave subcarrier modulated by spreading code bits at a rate of 5.115 M bits/s where the spreading code transitions are aligned with transitions of the square wave subcarrier [66]. For more detailed description on M code the reader should refer to [66] and references within.

L5 signal

Modernization of the GPS signals followed with L5 signal, which was introduced with Block IIF satellites in 2010 (Table 2.1), on a new carrier frequency at 1176.45 MHz [5]. Although the first satellite “equipped” with L5 signal was launched in May 2010, the first successful broadcast of experimental L5 signal was performed on the GPS IIR-20(M) satellite [57,67]. The L5 signal was developed for safety-of-life applications, particularly for aviation safety services. The signal gives the users two civil signals (the other being L1) in a protected Aeronautical Radio Navigation Services (ARNS) band (960–1215 MHz) [5,67,68]. Furthermore, the higher chipping rate on L5 enables more precise code phase measurements than available on other civil GPS frequencies [67]. Signal power was defined at a minimum of -154 dBW at the Earth’s surface with intention to facilitate compatibility with existing systems such as Distance Measuring Equipment (DME) navigation aids and the Joint Tactical Information Distribution System, which operate on nearby frequencies. The L1 C/A-code specified minimum power is -160 dBW, which makes the L5 signal four times stronger [5,68]. The L5 signal consist of two carrier components, in-phase and quadrature, where each carrier component is a binary phase shift keying (BPSK) signal with a chip rate of 10.23 MHz. While the quadrature component is only modulated by a primary code and secondary code without the navigation data, the in-phase component is modulated by a bit sequence of the modulo-2 sum of a primary code, a secondary code for synchronisation and navigation data [5,67,68]. The secondary codes for the quadrature and in-phase channels are 20-bit and 10-bit Neuman-Hoffman codes (which are the same for all satellites), respectively [67]. The modulation of L5 signal is presented in Fig. 2.4. The primary purpose for implementation of Neuman-Hoffman codes was to provide additional spectral spreading of narrowband inter-

Signal	Center frequency (MHz)	Modulation type	Data rate	Null-to-Null Bandwidth (bps)	PRN code length
L1 C/A code	1575.42	BPSK-R(1)	50	2.046	1023
L1 P(Y) code	1575.42	BPSK-R(10)	50	20.46	P: 6187104000000 Y: cryptographically generated
L2 P(Y) code	1227.6	BPSK-R(10)	50	20.46	P: 6187104000000 Y: cryptographically generated
L2C	1227.6	BPSK-R(1)	25	2.046	CM: 10 230; CL: 767 250 (2 PRN sequences are chip-by-chip multiplexed)
L5	1176.45	BPSK-R(10)	50	20.46	I5: 10 230; Q5: 10 230 (two components are in phase quadrature)
L1 M code	1575.42	BOC(10,5)	N/A	30.69	cryptographically generated
L2 M code	1227.6	BOC(10,5)	N/A	30.69	cryptographically generated
L1C	1575.42	BOC(1,1)	N/A	4.0962	N/A

Table 2.2: Summary of GPS signal characteristics [2].

ference, while the second benefit of implementation of Neuman-Hoffman codes is that they improve the cross-correlation properties between signals, given that the received codes do not line-up between the satellites [68].

L1C signal

The fourth civilian GPS signal, which will be introduced with Block III generation of satellites in the following years is L1C signal, which will be transmitted on the L1 carrier frequency (shown in Fig. 2.1 in the bottom line) [5,69]. L1C signal will employ a signal that is created using a BOC modulation with a 1.023 MHz chipping rate and time-multiplexed mixture of symbols that are derived from 1.023 and 6.138 MHz square wave subcarriers [5]. In addition that the L1C signal is being design for transmission from GPS satellites, it is also being designed for interoperability with GALILEO's Open Service signal and for virtually seamless interoperability with signals from Japan's Quazi-Zenith Satellite System (QZSS) [69]. The structure of the signal evolved from the earliest GPS signals; it shares with the C/A signal the L1 center frequency, coherence between the carrier frequency, the code clock rates, and the data rate, and the provision of a navigation data message. Furthermore, signal also inherent significant improvements from previous developments, specifically L2C, L5 and Wide Area Augmentation System-WAAS (which was the first GPS-related signal to use forward error correction-FEC) [70]. More on the signal design can be found in [69,71].

A summary of all above described GPS signals is provided in Table 2.2, where for each signal its center frequency, modulation type, data rate and PRN code length is provided.

2.1.3 GPS Observables

There are three GPS observables which are used to determine user (receiver) position: code-pseudoranges, carrier phase and Doppler measurements [1, 54, 60].

Doppler measurements

Doppler measurements are based on the Doppler effect, which is a phenomenon of frequency shift of the electromagnetic signal caused by the relative motion of the emitter and receiver, and is used to determine the velocity vector of the user [1, 54, 55]. In GPS receiver, the Doppler measurements are usually derived by sampling the frequency setting of the internal oscillator that tracks the phase of the incoming signal [55]. The measured Doppler shift is not the raw measurement itself but the deviation from what the raw internal oscillator measurement would be without presence of any Doppler shift [55]. Doppler count (also known as integrated Doppler) is the historical observable of the Transit system [1, 54], and presents the integration of the frequency shift over time. Complete mathematical derivation can be found in [54].

Code-Pseudorange Measurements

Code-Pseudorange measurement is a measurement of the distance or range between the GPS satellite and the GPS receiver, more precisely the distance between the receiver's antenna and the satellite's antenna [1, 54, 60]. The knowledge of the distance/range between the satellite and the receiver is needed for the position computation, where either C/A-code or P-code can be used for measuring the pseudorange. The procedure of GPS range determination is also known as pseudorangeing [60], which is defined as the difference between signal reception time (as determined by the receiver clock) and the transmission time at the satellite (as marked on the signal) [1]. The transmission time is measured through maximum correlation analysis of the receiver code and the GPS signal [54]. If we assume that both the satellite and receiver clock (which controls the signal generation) are perfectly synchronized with each other, then when the PRN code is transmitted from the satellite, the receiver will generate an exact replica of that code. After some time (which is equivalent to the signal travel time in space), the receiver will "pick up" the transmitted code. Comparing the transmitted code and its replica, the receiver can compute the signal travel time. Multiplying this travel time by the speed of light will give the range between the satellite and the receiver [54], as shown on Fig. 2.5. However, the measured pseudorange will differ from the true range between satellite and receiver due to several biases: satellite and receiver clock offsets, ionospheric and tropospheric effects in signal, Earth tide and loading tide effects, multipath and relativistic effects and any other errors [54].

The basic observation equation for pseudorange measurement between satellite s and a receiver r in frequency band j , can be written as [54, 72]

$$P_r^s(j) = \rho_r^s + c(\delta t_r - \delta t^s) + \delta_{\text{iono}}(j) + \delta_{\text{trop}} + \varepsilon_{\text{rx}} + \varepsilon_{\text{mul}}, \quad (2.1)$$

where $P_r^s(j)$ is the measured pseudorange observation, δt_r and δt^s are the receiver and satellite clock biases, ε_{rx} is the error due to the receiver noise, ε_{mul} is the error in the measurement due to the multipath, δ_{trop} are tropospheric effects, δ_{iono} are the ionospheric effects (can be estimated using Eq. (3.35)) and ρ_r^s is the geometric range between the receiver at the reception

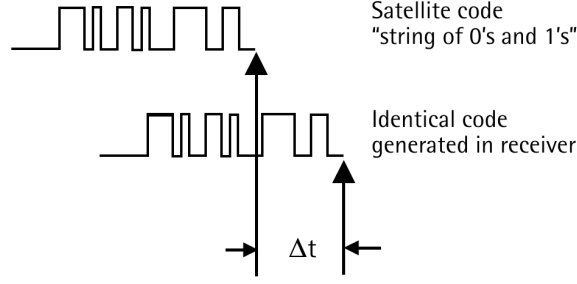


Figure 2.5: Example of a pseudorange measurement [60].

time and satellite at the emission time. The geometric range between satellite and receiver can be presented as [54]

$$\rho_r^s = |r^s - r_r| = \sqrt{(x^s - x_r)^2 + (y^s - y_r)^2 + (z^s - z_r)^2}, \quad (2.2)$$

where the r^s and r_r are the satellite and receiver position vectors, respectively. The satellite coordinate vector (x^s, y^s, z^s) is a function of the signal emission at the satellite, and the receiver coordinate vector (x_r, y_r, z_r) is a function of the reception time at the receiver.

Carrier phase Measurements

The carrier phase is a measure of the phase difference between the received satellite signal and the receiver-generated carrier signal at the reception time [54]. The range in this measurement is “simply” the sum of the total number of full carrier cycles plus fractional cycles at the receiver and the satellite, multiplied by the carrier wavelength [60], where a cycle is a full carrier wave and the ambiguous integer number of cycles in the carrier phase measurement is called ambiguity [54]. Due to the fact that the wavelength of the carrier phase (for example for L1 frequency is 19 cm) is much smaller than the wavelength for codes, the carrier phase measurement is more precise but carrier phase observables are needed for an accumulated carrier phase observation [54, 60].

The basic observation equation for carrier phase measurement for a satellite s , a receiver r and frequency band j , can be written as [54, 72]

$$L_r^s(j) = -\lambda_j \Phi_r^s(j) = \rho_r^s + c(\delta t_r - \delta t^s) - \delta_{\text{iono}}(j) + \delta_{\text{trop}} + \varepsilon_{\text{rx}} + \varepsilon_{\text{mul}} + \lambda_j N(j)_r^s, \quad (2.3)$$

where L_r^s is the measured carrier phase observation, δt_r and δt^s are the receiver and satellite clock biases, ε_{rx} is the error due to the receiver noise, ε_{mul} is the error in the measurement due to the multipath, δ_{trop} are tropospheric effects, δ_{iono} are the ionospheric effects (can be estimated using Eq. (3.35)), ρ_r^s is the geometric range between the receiver at the reception time and satellite at the emission time (see Eq. (2.2)), λ is the wavelength and N_j presents the carrier phase ambiguity term. The ambiguity term is composed of three parts [72]

$$N_r^s(j) = n_r^s + \delta\Phi(j)^s - \delta\Phi_r(j), \quad (2.4)$$

where $n_r^s(j)$ is the integer ambiguity, $\delta\Phi^s(j)$ and $\delta\Phi_r(j)$ are the uncalibrated phase delays in the satellite and in the receiver, respectively. The uncalibrated phase delays are not integer

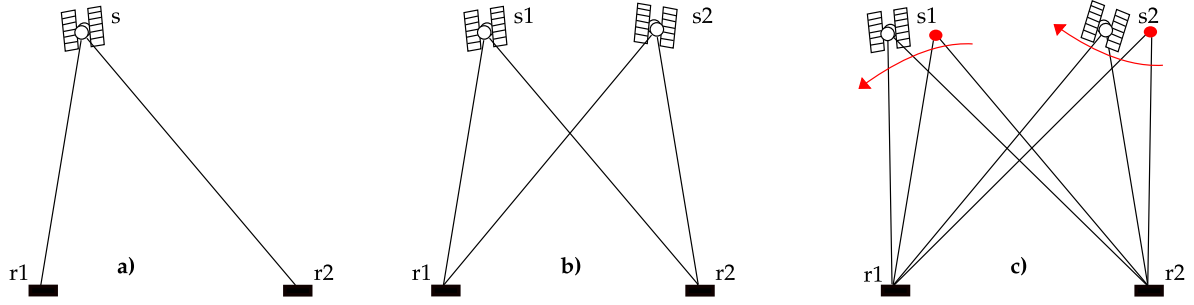


Figure 2.6: From left to right: a) single differencing geometry, b) double differencing geometry and c) triple differencing geometry illustration.

values, thus preventing the resolution of the integer ambiguities. However, they are identical for common instruments, are stable to better than a nanosecond and are estimated while forming double difference (described in detail in following sections) ambiguities between two satellites $s1, s2$ and two receivers $r1, r1$ [72]

$$N(j)_{r1,r2}^{s1,s2} = N(j)_{r1}^{s1} - N(j)_{r1}^{s2} - \left(N(j)_{r2}^{s1} - N(j)_{r2}^{s2} \right) = n(j)_{r1,r2}^{s1,s2}. \quad (2.5)$$

The ambiguity term in Eq. (2.3) is not the only part that distinguishes the carrier phase observable from pseudorange in Eq.(2.1). It is also notable that the sign of the ionospheric term in Eq.(2.3) is negative, while for pseudorange observations is positive. Reasons for that are discussed in Section 3.2.1.

Above described basic equations for forming pseudorange and carrier phase observation are performed in so called zero difference type. Beside zero difference one can also form single, double and triple difference observations as presented in Table 2.3 and schematically shown in Fig. 2.6. From Table 2.3 can also be seen that different strategies can be used, where unique mathematical operator for each is used.

Differencing method	Strategy	Mathematical operator
Single differencing	between-satellite	∇
	between-receiver	Δ
	between-epoch	∂
Double differencing	between-satellite difference followed by between-receiver or vice versa	$\nabla\Delta$
	difference two double differences between epochs	$\partial\nabla\Delta$

Table 2.3: GPS data differencing methods [73].

Single difference observations

In contrast to zero difference observations where one receiver is observing satellite, single difference (SD) presents a difference formed by data observed by two receivers $r1$ and $r2$ by the same satellite s and can be for carrier phase in frequency band j written as [1,2,54,73]

$$\begin{aligned}\Delta L_{r1,r2}^s &= L_{r1}^s - L_{r2}^s \\ &= \Delta\rho + c\Delta\delta t_r - \Delta\delta_{\text{iono}}(j) + \Delta\delta_{\text{trop}} - \lambda_j\Delta N_j,\end{aligned}\quad (2.6)$$

where $\Delta\delta_{\text{iono}}(j)$ and $\Delta\delta_{\text{trop}}$ are the differenced ionospheric and tropospheric effects, which are in case when baseline is short eliminated. It can be noticed that the most important property of single differencing is that the satellite clock error term (δt_s) is eliminated. Similarly the single difference for pseudorange is given by [1,2,54,73]

$$\begin{aligned}\Delta P_{r1,r2}^s &= P_{r1}^s - P_{r2}^s \\ &= \Delta\rho + c\Delta\delta t_r + \Delta\delta_{\text{iono}}(j) + \Delta\delta_{\text{trop}}.\end{aligned}\quad (2.7)$$

Double difference observations

Under assumption that two receivers $r1$ and $r2$ simultaneously observe a second satellite $s2$, one can form double difference (DD) for carrier phase observation in frequency band j as [1,10,54,73]

$$\begin{aligned}\Delta\nabla L_{r1,r2}^{s1,s2} &= (L_{r1}^{s1} - L_{r1}^{s2}) - (L_{r2}^{s1} - L_{r2}^{s2}) \\ &= \Delta\nabla\rho - \Delta\nabla\delta_{\text{iono}}(j) + \Delta\nabla\delta_{\text{trop}} - \lambda\Delta\nabla N(j),\end{aligned}\quad (2.8)$$

where $\Delta\nabla\delta_{\text{iono}}(j)$ and $\Delta\nabla\delta_{\text{trop}}$ are the double differenced ionospheric and tropospheric effects at the two stations related to the two satellites, respectively. As in case of single differencing also in double differencing both, ionospheric and tropospheric effects, are eliminated if the baseline is short. The most important property of double differencing is that completely eliminates both satellite and receivers clock errors. Similarly, the double differencing for pseudorange is given

$$\begin{aligned}\Delta\nabla P_{r1,r2}^{s1,s2} &= (P_{r1}^{s1} - P_{r1}^{s2}) - (P_{r2}^{s1} - P_{r2}^{s2}) \\ &= \Delta\nabla\rho + \Delta\nabla\delta_{\text{iono}}(j) + \Delta\nabla\delta_{\text{trop}}.\end{aligned}\quad (2.9)$$

Triple difference observations

While the main purpose of single and double differencing methods is to remove satellite and receiver clock errors, the purpose of triple differencing is to eliminate the integer ambiguity. The triple difference only removes the ambiguity if it has not changed during the time interval between epochs. Any cycle slips will appear as outliers, and can easily be removed by conventional techniques. This is unlike than in situation with double differencing, where cycle slips appear as step functions in the time series of data [54]. Triple difference for carrier phase is obtained by differencing two double differences between epochs [73]

$$\partial\Delta\nabla L = \partial\Delta\nabla\rho - \partial\Delta\nabla\delta_{\text{iono}} + \partial\Delta\nabla\delta_{\text{trop}},\quad (2.10)$$

and similarly for pseudorange

$$\partial\Delta\nabla P = \partial\Delta\nabla\rho + \partial\Delta\nabla\delta_{\text{iono}} + \partial\Delta\nabla\delta_{\text{trop}}.\quad (2.11)$$

2.1.4 Positioning modes

There are several different GPS positioning techniques available for user. They can be either static or kinematic, single point or relative positioning, real-time or post-mission. A detailed description of mentioned methods can be found in [1, 2, 54], while here a brief and short description is provided. The term static positioning describes the positioning mode, where usually a single receiver is stationary at some point on Earth's surface and collects observations from minimum four satellites, for example every 10 s (or other interval, depending on the user) for more longer period of time to achieve a more precise position than would be by a stand-alone instantaneous reading [1, 2, 10, 54]. This type of positioning is also known as absolute point positioning. In contrast to this, in kinematic positioning the receiver is in motion. However, static single point positioning is not suitable for applications where high accuracy are needed, mainly due to the errors discussed in Section 3.2 and 2.1.5. In order to minimize these errors and obtain higher accuracies, one can use GPS in relative or differential positioning mode (also known as differential GPS–DGPS) [10]. In DGPS technique code-pseudorange are simultaneously measured by two receiver where one is a known reference station which calculates the geometric pseudorange by making use of the satellites position. These are then used to correct those of the unknown station. In contrast to that, in relative positioning, the baseline vector is computed and then added to the coordinates of the reference station to obtain those of the unknown. Furthermore, relative positioning requires post-processing of data, where simultaneous carrier-phase observations from both reference and rover stations are processed [1, 2, 10, 54]. Relative positioning can be performed through single, double and triple differencing in both static and kinematic modes [10].

2.1.4.1 Precise Point Positioning (PPP)

According to [74], the evolution of PPP technique dates back to 1976, however it was not until the late 1990s that this technique was seriously studied and used [75]. Since then PPP has been extensively researched, and several PPP packages have been developed, such as GPS Inferred positioning System–Orbit Analysis and Simulation Software (GPSY-OASIS II), Bernese GNSS Software, Automatic Precise Positioning Service of the Global Differential GPS (GDGPS) System (<http://apps.gdgps.net/>) and Canadian Spatial Reference System (CSRS-PPP) (<http://webapp.geod.nrcan.gc.ca/geod/>).

PPP uses both, undifferenced carrier and pseudorange data for precise position determination of a single receiving station [10, 74, 76], and is capable of providing position solutions from centimeter to decimeter precision level. In contrast to the double differencing technique [1], where both the transmitter and receiver clock offset are cancelled out (Eq. (2.9)), PPP technique exploits precise GPS orbit and clock products during the post-processing. These precise orbit and clock data are provided by several different sources, e.g. International GNSS Service (IGS), Jet Propulsion Laboratory (JPL), and other commercial sources [10]. They are determined by processing in double difference mode using global network of GPS stations [75]. PPP has been widely based on the processing of the following ionosphere-free combinations of the undifferenced carrier and phase observations (called

the traditional model) [77]

$$P = \frac{f_1^2 P(L1) - f_2^2 P(L2)}{f_1^2 - f_2^2} \quad (2.12)$$

$$= \rho - c\delta t_r + \delta_{\text{trop}}$$

$$L = \frac{f_1^2 \Phi(L1) - f_2^2 \Phi(L2)}{f_1^2 - f_2^2} \quad (2.13)$$

$$= \rho - c\delta t_r + \delta_{\text{trop}} + \frac{cf_1 N_1 - cf_2 N_2}{f_1^2 - f_2^2}$$

where f_1 and f_2 are the GPS L1 and L2 frequencies, P , L are the code and phase observations; ρ is the true geometric range, c is the speed of light, δt_r is the receiver clock offset, δ_{trop} are the tropospheric effect and N is the phase ambiguity term in L . From equations it can be seen, that the unknown parameters to be estimated in PPP are position coordinates, phase ambiguity terms, receiver clock offset and the tropospheric effect [77]. Furthermore, PPP also requires a number of unconventional corrections to mitigate systematic effects that could cause centimeter variations in the undifferenced code and phase observations. Satellite antenna phase center variations, ocean tide loading effects, phase wind-up correction are some examples, which are not typically considered for standard point positioning and double difference RTK positioning. In general these unconventional corrections can be divided into two groups, non geophysical effects (phase wind-up, antenna phase center variations, differential code biases) and geophysical/site displacement effects (Earth tides, ocean tide loading, atmosphere pressure loading). Compared to DGPS and RTK positioning approaches, PPP can offer several advantages [10,77]:

1. PPP uses only one receiver for achieving cm-level accuracy hence it removes the requirement of a reference station and simultaneous observations to the same satellites from both rover and reference stations.
2. Use of a global reference frame in PPP, gives it a global outlook enabling it to provide much greater consistency than the DGPS whose positions are relative to a local reference station.¹
3. Because the PPP needs to estimate receiver clock and tropospheric effect parameter in addition to position coordinate parameters (see Eqs. (2.12) and (2.13)) thereby providing precise time transfer and water vapour estimation using single GPS receiver.

2.1.5 GPS errors and biases

The GPS errors can be divided [60] into three major groups:

1. satellite-related errors; these include ephemeris, satellite clock error and the effect of selective availability,

¹note, that if the base station coordinates are known in an absolute sense, then the absolute position of the user is obtained.

2. receiver-related errors; these include receiver clock errors, multipath error, receiver noise, and antenna phase center variations, and
3. atmospheric errors and biases; these include the delays on the GPS signal as it passes through the ionospheric and tropospheric layers of the atmosphere. These effects are explained in detail in Section 3.2.

Ephemeris error

Ephemeris errors stand for the difference between the expected and the actual orbital position of a GPS satellite, where the expected position is calculated using the satellite ephemeris. These satellite ephemeris are determined by the master control station based on monitoring of individual signals by four monitor stations [55]. This is done, typically, with overlapping 4-hour GPS data spans with intention to predict expected satellite positions for each 1-hour period [60]. Calculated orbital parameter estimates are then uploaded by the master control station to each satellite, which then transmits the data to users via navigation data message [55]. Ephemeris errors are usually in the order of 2 to 5 m [60].

An ephemeris error for a particular satellite is identical to all GPS users worldwide, but the satellite motion in the sky, which “causes” different users to see the same satellite at different viewing angles (i.e. azimuth and elevation), and makes the effect of the ephemeris error on the range measurement and consequently on the computed position different [60]. The effect of this is that taking a difference between the measurements of two receivers which are simultaneously tracking the same satellite cannot totally remove the error [60].

Multipath effect

Multipath presents a major error source for both, carrier-phase and pseudorange measurements. It refers to the phenomena when the GPS signal arrives to the antenna of the receiver via two or more different paths [1, 60]. This phenomenon occurs when antenna is receiving signal from a satellite in a direct line of sight and also from reflected signal, from objects surrounding it (see Fig. 2.7). The reflected signal will always have a longer propagation time and can thus significantly distort the amplitude and phase of the direct-path signal [55]. It affects both the carrier-phase and pseudorange measurements, but with larger effect on the pseudorange (pseudorange multipath can theoretically reach several tens of meters for the C/A code measurements) [1, 60], while the multipath error on carrier-phase typically can reach a few centimeters [54].

There are several methods which can reduce the error due to the multipath effect. One of the simplest methods is to set up an antenna far away as possible from potentially reflecting surfaces (i.e. water surface or buildings that are taller than antenna site). The second option is to chose antenna with build-in choke ring, a ground plane that has several concentric metal hoops which attenuate the reflected signals [60]. More detailed explanation of the multipath effect and techniques for its removal can be found in [1, 54, 55, 60].

Satellite and receiver clock errors

Each of the satellite uses its own atomic clock, running in the time frame called *space vehicle (SV) time*, to control the timing of the signal transmission [55]. In 2002 Block II and Block IIA

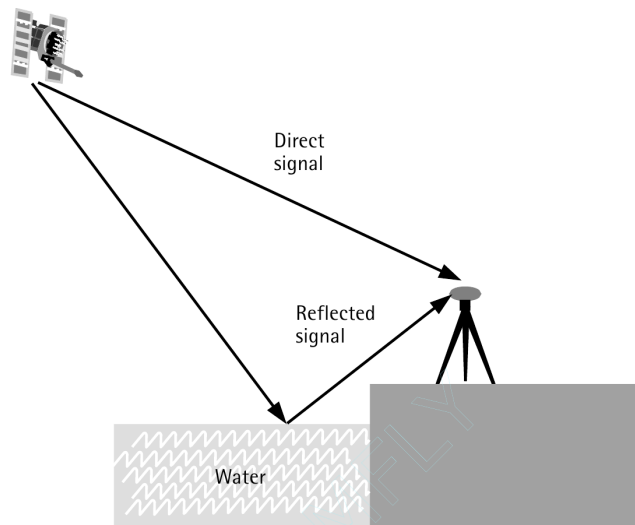


Figure 2.7: An example of multipath effect [60], where the signal is reflected due to the water surface causing antenna to receive signal via two different paths.

satellite contained four atomic clocks (two Cesium and two Rubidium), while Block IIR satellites carries only Rubidium clocks [60]. The errors can be removed through comparison of two receivers or by applying the satellite clock correction in the navigation message. However, applying corrections in navigation message leaves an error of the order of several nanoseconds which translates to a range error of a few meters [60]. On the other hand, receivers use inexpensive crystal clocks, which are less accurate than the atomic clocks on satellites, making receiver clock errors much larger than satellite clock errors. However, since the navigation solution already includes correction for the satellite clock error, the receiver clock error can be removed by taking a difference between two satellites [55, 60]. Applications which require high precision (such is geodesy) usually use precise external atomic clocks with better performance but higher costs [60].

Phase wind-up corrections

Phase wind-up effect is due to the electromagnetic nature of circularly polarised waves, such as GPS signals. Interesting fact is, that the wind-up affects only carrier phase measurements but not the pseudoranges. The satellite transmits right-hand circularly polarized radio wave and, therefore, the observed carrier phase depends upon the relative orientation of the satellite and receiver antennas, and the direction of the line of sight. A rotation of either antenna around its bore (vertical) axis will change the carrier phase by up to one cycle. The satellite antennas undergo rotations as their solar panels are being oriented toward the sun, mostly slowly, but sometimes completing a rotation in less than thirty minutes [1, 78]. More details on phase wind-up effect can be found in [78, 79], where a correction was proposed for crossed-dipole type antenna.

Solid Earth Tides and Ocean Tide loading

The Earth's surface is not rigid, but rather somewhat pliable. Its shape varies with time, dominated by diurnal and semidiurnal components, in response to gravitational forces. These Earth surface movements are referred to as solid Earth tides. Additional motion of the Earth's surface, especially in coastal locations, due to ocean tides is referred to as ocean loading. Site displacements due to the Earth tides and ocean tide loading can be as large as 30 cm. By convention, ECEF (Earth-Centered, Earth-Fixed) coordinate systems such as ITRF (International Terrestrial Reference Frame), are explicitly defined to not include solid Earth tides and ocean loading effects. Thus, these effects should be removed for applications where the user position in ECEF coordinates are desired. Accurate models for the Earth's deformation due to solid Earth tides and ocean loading can be found in [2].

Antenna Phase Center Variations

The geometric distance between the satellite (at the signal emission time) and the receiver (at the signal reception time), defined in Eq. (2.2), is actually the distance between the phase centres of the two antennas [1,54]. The position of the antenna phase center depends on the direction of the GPS signals from satellites to the receiver antenna which arrive from different directions. This direction dependence is known to us as the antenna Phase Center Variations (PVC). One must also take into account that the antenna Phase Center offset (PCO) (with respect to the antenna reference point) and the PVC (with respect to the mean antenna phase center) are also frequency and elevation, azimuth dependent. Furthermore, radomes (antenna cover) can also have an impact on the antenna phase center variations [54,80]. In case when highest accuracy is needed, one must calibrate antenna in order to obtain its phase center corrections which then have to be applied in analysis. For a GPS network (IGS for instance), antenna phase centre correction are usually predetermined and listed in a table for use [1,54].

Atmospheric Pressure Loading

Atmospheric pressure loading presents the displacement of the Earth's crust as a result of the movement of pressure systems over the Earth. While this effect has been known for a long time, it is only recently that it can be detected using space geodetic techniques [81]. The displacement on average can have the RMS of 2.6 mm for the vertical component and 0.6 mm for the horizontal component, however peak to peak variations can reach 40 mm for the vertical component and 7 mm for the horizontal one. Atmospheric pressure loading should be taken into account in observations when the accuracy better than 1 cm is required [82].

2.1.6 GPS monitors at the University of Nova Gorica

At the University of Nova Gorica we use two dedicated GPS Ionospheric Scintillation and TEC Monitor (GISTM) units [83]. The two units are installed at two campuses of the University of Nova Gorica, the first one located in Ajdovščina and the second one in Rožna Dolina, as shown in Fig. 2.8. The receivers (GSV4004) are capable of measuring phase, amplitude (at 50 Hz rate) and code/carrier divergence (at 1 Hz rate) on 12 channels for each satellite being tracked on the L1 band and the L2 band. The TEC is then computed from combined L1 and L2 pseudo-range and carrier-phase measurements. While 11 channels are used for

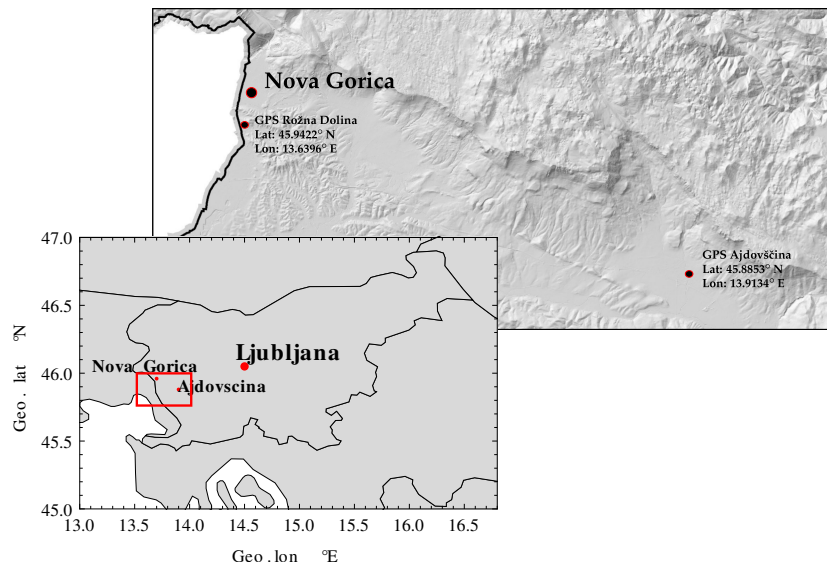


Figure 2.8: Geographical positions of the two GPS units in Ajdovščina and Rožna Dolina [85].

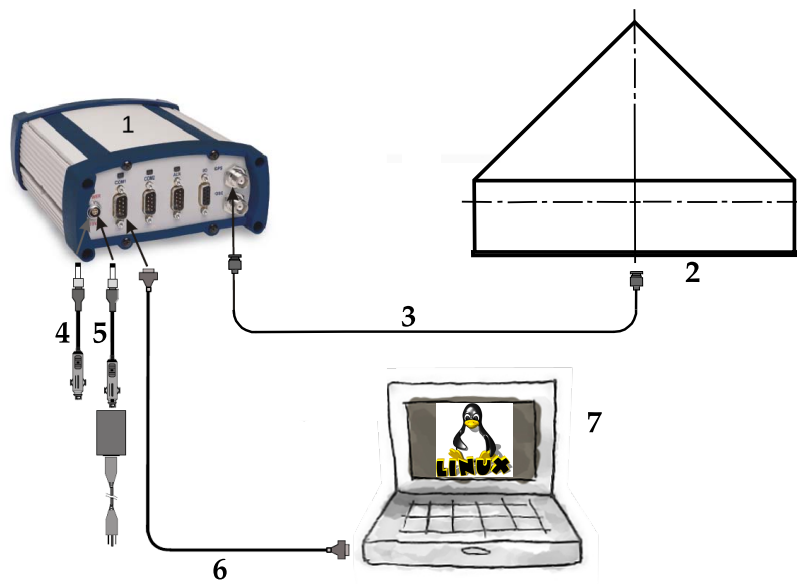


Figure 2.9: Schematic diagram of monitors setup at University of Nova Gorica. 1 – receiver (OEM4 – G3 GPSCard in ProPak – G2plus enclosure); 2 – GPS antenna (GPS – 533 model); 3 – RF cable; 4 – 12 V power adapter cable; 5 – optional AC adapter or aircraft power conditioner; 6 – null modem data cable; 7 – data communications equipment (PC unit with LINUX system) (adapted according to [83]).

tracking and measuring data from GNSS satellites, the 12th channel is configured for the tracking of the Satellite-based Augmentation System Satellites (SBAS) and is also being used for measurements of the noise level S/N_0 and S_4 correction computations [83,84].

Although the primary purpose of the monitors is to collect ionospheric scintillation and TEC data and to output them to data logs [83], the units are being used also for collecting



Figure 2.10: Recording setup at Rožna Dolina campus (left) and antenna setup at Ajdovščina campus (right).

tropospheric data, which are then used for obtaining information on water vapor content in troposphere. For recording the data at University of Nova Gorica, we are currently using GPS – SCINDA software (kindly provided to us by dr. Carrano, Boston College). GPS – SCINDA is a modular and portable program for real-time GPS data acquisition and ionospheric analysis which was developed for the Scintillation Network and Decision Aid – network of ground based receivers that monitors scintillations at UHF and L-band frequencies in the equatorial regions, developed by Air Force Research Laboratory (AFRL). Recording the data with GPS – SCINDA software can be done in two different modes. One can record the data in Campaign Mode (both raw and processed data are collected) or Normal Mode (where only processed data are collected) [86].

The basic setup of the two units is shown on Fig. 2.9, where one can see that one setup is composed from receiver (for details on receiver system please see Fig B.1), antenna (general specification are provided in Table B.1) and computer unit with Linux operating system. GPS antenna is in both cases mounted on a pole with clear view of the sky and is connected to the receiver using supplied antenna cable from NovAtel. The receiver is then with specialized serial cable connected to the computer via its serial port interface. Example of one of the setups (in Rožna Dolina campus) is shown in Fig. 2.10, together with antenna setup at Ajdovščina campus. Furthermore, some general statistics of the visible satellites are shown in Figs. 2.11 and 2.12, where Fig. 2.11 is presenting azimuth and elevation information for the satellite with PRN number 10 on 25 June 2012 while Fig. 2.12 shows so called sky-plot (PRN 10) and visibility plot for all satellites in view through one day – 25 June 2012.

2.2 LIDAR System

Lidar stands for **L**ight **D**etection **A**nd **R**anging. It is a laser based system operating on similar principles as sonar (sound navigation and ranging) or radar (radio detection and ranging) [22], where the light pulse is emitted into the atmosphere. When the light from a beam

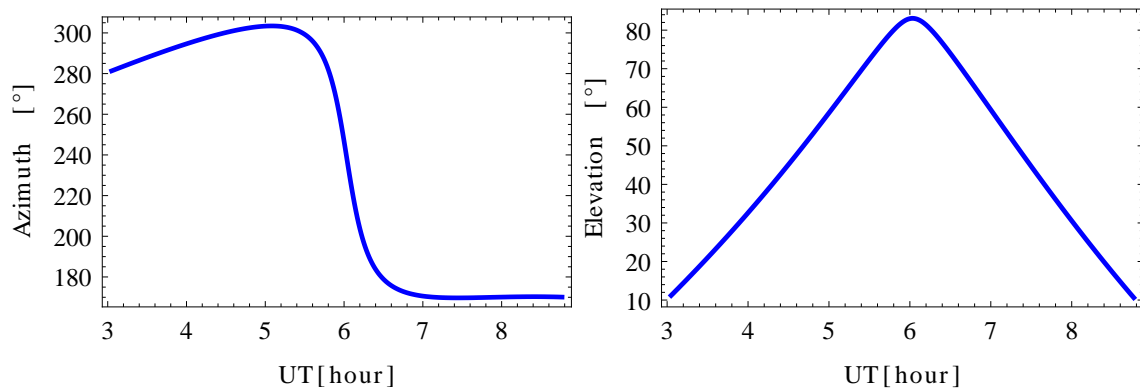


Figure 2.11: Azimuth (left) and elevation (right) plots for satellite with PRN 10 on 25 June 2012 obtained with the receiver stationed at Rožna Dolina.

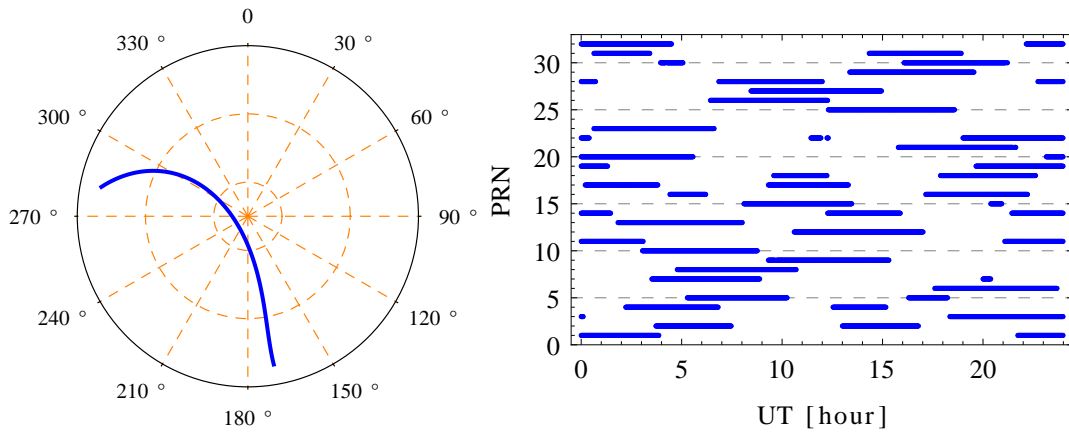


Figure 2.12: Sky-plot (left) for satellite with PRN 10 on 25 June 2012 and the visibility plot (right) for all satellites in view on 25 June 2012 at Rožna Dolina.

interacts with molecules or particulates in the atmosphere, it gets scattered in all directions and a portion of the light is scattered back towards the lidar system, where it is collected by telescope and focused on photodetector. Photodetector serves to measure the amount of backscattered light as a function of distance (expressed in roundtrip time delay) from the lidar [22]. The process described above is schematically shown in Fig. 2.13. In this section a short introduction to lidar systems at University of Nova Gorica is given, together with overview of lidar principles and properties.

2.2.1 Basic LIDAR setup

As can be seen from Fig. 2.13, the basic lidar system consists of two parts: (a) transmitter, which is the laser source of short and intense light pulses and (b) receiver, whose job is to collect the backscattered light (photons) from the atmosphere [88]. In the case of the Raman lidar at the Otlica Observatory, the transmitter is an ultraviolet Nd:YAG pulsed laser, with a pulse energy of 100 mJ (after 3rd harmonic generation) and a pulse repetition rate of 20 Hz. The receiver is a parabolic mirror (also used for Mie lidar), with an effective diameter

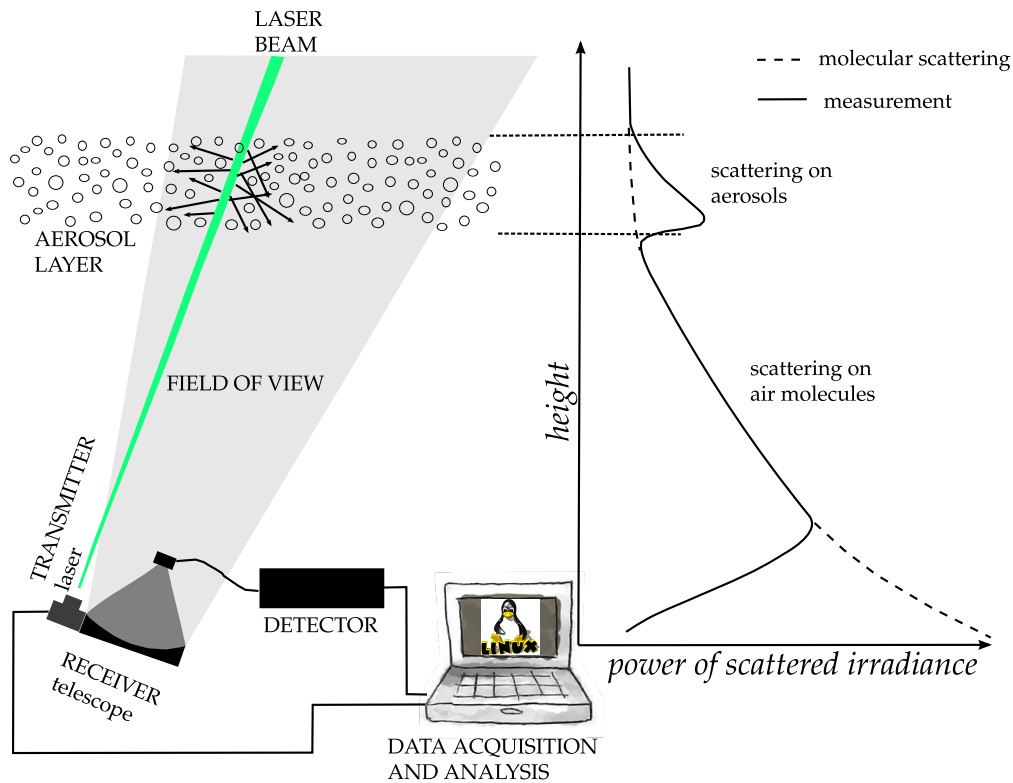


Figure 2.13: Principles of lidar system: emitted laser light scatters in all directions on particles and molecules in the atmosphere. Higher concentrations of aerosols and molecules results in more intensive scattering and more backscattered light reaches the lidars receiver. It has to be taken into consideration that the power density of irradiance decreases with the square of distance from the scatter [87].

of 585.7 mm, with fiber core diameter of 1000 μm and acceptance angle of 25.4° [89]. The schematics of the Raman lidar at the Otlica Observatory are shown in Fig. B.2.

As one can see from Fig. B.2, the received lidar signal is first collected and focused into the fiber, where it is collimated and then coupled into the spectroscopic filter box. Primary purpose of the spectroscopic filter box is to separate the vibrational Raman signals of N_2 and H_2O , using dichroic beam splitter and narrow-band interface filters. As detectors we use three photomultipliers (PMT) with the sensitivity in wavelength interval response spectra from 300 nm to 650 nm. The high voltages for all three PMTs (up to 3500 V) is provided by a 4-channel high voltage power supply² [89]. For more detailed description of development and system setup we refer to [89], however some specifications are provided in Table B.2. To record the received lidar traces three Licel transient recorders (TR40-160) are used, each capable of recording in both photo-counting and analog mode [89].

²CAEN Model N472, CAEN S.P.A.

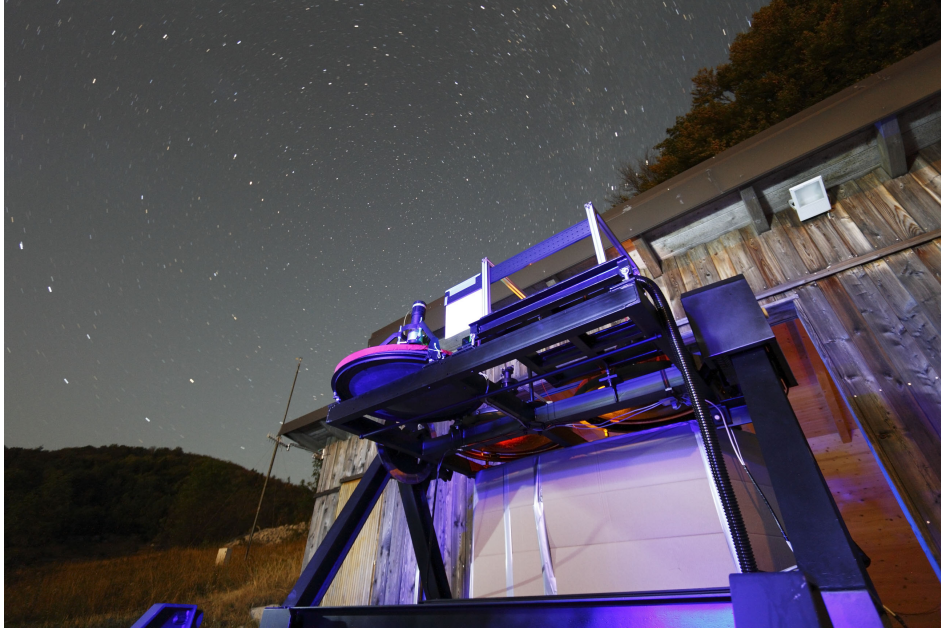


Figure 2.14: Photo of Raman lidar at Otlica Observatory during the August campaign measurements (photo by Robert Bremec, August 2012).

2.2.2 Elastic LIDAR equation

The detected lidar signal can be in the simplest form [88] written as

$$P(r) = K G(r) \beta(r) T(r), \quad (2.14)$$

where P is the power received from a distance r . As can be seen from Eq. 2.14, the elastic lidar equation is made of four factors [88], where the first two factors determine the lidar setup and efficiency and can be thus controlled by the operator, and the last two are the factors which contain the information on the atmosphere (i.e. all measurable quantities) and are thus the subject of investigation/measurements [88]:

The first factor is K , summarizing the performance of the lidar and is sometimes called also the system factor. It can be written as

$$K = P_0 \frac{c\tau}{2} A\eta, \quad (2.15)$$

where P_0 is the power of the laser pulse, τ is the temporal pulse length, A is the area of the primary receiver optics responsible for the collection of the backscattered light and η is the overall system efficiency.

The second factor is $G(r)$, describing the range dependent measurement geometry, also known as geometric factor, and can be written as

$$G(r) = \frac{\mathcal{O}(r)}{r^2}, \quad (2.16)$$

where $\mathcal{O}(r)$ is the beam–receiver field-of-view overlap function.

The third factor is $\beta(r)$, which presents the backscatter coefficient at distance r , and is the primary atmospheric parameter that determines the strength of the lidar return. It stands for the ability of the atmosphere to scatter light back into the direction from which it came, and can be written as

$$\beta(r, \lambda) = \sum_j N_j(r) \frac{d\sigma_{j,\text{sca}}}{d\Omega}(\pi, \lambda), \quad (2.17)$$

where N_j is the concentration of scattering particles of kind j in the volume illuminated by the laser pulse and $d\sigma_{j,\text{sca}}(\pi, \lambda)/d\Omega$ is the particle differential scattering cross section for the backward direction at wavelength λ . Due to the fact that the laser light in the atmosphere is scattered by air molecules and by aerosols (dust, particulate matter etc.), $\beta(r, \lambda)$ can be written as

$$\beta(r, \lambda) = \beta_{\text{mol}}(r, \lambda) + \beta_{\text{aer}}(r, \lambda). \quad (2.18)$$

The fourth factor is $T(r)$, which stands for transmission term. It describes how much light is lost on the way from the lidar to some distance r and back. The value of this factor varies between 0 and 1 and can be written as

$$T(r, \lambda) = \exp \left[-2 \int_0^r \alpha(r', \lambda) dr' \right], \quad (2.19)$$

where $\alpha(r, \lambda)$ is the extinction coefficient, defined in a similar way as the backscatter coefficient, as the product of the number concentration and the extinction cross section $\sigma_{j,\text{ext}}$ for each type of scatter j . With extinction coefficient we describe both attenuation processes, absorption and scattering. It can be written as

$$\alpha(r, \lambda) = \sum_j N_j(r) \sigma_{j,\text{ext}}(\lambda). \quad (2.20)$$

Using above described factors, the Eq. (2.14) can be now written as

$$P(r, \lambda) = P_0 \frac{c\tau}{2} A\eta \frac{O(r)}{r^2} \beta(r, \lambda) \exp \left[-2 \int_0^r \alpha(r', \lambda) dr' \right]. \quad (2.21)$$

2.2.2.1 Raman LIDAR equation

From lidar signal the mixing ratio of the N_2 and H_2O gases, can be determined by using the vibrational Raman backscattering signals. Raman N_2 backscatter signal is being used as a measure of the mass of the dry air due to the fact that it is in constant proportion to the dry air at the heights over which the measurements were made [89]. The water vapor mixing ratio w along the lidar laser path can be written as [20, 22, 88, 89]

$$w(r) = C_w \frac{P(\lambda_0, \lambda_H, r)}{P(\lambda_0, \lambda_N, r)} \Delta\tau(\lambda_N, \lambda_H, r), \quad (2.22)$$

where $P(\lambda_0, \lambda_N, r)$ and $P(\lambda_0, \lambda_H, r)$ are the Raman lidar equations for N_2 and H_2O backscattering signal respectively, given as [20, 22, 88, 89]

$$P(\lambda_0, \lambda_N, r) = \frac{K_N Y_N(r)}{r^2} N_N(r) \frac{d\sigma_N(\lambda_0, \pi)}{d\Omega} \exp \left[- \int_0^r [\alpha(\lambda_0, r') + \alpha(\lambda_N, r')] dr' \right], \quad (2.23)$$

$$P(\lambda_0, \lambda_H, r) = \frac{K_H Y_H(r)}{r^2} N_H(r) \frac{d\sigma_H(\lambda_0, \pi)}{d\Omega} \exp \left[- \int_0^r [\alpha(\lambda_0, r') + \alpha(\lambda_H, r')] dr' \right], \quad (2.24)$$

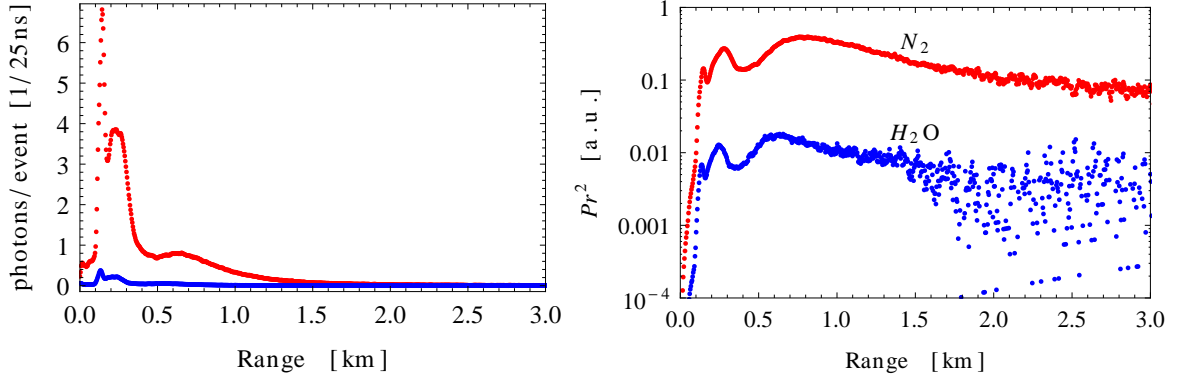


Figure 2.15: Example of photon-counting lidar data (left) from Raman lidar N_2 (red) and H_2O (blue) channel before (left) and after range correction (right). The measurement was performed on 24 August 2012.

C_w is the system calibration constant for the water vapor mixing ratio [20,22,88,89],

$$C_w = \frac{N_N}{N_{dry}} \frac{M_H}{M_N} \frac{K_N}{K_H} \frac{Y_N}{Y_H} \frac{d\sigma_N(\lambda_0, \pi)/d\Omega}{d\sigma_H(\lambda_0, \pi)/d\Omega'} \quad (2.25)$$

and $\Delta\tau(\lambda_N, \lambda_H, r)$ is the differential transmission correction function for the water vapor mixing ratio [20,22,88,89],

$$\Delta\tau(\lambda_N, \lambda_H, r) = \exp\left(\int_0^r [\alpha(\lambda_H, r') - \alpha(\lambda_N, r')] dr'\right), \quad (2.26)$$

which is primarily a result of the λ^{-4} dependence of the Rayleigh scattering by air molecules and λ^{-1} wavelength dependence of the Mie scattering by aerosols within the wavelength range from 354.7 nm to 407.5 nm [89]. In the case of clear air conditions the differential transmission is negligible, however, under the very hazy conditions when the aerosol optical depth is larger than 2 it must be corrected. In the case of our Raman lidar measurements where the aerosol optical depth was less or equal 0.5, the differential transmission can be neglected [89]. The measurement error in the water vapor mixing ratio can be estimated [89] as

$$\Delta w^2 = (\Delta w_{sys})^2 + (\Delta w_{stat})^2, \quad (2.27)$$

where the systematic error Δw_{sys} accounts for the uncertainty of the calibration constant,

$$\Delta w_{sys} = \Delta C_w \frac{\partial w}{\partial C_w} \quad (2.28)$$

and the statistical error Δw_{stat} is comprised of several error contribution such as background noise component in the detection signal. Fig. 2.15 shows example of the photon-counting data from N_2 and H_2O channels during performed measurements on 24 August 2012 (left), while on the right the corresponding range-corrected data are shown.

2.3 Summary

In first part of the Chapter basics of the Global Positioning System were discussed and presented. In particular, system architecture together with the evolution and development different series of GPS satellites Block's was presented. Discussion on signal structure and evolution followed with details. Different position modes were also discussed where the precise point positioning was presented in detail, including all errors and biases which one must take into account.

In the second part of the Chapter, presentation and discussion of LIDAR systems and their use in atmospheric science was given. In particularly, the derivation and use of Raman equation was discussed together with example of photon-counting data.

Atmospheric effects on EM wave propagation

Contents

3.1 Earth's atmosphere	35
3.1.1 Neutral Atmosphere	37
3.1.1.1 Chemical composition	37
3.1.1.2 Pressure	38
3.1.1.3 Water vapor	40
3.1.2 Ionosphere	43
3.1.2.1 Vertical profile of ionosphere	45
3.1.2.2 Geographical distribution of ionospheric regions	47
3.2 Propagation of electromagnetic waves in atmosphere	49
3.2.1 Ionospheric delay	51
3.2.2 Tropospheric delay	58
3.2.2.1 Tropospheric models	62
3.2.3 Light scattering in the lower atmosphere	69
3.2.3.1 Raman scattering	71
3.3 Summary	73

In this chapter short introduction to Earth's atmosphere, its structure and properties, such as chemical composition, temperature, pressure and electron density variations are given, with some examples. Moreover detailed introduction to electromagnetic wave propagation in atmosphere and its propagation error is given.

3.1 Earth's atmosphere

The Earth's atmosphere represents a mixture of gases, aerosols and ions that "envelops" the Earth. This envelope has no upper limit and it gradually merges into the interplanetary space [90]. Due to the Earth's gravity the atmosphere can be to first order considered as being horizontally stratified. Atmospheric structure can be identified from representative temperature profiles, as it is shown in Fig. 3.1 [91]. The lowest layer of the Earth's atmosphere is *troposphere*, representing the atmospheric volume where the temperature decreases with altitude (~ -6.5 K/km) [25,92] up to the *tropopause*. The height of the tropopause varies

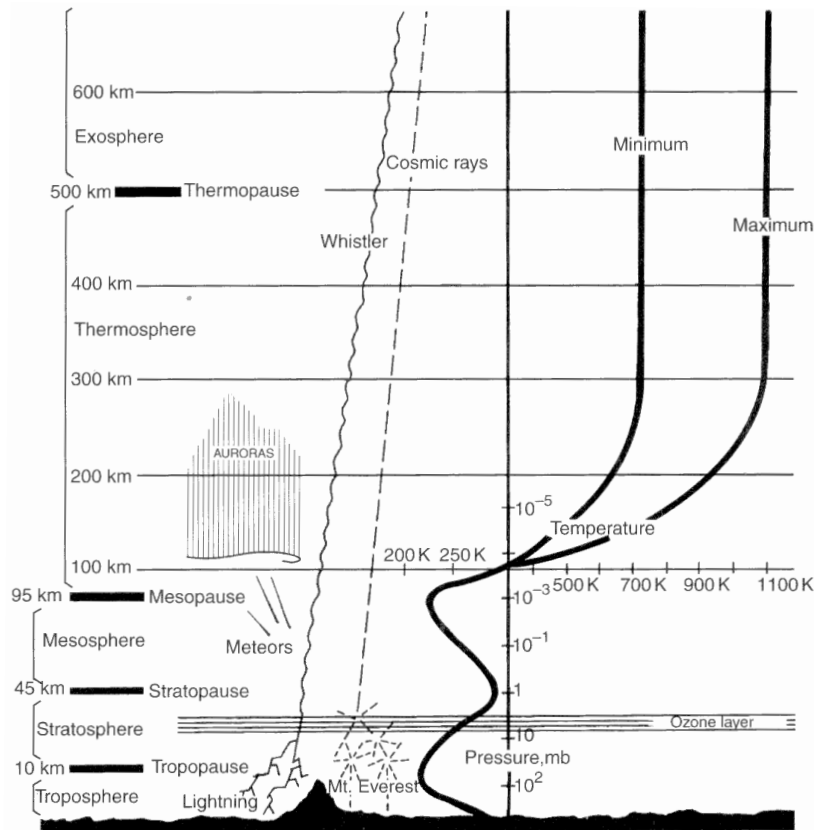


Figure 3.1: Schematic diagram of the Earth's atmosphere showing the different domains. The dark solid curves show atmospheric temperature profiles for solar maximum and minimum conditions [93].

with latitude (at tropics is between 16 km and 18 km and ~ 7 km at polar regions during summer while during winter can be entirely absent), season and weather situation [25, 92–94]. The tropopause defines the upper boundary layer of the troposphere. Troposphere contains about 80% of the total atmospheric mass and contains almost all of water vapor in the atmosphere. It is the most influenced between the atmospheric layers by the energy transfer that takes place at the Earth's surface in form of evaporation and heat conduction [92, 94]. Above the tropopause lies the *stratosphere*, which extends up to ~ 50 km to its top boundary, the *stratopause*. The stratosphere is a layer where ozone is present and the temperature starts to increase again up to a local maximum [93]. This increase in temperature is primarily due to the absorption by ozone [91]. From ~ 50 km to 90 km, in the *mesosphere*, the temperature starts to decrease again due to radiative cooling, up to its upper boundary layer called the *mesopause*. Mesopause represents the coldest region of the atmosphere, where the temperature can be between 130 K and 190 K. Above this region lies the *thermosphere*, where the temperature increase rapidly due to the absorption of even higher energy solar photons, up to an altitude of about 500 km [25, 91–94], where reaches an overall maximum value (~ 1000 K) [93].

An alternative way of characterizing different layers in the Earth's atmosphere is with respect to their electric properties. Its lower part, the troposphere, is electrically neutral,

while its upper part is ionized (manly due to solar radiation) and its called ionosphere.

3.1.1 Neutral Atmosphere

3.1.1.1 Chemical composition

Constituent Gas	By Mass [%]	By Volume [%]	Molecular Weight [g/mol]
Nitrogen (N ₂)	75.51	78.09	28.02
Oxygen (O ₂)	23.14	20.95	32.00
Argon (Ar)	1.3	0.93	39.94
Carbon dioxide (CO ₂)	0.05	0.03	44.01
Neon (Ne)	1.2×10^{-3}	1.8×10^{-3}	20.18
Helium (He)	8.0×10^{-4}	5.2×10^{-4}	4.00
Krypton (Kr)	2.9×10^{-3}	1.0×10^{-4}	83.7
Hydrogen (H ₂)	0.35×10^{-5}	5.0×10^{-5}	2.02
Xenon (X)	3.6×10^{-5}	0.8×10^{-5}	131.3
Ozone (O ₃)	0.17×10^{-5}	0.1×10^{-5}	48.0
Radon (Rn)	/	6.0×10^{-18}	222.0

Table 3.1: Composition of pure dry air up to 25 km [90]. It can be noticed that two main constituents are nitrogen (78.09%) and oxygen (20.95%).

The two main constituents of the Earth's atmosphere are nitrogen and oxygen, with their combined proportions approaching almost 99% of volume as well as by mass. Because their compositions vary little with time, they are called permanent gases [90]. The detailed composition of dry air is presented in Table 3.1. On the other hand, the concentrations of carbon dioxide, ozone and water vapor (Table 3.2) are variable. Although they occur in small proportions, they play an important role in atmospheric processes due to their radiative and thermodynamic properties [90]. Variations in CO₂ have a significant effect on atmospheric absorption and emission of infrared radiation. Such variations are caused by intake and release by oceans, by photosynthesis and by technological process (combustion of fossil fuels, biomass burning and industrial processes) [94, 95].

Constituent Gas	Fractional concentration by volume	Molecular Weight [g/mol]
Water vapor (H ₂ O)	0 to 5%	18.0160
Sulfur dioxide (SO ₂)	10 pptv - 1 ppbv	64.064
Nitrogen dioxide (NO ₂)	323.2 ppb	46.0055
Ozone (O ₃)	0 to 0.01	47.9982
Carbon dioxide (CO ₂)	0.01 to 0.1 (near the ground), average 0.04	44.00995

Table 3.2: Variable constituents of air [96–98].

The presence of water substance in the atmosphere is especially important, because it can exist in three phases, gaseous, liquid and solid. A change of phase involves either re-

lease or consumption of a large quantity of energy, affecting atmospheric properties and behaviour. Evaporation of water from the world's oceans, condensation of water vapor into clouds and rain, formation of polar ice caps, are all examples of phase change of water [90]. Water vapor is one of the most important greenhouse gases and is accounting for $\sim 60\%$ of the Earth's natural greenhouse effects. Although its concentration in the atmosphere is very variable (from barely traceable to $\sim 5\%$) [89] and is found mainly in the lower atmosphere its abundance is "controlled" mainly by evaporation and precipitation [95]. The above mentioned composition of the atmosphere undergoes changes above ~ 25 km under the effect of the Sun's ultra-violet (UV) radiation, where the gases most affected by this are oxygen and nitrogen. The result of this process is that their molecules break up and start to form ozone (O_3), from 20 to ~ 50 km of height, and ions and charged particles in the upper layers of atmosphere [90]. Ozone is a reactive oxidant gas which is produced naturally in trace amounts in the Earth's atmosphere. Almost 90% of atmospheric ozone is found in the stratosphere where it plays a critical role in absorbing UV radiation emitted by the Sun. It absorbs virtually all of the UV radiation of wavelengths between 240 and 290 nm which can be harmful to unicellular organisms and to surface cells of higher plants and animals [95].

3.1.1.2 Pressure

Just as temperature varies with height in the atmosphere, so does the pressure. The pressure profile can be calculated from the change in pressure, dp , over a small change of height dz [99]

$$dp = -g\rho dz, \quad (3.1)$$

where g is the gravitational acceleration and ρ is the density of air. Since the atmosphere is in principle a thin layer with respect to the Earth's radius, the acceleration due to gravity can be assumed to be constant. Although that the density of air varies with altitude it is a reasonable assumption that air behaves more like as an ideal gas, so that the density can be written as [95,99]

$$\rho = \frac{Mp}{RT}, \quad (3.2)$$

where M is the molar mass of air, R is the gas constant (8.314 J/mol K) and T the temperature in Kelvin [95,99]. Combing Eq. (3.1) and Eq. (3.2) we obtain

$$\begin{aligned} \frac{dp}{p} &= -\frac{gM}{RT} dz, \\ p &= p_0 \exp\left(-\frac{gM}{R} \int_0^z \frac{dz}{T}\right). \end{aligned} \quad (3.3)$$

Eq. (3.3) is also known as the *hydrostatic equation*, where the expression RT/gM presents characteristic length scale for decrease of pressure with height [95,99], also known as *scale height*. Scale height presents the vertical distance over which the pressure falls to $1/e$ of its initial value [95]. If we assume that the temperature is approximately constant, we can write simple approximation for change of pressure with height [95], known as barometric equation

$$\frac{p(z)}{p_0} = e^{-z/H}, \quad (3.4)$$

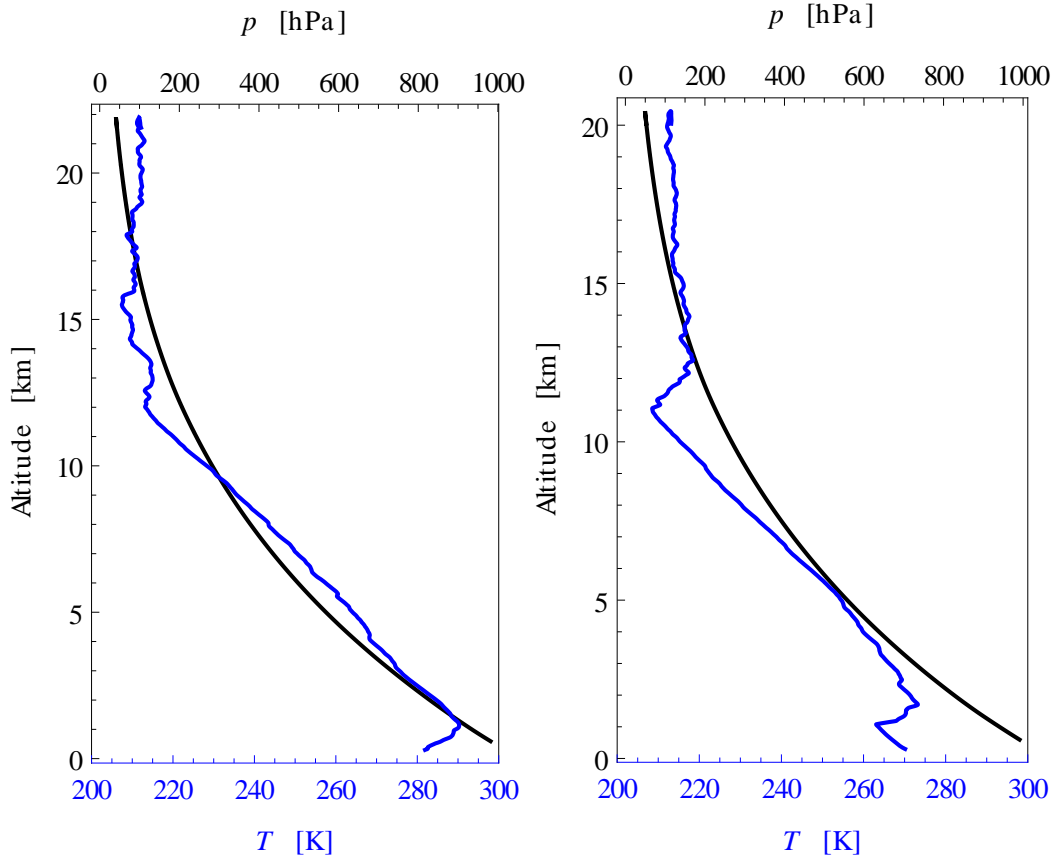


Figure 3.2: Temperature and pressure profiles obtained from radiosonde measurement in Ljubljana, Slovenia on 12 October 2011 (left) and on 1 February 2011 (right).

where $H = RT/gM$ is the scale height. Pressure, temperature and density variations with height in the atmosphere are shown in Table A.1, where it can be observed that temperature varies in the atmosphere by less than a factor 2, while the pressure changes by six orders of magnitude [95].

Due to the fact that the temperature for deriving Eq. (3.4) was assumed to be constant, the temperature at which H will be evaluated must be selected. According to [95] this can be done with calculation of the mean temperature of the troposphere, using surface temperature and a tropopause temperature. Fig. 3.2 shows two temperature and pressure profiles taken from radiosonde¹ measurements in Ljubljana on 12 October 2011 and on 1 February 2011 at 03:00 UT up to the height of stratosphere. The radiosonde measurements in Ljubljana are performed every day by ARSO² (46.06°N, 14.51°E, 298 m a.s.l.³) at either 02:00 UT or 03:00 UT, depending on weather conditions (Klemen Bergant, personal communication). At the time of first launch (12 October 2011) surface temperature was 281.91 K and the tropopause temperature 213.18 K at 12.023 km height, while for the second launch (1 February 2011) surface temperature was 270.13 K and the tropopause temperature 208.55 K

¹M2K2-DC GPSonde, Modem, France

²Slovenian Environmental Agency (Agencija Republike Slovenije za Okolje)

³a.s.l. stands for "above sea level"

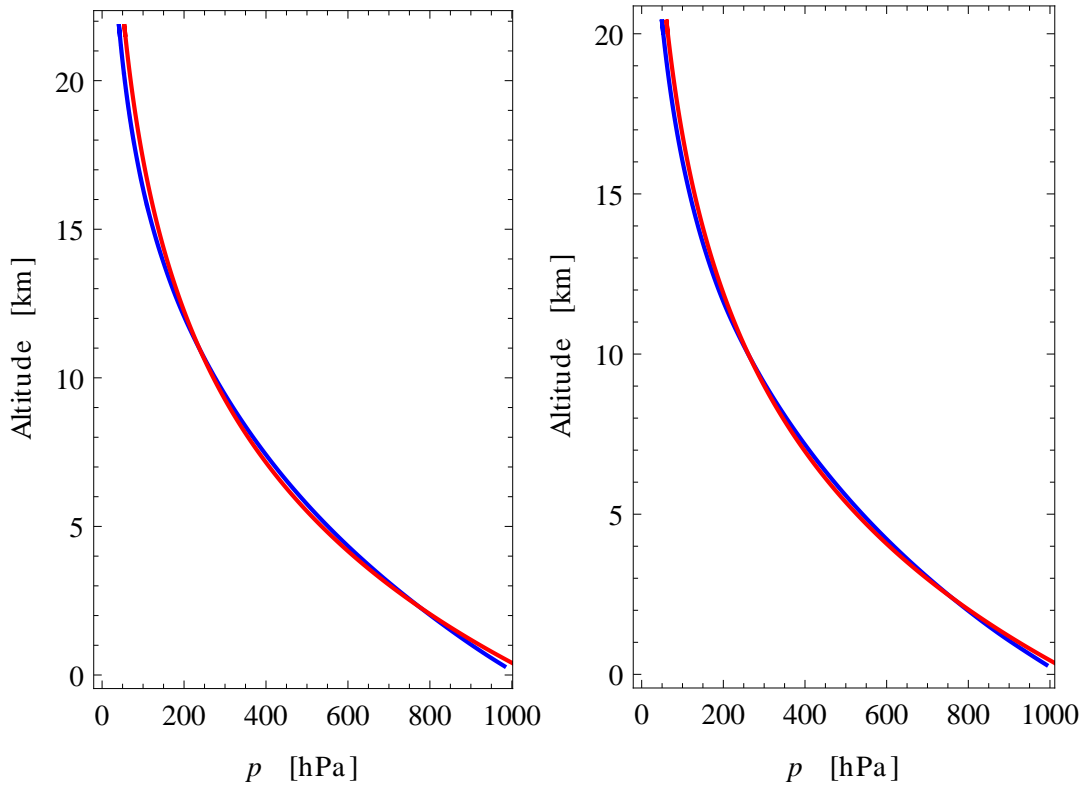


Figure 3.3: Pressure profiles obtained from radiosonde measurement in Ljubljana, Slovenia on 12 October 2011 (left) and on 1 February 2011 (right). Blue line presents the actual/measured pressure, while the red line corresponds to fitting function of Eq. (3.4).

at 11.054 km height. We can thus deduce that the mean temperature for first measurement was 247.54 K and for the second 239.34 K with scale heights 7.18 km and 6.946 km.

Another way to determine the scale height is to simply fit the function in Eq. (3.4) to the pressure change with height. Examples for both measurements are shown in Fig. 3.3, where the blue line presents the actual change of pressure with height and the red line corresponding fitting function. For first measurement the scale height is 7.35 km and for the second one 7.12 km. Calculating the mean temperature from $T = HgM/R$ gives us, 253.24 K and 245.1 K, respectively. As one can see there is a difference between the values of scale height obtained using two different methods. This difference is expected due to the fact that in first step a very simple approximation of a mean temperature was used for determination of the scale height, while in the second step fitting the pressure as an exponential function with height was used, where the whole profile was taken into account.

3.1.1.3 Water vapor

Water vapor, besides CO_2 , is one of the most important natural greenhouse gases in Earth's atmosphere. Such greenhouse gases "trap" infrared radiation that would otherwise escape into space, thus raising the temperature at the surface of the Earth [99]. Water in the atmosphere can appear in solid phase (as hail, snow, frost and cloud particles), in the liquid phase (as rain, fog, clouds) and in the gaseous phase as water vapor, in other words it can change

its phase under certain conditions of pressure and temperature. This change from one phase to another causes that a large amount of heat called *latent heat* is either withdrawn from or released to the atmosphere. For example, change in phase from solid to vapor phase causes withdraw of heat from environment hence cooling it, and reversely, when it changes the phase from vapor phase to a solid phase it release the heat to environment thereby warming the environment. A simple example of this change is formation and “degradation” of fog, while complex example would be the well known *hydrological cycle* [90]. One can use various parameters to quantity water vapor content in the atmosphere, such as named below [25,90,95,99].

Mixing ratio

Mixing ratio is one of the measures to express the amount of water vapor in the air. It represents water vapor content in proportion to the mass of dry (ambient) air, usually expressed in g of H₂O per kg of dry air. In order to relate the mixing ratio to the other measures of water vapor, the atmospheric pressure must be known. In the adiabatic lifting of unsaturated air, the mixing ratio will remain constant while the dew point will decrease with increasing height [25,90,95]. Mixing ratio is defined as [89, 100]

$$w = \frac{\rho_v}{\rho_d} = \frac{m_v}{m_d}, \quad (3.5)$$

where m_v is the mass of water vapor, m_d is the mass of dry air, ρ_v is the density of water vapor (also called the absolute humidity) and ρ_d is the density of dry air [100]. The ρ_v and ρ_d can be calculated as follows [100]

$$\begin{aligned} \rho_v &= eM_v/RT, \\ \rho_d &= p_dM_d/RT, \end{aligned} \quad (3.6)$$

were e is the vapor pressure, M_v is molecular weight of the water vapor (18.01 g/mol [100]), T is the temperature, p_d is the pressure of the dry air, M_d is the molecular weight of the dry air (~ 28.94 g/mol according to [89]). Using the relationship

$$p_d = p - e, \quad (3.7)$$

Eg. (3.5) can be written [100]

$$w = \epsilon \frac{e}{p - e}, \quad (3.8)$$

where ϵ is a constant obtained on following way [89,100,101]

$$\epsilon = \frac{R_d}{R_v} = \frac{M_v}{M_d} = 0.622, \quad (3.9)$$

with R_v as the specific gas constant for water vapor and R_d as the specific gas constant for dry air.

At saturation, the mixing ratio is called saturation mixing ratio. Saturation mixing ratio is defined as the ratio of m_{vs} of water vapor in a given volume of air saturated with respect to a plane surface of water to the mass m_d of the dry air [89,100–102]

$$w_s = \frac{m_{vs}}{m_d} = \epsilon \frac{e_s}{p - e_s}, \quad (3.10)$$

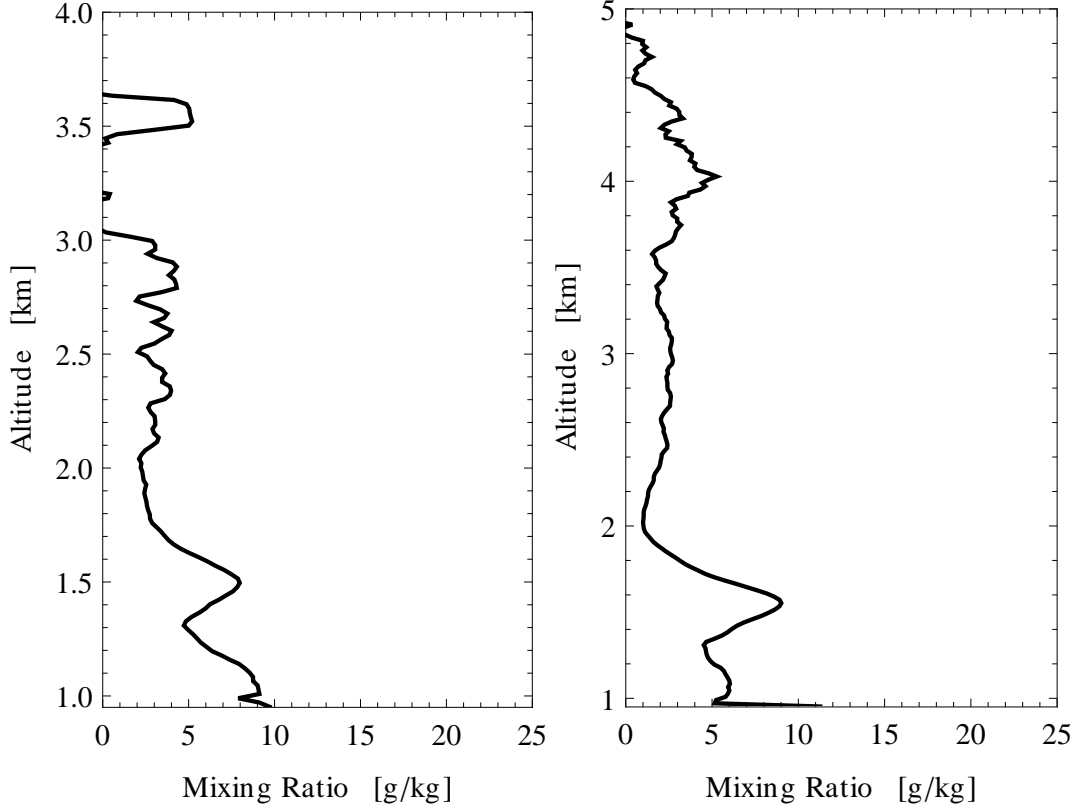


Figure 3.4: Mixing ratio profiles measured with Raman lidar, located at Otlica Observatory, Slovenia, on 12 October 2011 (left) and on 24 August 2011 (right).

where e_s is saturation vapor pressure for water (pure phase) [102]. For temperature range between 228 to 333 K (-45° to 60°C) is obtained from

$$e_s = e_0 \exp\left(a \frac{T - T_C}{T - T_1}\right), \quad (3.11)$$

with $e_0 = 611.2\text{ Pa}$, $a = 17.62$, $T_C = 273.15\text{ K}$ and $T_1 = 30.03\text{ K}$. Considering that e and e_s are much smaller than the total pressure of the moist air we write Eq. (3.8) and Eq. (3.10) [100]

$$w \approx \epsilon \frac{e}{p}, \quad (3.12a)$$

$$w_s \approx \epsilon \frac{e_s}{p}. \quad (3.12b)$$

Fig. 3.4 shows two mixing ratio profiles obtained with Raman Lidar stationed on Otlica Observatory, Slovenia (45.93°N , 13.91°E , 945 m a.s.l.). More detailed description on how to obtain mixing ratio from Raman lidar will be described in detailed in the following chapters.

Relative humidity

Relative humidity is defined as the ratio between the m_v and m_{vs} [100],

$$\text{RH} = \frac{m_v}{m_{vs}}, \quad (3.13)$$

where m_v is the mass of water vapor in a sample of moist air of volume V and m_{vs} is the mass of water vapor the sample would have had if saturated. Due to the ideal gas law we can write Eq. (3.13) as the ratio of the vapor pressure and saturation pressure, given in percent [89,90,95,100,101],

$$\text{RH} = 100 \frac{e}{e_s}. \quad (3.14)$$

Using Eq. (3.12) it follows [100] that approximately

$$\text{RH} \approx 100 \frac{w}{w_s}. \quad (3.15)$$

Dew point temperature

Dew point temperature represent the temperature to which a parcel of unsaturated air must be cooled at existing pressure and amount of water vapor for saturation to occur [25,90]. Further cooling produces condensation of part of water vapor to liquid water. These processes can be delayed when the parcel of air is cooled below the dew point at which point the air becomes supersaturated. When this happens, the condensation of air can occur abruptly, causing a rise in air temperature due to the released latent heat of vaporization [90]. The difference between the so-called dry-bulb temperature (“actual” air temperature) and the dew point temperature is known as the dew-point depression and gives a measure of the humidity of the air. This depression varies inversely with the humidity of the air [90]. When the dew point remains constant and temperature increases, relative humidity decreases. At high relative humidity (1 or 100%) the dew point will be equal to the ambient temperature [25,100].

Precipitable water

Precipitable water is the amount of water vapor in vertical column of unit cross-section extending between two specified levels measured in mass per unit area. Precipitable water can also be reported as the height at which the liquid would stand if it were all condensed in a “vessel” of the same unit cross-section as the air column. For example, a height of 1 cm corresponds to 1 g/cm² of precipitable water [25].

3.1.2 Ionosphere

The ionosphere represents the ionized portion of the upper atmosphere, where the main source for plasma is photoionization of neutral molecules via solar UV and soft X-ray radiation, although other production processes may dominate in certain regions [91,93]. As mentioned before, the ionosphere is vertically “organized” by the electron density variation with altitude.

As one can see from Fig. 3.5, the ionosphere extends from ~60 km to beyond 1000 km and can be, due to the changing electron density divided into several layers. The electron density in all layers varies with the time of day, season, solar cycle and level of magnetosphere or solar wind disturbance. At the uppermost altitudes the ionosphere merges with the magnetosphere of the Earth [25,91,93]. The variation of electron density with the time of day is shown on Fig. 3.5, where the peak plasma density occurs in F – layer near noon time. Additional information on major components and their corresponding production causes of ion

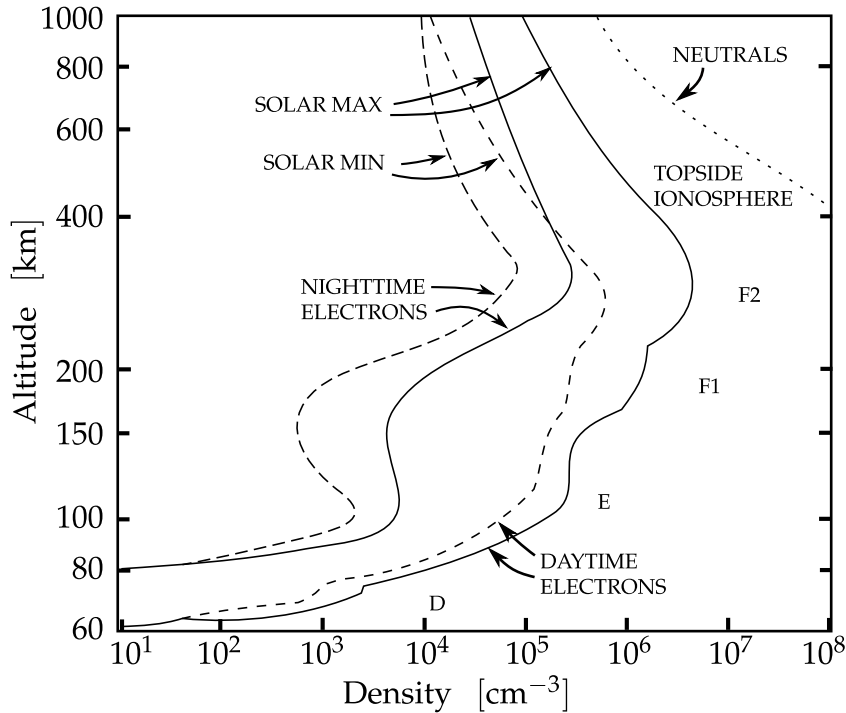


Figure 3.5: Ionospheric profiles for mid-latitude ionosphere [25].

Layer	Altitude	Major Comp.	Production Cause
D	~60 to ~90 km	$\text{NO}^+, \text{O}_2^+$	Lyman α , X-rays
E	95 to 140 km	$\text{NO}^+, \text{O}_2^+$	Lyman β , Soft X-rays, UV Continuum
F1	140 to 200 km	O^+, NO^+	He II, UV Continuum (100 to 800 Å)
F2	200 to 400 km	O^+, N^+	He II, UV Continuum (100 to 800 Å)
Topside F	>400 km	O^+	Transport from below
Plasmasphere	>1200 km	H^+	Transport from below

Table 3.3: Layers of daytime mid-latitude ionosphere [25], with corresponding major components and their main ionization processes.

production is shown in Table 3.3. Note that these characteristics are valid only for mid-latitude ionosphere, while at high latitudes (polar regions) the layer is distorted due to ionization by energetic particles, magnetospheric coupling and other effects (which will be explained in more detail in the following sections) and in the equatorial region (low latitude) where the profile is distorted by the geomagnetic field [25]. More detailed information on ionospheric composition can be seen in Fig. 3.6 [91].

The variations in electron density of the ionosphere can be divided into five major groups [25]:

- **diurnal** variation through the day, which is largely due to the variation of the solar zenith angle,
- **seasonal** variation throughout the year,

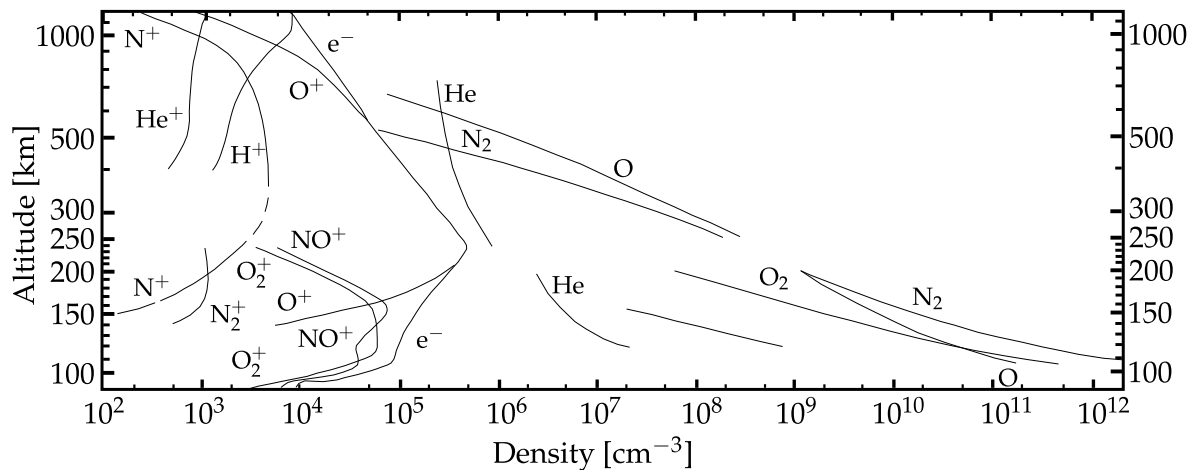


Figure 3.6: International Quiet Solar Year (IQSY) daytime atmospheric composition based on mass spectrometer measurements [91].

- **location** variation according to the geographic and geomagnetic position,
- **solar activity** variation according to solar activity (both long term activity and solar disturbances), and
- **height** variation in the atmosphere causing the formation of different layers.

3.1.2.1 Vertical profile of ionosphere

As already mentioned above and shown in Figs. 3.5, 3.6 and Table 3.3 the ionosphere is vertically organized in several layers: D, E and F (F1 and F2), depending on the time of day. The peak electron density in the ionosphere occurs in the F layer with values between $10^6 / \text{cm}^3$ and $10^7 / \text{cm}^3$ around midday. The factor which limits the peak density is called the recombination rate – the rate at which ions and electrons combine to form a neutral molecule or atom [91]. In Fig. 3.6 and in Table 3.3 the major chemical compositions are shown with their corresponding causes of ion production [25,91]. According to [103] there are several reasons for “developing” different and distinct ionospheric layers:

- the physics of recombination depends on atmospheric density,
- the solar spectrum deposits its energy at various heights depending on the absorption properties of the atmosphere, and
- because the composition of the atmosphere also changes with height.

The basic properties of each layer are described below.

D layer

D layer is the first layer in the ionosphere, extending from ~ 60 up to 90 km and is only present during daylight hours [25,61,91,93]. One of the primary sources of the ionization in

this layer is cosmic radiation, which is strongly affected by solar cycle variation and manifests itself in the electron density in the layer [61]. During the day, due to the Sun radiation, the electrons tend to detach themselves from ions, causing the D layer to appear. However, during the night, the electrons tend to attach back to atoms and molecules (primarily oxygen and nitrogen) causing the formation of negative ions and resulting in the D layer disappearance [61,93]. As can be seen from Fig. 3.5, the peak density of the D layer appears at ~ 90 km during solar minimum, while during the solar maximum when X-ray flux is enhanced, can depress up to ~ 78 km [25]. As can be seen from Fig. 3.6 and Table 3.3, in the D layer the molecular ions dominate with N_2 , O_2 and O being the most abundant neutral species. Additionally, in the D layer, there are both positive and negative ions, water cluster ions and products of three body chemical reactions, where the cluster ions dominate at altitudes below ~ 85 km and their formation occurs via hydration starting from primary ions NO^+ and O_2^+ [93].

E layer

Above D layer lies a so-called E layer, whose “behaviour” almost entirely depends on the level of solar activity and the zenith angle of the Sun. One of the primary sources of ionization in this layer is X-ray radiation which causes electron density with distinct solar cycle, seasonal and daily variations [61], ionizing O , O_2 and N_2 [103]. Additionally ionization of O_2 may also occur directly by absorption in the first ionization continuum ($h\nu > 12$ eV) [103]. From Fig. 3.5 it can be seen that the peak density occurs at ~ 110 km. At sunset the electron density in this layer can drop by a factor of 10 or even more in a very short period of time (tens of minutes) before reaching the nighttime equilibrium [25]. However, the E layer does not disappear entirely during the night but for practical purposes it is often assumed that its electron density drops to zero [61]. In this layer the chemical reactions are not so complicated and the most abundant ions are NO^+ , O_2^+ and N_2^+ [93].

F layer

F layer presents a combination of two different “sublayers” due to the different processes that dominate. The first “sublayer” is the F1 layer, for which the main source of ionization is UV light and has a peak density at ~ 200 km but is absent during the night [25,61]. The reason that the F1 layer is only observed during the day, is that the electron density is primarily controlled by the zenith angle of the Sun, and it is more pronounced during the summer than during the winter. Typical values of electron density for mid latitude ionosphere are in the range between 2.3×10^{11} and 3.3×10^{11} electrons/ m^3 (depending on the solar activity) [61]. Above the F1 layer lies the F2 layer, which has a peak density at ~ 300 km during the day and at higher altitudes during the night [25], and is the most important layer of ionosphere from the point of view of high frequency propagation (frequencies between 3 and 30 MHz) [61]. Typical mid-latitude noon time electron densities range between 2.8×10^{11} and 5.2×10^{11} electrons/ m^3 according to the solar activity [61]. In both (F1 and F2) the dominant atomic species are O^+ and O , where in F1 ion-atom interchange and transport process are important and in F2 the maximum ionization occurs due to the balance between plasma transport and chemical loss process [93].

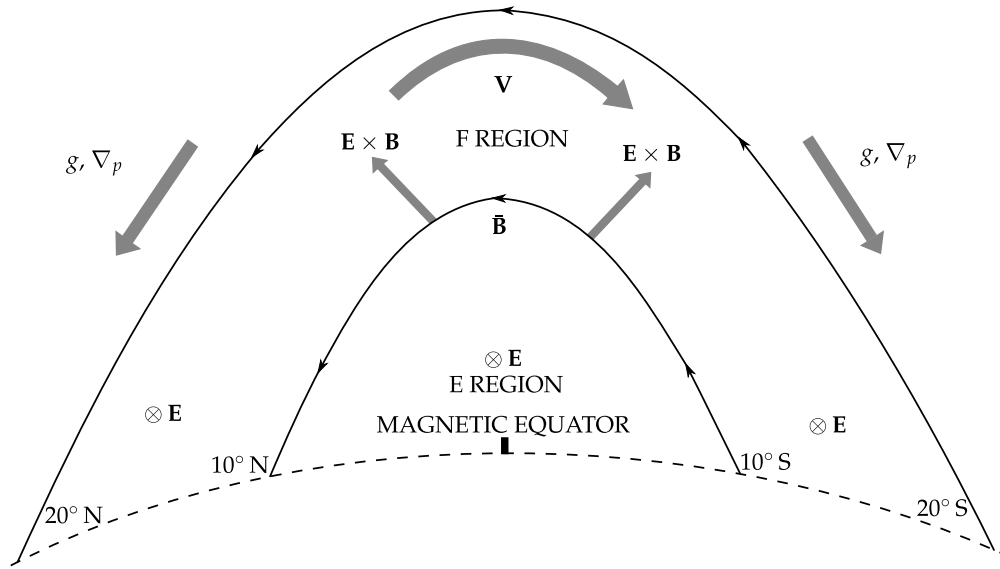


Figure 3.7: Schematic presentation of equatorial fountain that gives rise to the equatorial anomaly [104], where Fountain process is indicated with $\mathbf{E} \times \mathbf{B}$, \mathbf{B} indicates the magnetic field, g gravity, ∇_p pressure gradients, \mathbf{V} neutral wind and \mathbf{E} electric field.

3.1.2.2 Geographical distribution of ionospheric regions

Low latitude region

The *low latitude region*, also known as the *equatorial region*, can be characterized by the highest values of the peak electron density [61].

Equatorial plasma in the F2 layer is, due to the influence of pressure gradients and gravity, forced downward along the magnetic field lines. As a consequence of this, a belt of enhanced electron density is formed between latitudes 15° and 20° on both sides of the geomagnetic equator – the Equatorial Anomaly. The process, which is known as the Fountain Effect is shown in Fig. 3.7, where the Fountain process is indicated by the $\mathbf{E} \times \mathbf{B}$ drift, which drives the plasma upward. This plasma is then diffused along the magnetic field \mathbf{B} under the influence of gravity, g , and pressure gradient ∇_p . The whole process occurs in the daylight hemisphere, while at the dusk the electric field \mathbf{E} increases as the neutral wind \mathbf{V} increases and the $\mathbf{E} \times \mathbf{B}$ drifts raises the F layer in a process known as Pre-Reversal Enhancement [25,61,91,104] when the base of the F layer is forced against the gravity and thus creating the Rayleigh-Taylor Instability (the heavier fluid is held by the lighter). However, when a perturbation occurs, this unstable equilibrium is broken and the lighter fluid rises through the denser one creating bubbles in the equatorial region also known as Equatorial Plasma Bubbles [25,104].

During the day the field is eastward orientated and reverses to the west after sunset. Before reversal a dramatic enhancement of the electric field develops at F-region heights [14,104–113]. As a result, the ionosphere moves upwards developing steep density gradients. Through the Rayleigh-Taylor mechanism, the irregularities then develop into plasma-depleted bubbles and are upwelled to the topside of the ionosphere [105]. The effect of pre-reversal enhancement on the eastward electric field is two-fold and has both seasonal

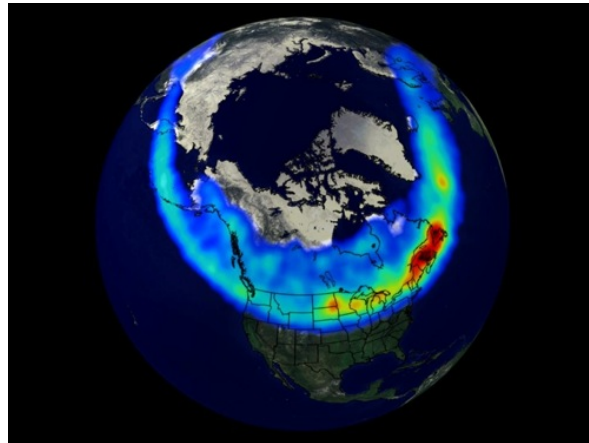


Figure 3.8: Schematic figure showing the extend of aurora oval around the north pole [116].

and solar activity dependences. The increased field causes a redistribution of ionization by a fountain like effect, thereby increasing the ionization density near the crest at the expense of that at the trough over the magnetic equator.

Mid latitude region

The mid-latitude ionosphere is the least variable and undisturbed part of the ionospheric regions. The ionosphere at mid-latitudes is usually free of the effects imposed by the horizontal field geometry that is important in low latitude region. Additionally, this region is the most observed region due to the fact that it has the most available observation data [61]. At middle latitudes the most relevant ionospheric structures are the so called Traveling Ionospheric Disturbances (TIDs) [114]. These ionospheric disturbances are characterized by the large scale of ionospheric enhanced plasma density as a response to Atmospheric Gravity Waves (AGWs) in the ionosphere [114, 115] or during disturbed magnetic conditions, forming at high latitudes and traveling southward. Their activity and amplitudes vary depending on latitude, longitude, local time, season, and solar cycle [115]. According to their scales, there are three different classes of TIDs [115]:

- Large Scale TIDs (LSTIDs) – their origin is in the auroral zone, with horizontal wavelengths greater than 1000 km and periods ranging from 30 minutes to 3 hours. Their horizontal phase velocities are in a range of 300 to 1000 m/s.
- Medium Scale TIDs (MSTIDs) – their origins are mostly in the lower atmosphere but also in the auroral zone with wavelength range from 100 km to 300 km, periods from about 12 minutes to 1 hour and horizontal phase velocities from 100 to 300 m/s.
- Small Scale TIDs (SSTIDs) – their origins are only in the lower atmosphere. The wavelengths, velocities and periods are smaller than those of MSTIDs, because they belong to the acoustic branch.

High latitude region

In contrast to the low latitude ionosphere, at high latitudes the magnetic field lines are nearly vertical which makes the ionosphere at high latitudes more complex than at middle or low latitudes [117]. Since the magnetic lines are nearly vertical, the charged particles can descend into the E layer (~ 100 km) causing collisions with neutral atmospheric gases and thus creating local enhancements in the electron concentration, phenomena associated with auroral activity [61]. Additionally, magnetic field lines connect the high latitude ionosphere to the outer part of the magnetosphere which is driven by solar winds and which makes this region more sensitive to external influence than middle or low latitude [117]. Auroral activity can also be regarded as an interaction between magnetosphere, ionosphere, and atmosphere. The auroral zones are relatively narrow rings situated between the northern and southern geomagnetic latitudes of about 64° and 70° . In general, the intensity and the positions of the auroral ovals are related to geomagnetic disturbances. The ovals expand towards the equator with increasing levels of geomagnetic disturbance [61], shown in Fig. 3.8.

3.2 Propagation of electromagnetic waves in atmosphere

Earth's atmosphere is by no means completely transparent for propagation of EM waves due to the fact that gases in the neutral atmosphere and plasma effects in ionosphere together form important barrier for transmission. Atmosphere selectively transmits EM waves of certain wavelengths. The ranges of wavelengths that are relatively easily transmitted through the atmosphere are *atmospheric windows* [8]. These atmospheric windows are shown in Fig. 3.9 (light blue), together with the amount of attenuation of EM waves as a function of their wavelength. The positions, extent and effectiveness of atmospheric windows is determined by the absorption spectra of atmospheric gases.

Gases that are the cause for most of absorption in atmosphere are ozone (O_3), carbon dioxide (CO_2) and water vapor (H_2O). As can be seen from Fig. 3.9, at short wavelengths Rayleigh scattering and attenuation dominate (Section 3.2.3), while at very long wavelengths, plasma effects in the ionosphere dominate atmospheric attenuation. For the wavelengths in-between, absorption by various molecular constituents dominate atmospheric attenuation. Therefore we can say the longer the wavelength, the less attenuation occurs in the atmosphere (except for the large IR window). As the EM wave propagates through atmosphere it is subject to modification also by physical processes other than absorption, such as scattering and refraction. Refraction, described by *Snell's law*, occurs in atmosphere as EM wave passes through different atmospheric layers with varying clarity, humidity, electron density and temperature. These variation influence the density of atmospheric layers, which in turn causes not only bending but also retardations of EM waves while passing from one layer to another [8,9]. On the other hand, scattering is the redirection of EM waves, caused mainly by molecules or by larger particles suspended in the atmosphere, where the amount of scattering depends on the sizes of these particles, the wavelength of the radiation (for instance the intensity of molecular scattering is sensitive to the wavelength of the EM wave: the scattering is proportional to λ^{-4}), their abundance and the depth of the atmosphere through which EM waves travel [22]. There are two main types of scattering occurring in the atmosphere – elastic scattering (e.g. Rayleigh scattering) and inelastic scattering (e.g. Raman scattering) [22,88].

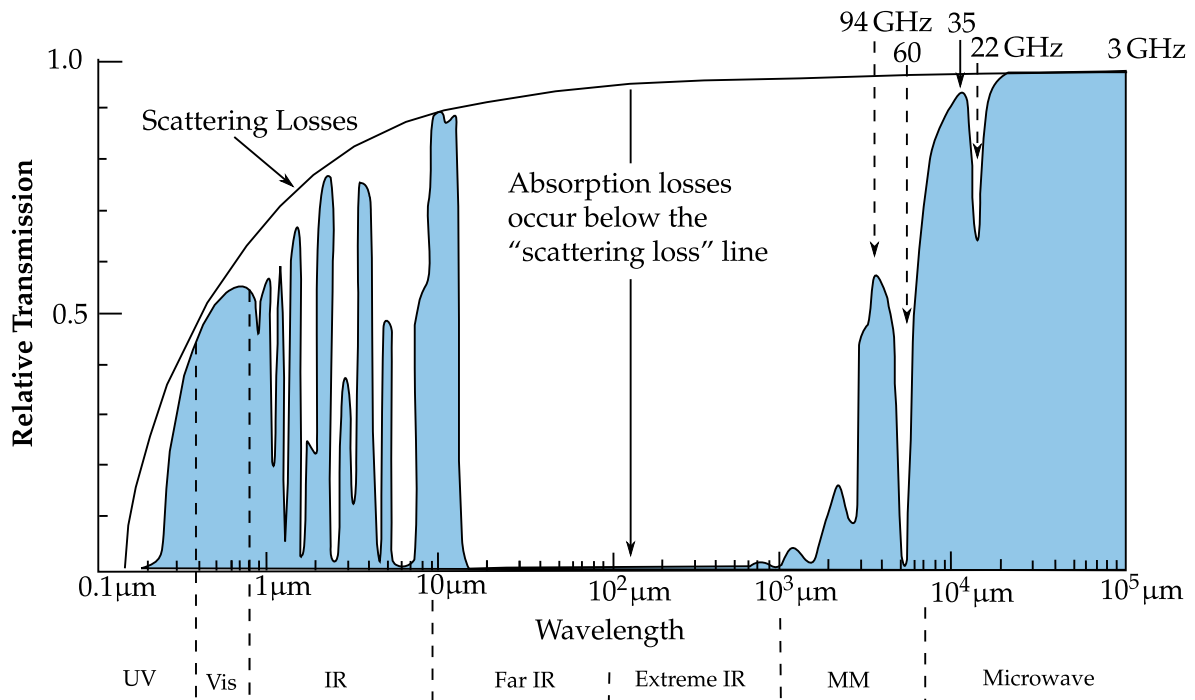


Figure 3.9: The amount of attenuation of an EM wave traveling through the atmosphere as a function of its wavelength, where atmospheric windows are colored in light blue (adapted from [118]).

The atmosphere affects the speed and direction of propagation of radio signals, such as GPS signals, in terms of *refraction*. The travel distance of the signal from GPS satellite to receiver ranges from $\sim 20\,000$ km (when the satellite is overhead) to $\sim 26\,000$ km (when the satellite is raising or descending). Almost all of signal path, except the last 5%, can be regarded as in a vacuum of free space, through which the electromagnetic waves can travel with constant speed $c = 299\,792\,458$ m/s, known as *universal constant* [1–4, 9]. However in the last 5% of the signal path at height ~ 1000 km the signal enters ionosphere and later at ~ 60 km neutral part of atmosphere [1], where the signal suffers refraction which translates into a delayed signal at the receiver (see Fig. 3.10). The “nature” of the delay primarily depends on the type of the medium through which it travels.

As can be seen from Fig. 3.10 that in case of atmosphere free environment (vacuum) the EM wave would travel along a geometrical (straight) path (G), however due to the presence of Earth’s atmosphere the signal travels along the path L , where the signal not only bends but also retards [1–4, 9]. The geometrical path between satellite (S) and receiver/user (U), can be written as

$$G = \int_S^U dg, \quad (3.16)$$

where dg is a line segment along the geometrical path G . However, due to Fermat’s principle of least time which states that the flight time of light between any two points should be a minimum, the path between receiver and satellite, defined as the minimum electrical path

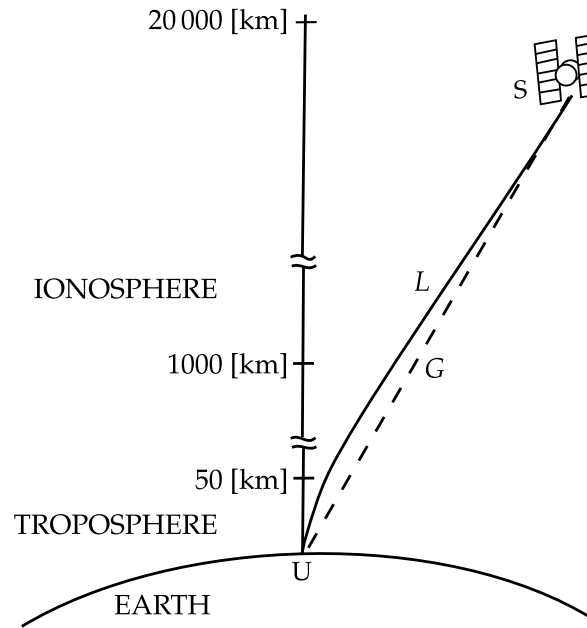


Figure 3.10: Schematic diagram showing the curved/bended signal path (denoted by L) and geometric straight-line signal path (denoted as G) between receiver/user U and satellite S (adapted from [1]).

length [2,9] is given by

$$L = \int_S^U n \, d\ell, \quad (3.17)$$

where n represent refractive index of media through which signal is passing. The total delay (including both bending and propagation delay) of GPS signals caused by atmosphere can be written as follows [2]

$$\Delta L = L - G = \int_S^U (n - 1) \, d\ell - \int_S^U dg, \quad (3.18)$$

where the first term presents the propagation delay and the second term bending [9].

3.2.1 Ionospheric delay

Ionosphere represents a dispersive medium for radio signals above 1 GHz and causes a delay that is frequency dependent, i.e. the lower the frequency the greater delay will be produced (for instance ionospheric delay on L2 frequency is greater than delay on L1 frequency) [60]. GPS signal passing the ionosphere will be delayed, causing the change in the signal propagation speed when compared to that of free space [55]. Interesting fact is that the ionosphere appears to speed up the propagation of the carrier phase by causing a phase advance but it slows down the signal modulation (PRN code and the navigation data) for the same amount [55,60]. The distance between satellite and receiver will be too long if measured by the code and shorter when measured by the carrier phase [60]. Within one day, the delay or advance of GPS signal can vary from few meters to more than twenty meters and it mainly depends on electron density varying with geographical location, time of day, solar activity

etc [54, 60]. Although it is difficult to model the ionospheric delay due to the complicated physical interactions between the geomagnetic field and solar activities, it can be measured or corrected for [54].

In terms of refraction, the indices of refraction for the phase and group propagation can be written [1, 2, 54]

$$n_p = \frac{c}{v_p} \quad n_g = \frac{c}{v_g}, \quad (3.19)$$

respectively, where c is the speed of light, v_p and v_g are the phase and group velocities in the medium, respectively. The index of refraction for the phase propagation in the ionosphere can be approximated as [2, 54, 92]

$$n_p = 1 + \frac{c_2}{f^2} + \frac{c_3}{f^3} + \frac{c_4}{f^4} \dots \quad (3.20)$$

and for group velocity

$$n_g = 1 - \frac{c_2}{f^2} - \frac{2c_3}{f^3} - \frac{3c_4}{f^4} \dots \quad (3.21)$$

where f is the frequency of the signal, c_2 , c_3 , c_4 and c_5 are frequency independent coefficients but are still function of the number of electrons along the signal propagation path (in case of GPS signals the path between the satellite and the receiver). Neglecting the high-order terms, we can obtain the following approximations for Eqs. (3.20) and (3.21)

$$n_p = 1 + \frac{c_2}{f^2} \quad n_g = 1 - \frac{c_2}{f^2}, \quad (3.22)$$

with c_2 being estimated as $c_2 = -40.3 n_e \text{ Hz}^2$, where n_e is the electron density. Using this definition of phase and group refractive index and inserting it to Eq. (3.18), the delay induced by phase refractive index in the ionosphere can be written as [2, 54, 92]

$$\Delta L_{\text{iono},p} = \int_S^U \left(1 - \frac{40.3 n_e}{f^2} \right) d\ell - \int_S^U dg, \quad (3.23)$$

and the delay caused by group refractive index

$$\Delta L_{\text{iono},g} = \int_S^U \left(1 + \frac{40.3 n_e}{f^2} \right) d\ell - \int_S^U dg. \quad (3.24)$$

The Eqs. (3.23) and (3.24) can be simplified [2], due to the fact that the delay is small compared to the satellite-user distance, by integrating the first term along the geometric path

$$\Delta L_{\text{iono},p} = -\frac{40.3 n_e}{f^2} \int_S^U dg, \quad (3.25a)$$

$$\Delta L_{\text{iono},g} = \frac{40.3 n_e}{f^2} \int_S^U dg. \quad (3.25b)$$

The electron density along the path length is defined as the *total electron content* (TEC) [1, 2, 92]

$$\text{TEC} = \int_S^U n_e dg, \quad (3.26)$$

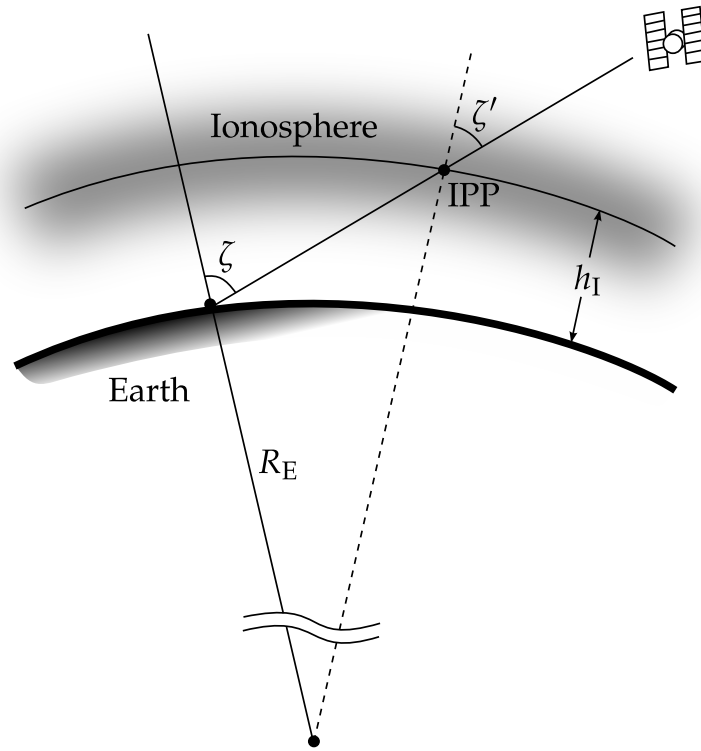


Figure 3.11: The propagation path length of a signal through the ionosphere increases with the zenith angle ζ . The increased path length is accounted for in terms of a multiplier of the zenith delay called as obliquity factor [1]. R_E – average radius of the Earth, h_I – mean ionospheric height, IPP – ionospheric pierce point, ζ and ζ' – zenith angles of the satellite.

which is expressed in units of electrons/ m^2 or TECU (TEC Units) where 1 TECU is defined as 10^{16} electrons/ m^2 . In terms of TEC, Eqs. (3.25) can be now rewritten as

$$\Delta L_{\text{iono,p}} = -\frac{40.3 \text{ TEC}}{f^2}, \quad (3.27a)$$

$$\Delta L_{\text{iono,g}} = \frac{40.3 \text{ TEC}}{f^2}. \quad (3.27b)$$

The TEC derived above is generally known as the vertical TEC (TECV), the measured TEC when the satellite is at an elevation angle 90° (zenith direction). Therefore, for other elevation angles we must modify the expression in Eqs. (3.27) with a multiplier which accounts for the longer path length. This multiplier is called *obliquity factor* [1, 2], also referred to as a *mapping function*. There are various models which describe the determination of obliquity factor. One model [1] is shown in Fig. 3.11 where h_I is the mean ionospheric height (usually taken between 300 and 400 km), IPP is the ionospheric pierce point (defined as the point of intersection of the line of sight with the spherical shell at height h_I), ζ and ζ' are the zenith angles of the satellite and the R_E is the average radius of the Earth (~ 6400 km).

Obliquity factor (OF) for zenith angle ζ can be defined as [1,2]

$$\text{OF}_I = \left[1 - \left(\frac{R_E \sin \zeta}{R_E + h_I} \right)^2 \right]^{-1/2}. \quad (3.28)$$

With the definition of the obliquity factor, the path delay expressions in Eqs. (3.27) become

$$\Delta L_{\text{iono,p}} = -\text{OF}_I \frac{40.3 \text{ TEC}}{f^2} \quad (3.29a)$$

$$\Delta L_{\text{iono,g}} = \text{OF}_I \frac{40.3 \text{ TEC}}{f^2}. \quad (3.29b)$$

Due to the fact that the ionospheric delay is frequency dependent it can be effectively eliminated by making ranging measurements with a dual-frequency receiver. These first-order estimates are based on Eqs. (3.22) where taking a difference on pseudorange measurements for L1 and L2 frequencies enables the estimation of both L1 and L2 delays [2, 60]. If one rewrites the ionospheric effect on phase (or carrier) as follows

$$\Delta L_{\text{iono,p}} = \frac{C_1}{f^2}, \quad (3.30)$$

with C_1 as [1,2,54]

$$C_1 = \int c_2 dg, \quad (3.31)$$

and further in case of dual frequency (L1 and L2) GPS phase (or carrier) observations as

$$\Delta L_{\text{iono,p}}(f_1) = \frac{C_1}{f_1^2}, \quad \Delta L_{\text{iono,p}}(f_2) = \frac{C_1}{f_2^2}, \quad (3.32)$$

one can notice that performing following combination

$$f_1^2 \Delta L_{\text{iono,p}}(f_1) - f_2^2 \Delta L_{\text{iono,p}}(f_2) = 0, \quad (3.33)$$

will lead to an elimination of the ionospheric effects. However, the combination in Eq. (3.33) has to be standardised by dividing with $f_1^2 - f_2^2$, so that the combined phase (or carrier) observations also have the sense that they are phase (or carrier) observables at specific frequency. The first order ionosphere-free phase combinations can be represented then as [54]

$$\frac{f_1^2 \Delta L_{\text{iono,p}}(f_1) - f_2^2 \Delta L_{\text{iono,p}}(f_2)}{f_1^2 - f_2^2} = 0. \quad (3.34)$$

Formally the combined observations are observed at frequency [54]

$$f = \frac{f_1^2 f_1 - f_2^2 f_2}{f_1^2 - f_2^2} \quad (3.35)$$

with the wavelength of $\lambda = c/f$. The combination derived in above is know as ionosphere-free linear combination, and it is a first order elimination of ionospheric effects while higher order effects remain. One can remove second order by performing triple frequency combination (for details please see [54]). Single-frequency receivers cannot take advantage of the

dispersive nature of the ionosphere. They use one of the empirical models to correct for up to 60% of the delay. The most widely know is so-called Klobuchar model, whose coefficients are transmitted as part of the GPS navigation message [2, 60].

Besides the above described ionospheric delay, (code delay and phase advance), there are also other effects that the ionosphere has on GPS signals that travel through it. These are [25]

- Doppler shift of the carrier of the radio wave,
- Faraday rotation of the plane of polarization of linearly polarized waves,
- angular refraction or bending of the radio wave path as it travels through the ionosphere,
- distortion of the waveform of transmitted pulses, and
- amplitude and phase scintillation, also known as ionospheric scintillation.

While the first four effects listed above are, at least to first order, proportional to the total number of electrons encountered by the signal during its passage through the ionosphere, this is not the case for ionospheric scintillations. In fact, phase scintillation is simply the short term time rate of change of total electron content after the longer term variations have been removed [25]. According to [105], ionospheric scintillation can be described as a form of space-based multipath, where instead of radio waves reflecting from nearby surfaces and then adding at the antenna, planar radio waves strike a volume of irregularities and then emerge as a surface of nearly constant amplitude but variable phase. Irregularities producing scintillations are predominately in the F layer at altitudes ranging from 200 km to 1000 km, where the primary disturbance region for equatorial and high latitude regions ranges between 250 km and 400 km (Fig. 3.12) [25]. The process is schematically shown in Fig. 3.12, where L represent thickness of the irregularity slab with random irregular electron density structures, which can be characterized by a dielectric permittivity [119],

$$\epsilon(\vec{r}, t) = \langle \epsilon \rangle [1 + \epsilon_1(\vec{r}, t)], \quad (3.36)$$

at location \vec{r} and time t , where $\langle \epsilon \rangle$ is the background average dielectric permittivity which for the ionosphere is given by [119]

$$\langle \epsilon \rangle = (1 - f_{p0}^2/f^2)\epsilon_0, \quad (3.37)$$

and $\epsilon_1(\vec{r}, t)$ is the fluctuating part characterizing the random variations caused by irregularities and is given by

$$\epsilon_1(\vec{r}, t) = -\frac{(f_{p0}/f)^2[\Delta N(\vec{r}, t)/N_0]}{1 - (f_{p0}/f)^2}, \quad (3.38)$$

with f_{p0} as plasma frequency corresponding to the background electron density N_0 and f is the frequency of the incident wave [119]. These irregularities through which GPS signal propagates towards the receiver, distort the original wavefront giving rise to a randomly phase-modulated wave $k_0(\Delta\phi)$ where for a radio wave of length λ , $k_0 = 2\pi/\lambda$ is the free-space wavenumber and $\Delta\phi$ is the variation of the optical path length within the layer with irregularities, defined as [106, 119]

$$\Delta\phi = -2\pi r_e \Delta N_T / k_0^2, \quad (3.39)$$

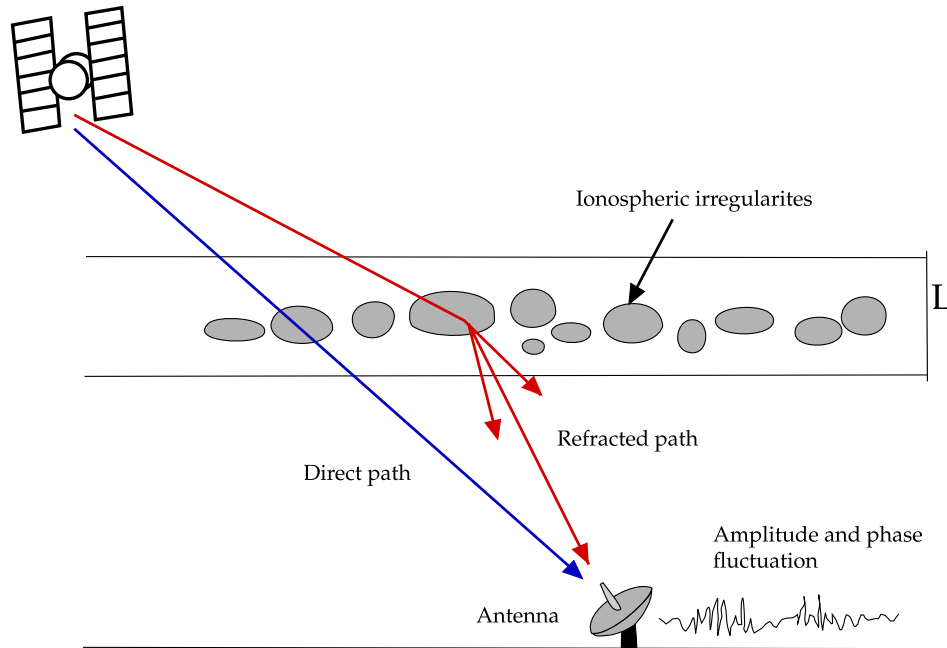


Figure 3.12: The schematic figure presenting geometry of ionospheric scintillation. Irregularities in the ionosphere introduce phase shifts that become amplitude perturbations as the wave propagates into the regions below the ionosphere [105, 119].

with r_e the classical electron radius and N_T as the fluctuations in the total electron content. In other words, when the radio waves emerge from an irregularity slab the phase along the wavefront varies.

At this point the amplitude of the signal is still unchanged, however, as it continues propagation towards the receiver, the waves emerging from different points along the bottom of ionosphere begin to add (see Fig. 3.12), and depending on relative phases, the signal amplitudes may either fade or increase [105, 106]. Simple considerations show that the major contribution to the amplitude fluctuations comes from the phase front deviations caused by the irregularities of the sizes of the order of the first Fresnel zone $d_F = \sqrt{\lambda(z - L/2)}$, where z is the height of the upper boundary of the irregular layer [106, 119], and λ is the wavelength of the radio wave [105]. This process of scintillation generation qualitatively describes the amplitude scintillation when the phase deviations are small, however when the electron density fluctuations are strong (so that ϵ_1 is relatively large), then the phase deviations are so large that the wave is no longer coherent and the interference of rays is not possible [106, 119].

According to [106] scintillation theory relates the observed signal statistics to the statistics of ionospheric electron density, where the most general problems of propagation of a wave in random media is difficult to treat numerically. In cases with wavelength much smaller than the characteristic scale size of the irregularities, the scintillation theory can be greatly simplified by noting that the wave is scattered predominantly in the forward direction and the wave propagation is described by the parabolic equation [106, 119]. If we assume that the irregular layer is so thin that $\sqrt{\lambda L}$ is much smaller than the size of largest irregularity, further simplifications are possible. This assumption leads to phase screen theory of scintillation in

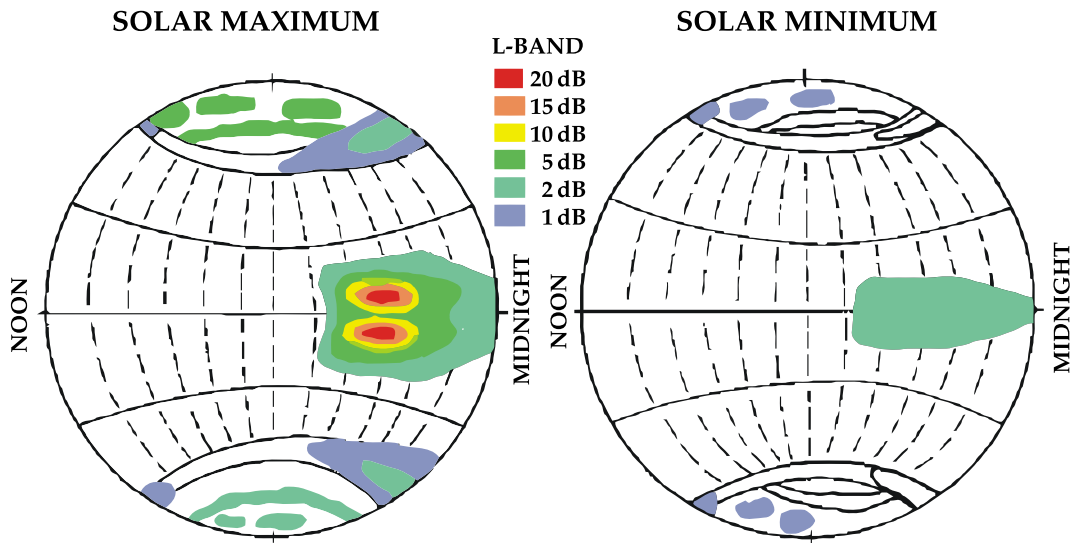


Figure 3.13: Global occurrence pattern for scintillations at 1.5 GHz during both sunspot maximum and minimum. The figure shows three major scintillation regions: magnetic equator at post-sunset, night-side auroral oval, and the polar cap (including the day-side cusp) at all times of the day [25, 103, 106].

which the irregularity layer is replaced by a screen, which changes only the phase of the waves [106, 119].

Ionospheric scintillations vary widely with frequency, magnetic and solar activity, time of day, season and latitude [25, 103]. Fig 3.13 shows three major regions of scintillation activity at 1.5 GHz during both minimum and maximum solar activity: the equatorial region, the middle latitudes and the high latitude region. As can be seen from Fig. 3.13, the occurrence of scintillation at high latitudes takes place both during the day and the night with two regions of peak scintillation observed – one corresponds to auroral oval and the other in the region above 80° [120].

The scintillation intensity in the high latitude region is moderate to extreme, with increase in occurrence and intensity during solar maximum and magnetic activity. The scintillation activity at high latitudes also shows diurnal variation, however this is weak and well defined only during the winter months [121]. The region where the occurrence of scintillations is the least pronounced is the middle latitudes (see Fig. 3.13). Middle latitudes represent the region between high latitudes and equatorial region in geomagnetic latitudinal range between 20° and 50° [25, 103]. The scintillation intensity here is slight to moderate and may be associated with rapid changes in magnetic activity level, moreover measurements shows that scintillation activity is proportional to solar activity [103, 120]. The last region of global scintillation activity, where the scintillations activity is most intense (scintillations can reach the greatest extremes), is the equatorial region (area within $\pm 20^\circ$ of the magnetic equator) [25, 103]. As at high latitudes, also in the equatorial region the probability of scintillation activity and its intensity increase with solar and magnetic activity, moreover the scintillations shows high diurnal variations with maximum activity starting to occur between 20:00 and 21:00 LT and lasting for ~ 4 h [103, 107]. Furthermore, the scintillation activity also shows high seasonal dependence with maximum pronouncement near equinoxes

with slight longitudinal variations (i.e. in the Afro-American sector the maximum scintillation activity occurs between November and December with minimum in May and July, while in the Pacific sector the opposite "behavior" is observed [120]).

For measuring scintillation activity one can use various parameters. One of these parameters, used for measuring ionospheric amplitude scintillation, is the S_4 index. The S_4 index is derived from the signal intensity of signals received from satellites and is defined [25, 108–110, 119] as the normalized standard deviation of the received signal power intensity expressed as

$$S_4 = \sqrt{\frac{\langle I^2 \rangle - \langle I \rangle^2}{\langle I \rangle^2}}, \quad (3.40)$$

where I is the signal intensity and symbol $\langle \rangle$ implies the average (mean) value. The second index, used for measuring amplitude scintillation was proposed by Whitney *et al.* in 1969, as a less rigorous but simple measure of scintillation [25],

$$SI = \frac{P_{\max} - P_{\min}}{P_{\max} + P_{\min}} \quad (3.41)$$

where P_{\max} is the power level of the third peak down from the maximum excursion of the scintillations and P_{\min} is the power level of the third peak up from the minimum excursion, measured in dB [25]. The SI index has been widely adopted by many researchers in the field for scaling long-term chart records, where the scaling of the chart records is facilitated by simply measuring the decibel change between P_{\max} and P_{\min} [25].

The scintillation index widely used for measuring phase scintillation is σ_ϕ , which is characterized by the standard deviation of the phase over a given interval of fluctuation frequency [25, 122]

$$\sigma_\phi = \sqrt{\langle \phi^2 \rangle - \langle \phi \rangle^2}. \quad (3.42)$$

Fig. 3.14 shows measured S_4 and σ_ϕ in two different regions of global ionospheric scintillation activity. The top of Fig. 3.14 shows amplitude and phase indices measured⁴ at Douala, Cameroon (geog. latitude 4°3'0" N and longitude 9°41'0" E) while in the bottom part of Fig 3.14 S_4 and σ_ϕ as measured⁵ at Ny-Ålesund, Svalbard (geog. latitude 78°55'0" N and longitude 11°56'0" E). At both locations ionospheric scintillation indices were measured with a GSV4004 ionospheric monitor [83] (for the description of the GPS receiver, please see Section 2.1.6), and in both cases elevation cut-off 20° was used, in order to discard any undesired tropospheric effects.

3.2.2 Tropospheric delay

In contrast to the ionosphere, the neutral part of the atmosphere is a non-dispersive medium for frequencies up to 15 GHz, i.e. the effects induced by neutral atmosphere on GPS signal transmissions are independent of operating frequency [54]. Due to this fact the phase and group velocities associated with GPS carrier and signal information (PRN code and navigation) are equally delayed [2, 62]. In case of the tropospheric delay, the GPS signals are affected by the neutral atoms and molecules in the troposphere. Note that the word

⁴data provided by dr. R. Prieto-Cerdeira, European Space Agency

⁵data provided by the Istituto Nazionale di Geofisica e Vulcanologia (INGV)

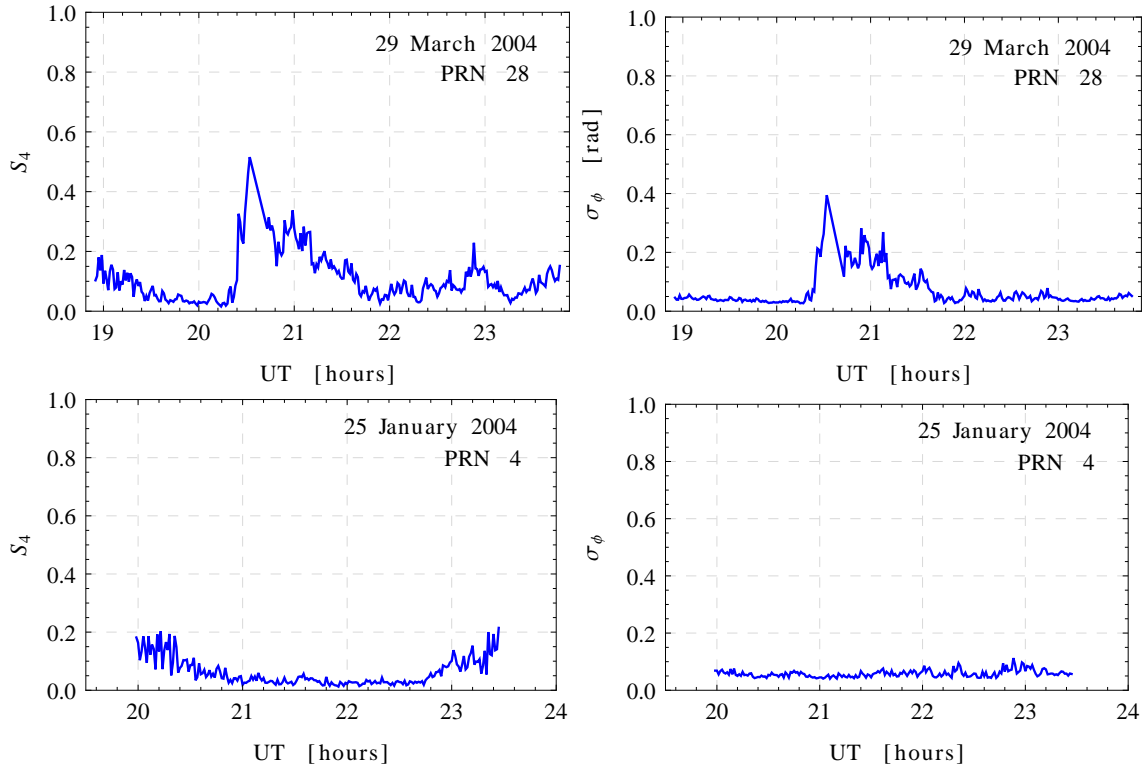


Figure 3.14: Measured scintillation indices at two different locations. The first two at the top are display S_4 and σ_ϕ measured in Douala, Cameroon (equatorial region), while the two bottom ones show measured S_4 and σ_ϕ measured at Ny-Ålesund, Svalbard.

“tropospheric” is used loosely here since due to historical reasons, tropospheric effects are simply considered to be the effects of the atmosphere below the ionosphere [54]. While the delay caused by the ionosphere can be simply reduced with a linear combination of data from both frequencies (as shown in the previous section), this cannot be done in case of a delay caused by troposphere [123]. Tropospheric effects on GPS signals can be divided into several components [62]:

- atmospheric attenuation,
- rainfall attenuation,
- tropospheric scintillation and,
- tropospheric delay.

While the first three components have very small effects on GPS signal, the range of tropospheric delay can vary from 2.4 m, (for a satellite at the zenith) to 25 m (for a satellite at an elevation angle of approximately 5°) [2]. Tropospheric delay is produced when the signal received from a GPS satellite is refracted by the troposphere as it travels to the receiver on the ground. The delay is due to the larger refractive index n of atmospheric gases ($n > 1$) than of vacuum ($n = 1$). This larger refractive index causes the decrease of speed of light (group velocity) in medium below its vacuum value c . The cause of this effect is that the

signal path has a slight curvature with respect to the geometric straight line path [2,3,62], as shown in Fig. 3.10.

Tropospheric delay is a function of the tropospheric refractive index which depends on the local temperature, pressure and relative humidity. From Eq. (3.18) it can be seen that the path length difference attributed to the tropospheric delay is [2]

$$\Delta L_{\text{tropo}} = \int_S^U (n - 1) d\ell, \quad (3.43)$$

where the integration is summing along the signal path. Usually, instead of the refractive index, a *refractivity* is introduced as [1,2,92,124]

$$N \equiv 10^6(n - 1). \quad (3.44)$$

Since the neutral atmosphere contains both dry air and water vapor, the refractivity can also be split the dry and the water vapor part [18]

$$N = N_d + N_w, \quad (3.45)$$

where N_d is the dry refractivity and N_w is the wet (water vapor) refractivity. Many authors refer to the hydrostatic delay as the “dry delay”, which is the usage in this thesis. Although that the largest contribution to the hydrostatic delay is that of the dry air, it usually includes also a significant contribution from water vapor, due to the nondipole component of water refractivity [3, 18]. Although wet delay is a more appropriate term in that it is produced solely by atmospheric water vapor, due to the dipole component of its refractivity [3], it should be kept in mind that is not the only delay produced by water vapor.

Inserting Eq. (3.45) into Eq. (3.43) gives us the total excess due to the tropospheric refraction [1],

$$\begin{aligned} \Delta L_{\text{tropo}} &= 10^{-6} \int_S^U N(\ell) d\ell = \\ &= 10^{-6} \int_S^U [N_d(\ell) + N_w(\ell)] d\ell \end{aligned} \quad (3.46)$$

where ZHD and ZWD are dry and wet delay, respectively [1,3], written as

$$\text{ZHD} = 10^{-6} \int_S^U N_d(\ell) d\ell \quad (3.47a)$$

$$\text{ZWD} = 10^{-6} \int_S^U N_w(\ell) d\ell. \quad (3.47b)$$

Because the refractivity of a parcel of air in atmosphere depends on temperature, pressure and water vapor pressure, we can write Eq. (3.45) [1,3]

$$N = k_1 \frac{p}{T} + k_3 \frac{e}{T^2}, \quad (3.48)$$

with k_1 and k_3 approximately as $k_1 = 77.64 \times 10^{-2} \text{ K/Pa}$ and $k_3 = 3.73 \times 10^3 \text{ K}^2/\text{Pa}$. More accurately [18],

$$N_d = k_1 \frac{p_d}{T} Z_d^{-1} \quad (3.49a)$$

$$N_w = \left[k_2 \frac{e}{T} + k_3 \frac{e}{T^2} \right] Z_w^{-1}, \quad (3.49b)$$

Reference	k_1 [10^{-2} K/Pa]	k_2 [10^{-2} K/Pa]	k_3 [10^3 K ² /Pa]	k'_2 [10^{-2} K/Pa]
Boudouris, 1963	77.59±0.08	72±11	3.75±0.03	24±11
Smith & Weintraub, 1953	77.61±0.01	72±9	3.75±0.03	24±9
Thayer, 1974	77.60±0.01	64.79±0.08	3.776±0.004	17±10
Hill <i>et al.</i> , 1982	/	98±1	3.583±0.003	/
Hill, 1988	/	102±1	3.578±0.003	/
Bevis <i>et al.</i> , 1994	77.6±0.05	70.4±2.2	3.739±0.012	22.1±2.2

Table 3.4: Some empirical values of refractivity coefficients [18, 125]. Values that are used in the scope of dissertation are presented with bold text.

where, k_i are refractivity constant, which were determined empirically (some different values are given in Table 3.4), Z_d is compressibility factor of dry air, and Z_w is compressibility factor of water vapor.

The two compressibility factors, which are corrections for nonideal gas behavior, have nearly constant values that differ from the unity only by a few parts per thousand. Often, both dry air and water vapor, are considered to be ideal gases with ideal compressibility factors so that the Eqs. (3.49) can be written as [3, 18]

$$N_d = k_1 \frac{p_d}{T} \quad (3.50a)$$

$$N_w = k_2 \frac{e}{T} + k_3 \frac{e}{T^2}. \quad (3.50b)$$

However, instead of splitting the refractivity into a dry and vapor part, one can also split into a more compact form, using the equation of state for dry air and water vapor and Eqs. (3.49),

$$\begin{aligned} N &= k_1 R_d \rho_d + k_2 R_v \rho_v + k_3 \frac{e}{T^2} Z_v^{-1} = \\ &= k_1 R_d \rho_m + \left(k_2 - k_1 \frac{R_d}{R_v} \right) R_v \rho_v + k_3 \frac{e}{T^2} Z_v^{-1}, \end{aligned} \quad (3.51)$$

where $\rho_m = \rho_d + \rho_v$ is the density of moist air. With definition

$$k'_2 = k_2 - k_1 \frac{M_v}{M_d} \quad (3.52)$$

and equation of state for water vapor, Eq. (3.51) becomes

$$\begin{aligned} N &= k_1 R_d \rho_m + \left(k'_2 \frac{e}{T} + k_3 \frac{e}{T^2} \right) Z_v^{-1} = \\ &= N_d + N_w. \end{aligned} \quad (3.53)$$

While the dry refractivity and the first term of the vapor of the refractivity are the result of induced molecular polarization of air and water vapor, the second term (and much larger) of the vapor refractivity represents the effects of the permanent dipole moment of the water vapor molecule. This permanent dipole constitutes are the main part of the delay caused by water vapor [18].

The total tropospheric delay can be estimated in two steps [1, 3]:

1. estimation of total zenith delay – the delay of the signal in the zenith direction and,
2. estimation of slant delay, which requires use of mapping functions of elevation angle.

In both cases the knowledge of pressure, temperature and humidity along the signal path can determine the refractivity profile and tropospheric delay. In atmospheric research these profiles can be easily determined using radiosonde. However, because GPS users rarely have access to such measurements, a less onerous approach is to measure the meteorological conditions (such as pressure, temperature, humidity) at the antenna location [1] and relate these measurements to conditions along the signal path using empirical models or gas laws. Simple models which are commonly used in GPS meteorology are described in the following section.

3.2.2.1 Tropospheric models

The Saastamoinen model was determined using gas laws and simplifying assumptions regarding changes in pressure, temperature and humidity. In the case of dry/hydrostatic delay, Saastamoinen employed approach in which the hydrostatic equilibrium was assumed [1, 124], while for the wet delay, Saastamoinen assumed that there is a linear decrease of temperature and the water vapor pressure with height [124]. The zenith and wet delay are

$$\text{ZHD} = a \left(1 + b \cos 2\phi + \frac{H}{H_0} \right) p, \quad (3.54a)$$

$$\text{ZWD} = a \left(\frac{T_0}{T} + d \right) e_s, \quad (3.54b)$$

where $a = 2.277 \times 10^{-5} \text{ m/Pa}$, $b = 0.0026$, $H_0 = 3.571 \times 10^6 \text{ m}$, $T_0 = 1225 \text{ K}$, $d = 0.05$, T is the surface temperature, p is the total pressure, e_s is the partial pressure of water vapor, ϕ is the latitude and H is the orthometric height of the antenna [1]. All meteorological parameters used in Saastamoinen model are determined by antenna location, either by measurements or from models of standard atmosphere.

The Hopfield model is based on a relationship between the dry refractivity at height h and that to surface. The dry refractivity can be written as [1]

$$N_d(h) = N_{d0} \left(1 - \frac{h}{h_d} \right)^\mu, \quad (3.55)$$

where h denotes the height above the antenna, N_{d0} is the dry refractivity at the surface (calculated using Eq. (3.50)), h_d is defined as height above the antenna at which the $N_{d0}(h_d) = 0$, and μ stems from the underlying use of the ideal gas law. Hopfield found that setting $\mu = 4$ gives the best result for the model [2]. According to [1] h_d can be assumed to be $\sim 43 \text{ km}$, or can be determined as

$$h_d/\text{m} = 40\,136 + 1482(T_s/\text{K} - 273.15), \quad (3.56)$$

where T_s is the surface temperature. Substitution Eq.(3.56) and Eq. (3.55) into Eq. (3.47a) and performing integration in vertical direction, gives us the dry delay in the zenith direction

$$\text{ZHD} = a p_s - b \frac{p_s}{T_s}, \quad (3.57)$$

with $a = 2.29029 \times 10^{-5} \text{ m/Pa}$ and $b = 7.52 \times 10^{-5} \text{ K m/Pa}$, T_s as surface temperature and p_s as surface pressure. Similarly as for the dry refractivity, Hopfield assumes the same functional model also for the wet refractivity is determined as [1, 2, 124]

$$N_w(h) = N_{w0} \left(1 - \frac{h}{h_w} \right)^\mu, \quad (3.58)$$

with $h_w = 12 \text{ km}$ [1], or

$$h_w/\text{m} = 7508 + 0.002421 \exp \left(\frac{T_s/\text{K} - 273.15}{22.90} \right). \quad (3.59)$$

Inserting Eq. (3.59) into Eq. (3.58) and the further into Eq. (3.47b) gives us

$$\text{ZWD} = \left(a + b \exp \left(\frac{T_s}{T_a} \right) \right) \frac{e_s}{T_s^2}, \quad (3.60)$$

with $a = 5.557 \text{ K}^2\text{m/Pa}$, $b = 1.792 \times 10^{-6} \text{ K}^2\text{m/Pa}$ and $T_a = 22.9 \text{ K}$.

Fig. 3.15 shows comparison between Saastamonien and Hopfield model for the period of 7 years (2005 – 2007), while Fig. 3.16 corresponds to year 2010. The delays were calculated using data from ground meteorological station located in Ljubljana, Slovenia (geog. latitude $46^\circ 03' 53'' \text{ N}$, geog. longitude $14^\circ 30' 44'' \text{ E}$, height 298 m), which is being operated by Slovenian Environmental Agency. In order to exclude all outliers in the data set, only the data with temperature range $250 \text{ K} \leq T_s \leq 350 \text{ K}$ and pressure range $950 \text{ hPa} \leq p_s \leq 1060 \text{ hPa}$ were used. As can be seen from Fig. 3.15 and 3.16 the calculated delays, using both models, are showing high seasonal variations with pronounced maximum in summer and minimum in winter, as expected due to the fact that both models are directly connected with surface temperature and pressure. Furthermore, there is visible difference between the two models. One explanation is that although that both models for dry delay were developed with starting point that air is treated as an ideal, in case of Hopfield there are two important approximation taken into account: one is that the temperature lapse is assumed to be constant and the second the gravity is not modeled with dependence on height. Additionally, it should be also noted that in case of Saastamonien model for dry delay no surface measurements of temperature are needed, but instead the height of the station and its latitude are used for the computation of the gravity constant.

Besides the above described models there are numerous others, e.g. Davies model, which differs from Saastamonien model only in the choice of the k_1 refractivity constant, Ifadis model, modified Hopfield model etc [18, 53, 92, 124]. In case of modified Hopfield model a modification was introduced by replacing heights in Eqs. (3.55) and (3.58) with length of positions vectors. More on different tropospheric models and their derivations can be found in [18].

However, the two models defined above (and others), do not apply for elevation angles other than 90° . Therefore, for other elevation angles one must use **mapping functions** [1, 2]

$$\Delta L_{\text{tropo}} = m_d(\alpha) \times \text{ZHD} + m_w(\alpha) \times \text{ZWD} \quad (3.61)$$

or

$$\Delta L_{\text{tropo}} = m(\alpha) \times (\text{ZHD} + \text{ZWD}) \quad (3.62)$$

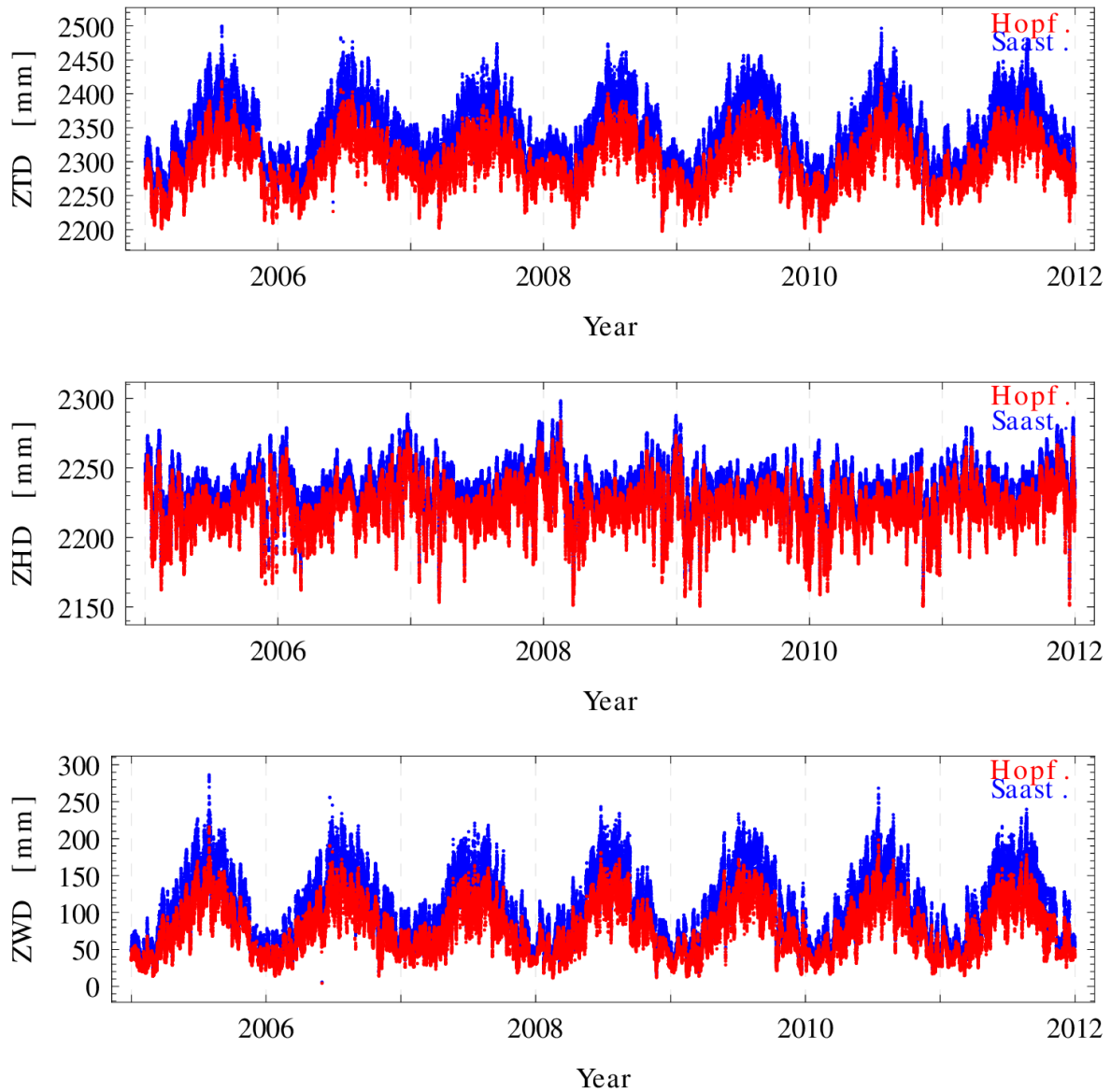


Figure 3.15: Comparison between Saastamonian (blue) and Hopfield (red) model for calculation of tropospheric delays for the period of 7 years (2005 – 2011). From top to bottom – ZTD (total delay in zenith direction), ZHD (dry delay in zenith direction) and ZWD (wet delay in zenith direction).

where m_d is dry component mapping function, m_w is wet component mapping function, m is general mapping function and α is the elevation angle of the satellite. One of the models for general mapping function, which takes into account both the dry and wet component, is $1/\sin \alpha$. This model is consistent with flat Earth surface, however is a poor approximation for low elevation satellites ($\alpha < 15^\circ$). A more accurate model for general mapping function

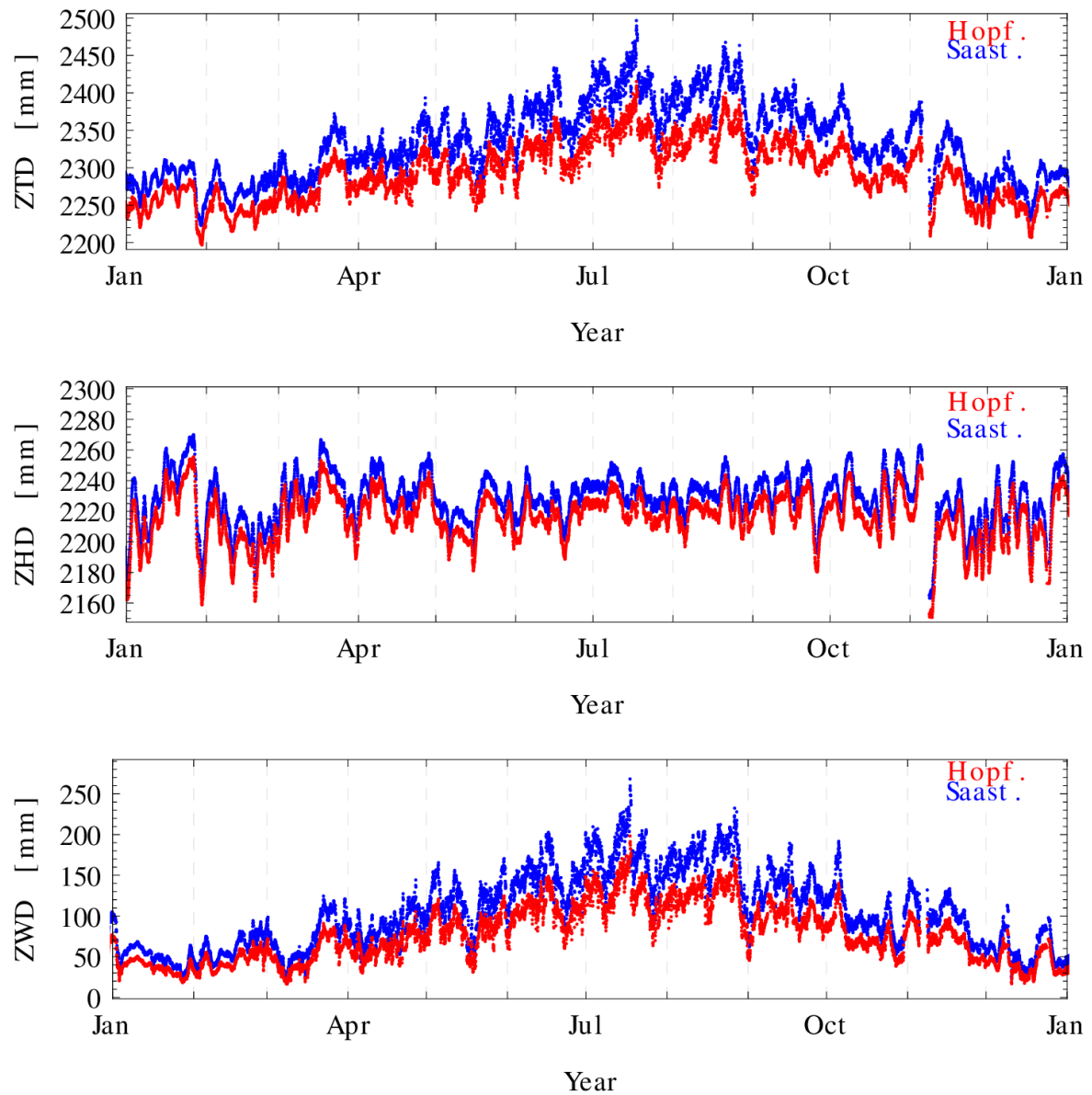


Figure 3.16: Comparison between Saastamonian (blue) and Hopfield (red) model for calculation of tropospheric delays for the year 2010. From top to bottom – ZTD (total delay in zenith direction), ZHD (dry delay in zenith direction) and ZWD (wet delay in zenith direction).

is [2]

$$m(\alpha) = \frac{1.001}{\sqrt{0.002001 + \sin^2 \alpha}}. \quad (3.63)$$

More complex formula, based on a truncated form of continued fractions, was developed by Herring in 1992 [1,2]

$$m_i(\alpha) = \frac{1 + \frac{a_i}{1 + \frac{b_i}{1 + \frac{c_i}{1 + \dots}}}}{\sin \alpha + \frac{a_i}{\sin \alpha + \frac{b_i}{\sin \alpha + \frac{c_i}{\sin \alpha + \dots}}}} \quad (3.64)$$

where i represents either dry or wet component, a_i , b_i and c_i are the mapping parameters determined in different models as functions of variables such as latitude, height, surface temperature and pressure and day of the year [1,2]. The derivation of a_i , b_i and c_i parameters [18] was carried out by ray tracing of radiosonde data with surface temperature, site latitude and height above sea level were introduced. The coefficients for hydrostatic mapping function are [18,53]

$$\begin{aligned} a &= 1.2320 + 0.0139 \cos \phi - 0.0209H_s/\text{km} + 0.00215 \times 10^{-3}(T_s/\text{K} - 283.15) \\ b &= 3.1612 - 0.1600 \cos \phi - 0.0331H_s/\text{km} + 0.00206 \times 10^{-3}(T_s/\text{K} - 283.15) \\ c &= 171.244 - 4.2930 \cos \phi - 0.1490H_s/\text{km} - 0.00210 \times 10^{-3}(T_s/\text{K} - 283.15) \end{aligned}$$

and for wet mapping function

$$\begin{aligned} a &= 0.583 - 0.011 \cos \phi - 0.052H_s/\text{km} + 0.0014 \times 10^{-3}(T_s/\text{K} - 283.15) \\ b &= 1.402 - 0.102 \cos \phi - 0.101H_s/\text{km} + 0.0020 \times 10^{-3}(T_s/\text{K} - 283.15) \\ c &= 45.85 - 1.91 \cos \phi - 1.29H_s/\text{km} + 0.015 \times 10^{-3}(T_s/\text{K} - 283.15) \end{aligned}$$

where T_s is the temperature at the site, ϕ is the latitude of the site and H_s is the height of the site above sea level [18,53].

One of the most commonly used mapping function in atmospheric science is Niell mapping function (NMF), developed by Arthur Niell in 1996. NMF also uses Herring's continued fraction (Eq. (3.64)) with difference that the coefficients defined in Eq. (3.64), are here based on temporal changes and geographic location and not on surface meteorological parameters as in Herring mapping function [2,53,126,127]. For the hydrostatic mapping function parameters defined in Eq. (3.64) at latitude ϕ_i (see Table 3.5 and 3.6) and time t from January 0.0 can be calculated as [126,127]

$$\beta(\phi_i, t) = \beta_{\text{avg}}(\phi_i) - \beta_{\text{amp}}(\phi_i) \cos \left(2\pi \frac{t - T_0}{365.25 \text{ day}} \right), \quad (3.65)$$

where β stands for coefficients a , b , c ; T_0 is the adopted phase – it is set to the day for winter maximum ($T_0 = 28$ day for the northern hemisphere and 211 day for the southern hemisphere). The value of parameter $\beta(\phi, t)$ is then obtained by interpolating linearly between the nearest $\beta(\phi_i, t)$. On the other hand, for the wet mapping function, only an interpolation in latitude for each parameters is needed [126,127].

coeff.	latitude				
	15°	30°	45°	60°	75°
a_{avg}	1.2769934×10^{-3}	1.2683230×10^{-3}	1.2465397×10^{-3}	1.2196049×10^{-3}	1.2045996×10^{-3}
b_{avg}	2.9153695×10^{-3}	2.9152299×10^{-3}	2.9288445×10^{-3}	2.9022565×10^{-3}	2.9024912×10^{-3}
c_{avg}	62.610505×10^{-3}	62.837393×10^{-3}	63.721774×10^{-3}	63.824265×10^{-3}	64.258455×10^{-3}
a_{amp}	0	1.270962×10^{-5}	2.6523662×10^{-5}	3.4000452×10^{-5}	4.1202191×10^{-5}
b_{amp}	0	2.1414979×10^{-5}	3.0160779×10^{-5}	7.2562722×10^{-5}	11.723375×10^{-5}
c_{amp}	0	9.0128400×10^{-5}	$4.34970737 \times 10^{-5}$	84.795348×10^{-5}	170.37206×10^{-5}
a_{ht}	2.53×10^{-5}				
b_{ht}	5.49×10^{-3}				
c_{ht}	1.14×10^{-3}				

Table 3.5: Coefficients of the hydrostatic mapping function in NMF [53, 126].

coeff.	latitude				
	15°	30°	45°	60°	75°
a	5.8021897×10^{-4}	5.6794847×10^{-4}	5.8118019×10^{-4}	5.9727542×10^{-4}	6.1641693×10^{-4}
b	1.4275268×10^{-3}	1.5138625×10^{-3}	1.4572752×10^{-3}	1.5007428×10^{-3}	1.7599082×10^{-3}
c	4.3472961×10^{-2}	4.6729510×10^{-2}	4.3908931×10^{-2}	4.4626982×10^{-2}	5.4736038×10^{-2}

Table 3.6: Coefficients of the wet mapping function in NMF [53, 126].

Besides the seasonal (due to varying solar illumination) and latitudinal dependence, the hydrostatic part of the mapping function is also dependent on the height above the geoid. This is primarily due to the fact that the ratio of the atmosphere “thickness” to the radius of curvature decreases with height. However this does not apply for the wet component of the mapping function since the water vapor is not in hydrostatic equilibrium and the distribution of water vapor with height is not expected to be predictable from the station height [126]. The height correction for hydrostatic mapping function is then [53, 126]

$$\Delta m(\alpha) = \frac{dm(\alpha)}{dh} H, \quad (3.66)$$

where H is the height of the observation site above sea level with

$$\frac{dm(\alpha)}{dh} = \frac{1}{\sin \alpha} - f(\alpha, a_{\text{ht}}, b_{\text{ht}}, c_{\text{ht}}), \quad (3.67)$$

where α is the elevation angle, $f(\alpha, a_{\text{ht}}, b_{\text{ht}}, c_{\text{ht}})$ is the three term continued fraction from Eq. (3.64), and $a_{\text{ht}}, b_{\text{ht}}, c_{\text{ht}}$ parameters were determined by least squares fit to the height corrections at nine elevation angles (listed in Table 3.5) [126].

Vienna Mapping Function

In contrast to mapping functions described above, which requires station height, station latitude and day of the year as input parameters (in case of NMF function these parameters were determined using radiosonde data), there was also a lot of effort put into the development of mapping functions based on the data from numerical weather prediction models

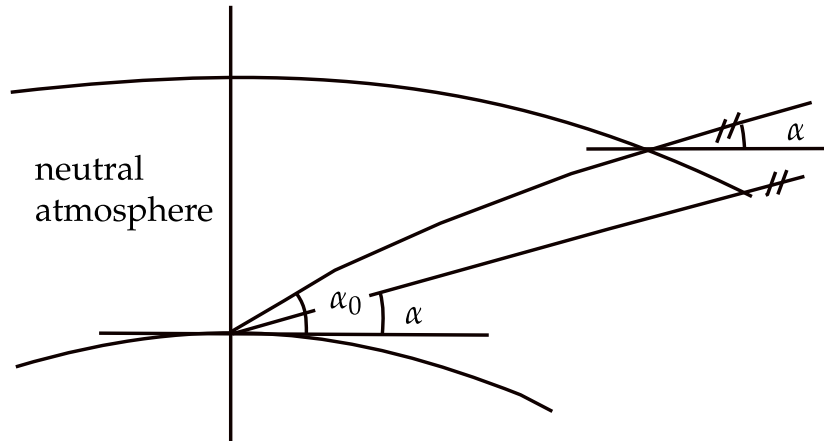


Figure 3.17: Bending of the ray in the neutral atmosphere. It can be noticed that the outgoing (vacuum) elevation angle α is smaller than the initial elevation angle α_0 [128, 130].

(NWP models) [128]. One of the first mapping function based on NWP models was developed by Neill in 2000 [129], known as Improved/Isobaric Mapping Function (IMF), which applies as input parameters the height of the 200 hPa pressure level (z_{200}) and the ratio of the wet path delay along the straight line at 5° elevation and zenith delay ($smfw_3$) [128, 129]. The equations relating these two parameters to the coefficients of the continued fraction, are based on ray tracing through radiosonde data.

The development of mapping functions based on NWP models continued with the Vienna Mapping Function (VMF), where the main idea behind the development was to directly use the ray tracing through the NWP model instead of taking intermediate steps [128] for determination of coefficients a , b and c in the continued fraction form (Eq. (3.64)) [128, 130]. As an input parameters for the ray tracing program, initial elevation angle α_0 , and values for height, temperature and water vapor pressure at distinct pressure levels in the neutral atmosphere (e.g. 15 levels from 1000 hPa to 10 hPa total pressure) are used. Outputs of the program are the outgoing (vacuum) elevation angle α (Fig. 3.17) and the values needed for the hydrostatic and wet mapping function, where the hydrostatic mapping function includes also the geometric bending effect [128]. The full ray tracing is based on the European Center for Medium Range Weather Forecasts (ECMWF) operational analysis data [128, 130]. VMF uses two different approaches: rigorous approach VMF (rig) and the fast approach VMF (fast). While in the VMF (rig) ray tracing approach uses 10 different elevation angles (from 90° to 3.3° elevation) and the estimation of coefficients a , b and c is performed in least-square adjustment [130], the fast approach requires the ray tracing for only one initial elevation angle of 3.3° [128]. Result of the fast approach is one value for the hydrostatic mapping function, one value for the wet mapping function and the vacuum elevation angle α , while for the coefficients b and c the predefined formulas are used and the coefficient a can be determined by simply inverting the continued fraction from Eq. (3.64) [128]. Later Boehm *et al* in 2006 [131] proposed an “upgrade” of VMF known as VMF1, where new values for the hydrostatic coefficients b and c were redetermined, using one year of the ECMWF Re-Analysis 40-years (ERA-40) data set. In contrast to previous mapping function based on NWP models (for instance IMF and VMF), the coefficients c in VMF1 are dependent on the day of the year and unlike in the Niell mapping functions they are no longer symmetric with

Hemisphere	c_0	c_{10}	c_{11}	ϕ
Northern	0.062	0.000	0.006	0
Southern	0.062	0.001	0.006	π

Table 3.7: Values of the parameters c_0 , c_{10} , c_{11} and ϕ , needed for the determination of the coefficient c in Eq. (3.68) for the hydrostatic mapping function in VMF1 [131].

Hemisphere	c_0	c_{10}	c_{11}	ϕ
Northern	0.063	0.000	0.004	0
Southern	0.063	0.001	0.006	π

Table 3.8: Values of the parameters c_0 , c_{10} , c_{11} and ϕ , needed for the determination of the coefficient c in Eq. (3.68) for the total mapping function in VMF1 [131].

respect to the equator (apart from the opposite phase for the two hemispheres) [131]. In first step the total and hydrostatic mapping functions as well as the elevation angle α were determined for 10 different elevation angles α_0 on 156 grid points over 12 months times 4 epoch per day (denoted as 00, 0, 6, 12 and 18) using 7488 profiles. Then, the three coefficients a , b , and c for both total and hydrostatic mapping functions (Eq. (3.64)) were fitted to the 10 discrete mapping function values for each profile using least-square adjustment. The mean value of all b coefficients was found to be [131]

$$b_t = b_h = 0.0029$$

where subscript t denotes total mapping function and subscript h hydrostatic mapping function. The procedure of calculating the coefficient then repeated with b coefficient held fixed, and coefficient c was found to be [131]

$$c = c_0 + \left[\left(\cos \left(\frac{\text{doy} - 28}{365} \times 2\pi + \Psi \right) + 1 \right) \times \frac{c_{11}}{2} + c_{10} \right] \times (1 - \cos \phi) \quad (3.68)$$

where doy is the day of the year, 28 is the 28 January (adopted as a reference epoch) [126], ϕ is the latitude and the Ψ is parameter that specifies the Northern or Southern hemisphere, while the values of c_0 , c_{10} and c_{11} are given in Tables 3.7 and 3.8 for the hydrostatic and total mapping functions, respectively.

In this section I have introduced the use of GPS signals for the estimation of wet delays, which can be later used for calculating water vapor content. Because the visible range of the electromagnetic spectrum is also sensitive to the water vapor, in the next section I will discuss the use of light scattering to obtain complementary information about water vapor in the atmosphere, in particularly with the use of Raman LIDAR system.

3.2.3 Light scattering in the lower atmosphere

Scattering is (beside refraction) another physical process in the atmosphere to which the electromagnetic wave, while passing through atmosphere, is also subjected to. Scattering occurs when particles or molecules interact with electromagnetic radiation causing change

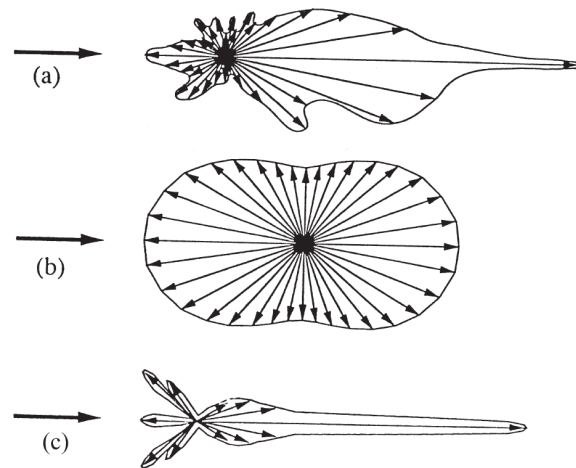


Figure 3.18: Scattering behaviors for three different types of atmospheric particles [8], where (a) presents atmospheric dust and smoke particles, (b) atmospheric molecules and (c) large water droplets.

in its initial direction. Scattered light may include several scattering constituents: molecular and particulate elastic scattering has the same wavelength as the incident light, resonance scattering has no change in wavelength under specific conditions, and additional spectral constituents, for which wavelengths are shifted relative to that of the incident light [89]. In Fig. 3.18 scattering behaviour for three different atmospheric particles is shown, where each letter denotes different type of particles and scattering, and the arrow the direction of the electromagnetic wave (incident light) [8]:

- (a) atmospheric dust and smoke (aerosols) – rather large and irregular particles that create a strong forward scattering peak and smaller backscattering,
- (b) atmospheric molecules – due to their nearly symmetrical shape, scattering creates a pattern characterized by preferential forward and backward scattering, but without the pronounced peak like in example a), and
- (c) large water droplets – they will create a pronounced forward scattering peak with smaller backscattering peaks.

Besides the size and shape of the particles/molecules, the magnitude of the scattering also depends on the wavelength of the electromagnetic radiation, the abundance of the particles and the travel distance of the radiation through the atmosphere [8]. There are following types of scattering in the atmosphere [132], used in laser remote sensing tools such as lidar: Rayleigh scattering, Mie scattering, Raman scattering and resonance scattering. Besides these mentioned scatterings types in the atmosphere, there are also other atmospheric processes used in laser remote techniques (fluorescence, absorption etc.) [22, 132].

Elastic scattering

Two most widely used types of elastic scattering in lidar application are Rayleigh scattering and Mie scattering. Rayleigh scattering occurs when atmospheric particles have diameters



Figure 3.19: Example of Rayleigh scattering in the atmosphere at sunset where one can see different variations in colors (from blue to reddish orange color at horizon). This variation in colors is caused either by variations of concentrations of fine atmospheric dust or tiny droplets in the atmosphere which contribute to variations in atmospheric clarity [8]. Photo by Darko Veberič.

smaller relative to the wavelength of the incident electromagnetic wave. Strength of the Rayleigh scattering is proportional to λ^{-4} [22, 88, 132]. Here the term elastic scattering describes the process in which the scattering will occur without the change in the energy of the photon, in contrast to the Raman scattering [88, 89, 101]. Process of Rayleigh scattering is schematically shown in Fig. 3.20 (left), where it can be seen that the wavelength/energy of incoming photon is the same as for outgoing photon. Due to the fact that the Rayleigh scattering can occur in the absence of atmospheric impurities, it is sometimes referred to us as the *clear atmosphere scattering* and is the “cause” of both the blue color of the sky and the brilliant red and orange colors often seen at sunset (Fig. 3.19) [8].

In contrast to Rayleigh scattering, the Mie scattering occurs when the particle size is comparable or greater than the wavelength of the electromagnetic wave [22, 89]. It is named after the German physicist Gustav Mie (1686 – 1957) who in 1906 published an analysis that describes atmospheric scattering involving broader range of atmospheric particles (dust, smoke, water droplets ...) than Rayleigh scattering [8].

3.2.3.1 Raman scattering

Raman scattering is inelastic weak molecular scattering of the light in the atmosphere and presents the basis for understanding the concept and performance of a Raman lidar, which can be used for profiling of water vapor in the troposphere. Although the Rayleigh scattering is the dominant mode of molecular scattering in the atmosphere, it is also possible for the incident electromagnetic waves to interact inelastically with the molecules using principles

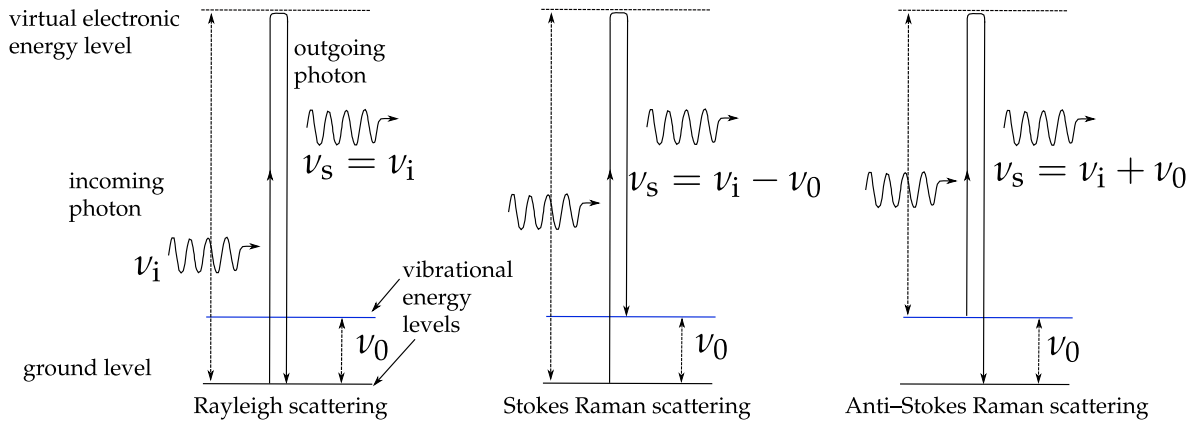


Figure 3.20: Schematic description of Rayleigh and two types of Raman scattering [132], where ν_i is the frequency of the incoming photon, ν_s is the frequency of the scattered/outgoing photon and ν_0 represents the frequency shift in different types of scattering.

of Raman scattering [20,22,89]. While in the case of Rayleigh scattering there is no frequency shift – i.e. the molecule will preserve its vibration-rotational energy level during the elastic scattering process, this is not the case of Raman scattering [89].

As can be seen from Fig. 3.20, there are two types of Raman scattering. In the middle, the so-called Stokes-Raman scattering is presented, which occurs when the molecule is absorbing the energy, i.e. a higher energy level will be excited and the frequency of the scattered photon is decreased [88, 89]

$$\nu_s = \nu_i - \nu_0, \quad (3.69)$$

where ν_s is the frequency of the scattered/outgoing photon, ν_i is the frequency of the incoming photon, and ν_0 represents the frequency shift in different types of scattering. On the right side of Fig. 3.20 the second type of the Raman scattering is presented, the anti-Stokes-Raman scattering, where the molecule transfers the energy to the scattered photon by decreasing its energy level and increasing the frequency of the scattered photon [88, 89]

$$\nu_s = \nu_i + \nu_0. \quad (3.70)$$

The frequency shift ν_0 , which is characteristic for the scattering molecule, can be calculated as [88]

$$\nu_0 = \nu_i - \nu_s = \frac{\Delta E}{hc}, \quad (3.71)$$

where ΔE is the energy difference between the involved molecular energy levels, h is the Planck's constant (6.626×10^{-34} kg m²/s) and c is the speed of light in vacuum [88, 89]. Raman wavenumber shift for two most important gases in Raman lidar applications are $\Delta\nu_{\text{vib}} = 2331/\text{cm}$ for N₂ and $\Delta\nu_{\text{vib}} = 3654/\text{cm}$ for H₂O [133]. The type of Raman scattering occurring more likely at typical atmospheric temperatures is the Stokes type [20].

The intensity of an observed Raman line depends on the cross section of the corresponding vibrational-rotation scattering process, which is the product of the transition probability and the population of the initial energy level. Furthermore, the Raman scattering cross section depends also on the polarizability of the molecules. In case of remote sensing of the Earth's atmosphere with the Raman lidar, two types of molecules are of interest, H₂O and

Wavelength [nm]	Rayleigh scattering [cm ² /sr]	Raman N ₂ scattering [cm ² /sr]	Raman H ₂ O scattering [cm ² /sr]
355	3.2×10^{-27}	2.8×10^{-30}	6.2×10^{-30}
532	6.3×10^{-28}	4.6×10^{-31}	8.9×10^{-31}

Table 3.9: Cross section of Rayleigh and Raman scattering of N₂ and H₂O [89].

N₂, since their backscattering signals can be used to retrieve both, the aerosol extinction and water vapor mixing ratio [89]. The cross section that are used in case of our Raman lidar system, are provided in Table 3.9.

3.3 Summary

In this Chapter detailed information on Earth's atmosphere and its properties was given. In first part of the Chapter, I have given a short description on chemical composition of the variable constituents and their role in atmosphere. The temperature and pressure variations with height were presented using empirical definitions and real-time data from radiosonde profiles. Furthermore, detailed description and role of the water vapor in the atmosphere was also provided. After the discussion of the neutral part of atmosphere, the description of the ionosphere followed, where I have introduced the structure, composition and geographical distribution of ionospheric regions.

In the second part of the Chapter, the discussion on the propagation of the electromagnetic waves in the atmosphere followed. Here first the discussion on propagation of the GPS signals through atmosphere and its effects on them was introduced, while in the second part the use of the effect of light scattering in the lower atmosphere in remote sensing techniques was discussed and presented. In particular, Raman scattering was presented in detail.

Water vapor estimation

Contents

4.1 Introduction	75
4.2 Methodology	76
4.2.1 GPS Inferred Positioning System-Orbit Analysis and Simulation Software (GIPSY-OASIS II)	76
4.2.2 Processing strategy	77
4.3 From GPS wet delay to IWV	78
4.3.1 Validation of T_m parameter	80
4.3.1.1 Simple linear regression method	80
4.3.1.2 Extended linear method	82
4.3.2 Error analysis	83
4.4 Water vapor measurements at UNG	88
4.4.1 Water vapor mixing ratio measurements	89
4.4.2 GPS measurements	91
4.5 Conclusions	95

4.1 Introduction

Water vapor plays an important role in weather forecasting, since accurate knowledge of its spatial and temporal distribution could significantly enhance weather analysis and forecasting on the local, regional and global scale. The critical roles played by water vapor in the global climate system may be listed as follows [10]: it plays a major role in the hydrological cycle; it provides the medium for energy transfer during evaporation and during condensation (thus providing the energy required for atmospheric circulation); it plays a significant role in controlling the amount and type of cloud cover due to its concentration and spatial distribution; it plays a critical role not only in atmospheric chemistry but also in atmospheric processes from global climate to micrometeorology [10]. Furthermore, it is one of the most important natural greenhouse gases in Earth's atmosphere, which "trap" infrared radiation that would otherwise escape into space, thus raising the temperature at the surface of the Earth [99].

While in Chapters 2 and 3 remote sensing techniques and theoretical background on the Earth's atmosphere are presented, this Chapter provides an overview of preliminary results and measurement campaigns. In the first part of the Chapter we present GPS data processing scheme, which was used throughout my research work, while in the second part the results of experimental work are presented. In particular we present validation of weighted "mean temperature" (T_m) parameter together with final results of integrated water vapor (IWV) measurements.

4.2 Methodology

4.2.1 GPS Inferred Positioning System-Orbit Analysis and Simulation Software (GIPSY-OASIS II)

For estimating integrated water vapor one needs to estimate tropospheric delay. For this purpose, several programs were developed during the years. One of those is the **GPS Inferred Positioning SYstem-Orbit Analysis and Simulation Software (GIPSY-OASIS II)** version 6.1.2 software package, which was developed at the **Jet Propulsion Laboratory (JPL)**, with the purpose of calculating precise or relative GPS positioning. GIPSY-OASIS can process data in all modes from static to fully kinematic [134]. It is in the last years widely used not only for estimating atmospheric delays but also for monitoring volcanic activity, Earth's rotation rate and crustal movements due to earthquakes [135]. The major difference with respect to other precise GPS software packages is that GIPSY does not use double-differences (instead it solves for the clock parameters), and that it reduces phase and pseudorange data simultaneously [134].

Several data elements are required by GIPSY for the calculation of the receiver's position. These include RINEX format (Appendix C) data with carrier and pseudorange information from the receiver, satellite orbital data – required for the calculation of the satellite-receiver distance and satellite clock errors need to be known and corrected for. Both satellite clock data and orbital data are obtained during processing with software via anonymous ftp server¹, and are routinely generated and provided by JPL [135, 136], where user can choose from several available products, from ultra-rapid, rapid to final orbit data. Difference between each of them is in the latency and accuracy (see Table 4.1) [136]. There were several analyses already carried out which show that using final products can improve accuracy in integrated water vapor (for instance see [135] and references within), however if we want to have near real-time water vapor information obtained with GPS, we must use ultra-rapid products.

Product	Latency	3D RMS Accuracy (cm)	High-Rate Clock Product Availability	Ambiguity Reso. Product Availability
ultra-rapid	< 2 hours	5	none	all dates
rapid	next-day (16:00 UTC)	3.5	from 1 July 2011	all dates
final	< 14 days	2.5	from 5 May 2000	from 16 August 1992

Table 4.1: Different JPL's Precise Orbit and Clock products with information about their latency, 3D RMS accuracy and product availability [136].

Calculation of integrated water vapor from GPS wet delay is generally done in two separate steps (see also Fig. 4.1):

1. GPS data processing

- collection of GPS data in RINEX format,
- estimation of tropospheric delays (ZTD or direct estimation of ZWD) using specialised processing software (GIPSY-OASIS II, GAMIT/GLOBIT, BERNESSE).

¹ftp://sideshow.jpl.nasa.gov/pub/JPL_GPS_Products/

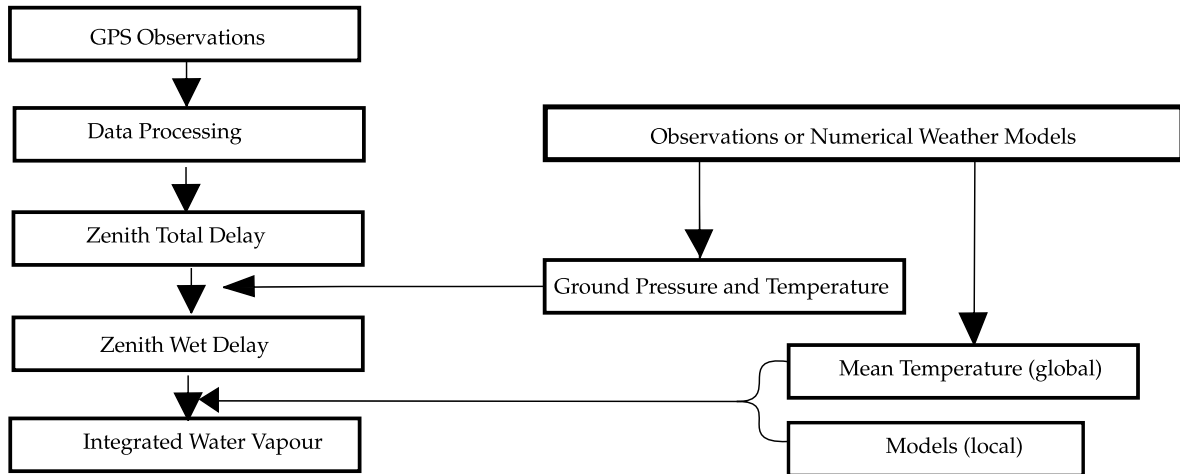


Figure 4.1: Schematic presentation of typical GPS data processing flow for obtaining IWV from GPS observations.

2. Collection of meteorological data

- collection of radiosonde profiles and/or surface, meteorological data by the GPS stations or in their near vicinity,
 - calculation of T_m , using empirical models (surface meteorological data) or weighted averages (radiosonde data).
3. Estimating integrated water vapor as a function of ZWD and T_m , using well know model $IWV=f(ZWD, T_m)$.

4.2.2 Processing strategy

Because one of the main objectives of this PhD research was to set up the processing strategy for obtaining wet delay from GPS data and further calculation of IWV, two different processing strategies were used, giving us different results, discussed and presented in following sections. In both strategies the main goal was to obtain the most precise estimation of zenith wet delay where final result of IWV was compared with radiosonde results.

GIPSY was set to run in precise point positioning (PPP) mode (Section 2.1.4.1) [75], using recommended script `gd2p`, with applied IERS2010 recommendations for the solid Earth tides model [137] and FES2004 model for ocean tide loading [138]. Antenna phase corrections and an elevation cut-off 10° were also applied. The wet delay and gradient parameters were modeled as random walk variables with 5 and $0.5 \text{ mm}/\sqrt{h}$, as recommended by GIPSY OASIS II manual when using data down to 7° , respectively. A priori wet delay was fixed to 100 mm. Phase ambiguities were fixed using `amb_res` function. Function allows the constraint of double difference integer ambiguities using data from a single receiver, when using clock and orbital data (see Table 4.1). The products contain a file with wide-lane bias and phase bias information from the global network used to compute the bias fixed orbits and clocks [139]. Detailed description on algorithm can be found in [140]. The station coordinates were first estimated and then held fix.

The two strategies differentiated in following steps. In first run, the dry delays were calculated based on the station height by using the following equation [139]

$$\text{ZHD} = 1.013 \times 2.27 \times \exp(-0.166 \times 10^{-3} \times h), \quad (4.1)$$

where h is the height of the station. As a mapping function Niell mapping function was applied (Section 3.2.2). In the second run, for the estimation of ZWD from GPS data VMF1 mapping function was used instead of Neill mapping function [131], and a priori dry delays were imported in the GPS processing scheme via tropnominal function.

4.3 From GPS wet delay to IWV

With knowledge of the estimated ZWD from a GPS receiver at a given time and location, it is possible to derive the IWV, given in kg/m^2 [3] as

$$\text{IWV} = \int \rho_v dz \approx \kappa \times \text{ZWD}, \quad (4.2)$$

with ρ_v the density of water

$$\rho_v = \frac{e}{R_v T}, \quad (4.3)$$

and κ given by

$$\kappa = \frac{10^6}{R_v \left(\frac{k_3}{T_m} + k_2' \right)}, \quad (4.4)$$

where R_v is the specific gas constant for water vapor (461.5181 J/kg K), and k_2' and k_3 are refractivity constants (Table 3.4). T_m is the weighted mean temperature² of the atmosphere, defined as [3]

$$T_m^{-1} = \langle T^{-1} \rangle_{\rho_v} = \frac{\int T^{-1} \rho_v dz}{\int \rho_v dz}, \quad \text{i.e.} \\ T_m = \frac{\int (e/T) dz}{\int (e/T^2) dz}, \quad (4.5)$$

where e is the partial pressure of water vapor and T is the air temperature. The water vapor content in the atmosphere is sometimes stated also as the height of an equivalent column of liquid water, which we refer to us as the *precipitable water* (PW). Numerically, IWV is just the product of the density of liquid water (ρ_v) and PW. Since both have units of length, their ratio can be written [3,53]

$$\frac{\text{PW}}{\text{ZWD}} = \frac{\kappa}{\rho_v}. \quad (4.6)$$

Thus, by using following equation, we can obtain PW directly from ZWD [53] as

$$\text{PW} = \Pi(T_m) \times \text{ZWD}, \quad (4.7)$$

²or more appropriately: $1/T_m$ is the water-weighted mean inverse temperature

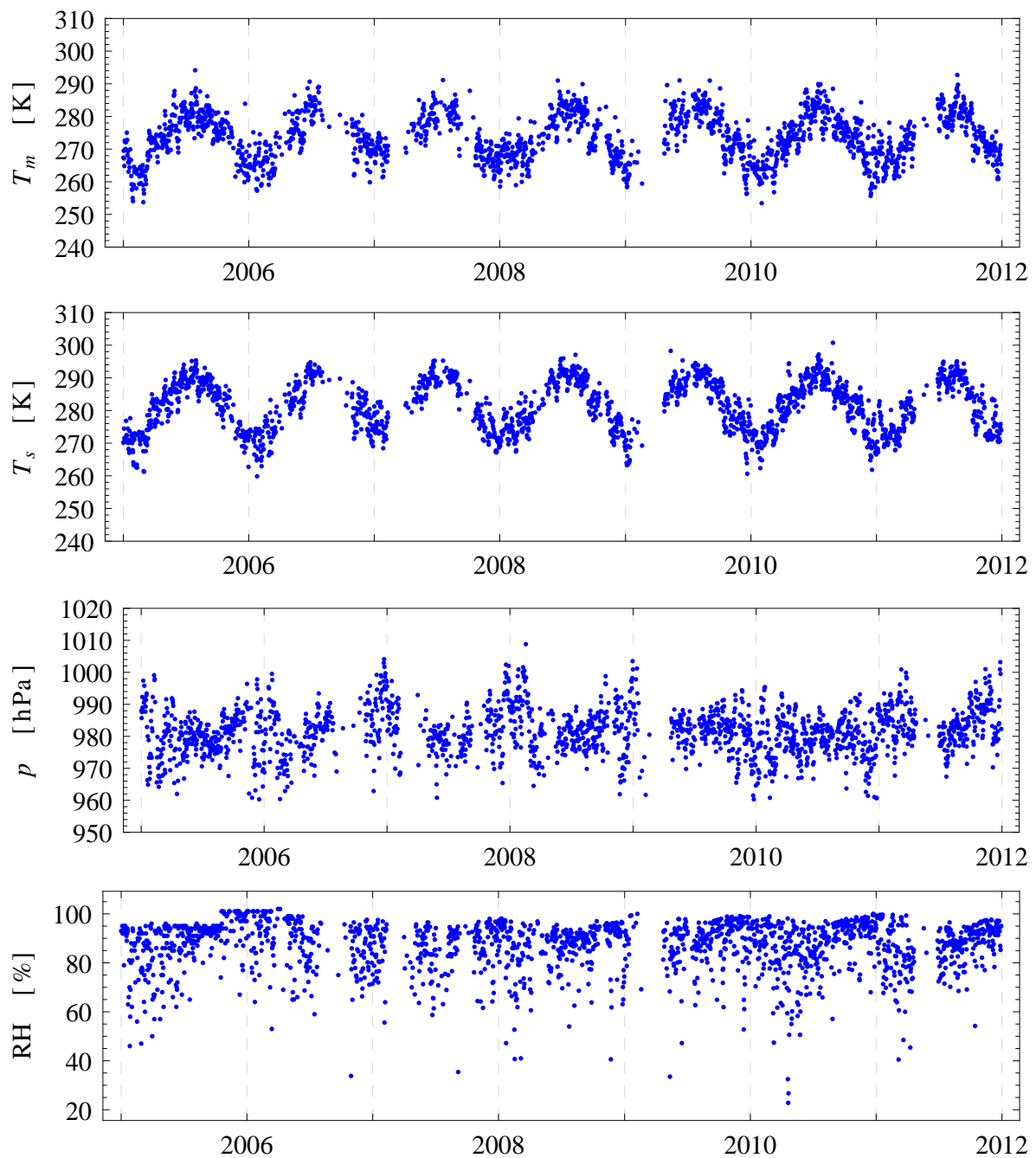


Figure 4.2: Calculated weighted mean temperature (T_m) using Eq. (4.5), where the profile of partial pressure of water vapor and temperature were taken from radiosonde measurements performed by ARSO in Ljubljana, Slovenia in a 7 year period (2005 – 2011), together with surface temperature (T_s), pressure (p) and relative humidity (RH %) at the time of radiosonde launch. It can be clearly noticed that T_m has similar seasonal variation as T_s , with pronounced maximum in the summer time and minimum in the winter time. It can be also noted that some seasonal variation is present also in pressure and humidity time series.

with $\Pi(T_m)$ defined by

$$\Pi(T_m) = \frac{10^6}{\rho_v \left(\frac{k_3}{T_m} + k'_2 \right) R_v}. \quad (4.8)$$

Mean weighted temperature of atmosphere (Eq. (4.5)) is an important parameter in the relations between IWV (or PW) and ZWD because the accuracy of GPS estimates of IWV is directly related to the accuracy of the parameter κ (Eq. (4.4)), where nearly all of the variability in κ is due to the changes in T_m . Therefore the estimation of T_m is an important part of the IWV calculations [3]. From Eq. (4.5) it can be seen that if the vertical profiles of the temperature and water vapor partial pressure were known exactly, then the calculation of T_m and consequently of IWV would be exact. These vertical profiles can be obtained either from radiosonde data or numerical weather prediction models. Fig. 4.2 shows the relationship between calculated T_m using radiosonde profiles and surface temperature, pressure and relative humidity at the time of the radiosonde launch over a period of 7 years (2005 – 2011). The ground meteorological data are being recorded by ARSO in Ljubljana every half an hour. As can be seen from Fig. 4.2, T_m shows the same seasonal relationship throughout the years as T_s , furthermore it has “opposite” correlation with pressure, while with humidity the correlation is present but not so pronounced and visible. For example, correlation coefficient between pressure and temperature is $R_{p,T_m} = -5 \times 10^{-3}$ and between humidity and temperature $R_{T_m,RH} = 0.16$. Partial pressure of water vapor, needed for calculation of T_m (according to Eq. (4.5)), was calculated using the relationship between relative humidity, saturated water vapor pressure and temperature from radiosonde profiles, using Eqs. (3.11) and (3.14) defined in Section 3.1.1.3.

4.3.1 Validation of T_m parameter

4.3.1.1 Simple linear regression method

Due to the fact that radiosondes are usually launched once or twice per day, they are very sparse in time. For this reason Bevis *et al.* (1992) proposed an alternative approach for estimating T_m solely on the basis of the observed surface temperature. If the Earth’s atmosphere was isothermal, then T_m would be constant and equal to the surface temperature. However, since the atmosphere has a negative temperature gradient up to the tropopause, T_m presents the average temperature of the atmosphere weighted by the pressure of water vapor, as indicated by Eq. (4.5). Additionally, due to the fact that the majority of water vapor is in the lower part of the atmosphere (~ 2 to 3 km), we could expect that T_m is correlated with surface temperature (Fig. 4.2) as follows [3, 53, 141]

$$T_m = a + b T_s, \quad (4.9)$$

were the regression coefficients a and b can be determined by fitting between T_m (calculated using Eq. (4.5)) and surface temperature T_s at the time of the radiosonde launch. Bevis *et al.* (1992) carried out linear regression using 8718 radiosonde profiles, spanning approximately over a two year interval from a United States of America sites (from 27° to 65° latitude range), which yielded the following linear regression

$$T_m \approx 70.2 \text{ K} + 0.72 T_s, \quad (4.10)$$

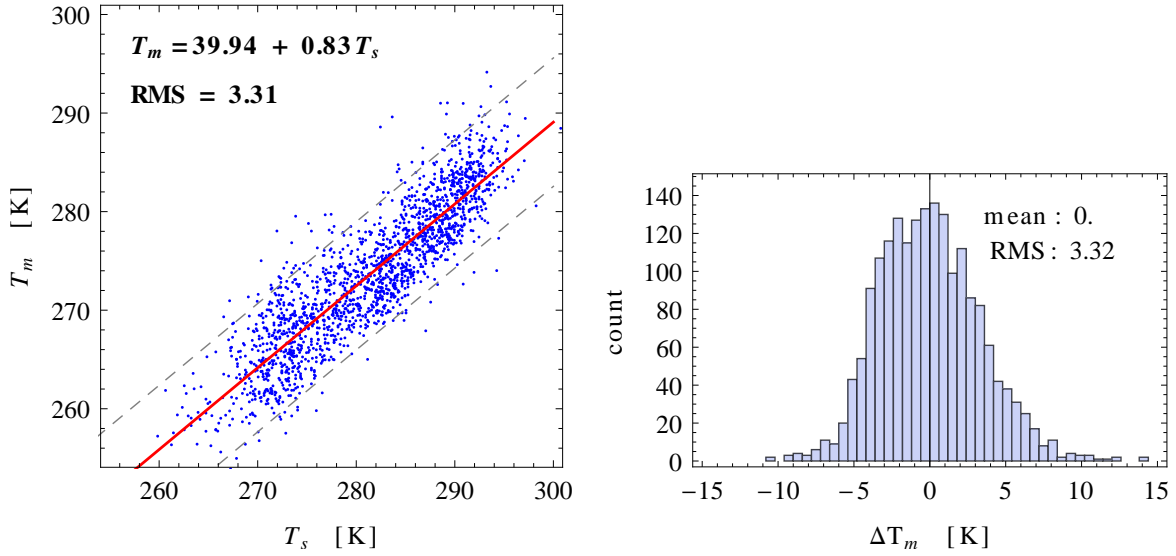


Figure 4.3: Mean weighted temperature of the atmosphere displayed as a function of surface temperature with linear regression gradient and RMS of 3.32 K (left) and histogram distribution of residuals (observed T_m minus predicted T_m) (right).

with RMS deviation of 4.74 K and relative error less than 2% and in worst case up to 4% [3]. However, this approach can suffer from systematic T_m overestimation at mid and high latitudes (up to 5 K) and underestimation at low latitudes (up to 6 K) [142]. Due to this fact, it was prudent that the same type of analysis are carried out also in our research. An analysis was performed on 1947 radiosonde profiles from Ljubljana. In order to discard all outliers only the data with a temperature range $250 \text{ K} \leq T_i \leq 310 \text{ K}$ was chosen, where the subscript i stands for T_m and T_s , respectively. The analysis yielded the following relationship between T_m and T_s

$$T_m = (39.94 \pm 2.79) \text{ K} + (0.83 \pm 0.01) T_s, \quad (4.11)$$

with an RMS deviation of 3.32 K. The results of the analysis are presented in Fig. 4.3, where on the left side the scatter plot with linear regression gradient (red) is presented, together with 95% confidence levels (dashed gray lines), while on the right side the histogram distribution of residuals (observed T_m minus predicted T_m) is shown. In order to see which linear regression gives more accurate results for T_m , values of the mean temperature were calculated using Eqs. (4.10) and (4.11) and compared to those values obtained with Eq. (4.5) (regarded as the most accurate results). Results are shown in Fig. 4.4, where the top two plots present the annual distribution of T_m values obtained using different equations, while the bottom two are the corresponding scatter plots. The black line denotes T_m calculated with Eq. (4.5), the blue line T_m obtained with Eq. (4.10) and the red T_m using Eq. (4.11). It can be noticed that T_m obtained with Eq. (4.11) shows slightly more comparable results with T_m obtained with Eq. (4.5) than the T_m obtained with Eq. (4.10), especially during the summer months.

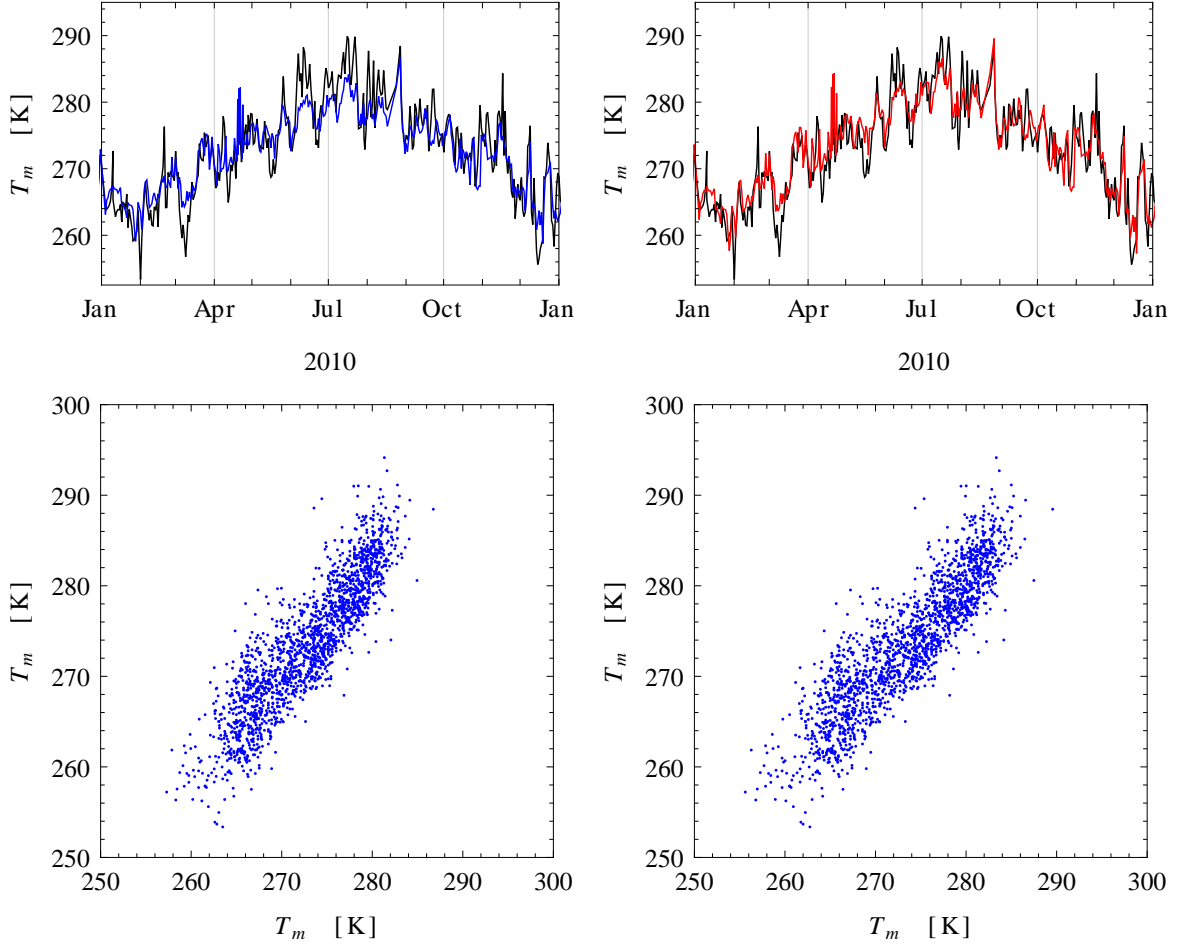


Figure 4.4: Top – annual distribution of mean weighted temperature (T_m) using different parametrizations. On the left side comparison between T_m using Eq. (4.5) (black line) and T_m from Eq. (4.10) (blue line) is shown, while on the right side comparison between T_m using Eq. (4.11) (red line) and T_m from Eq. (4.5) is shown. Bottom – corresponding scatter plots where y -axis in both plots is T_m from radiosonde, while x -axis is T_m using Eqs. (4.10) and (4.11), respectively.

4.3.1.2 Extended linear method

Although T_m shows very similar variation as the surface T_s , some dependence on RH and p is also expected (Fig. 4.2). Therefore, an additional analysis was performed where T_m was found to be

$$\frac{\tilde{T}_m}{\text{K}} = 440 + 0.1134 \frac{H}{\%} + 0.001632 \frac{p}{\text{Pa}} + 0.007446 \left(\frac{T_s}{\text{K}} \right)^2 - 3.292 \frac{T_s}{\text{K}}, \quad (4.12)$$

with an RMS deviation of 2.91 K. The above derived equation was obtained using Eureka software [143], where in the calculation of best solution not only humidity, temperature and pressure were taken into account but also wind speed, wind direction and day of the year. However, the effects of wind speed, wind direction and day of the year had little effect on the final result, in other words the best correlation was found between surface temperature,

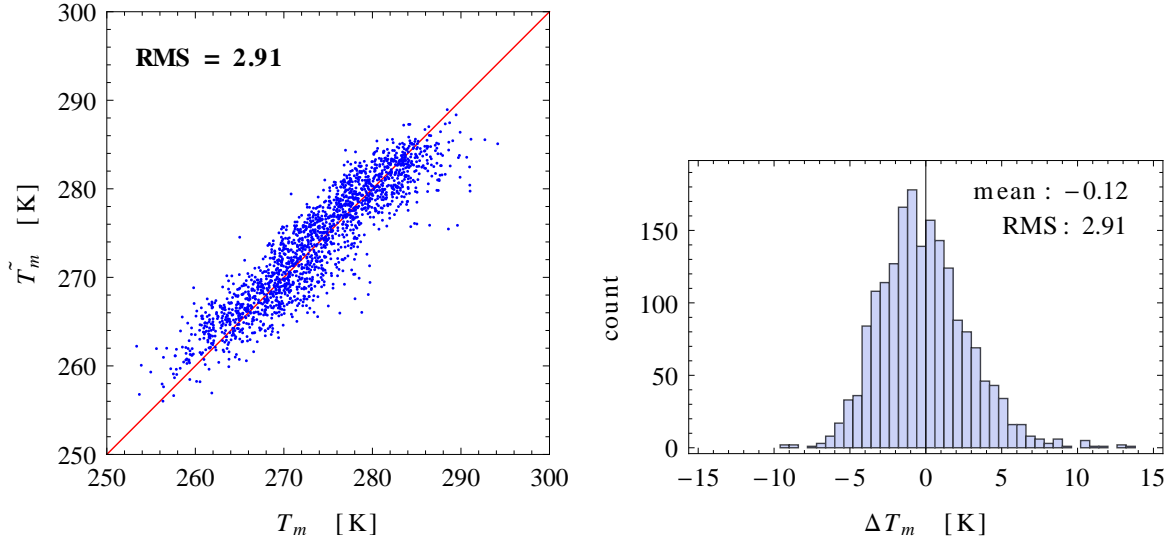


Figure 4.5: Mean weighted temperature of the atmosphere displayed as a function of surface temperature, humidity and pressure with RMS of 2.91 K (left) and histogram distribution of residuals (observed \tilde{T}_m minus predicted T_m) (right).

pressure and humidity. Fig. 4.5 presents the relationship between T_m calculated from radiosonde data (denoted as T_m) and T_m calculated using Eq. (4.12) (denoted as \tilde{T}_m). On the left side of Fig. 4.5 the scatter plot with linear regression gradient (red line) is presented, where the x -axis presents T_m obtained from radiosonde and the y -axis presents \tilde{T}_m . On the right side the corresponding histogram distribution of residuals (\tilde{T}_m observed minus T_m predicted) is presented. One can notice that in comparison with Fig. 4.3, the histogram shows a more narrow Gaussian-like distribution indicating that \tilde{T}_m has less error than T_m from simple linear model. This is even more evident in Fig. 4.6, where the top two plots present the annual distribution of T_m values obtained using different equations, while the bottom two plots present the corresponding scatter plots. The black line denotes T_m calculated with Eq. (4.5), the red line T_m using Eq. (4.11) and the green line \tilde{T}_m . As in Fig. 4.4 also in Fig. 4.6 a new parametrization of T_m (\tilde{T}_m) shows even more comparable results with T_m obtained with Eq. (4.5) than in previous case.

4.3.2 Error analysis

For both simple linear regression and extend linear method, correlations between surface meteorological data turned out to be useful. Although it was shown that different parametrizations of T_m can affect their final values (Figs. 4.4 and 4.6) compared to those from radiosonde profiles, the question how much this effects the final value of the κ coefficient (Eq. (4.4)) and furthermore final value of IWV obtained using GPS wet delay data, still remained. Therefore, the coefficient κ was calculated using T_m obtained with different equations (Eqs. (4.10) and (4.11)) and compared in order to obtain the difference.

Fig. 4.7 shows the results of the analysis, where on the right side the calculated κ for the year 2010 is shown while on the left side κ in a given T_m interval is presented, where the red line denotes κ calculated using Eq. (4.10), the blue line κ obtained using Eq. (4.11) and the dashed black line (right side of Fig. 4.7) κ calculated using Eq. (4.4). It turns out that the

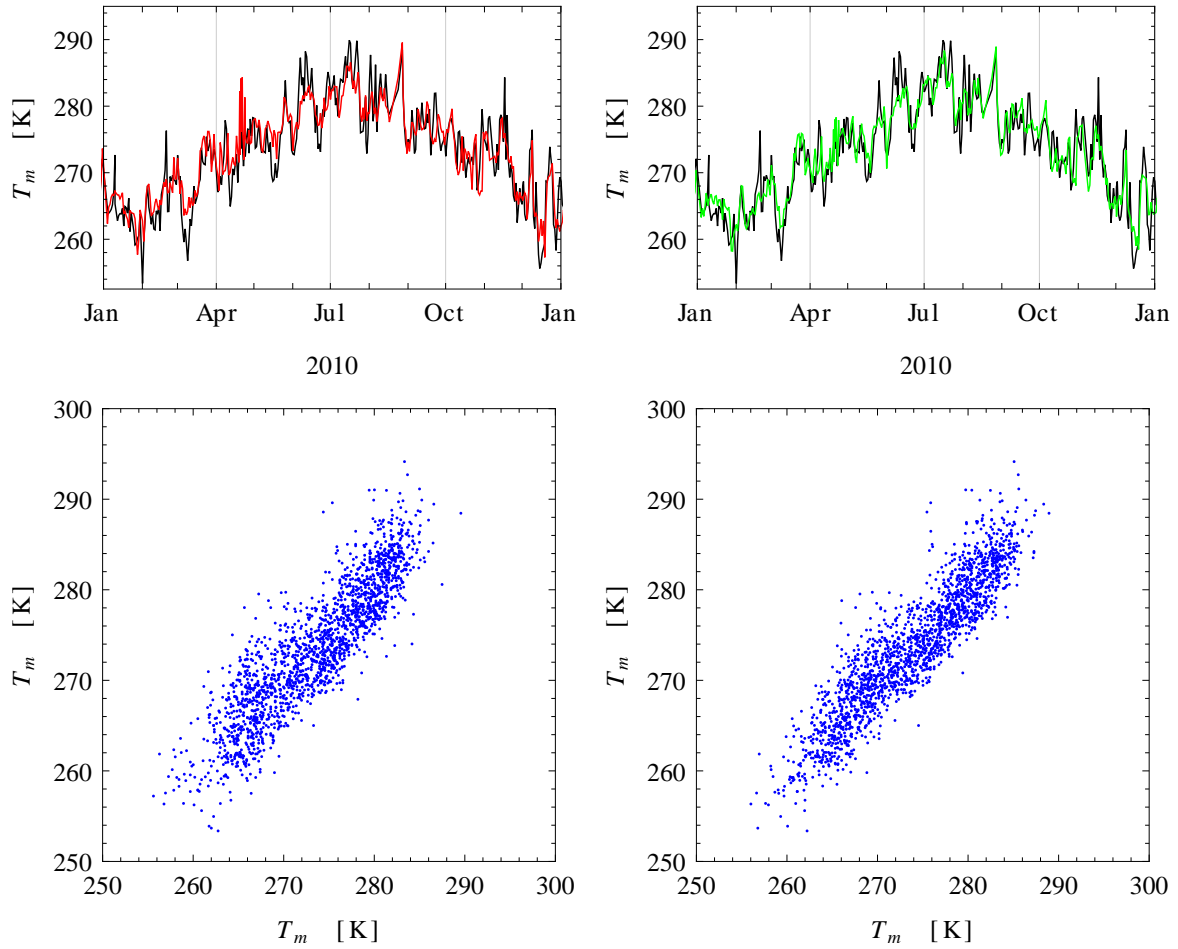


Figure 4.6: Top – annual distribution of mean weighted temperature (T_m) using different parametrizations. On the left side a comparison between T_m using Eq. (4.5) (black line) and T_m from Eq. (4.11) (red line) is shown, while on the right a comparison between T_m using Eq. (4.12) (green line) and T_m from Eq. (4.5) is shown. Bottom – corresponding scatter plots where y -axis in both plots is T_m from radiosonde, while the x -axis is T_m using Eqs. (4.11) (left) and (4.12) (right), respectively.

κ formula is not very sensitive to the value of T_m , resulting in only a small difference of κ when using the different T_m parametrizations. This difference in κ appears to be greatest during summer and winter months. This is even more evident when a comparison between IWV obtained from radiosonde (denoted as IWV_{rad}) and IWV from GPS wet delay data (calculated using different T_m parametrizations) was made. The description of different T_m parametrizations and their obtained statistical parameters are presented in Table 4.2.

Integrated water vapor from radiosonde profiles, needed for comparison, was calculated using [3]

$$IWV = \int \rho_v dh, \quad (4.13)$$

where ρ_v is the density of water vapor. Because we had radiosonde profiles from 2005 to 2011 whereas our GPS monitors became operational in 2012, the data from GPS receiver located in

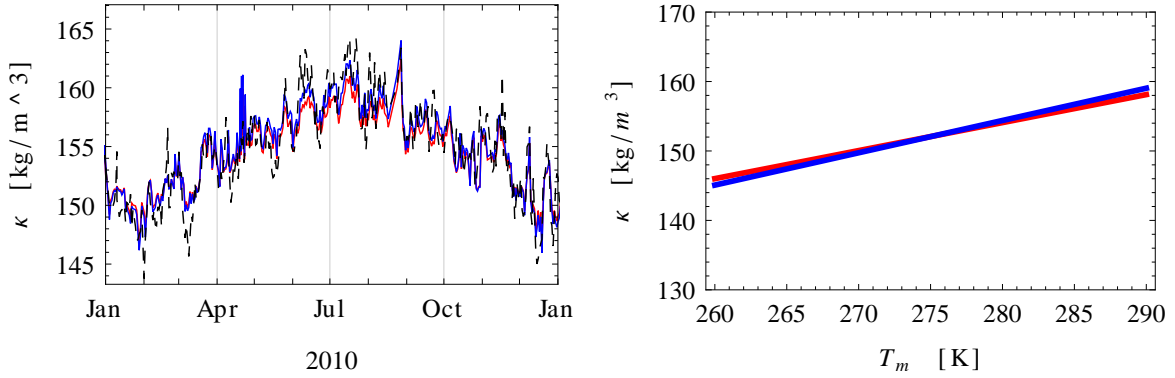


Figure 4.7: On the left side calculated κ is presented, using the three different equations, where the blue line denotes κ obtained with Eq. (4.11), the red line stands for κ calculated with Eq. (4.10) and the dashed black is κ obtained with Eq. (4.4). On the right side calculated κ is presented, using Eqs. (4.11) (blue line) and (4.10) (red line).

Ljubljana were downloaded from EPN (or EUREF Permanent Network) [144]. The receiver (type LEICA SR9500) is located about 2 km to the SE from the centre of Ljubljana at 46.05° N latitude, 15.54° E longitude and at an altitude of 351.7 m and is operated by The Surveying and Mapping Authority of the Republic of Slovenia [145].

The results are shown in Fig. 4.8, where the top figures display the results of the linear regression analysis and the bottom ones the corresponding histograms showing distribution of residuals. As a reference in all models, the IWV calculated from the radiosonde was chosen since it provides the most accurate estimates. Furthermore, to obtain the most accurate results from our analysis, only those GPS data were chosen that were recorded at the time of the launch of the radiosonde. The same method was applied in the calculations of T_m from surface data. Each scatter plot presents a comparison between the IWV, calculated from radiosonde profiles (denoted as IWV_{rad}) and IWV from GPS wet delay (denoted as IWV_{gps}), where for calculations of the integrated water vapor from ZWD different T_m parametrization were used (Table 4.2). ΔIWV , shown on the corresponding distributions of residuals for each model, presents the $IWV_{\text{gps}} - IWV_{\text{rad}}$.

T_m using	Model	StdDev [kg/m ²]	Mean [kg/m ²]
Eq. (4.5)	I	4.33	3.39
Eq. (4.10)	II	4.28	3.30
Eq. (4.11)	III	4.27	3.37
Eq. (4.12)	IV	4.31	3.41

Table 4.2: Description of the regression models (denoted with different roman numbers) presented in Fig. 4.8 together with their statistical information.

As can be noticed from Fig. 4.8 and Table 4.2, using different T_m parametrizations does not have a large effect on the final results. This can be verified from the observation that the dependency of the relative change of κ with T_m , i.e. $(d\kappa/dT_m)/\kappa \times \Delta T_m$, is far below a percent level for a typical range of T_m values.

T_m using	Model	a [kg/m ²]	b	StdDev' [kg/m ²]
Eq. (4.5)	I	-2.626	0.964	4.32
Eq. (4.10)	II	-2.828	0.978	4.27
Eq. (4.11)	III	-2.720	0.969	4.26
Eq. (4.12)	IV	-2.598	0.962	4.29

Table 4.3: Description of the regression models (denoted with different roman numbers) presented in Fig 4.9 together with their statistical information. StdDev' denotes standard deviation after the new estimate of IWV (Eq. (4.14)) where parameters a and b were obtained by linearly fitting the IWV_{rad} vs. IWV_{gps} .

However, the analysis showed that there is some systematical bias evident in all of the models. The histograms at the bottom of Fig. 4.8 show that distributions of residuals are Gaussian like, however with mean not being zero hence pointing to the origin of an error somewhere in IWV obtained with GPS data. Additional error source in the above mentioned analysis also lies in the radiosonde humidity sensors, which have been known to be not fully reliable. There were numerous analyses carried out revealing such problems. In particular, measurements are not accurate at high altitudes, humidity is underestimated in extremely dry environments, and in relatively humid environments, the radiosonde is slow to respond to dry layers and therefore overestimating the humidity (see [146] and references within).

We can remove this bias by linearly fitting the IWV_{rad} vs. IWV_{gps} . The new estimate of IWV from GPS becomes

$$IWV'_{gps} = a + b IWV_{gps}. \quad (4.14)$$

The difference between new IWV'_{gps} and IWV_{rad} is now without the systematical bias and its distribution can be seen in Fig. 4.9. The obtained parameters a and b for different T_m models are given in Table 4.3.

Another way of improving the accuracy of IWV_{gps} is to reuse GIPSY-OASIS II with different settings. There are several ways for obtaining ZWD using GIPSY-OASIS II software. First, by estimating ZTD and then using Eq. (3.54a) or Eq. (3.57) for calculating the dry delay from ground meteorological data (or any other tropospheric model). The wet delay can be then obtained by simply subtracting dry delay from total delay. The second option for estimating ZWD can be done directly using GIPSY-OASIS II where a priori dry delay can be imported in the processing scheme via tropnominal function. Here priori dry delay can also be calculated using any tropospheric model, or by using Vienna Mapping Functions 1³ (VMF1 mapping function). Therefore a second analysis was performed, where for the estimation of ZWD from GPS data a different mapping function was used, instead of Niell mapping function, we used VMF1 [131] and a priori dry delays were imported in the GPS processing scheme via tropnominal function. As before, also here error analysis was performed using the same models. The results are shown in Fig. 4.10. It can be clearly noticed that using VMF1 mapping function and a priori dry delay from VMF1, the IWV obtained from GPS estimated wet delay is now more closely correlated with the radiosonde. This is even more evident on the corresponding histogram distributions of residuals (bottom plots

³<http://ggosatm.hg.tuwien.ac.at/delay>

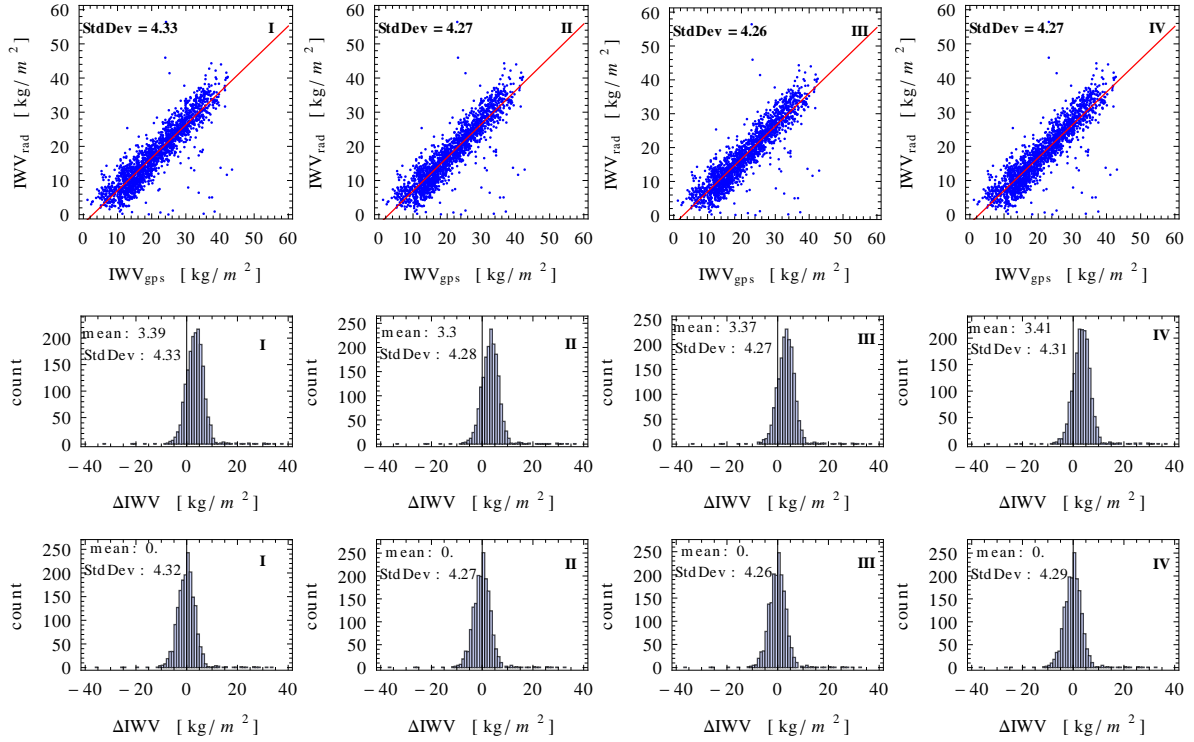


Figure 4.8: Top—scatter plots presenting the correlation between the IWV from radiosonde profiles and the IWV from GPS ZWD, where I, II, III, IV denote different models (Table 4.2). Bottom—the corresponding histogram distributions of residuals.

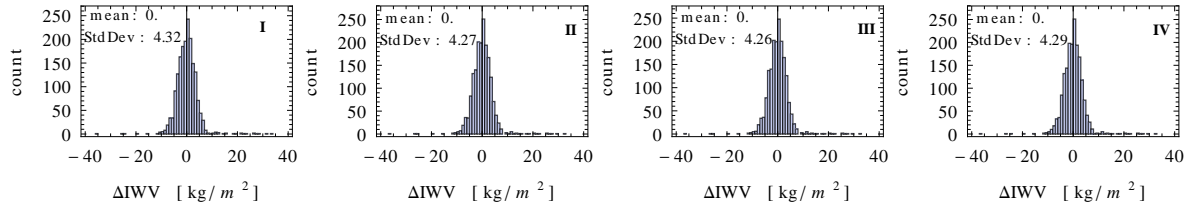


Figure 4.9: Histogram showing distributions of residuals after applying the linear correction to the data set, where the numbers I, II, III, IV refer to different models (Table 4.3).

in Fig. 4.10) where it can be noticed that the distributions which are more Gaussian-like have lesser spread and smaller StdDev than the ones in Fig. 4.8.

The difference between IWV obtained using different GIPSY-OASIS II setups and T_m models is shown in Fig. 4.11, where black dots represent integrated water vapor from radiosonde, red dots the IWV using first GIPSY setup and T_m from radiosonde profiles, green dots are denoting the second GIPSY run with T_m from radiosonde and the black triangles are the IWV from the second GIPSY run with T_m from surface pressure, temperature and humidity data, for a period of 6 months (from 1 January 2010 to 1 July 2010).

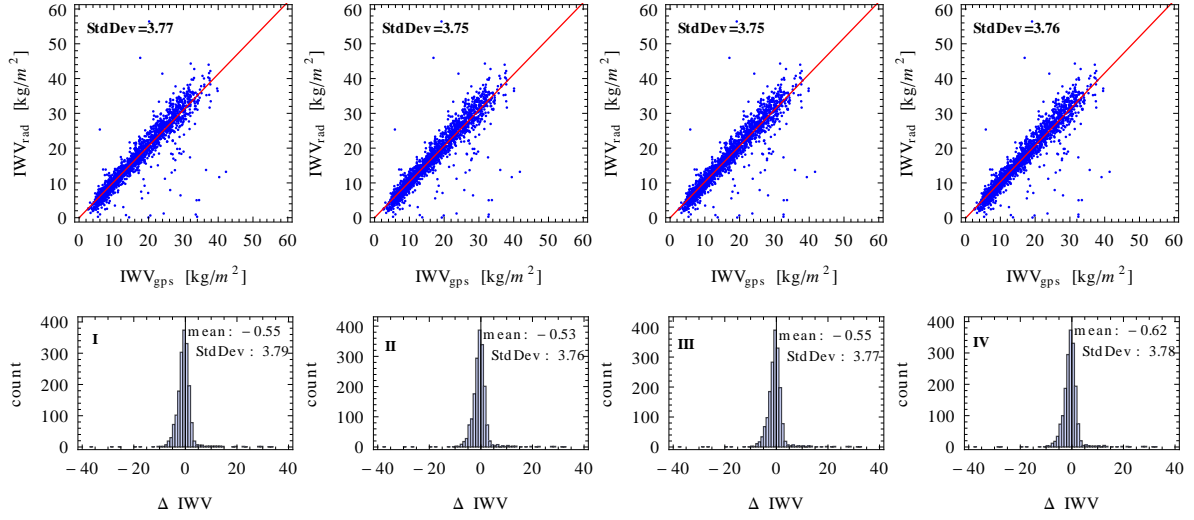


Figure 4.10: Top–scatter plots presenting the correlation between the IWV from radiosonde profiles and IWV from GPS ZWD (second usage of GIPSY-OASIS software), where I, II, III, IV denote different models (Table 4.4). Bottom–corresponding histogram distributions of residuals.

T_m using	Model	StdDev-New [kg/m ²]	Mean [kg/m ²]
Eq. (4.5)	I	3.79	-0.55
Eq. (4.10)	II	3.76	-0.53
Eq. (4.11)	III	3.77	-0.55
Eq. (4.12)	IV	3.78	-0.62

Table 4.4: Description of the regression models (denoted with different roman numbers) presented in Fig. 4.10 together with their statistical information. StdDev-New denotes standard deviation after the second GIPSY run.

4.4 Water vapor measurements at UNG

By the end of the year 2011, beside setting up two GPS monitors, we have also successfully upgraded the Mie lidar (located at Otlica Observatory) to a Raman lidar with the intention of performing continuous measurements of the water vapor mixing ratio over the Vipava Valley. One of the first measurements was performed in October 2011, when combined measurements with radiosonde (deployed by Slovenian military) and GPS monitors were performed. The radiosonde⁴ was launched twice. The first launch was performed at 18:00 CET in Potoče where radiosonde was launched from an altitude of 111 m. Data sampling of air temperature, dew temperature, virtual temperature, humidity and pressure was terminated at an altitude of 11 394 m at 18:39 CET, while the second launch started at 21:48 CET at altitude of 948 m from the Otlica Observatory and data sampling was terminated at a altitude of 8218 m at 22:14 CET. Furthermore, measuring campaign was performed during the summer of 2012 together with the scanning mobile Mie lidar to monitor aerosol information during

⁴ZEEMET™Mark II MICROSONDE, Sippican, Inc.

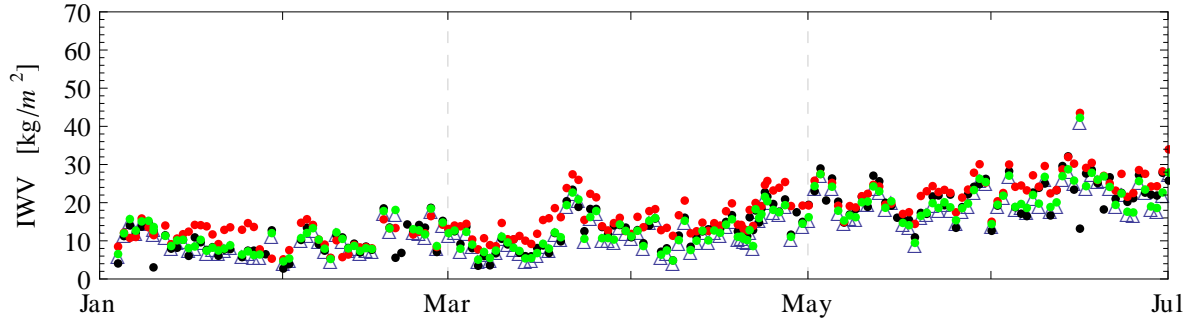


Figure 4.11: IWV, where black dots represent IWV from radiosonde, red dots the IWV using first GIPSY setup and T_m from radiosonde profiles, green dots are denoting the second GIPSY run with T_m from radiosonde and the black triangles are the IWV from the second GIPSY run with T_m from surface pressure, temperature and humidity data, for a period of 6 months (from 1 January 2010 to 1 July 2010).

measurements of the water vapor mixing ratio. Although the measurements of water vapor mixing ratio profiles with Raman lidar were not a primary topic of my research work, some results in the following sections will be presented. The main goal of measurements was to obtain mixing ratio profiles, from which we would be able to calculate integrated water vapor and use these results for verification of GPS IWV. However, as it will be shown, we were not able to perform this. One of the major disadvantages was the detectable range of the Raman lidar. Furthermore, the analysis would be also limited due to the fact that at the time of measurements we did not have co-located GPS monitor and Raman lidar.

4.4.1 Water vapor mixing ratio measurements

While the theoretical background on obtaining water vapor mixing ratio using Raman lidar backscatter signal was given in Section 2.2, here the results of water vapor mixing ratio measurements obtained with Raman lidar are presented (Fig. 4.12).

The lidar mixing ratio values are plotted as the ratio $R = k a / b$, where k is the calibration constant, a the photon counting data for H_2O and b the photon counting data for N_2 (see Eq. (2.22)). The error bars shown in Fig. 4.12 were calculated using Poisson statistics for H_2O defined as $\sigma_a = \sqrt{a}$ and for N_2 defined as $\sigma_b = \sqrt{b}$, as follows

$$R = k \frac{a}{b} = R(a, b), \quad (4.15)$$

$$\sigma_R^2 = \left(\frac{\partial R^2}{\partial a} \right)^2 \sigma_a^2 + \left(\frac{\partial R^2}{\partial b} \right)^2 \sigma_b^2 = k^2 \left(\frac{a}{b^2} + \frac{a^2}{b^3} \right), \quad (4.16)$$

$$\sigma_R = k \sqrt{\frac{a}{b^2} + \frac{a^2}{b^3}} = k \frac{a}{b} \sqrt{\frac{1}{a} + \frac{1}{b}}. \quad (4.17)$$

The mixing ratio profiles shown in Fig. 4.12 are therefore plotted up to maximum reasonable height at which the error is not bigger than 50%. On the left side of Fig. 4.12 the mixing ratio profile as a result of 3.5 h of consecutive sampling on 12 October 2011 starting at 20:00 CET is shown, while on the right side the mixing ratio profile as a result of 5.5 h of consecutive sampling on 8 August 2012 starting at 22:42 CET is presented. The difference in

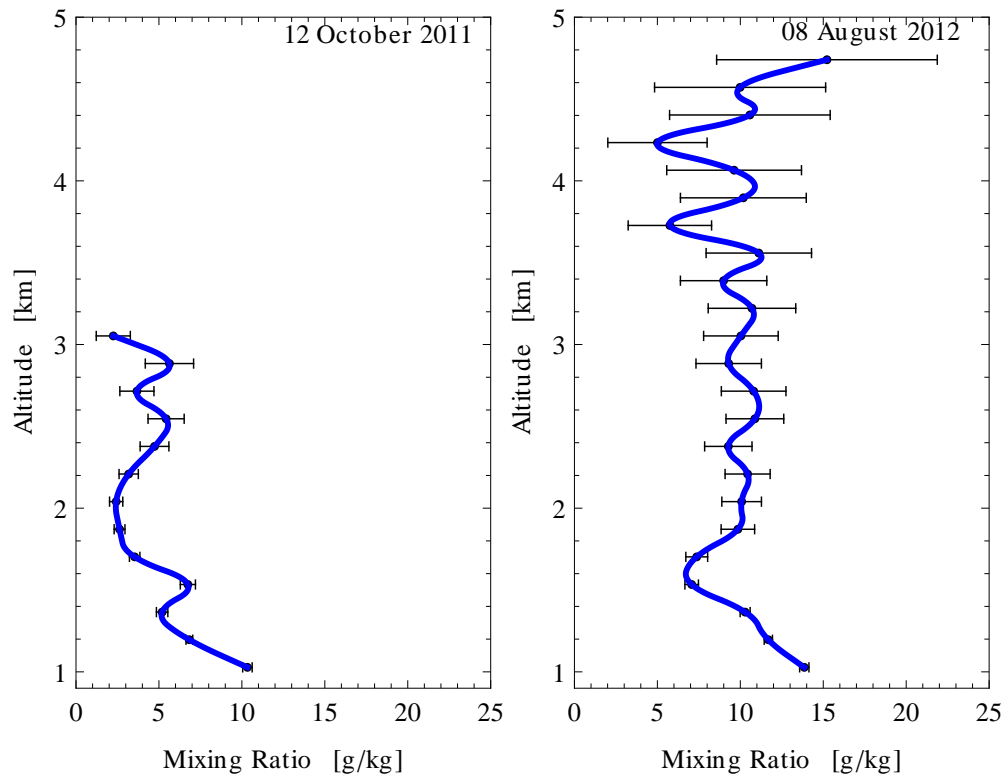


Figure 4.12: Water vapor mixing ratio measured with Raman lidar at Otlica Observatory on 12 October 2011 as a result of consecutive 3.5 h sampling from 20:00 CET (left), and on 8 August 2012 as a result of consecutive 5.5 h sampling from 22:42 CET. The mixing ratio is plotted up to the height until error exceeds 50% of the value.

range between the two measurements is a consequence of the weather conditions during the measurements and the difference between the measurement durations. In contrast to 12 October 2011 when the weather conditions were not stable (cloudy during the day and most of the evening) [89], on 8 August 2012 the weather conditions were stable (there were no clouds in the sky during the measurements) which gave us larger detectable range in the water vapor mixing ratio profile in comparison to 12 October 2011 (for about 2 km larger). However, in comparison to several other Raman lidar systems, the detectable range is small. The main reason is this is in hardware configuration, more precisely in the laser system and telescope optics [89]. While in general the laser should have high pulse energies of 0.5 to 1.5 J (which results in average power $P_0 > 10$ W at repetition rates of 20 to 50 Hz) our laser has maximum power of 2 W at the repetition rate of 20 Hz (five times less than for most known other systems). While the effective diameter of the telescope is comparable with other systems, it is not designed for this kind of application because it suffers from aberration and can only produce a relatively large beam spot [89]. The limitation due to the small detectable range becomes even more evident in Fig 4.13 where the 2D plot of water vapor mixing ratio through out the night is presented. Here, from consecutive, 6 hours and 45 minutes, measurement of the water vapor mixing ratio profile, we have extracted profiles in 15 minutes intervals. The main goal of the performed analysis was to calculate the IWV along the line of sight of Raman lidar from extracted 15 minutes profiles and compare them with GPS-IWV. However, as can

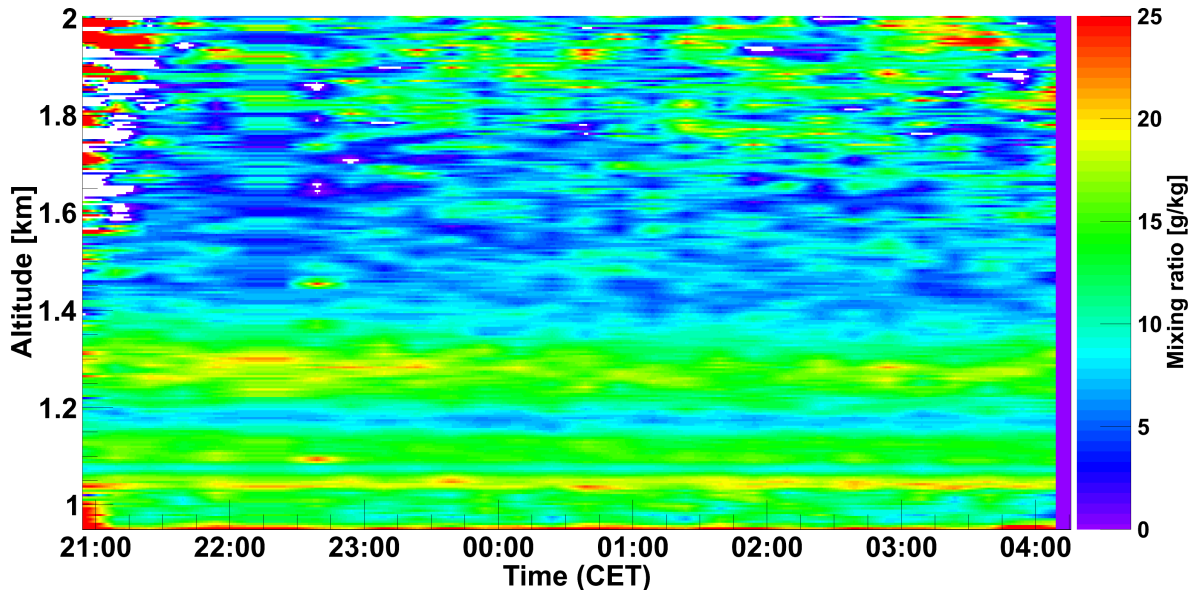


Figure 4.13: Water vapor mixing ratio measured with the Raman lidar at Otlica Observatory on 8 August 2012 as a result of consecutive 6 hours and 45 minutes sampling starting at 20:53 CET. Two layers of water vapor can be seen at ~ 1 km and between ~ 1.2 to ~ 1.4 km above the lidar site.

be seen from Fig. 4.13, the detectable range decreased almost by a factor of a half (compared to the same profile on the right in Fig. 4.12). Nevertheless, we can still see two distinct layers of water vapor mixing ratio, where the first one is between ~ 1 km and ~ 1.1 km, and the second between ~ 1.2 km and ~ 1.4 km above the lidar site.

4.4.2 GPS measurements

Due to the limitation on the detectable range of our Raman lidar, only the IWV calculation from radiosonde measurements carried out by the Slovenian Armed Forces and regular radiosonde measurements carried out by Slovenian Environmental Agency in Ljubljana was performed and compared with the IWV calculated from the GPS wet delay. The results are presented in Figs. 4.15 and 4.16, where Fig. 4.15 presents the results from October 2011 measurement campaign while Fig. 4.16 presents results from the August 2012 measurement campaign. Furthermore, both figures also shows, measurements of pressure, humidity and temperature at the ground meteorological station for comparison. T_m was calculated using Eq. (4.12). Integrated water vapor obtained from GPS wet delay measured with GPS receivers located in Rožna Dolina and Ajdovščina appears to be in good agreement with the IWV calculated from the radiosonde and GPS in Ljubljana. Small variations in the values are probably consequences of local differences in weather conditions during the measurements, more precisely differences in temperature, humidity and pressure. While the local effects can explain differences between Ljubljana and Rožna Dolina / Ajdovščina, they cannot entirely explain the difference between IWV from GPS and IWV from radiosonde measurements performed by the Slovenian Armed Forces. Although one would expect the difference between radiosonde launched at Otlica, due to the height difference between Otlica Observatory and

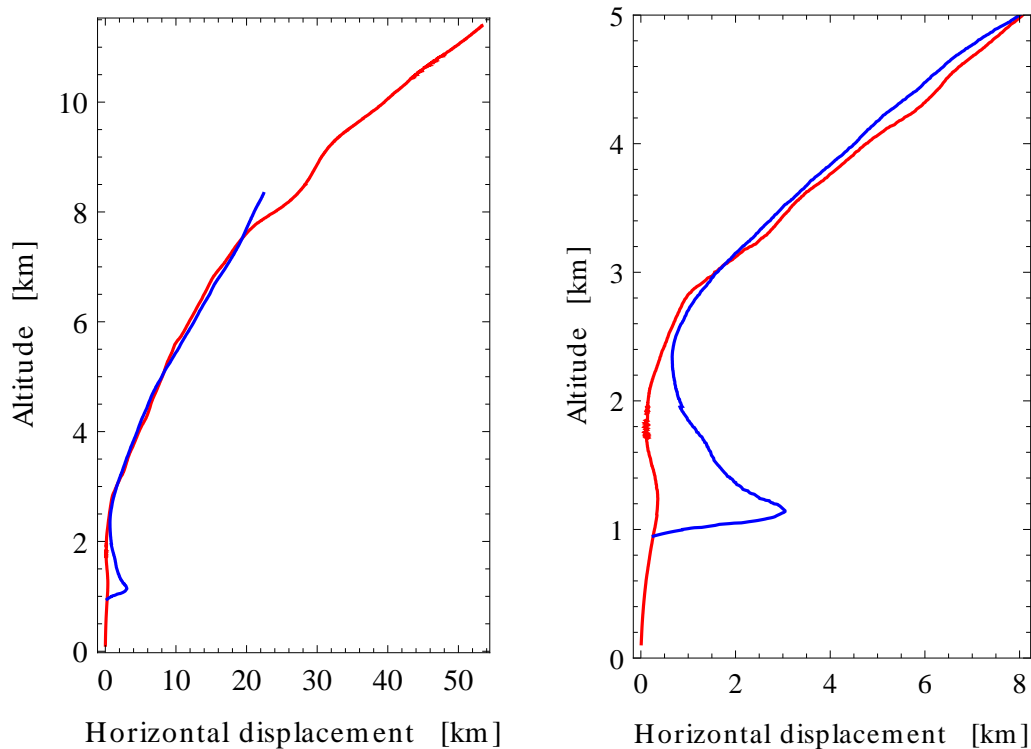


Figure 4.14: Horizontal displacement of the radiosonde along the ascend path on 12 October 2011. The blue line denotes the path of the radiosonde launched from Otlica Observatory (948 m a.s.l.) and the red line presents the path of the radiosonde launched from Potoče (111 m a.s.l.). Note, the right plot is presenting zoom of the left figure up to the altitude of 50 km.

GPS receiver in Rožna Dolina (almost 800 m) thus the difference in pressure and temperature, this is not the only reason for the difference between Potoče launch of radiosonde and GPS-IWV. As already mentioned above, on the day of the joint experiment the weather conditions were not stable. During the day it was not only cloudy but also windy. This can be seen in Fig. 4.14, where the horizontal displacement of the radiosonde along the ascend path is presented (blue line denotes radiosonde path launched on Otlica and red line is presenting radiosonde path launched in Potoče). It can be noticed from Fig. 4.14 (left) that in the case of the Potoče launch the horizontal displacement during 40 minutes of ascent was almost 50 km while in the second the horizontal displacement was not so large.

Overall the relationship between the IWV from UNG GPS monitors is in good agreement not only with GPS receiver in Ljubljana, but also with the IWV calculated from the radiosonde profiles. Furthermore, the IWV shows strong dependence on ground weather conditions (T , p , and RH).

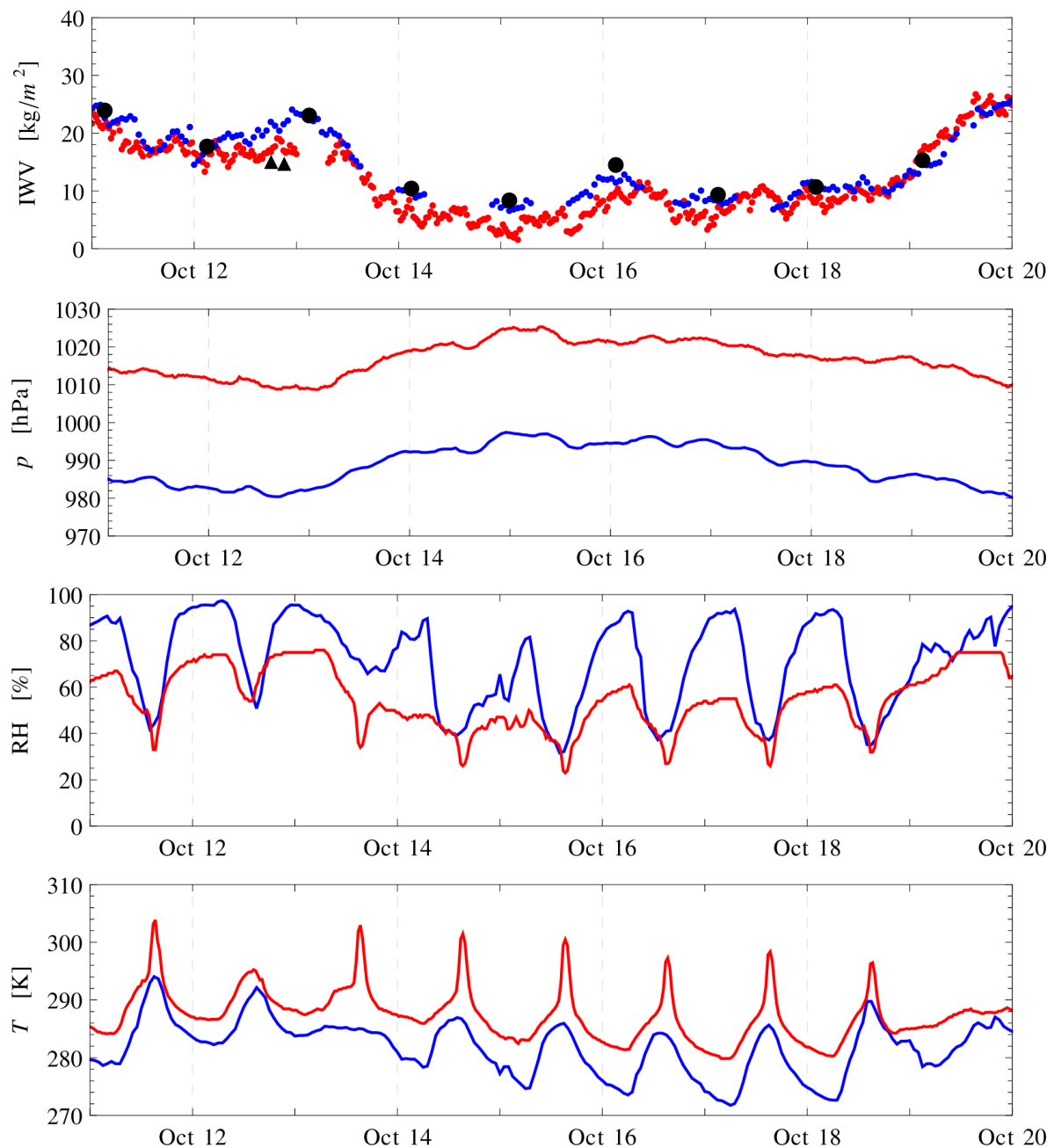


Figure 4.15: From top to bottom—IWV calculated from GPS delay (blue dots denotes Ljubljana receiver and red dots receiver located in Rožna Dolina), radiosonde (black dots present radiosonde launched in Ljubljana and black triangle radiosonde launched at Potoče and at Otlica Observatory, respectively); ground pressure, temperature and corresponding humidity measurements (where blue line presents station in Ljubljana and red line station in Rožna Dolina), between 11 October and 20 October 2011.

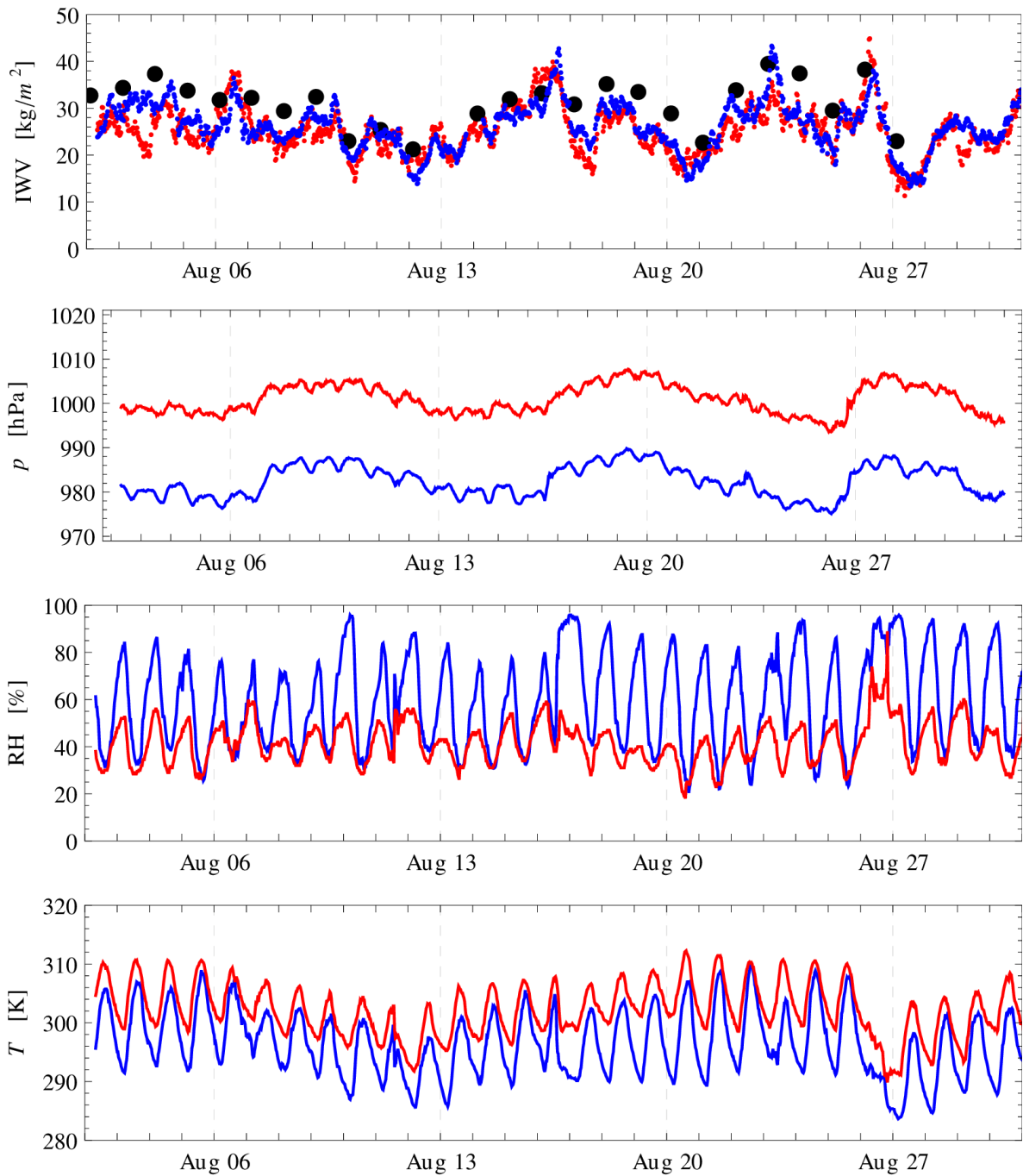


Figure 4.16: From top to bottom—IWV calculated from GPS delay (blue dots denotes Ljubljana receiver and red dots receiver located in Ajdovščina) and IWV calculated from radiosonde in Ljubljana; ground pressure, temperature and corresponding humidity measurements (where blue line presents station in Ljubljana and red line station in Ajdovščina, between 1 August and 31 August 2012).

4.5 Conclusions

It was shown that the accuracy of estimating wet delays from GPS signals and consequently the accuracy of integrated water vapor strongly depends not only on local meteorological conditions but also on the processing scheme in the GPS software that one uses. The validation of the weighted mean temperature was performed and analyzed in details. It was found that, beside simple linear correlation of the T_m with surface temperature, the weighted mean temperature shows also correlation with the surface measurements of humidity and pressure. Therefore additional linear correlation was made, resulting in new T_m parametrization. Although it was shown that different parametrization of weighted mean temperature can affect their final values, the comparison of different values of the coefficient κ (obtained with different T_m equations), showed that κ is not so sensitive to the value of T_m therefore resulting in only small differences. Even though that different T_m parametrizations were performed using data from meteorological station in Ljubljana, Slovenia (~ 130 km from Nova Gorica), comparison between Bevis *et al.* (1992) and our T_m values showed little discrepancies, which leads to the conclusion that T_m is valid not only for Ljubljana region but also for Nova Gorica.

Beside radiosondes also the Raman LIDAR seems to be a promising tool for calibration of GPS estimates of IWV, mainly due to the high temporal resolution of measurements and closer location to the available GPS monitors. However, in case of University of Nova Gorica system, the current configuration does not enable sufficient measurement range for reliable estimation of IWV. Furthermore, for absolute calibration, both GPS receiver and Raman LIDAR should be co-located.

Ionospheric scintillations

Contents

5.1 Introduction	97
5.2 Methodology	97
5.2.1 Data selection	97
5.2.2 Ionospheric pierce-point calculation	99
5.3 Results and discussion	100
5.3.1 Amplitude scintillations	101
5.3.2 Phase scintillations	104
5.3.3 Spatial distribution of scintillation occurrence	105
5.4 Summary	106

5.1 Introduction

While the characteristics and morphology of ionospheric scintillations were presented and discussed in Section 3.2.1, in this chapter we will describe statistical analysis of GPS scintillations with data taken in a period spanning from March 2004 to February 2005 and collected with a GSV4004 [83] ionospheric monitor located in Douala, Cameroon. The variations of the scintillations with local time, season and spatial distributions are investigated and presented. The results presented and discussed in this chapter were presented at the *XXXth URSI General Assembly and Scientific Symposium, 2011* [147] and *European Geoscience Union, General Assembly 2011* [148].

At low latitudes scintillations can be observed not only during geomagnetic storms but also during magnetically quiet periods. The equatorial electric field plays a major role in the development and shaping of both nighttime density irregularities and the daytime equatorial anomaly. The occurrence of scintillations at the low latitude regions is seasonally governed with maximum fading taking place during equinoctial nights. They can start abruptly, frequently reaching maximum fading in few minutes.

5.2 Methodology

5.2.1 Data selection

The data used in this analysis were collected with Novatel GPS Ionospheric Scintillation and TEC Monitor (GISTM), stationed in a near-equatorial location in Africa (Douala, Cameroon – $4^{\circ} 00' 49.5756''$ East Latitude, $9^{\circ} 42' 55.4544''$ North Longitude, and 48.3 m altitude), see Fig. 5.1. The receiver measures the amplitude and phase scintillations together with TEC

over one minute interval [15] and outputs data in so-called ISMR logs. The receiver calculates S_4 (defined in Eq. (3.40)) over 1-minute period from raw amplitude measurements at 50 Hz. The obtained S_4 , also known as Total S_4 , includes also effects of the ambient noise (and multipath) which have to be removed, since the ambient noise at the L_1 frequency can translate to relatively high S_4 values at lower VHF and UHF frequencies [108–110].

This can be carried out by estimating the average signal-to-noise density over the entire evaluation interval (60 s), and using this estimate to determine the expected S_4 due to ambient noise. If the signal-to-noise density (S/N_0) is known, then the predicted S_4 due to the ambient noise can be expressed as

$$S_{4N_0} = \sqrt{\frac{100}{S/N_0} \left[1 + \frac{500}{19 S/N_0} \right]}. \quad (5.1)$$

By replacing S/N_0 with the 60 s estimated signal-to-noise density \hat{S}/\hat{N}_0 in Eq. (5.1), we obtain an estimate of the S_4 due to noise S_{4N_0} [109]

$$S_{4\hat{N}} = \sqrt{\frac{100}{\hat{S}/\hat{N}_0} \left[1 + \frac{500}{19 \hat{S}/\hat{N}_0} \right]}. \quad (5.2)$$

Subtracting the square of this value from the square of Eq. (3.40) yields the revised value of S_4 as follows [109]

$$S_4 = \sqrt{\frac{\langle I^2 \rangle - \langle I \rangle^2}{\langle I \rangle^2} - \frac{100}{\hat{S}/\hat{N}_0} \left[1 + \frac{500}{19 \hat{S}/\hat{N}_0} \right]}. \quad (5.3)$$

Phase scintillation measurements (Eq. (3.42)) are obtained by monitoring measurements of the standard deviation and the power spectral density of detrended carrier phase from received signals. The receiver computes the phase scintillation index every minute on the minute over 5 intervals (1, 3, 10, 30 and 60 second). In analysis presented in this thesis we used the 60 s σ_ϕ values, where the values can vary from 0.05 radians for very weak scintillation to 1.0 radian for a strong scintillation.

Furthermore, to eliminate all the data collected before the phase detrending filter converged, the data with lock time less than 200 seconds and a value of σ_ϕ greater than 1 were discarded. In order to discard all the effects that the troposphere might have on the signal, a satellite elevation cut-off of 20° was used. Additionally, the data were also divided according to value of S_4 and σ_ϕ in order to distinguish between weak, medium and strong scintillations as shown in Table 5.1.

Value of S_4	Value of σ_ϕ	Description	Model
$0.1 < S_4 < 0.3$	$0.1 < \sigma_\phi < 0.3$	weak scintillation	I
$0.3 < S_4 < 0.6$	$0.3 < \sigma_\phi < 0.6$	medium scintillation	II
$0.6 < S_4$	$0.6 < \sigma_\phi$	strong scintillation	III

Table 5.1: Division of the scintillations according to the value of S_4 with denoted roman number used in text.

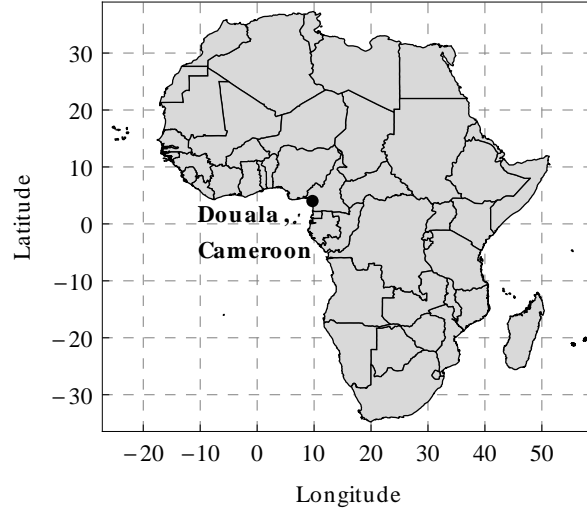


Figure 5.1: Geographical location of Douala, Cameroon.

5.2.2 Ionospheric pierce-point calculation

Pierce point needed for geographical plots was calculated in the following way, with φ , λ as latitude and longitude of the receiver position respectively and \vec{g} defined as (see Fig. 5.2)

$$\vec{g} = R \begin{bmatrix} \cos \varphi \cos \lambda \\ \cos \varphi \sin \lambda \\ \sin \varphi \end{bmatrix} = R(\cos \varphi \hat{x} + \cos \varphi \sin \lambda \hat{y} + \sin \varphi \hat{z}), \quad (5.4)$$

where

$$\hat{x}' = \frac{\hat{z} \times \vec{g}}{|\hat{z} \times \vec{g}|}, \quad \hat{y}' = \frac{\hat{x} \times \vec{g}}{|\hat{x} \times \vec{g}|} = \frac{\vec{g} \times (\hat{z} \times \vec{g})}{|\vec{g} \times (\hat{z} \times \vec{g})|}, \quad \hat{z}' = \frac{\vec{g}}{|\vec{g}|}. \quad (5.5)$$

Direction towards the satellite (\hat{s}) in the local system C' (Fig. 5.3) is then defined as

$$\begin{aligned} \hat{s} &= \cos \varepsilon \sin \alpha \hat{x}' + \cos \varepsilon \cos \alpha \hat{y}' + \sin \varepsilon \hat{z}' = \\ &= \cos \varepsilon \sin \alpha \frac{\hat{z} \times \vec{g}}{|\hat{z} \times \vec{g}|} + \cos \varepsilon \cos \alpha \frac{\vec{g} \times (\hat{z} \times \vec{g})}{|\vec{g} \times (\hat{z} \times \vec{g})|} + \sin \varepsilon \frac{\vec{g}}{|\vec{g}|}. \end{aligned} \quad (5.6)$$

Therefore for calculation of pierce point \vec{p} , defined as

$$\vec{p} = \vec{g} + d \hat{s} \quad (5.7)$$

we require the pierce point \vec{p} to lie on the ionosphere radius $R + h$

$$\begin{aligned} |\vec{g} + d \hat{s}| &= R + h \\ |\vec{g}|^2 + 2d(\vec{g} \cdot \hat{s}) + d^2|\hat{s}|^2 &= (R + h)^2 \\ d^2 + 2d(\vec{g} \cdot \hat{s}) + R^2 - (R + h)^2 &= 0, \end{aligned} \quad (5.8)$$

which give us quadratic equation in d

$$d_{1,2} = -(\vec{g} \cdot \hat{s}) \pm \sqrt{(\vec{g} \cdot \hat{s})^2 + (R + h)^2 - R^2}. \quad (5.9)$$

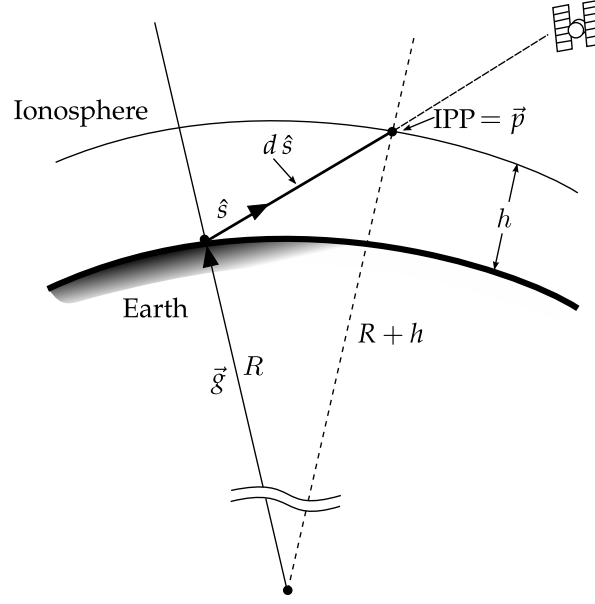


Figure 5.2: Geometry of ionospheric pierce point calculation.

From the two possible solutions we chose the one which does not go through the Earth and corresponds to sign +, i.e.

$$d = \sqrt{(\vec{g} \cdot \hat{s})^2 + 2Rh + h^2} - (\vec{g} \cdot \hat{s}). \quad (5.10)$$

With the solution for d we obtain the location of the pierce point \vec{p} and decompose it into its latitude φ_{pp} and longitude λ_{pp} ,

$$\vec{p} = \vec{g} + d\hat{s} = (R + h) \begin{bmatrix} \cos \varphi_{pp} \cos \lambda_{pp} \\ \cos \varphi_{pp} \sin \lambda_{pp} \\ \sin \varphi_{pp} \end{bmatrix}. \quad (5.11)$$

The latitude can be then obtained from the z component of \vec{p} ,

$$p_z = (R + h) \sin \varphi_{pp}, \quad \sin \varphi_{pp} = \frac{p_z}{R + h}, \quad \varphi_{pp} = \arcsin \frac{p_z}{R + h} = \arcsin \frac{p_z}{|\vec{p}|}, \quad (5.12)$$

and the longitude from the fraction of the y and x components,

$$\frac{p_y}{p_x} = \frac{\sin \lambda_{pp}}{\cos \lambda_{pp}} = \tan \lambda_{pp}, \quad \lambda_{pp} = \arctan \frac{p_y}{p_x}. \quad (5.13)$$

5.3 Results and discussion

Figs. 5.4 and 5.5 are presenting general behavior of amplitude and phase scintillations for all three thresholds (see Table 5.1), respectively. Note that white “spots” are missing data probably due to the technical problems with receiver, and not an indication that there was no scintillation activity (the same “spots/gaps” can be also seen in Fig. 5.6).

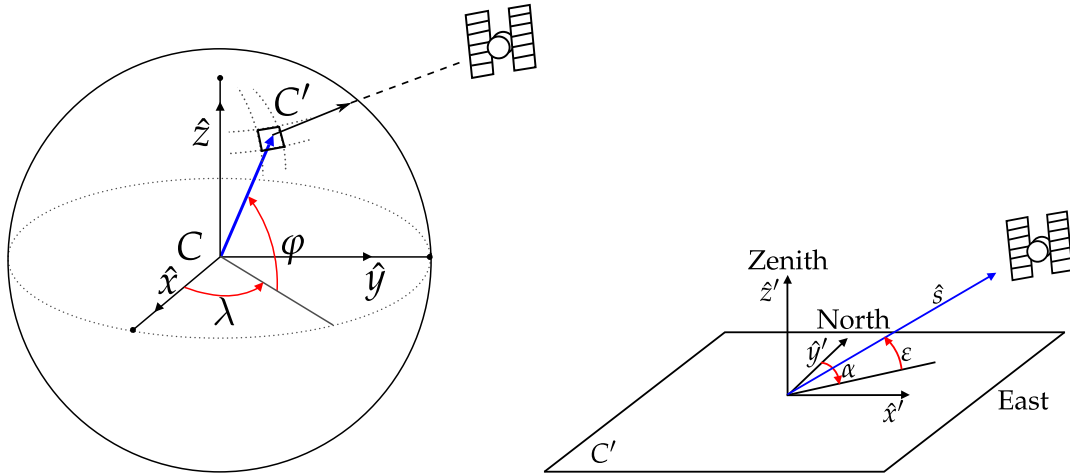


Figure 5.3: C is earth-fixed-centered coordinate system (left) and C' is local coordinate system, tangential to the Earth's surface at the geographical position \vec{g} .

It can be noticed that the pattern of scintillation activity slowly decreases towards the end of the data set, with slight increases during the equinox months (March–April and September–October). Here, the percentage of occurrence was calculated as the ratio between the number of minutes with S_4 and σ_ϕ in a given threshold and the total number of minutes within one day. The general behaviour of amplitude scintillation activity through out the data set and from day to day is presented in Fig. 5.6, where it can be seen that the majority of scintillation activity started to occur around 19:00 UT throughout the whole year. Furthermore, it can be noticed that scintillation activity is seasonally governed.

5.3.1 Amplitude scintillations

In contrast to Fig. 5.4 where the plots are presenting the occurrence of S_4 through the year for all three thresholds, Figs. 5.7 presents diurnal variations of the percentage of occurrences of amplitude scintillations throughout the day in a given month (denoted with different numbers on plots: 3 \mapsto March 2004, 4 \mapsto April 2004, 5 \mapsto May 2004, 6 \mapsto June 2004, 7 \mapsto July 2004, 8 \mapsto August 2004, 9 \mapsto September 2004, 10 \mapsto October 2004, 11 \mapsto November 2004, 12 \mapsto December 2004, 1 \mapsto January 2005 and 2 \mapsto February 2005). As can be noticed the majority of scintillation activity starts to occur in the pre-midnight hours (around 19:00 UT) reaching scintillation peak between 20:00 and 22:00 UT (in case of S_4 also visible in Fig. 5.6).

As in Fig. 5.6 and Fig. 5.4, also in Fig. 5.7 the majority of amplitude scintillations (more than 50%) occurred in the months of April and September, while the winter months (November to December) had less than 20% percentages of occurrence. Here, different thresholds are shown with different colors (threshold I-light blue, threshold II-red and threshold III-brown). It can be noticed that scintillations were most “intense” for threshold I, while for threshold II there was almost none scintillation activity, except in March, April and September. Furthermore, scintillation for threshold III stayed below 5% through out the data set. This is even more visible in Fig. 5.9, where the percentage of occurrence, calculated as the ratio between the number of minutes with S_4 in a given threshold and the total number of minutes within one day for a given month is shown. As in Fig. 5.7 also here can be noticed

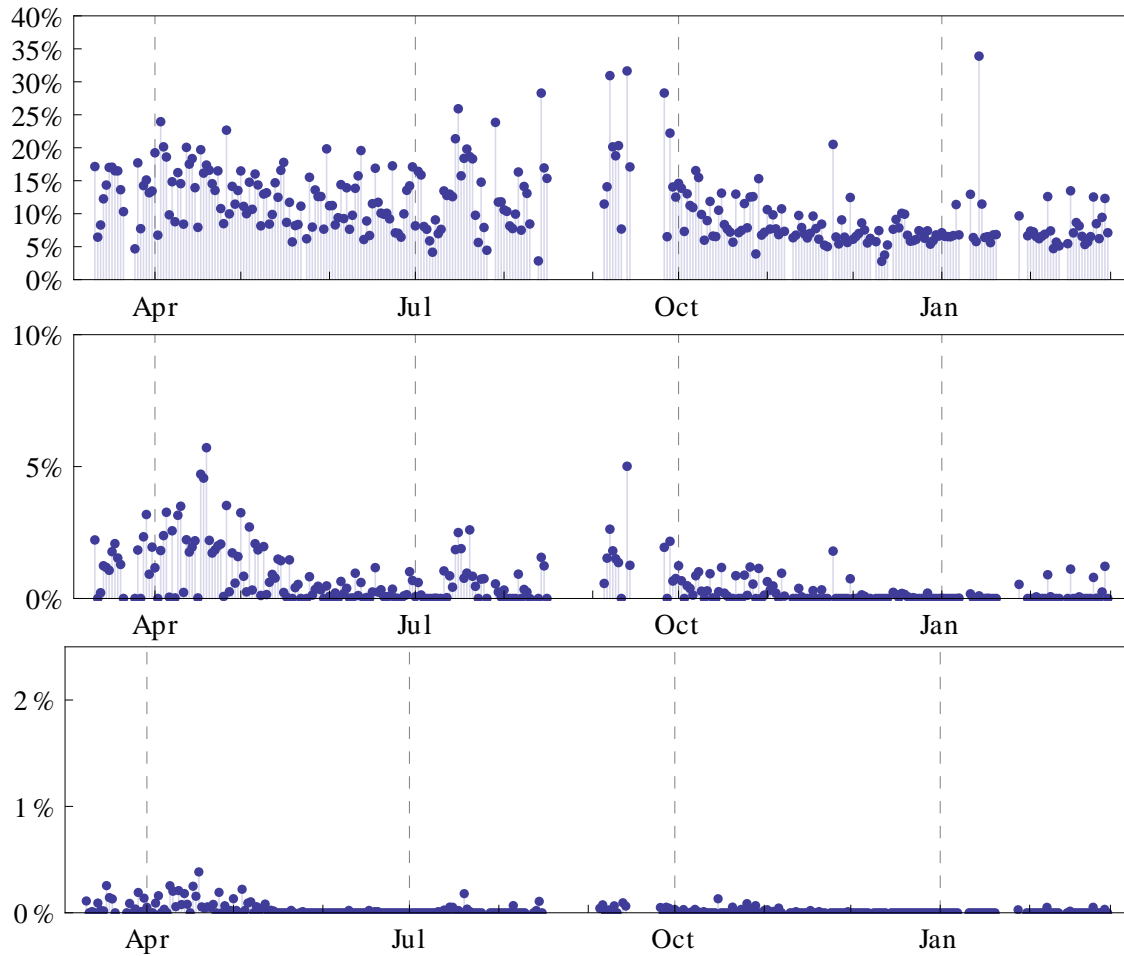


Figure 5.4: Top – Percentage of occurrence of S_4 for threshold I between 13 March 2004 and 29 February 2005. Middle – Percentage of occurrence of S_4 for threshold II between 13 March 2004 and 29 February 2005. Bottom – Percentage of occurrence of S_4 for threshold III between 13 March 2004 and 29 February 2005. The percentage of occurrence of S_4 was calculated as the ratio between the number of minutes with S_4 in a given threshold and the total number of minutes within one day. Note, white “spots” are data gaps and not indication that there was no scintillation activity.

that months with largest % of occurrence are in the spring and fall equinoxes (March-April and September). Furthermore, the results show that there are two peaks of scintillation activity in post-sunset hours, the first starts 19:00 UT reaching its peak between 20:00 UT and 21:00 UT depending on the month, while the second peak (smaller than first one) occurs at around 22:00 UT. In post-midnight hours the scintillation activity starts to decrease (Fig. 5.9) reaching its minimum % of occurrence in pre-sunrise hours.

Figs. 5.11 and 5.13 are present histograms where the number of satellites observing S_4 for threshold I (Fig. 5.11) and threshold II (Fig. 5.13) is shown on a monthly basis. The x axis presents the number of satellites while the y axis is the total number of events for corresponding number of satellites in log scale. Different months are denoted with numbers (i.e. 3 \mapsto March 2004, 4 \mapsto April 2004, 5 \mapsto May 2004, 6 \mapsto June 2004, 7 \mapsto July 2004, 8 \mapsto August

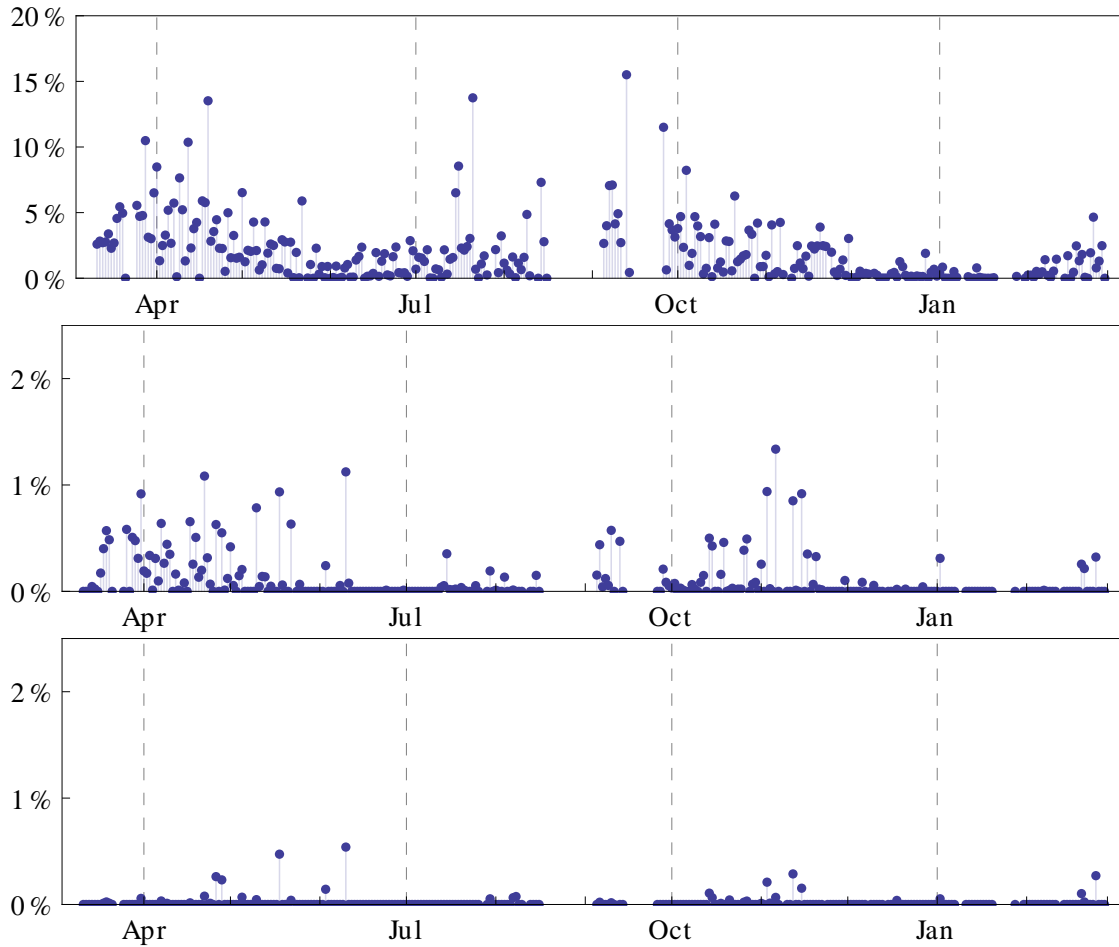


Figure 5.5: Top – Percentage of occurrence of σ_ϕ for threshold I between 13 March 2004 and 29 February 2005. Middle – Percentage of occurrence of σ_ϕ for threshold II between 13 March 2004 and 29 February 2005. Bottom – Percentage of occurrence of σ_ϕ for threshold III between 13 March 2004 and 29 February 2005. The percentage of occurrence of σ_ϕ was calculated as the ratio between the number of minutes with σ_ϕ in a given threshold and the total number of minutes within one day. Note, white “spots” are data gaps and not indication that there was no scintillation activity..

2004, 9 \mapsto September 2004, 10 \mapsto October 2004, 11 \mapsto November 2004, 12 \mapsto December 2004, 1 \mapsto January 2005 and 2 \mapsto February 2005). Here only those satellites that were observing scintillations in a given threshold for more than one minute were chosen and presented. This analysis was partially limited due to the fact that we had data only from one station. As can be seen from Fig. 5.11 through the year the distribution of the number of satellites is more or less equal, where in all months the dominant number is 1, while the number of events changes quite rapidly. In contrast to Figs. 5.7 and 5.9, where scintillations have maximum % of occurrence during equinox months, the number of satellites does not follow similar pattern. In addition it seems that the months June and July have the maximum number of events compared to April and September. One possible explanation for this is that the total number of events was lower for June and July resulting in a higher number of events and

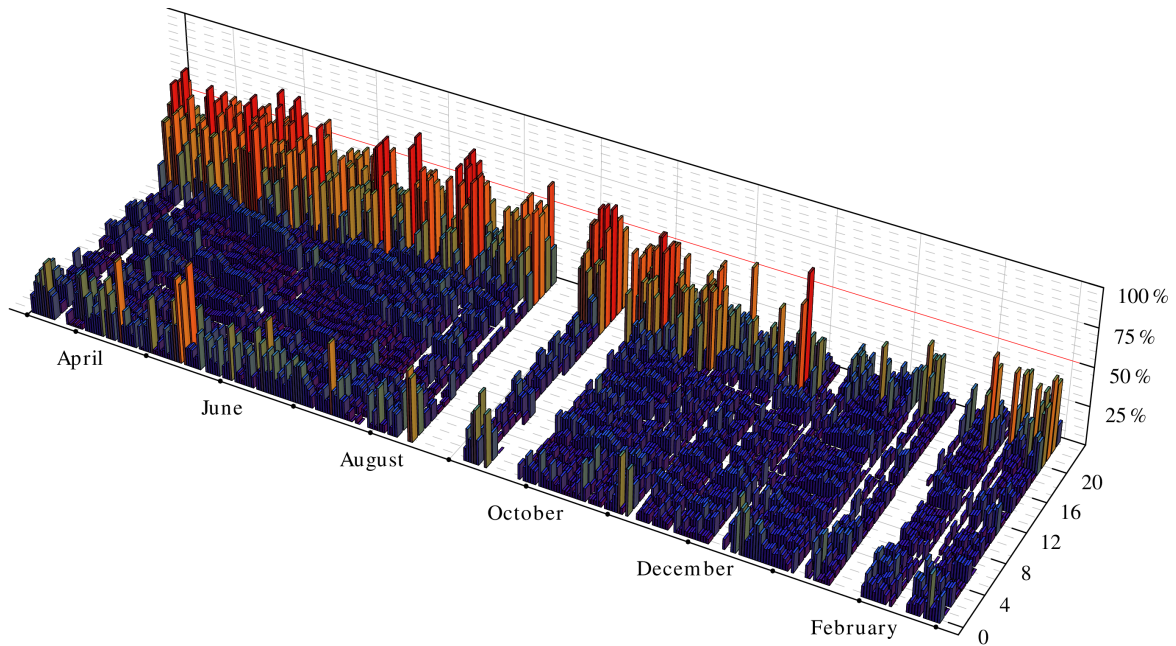


Figure 5.6: Histogram presenting percentage of occurrence of S_4 for threshold I between 13 March 2004 and 29 February 2005. Note, white “spots” are data gaps and not indication that there was no scintillation activity.

satellites observing S_4 in threshold I.

5.3.2 Phase scintillations

As amplitude scintillations (Fig. 5.4), also phase scintillations shows strong seasonal dependence (Fig. 5.5) with slight increases during the equinox months. In contrast to occurrence of S_4 through out the year, where maximum was almost 40 %, the occurrence of σ_ϕ is reduced by almost half. As in case of S_4 also for σ_ϕ diurnal variations of the percentage of occurrences of amplitude scintillations throughout the day in a given month where calculated. Results are shown in Fig. 5.8, where the numbers on plots presents different month (as for Fig. 5.7) and different thresholds are shown with different colors (threshold I-light blue, threshold II-red and threshold III-brown). While the majority of amplitude scintillation started to occur on the pre-midnights hours, σ_ϕ shows slightly different pattern. Although in overall phase scintillation activity reaches its maximum (almost 30% in September), one can notice that there is also second peak reaching almost 15% in March, while for the other months is 5% or less. Moreover, the percentages of occurrence stays below 30%, which is 20% less as for percentages of occurrence of S_4 (Fig. 5.7). Despite this difference, the percentages of occurrence for phase scintillations are following the same monthly dependence as occurrence of S_4 . It can be noticed that majority of phase scintillations (more than 20%) occurred in the months of April and September, while the winter months (November, December and January) had less than 5% percentages of occurrence. Furthermore, phase scintillations were most “intense” for threshold I, while for threshold II there was almost n scintillation activity, except in March, April and September, while scintillation activity for threshold III stayed

below 1% through out the data set. This is even more visible in Fig. 5.10, where the percentage of occurrence, calculated as the ratio between the number of minutes with σ_ϕ in a given threshold and the total number of minutes within one day for a given month is shown. As in Fig. 5.7 also here can be noticed that months with largest % of occurrence are in the spring and fall equinoxes (March-April and September). Furthermore, the results show that there are two peaks of scintillation activity in post-sunset hours, the first starts 19:00 UT reaching its peak between 20:00 UT and 21:00 UT depending on the month, while the second peak (smaller than first one) occurs at around 22:00 UT. In post-midnight hours the scintillation activity starts to decrease (as in case of S_4 in Fig. 5.9) reaching its minimum % of occurrence in pre-sunrise hours.

Figs. 5.12 and 5.14 are presenting histograms where the number of satellites observing σ_ϕ for threshold I (Fig. 5.12) and threshold II (Fig. 5.14) is shown on a monthly basis. The x axis presents the number of satellites while the y axis is the total number of events for corresponding number of satellites in log scale (as for Figs. 5.11 and 5.13). As for amplitude scintillations also for phase scintillations only those satellites that where observing scintillations in a given threshold for more than one minute were chosen and presented. While for threshold I (Fig. 5.12), the distribution of the number of satellites is having similar pattern as for % of occurrence in case of S_4 (Fig. 5.11), where for all months the dominant number is 1, there are some differences between Fig. 5.13 and Fig. 5.14. The difference is most visible for August, where for given S_4 threshold the maximum number of satellites was 3 (only one event) while for σ_ϕ occurrence there where 6 satellites having scintillations. One possible reason for this is, that August the gap in the data set was the largest, and therefore affected the final result of statistical analysis.

5.3.3 Spatial distribution of scintillation occurrence

The overall picture of scintillation activity becomes complete with spatial distribution of % occurrence of S_4 and σ_ϕ in a given threshold. Here the variations throughout one day in a given month are presented, where the days taken in consideration were 4 April 2004, 15 June 2004, 29 September 2004 and 19 December 2004. The days were chosen for two reasons. First they present the most complete data set (no “gaps”) and secondly, they are closest to and therefore present spring equinox (April), summer solstice (June), fall equinox (September) and winter solstice (December). The height of the ionosphere, at which the ionospheric pierce points were calculated, was taken to be 350 km with a geographical grid taken of 0.5° . The percentage of occurrence was calculated as the ratio between the number of satellites observing S_4 and σ_ϕ in a given threshold in $0.5^\circ \times 0.5^\circ$ grid to a total number of IPP points in that grid.

Results are shown in Figs. 5.15 and 5.16, where on both figures the left column of the figure is presenting geographical distribution of % S_4 and % σ_ϕ for threshold I and the right column sky-plot for all satellites on view on the same day, respectively. In both cases the values of S_4 and σ_ϕ are presented with color range. Dashed lines on geographical plots present magnetic inclination for the year 2004 [149]. As can be seen from Figs. 5.15 and 5.16, there are two major geographical regions of scintillation activity. One in the geographical grid below -1°N (4° and 15° E) and another above 6°N (the same longitudinal range as before), although more visible for S_4 than for σ_ϕ . The same regions can be observed for all four months taken in consideration small variation in the range. Furthermore, the majority of scintillation with S_4 and σ_ϕ bigger than 0.2 occurred when satellites were either descending

or ascending (i.e. elevation angle below 50% with azimuthal range between 90° and 345°).

5.4 Summary

In this study scintillations observed using the GPS monitor station in Douala, Cameroon, located near the crest of the equatorial anomaly, were investigated and presented. Although the study was limited due to the data gaps, one station, and the absence of “raw” data (from which we could have also calculate SI and S_ϕ indexes and performed spectral analysis), we can still list our main conclusions as follows.

GPS scintillation at low latitudes is predominantly post-sunset event, starting to occur in pre-midnight hours $\sim 18:00$ UT and lasting until $\sim 01:00$ UT (Fig. 5.6). Additionally, from Figs. 5.7, 5.8, 5.9 and 5.10 it can be observed that during the post-sunset event, scintillation shows to have two peaks, the first starts to occur at around 20:00 UT and the second around 22:00 UT for all thresholds. The occurrence of pre-midnight scintillation was found to be higher in equinox month than in summer solstice by almost 20%. Furthermore, throughout the whole data set (from 13 March 2004 to 29 February 2005) weak scintillations ($0.1 < S_4 < 0.3$ and $0.1 < \sigma_\phi < 0.3$) dominant, while moderate scintillations were found to be small and practically no occurrence of strong scintillations. We found that the occurrence of scintillations was higher during equinox months (March, April; September, October; see Figs. 5.4, 5.13 and 5.13). Analysis also show, that amplitude scintillations are significantly higher and more pronounced than phase scintillations in low latitude regions. The same seasonal pattern was found by [150] who investigated GPS scintillation activity at the northern crest of the equatorial anomaly stations in Guangzhou and Shenzhen of South China. Although they reported similar pattern of seasonal dependence of scintillation activity, they also found that differs from others studies. According to [150] (and the references within) the seasonal dependence of GPS scintillation could be explained by the seasonal dependence of the pre-reversal enhancement where the average values of the pre-reversal enhancements show significant seasonal and longitudinal variations. Therefore the occurrence of irregularities causing scintillation depend not only on season but may also vary with longitude. The same durinial pattern of scintillation activity was found by [113], who investigated equatorial scintillations and the occurrence characteristics of the scintillations observed at Legon, Ghana. It that paper it was reported that scintillations in that region are essentially a nighttime phenomena, with the biggest scintillations having maximum around 22:00 LT, which is in general agreement with the results of our study. Equatorial region presents highly dynamical and unpredictable region which is characterized by the intense equatorial plasma bubble associated irregularities. Beside bubbles there are also significant differences in the structure and effects of the ionosphere on GPS signals, such as equatorial electrojet and accompanying equatorial anomaly, greater absorptions and the fact that the geomagnetic field orientation is almost nearly horizontal [14, 104–113].

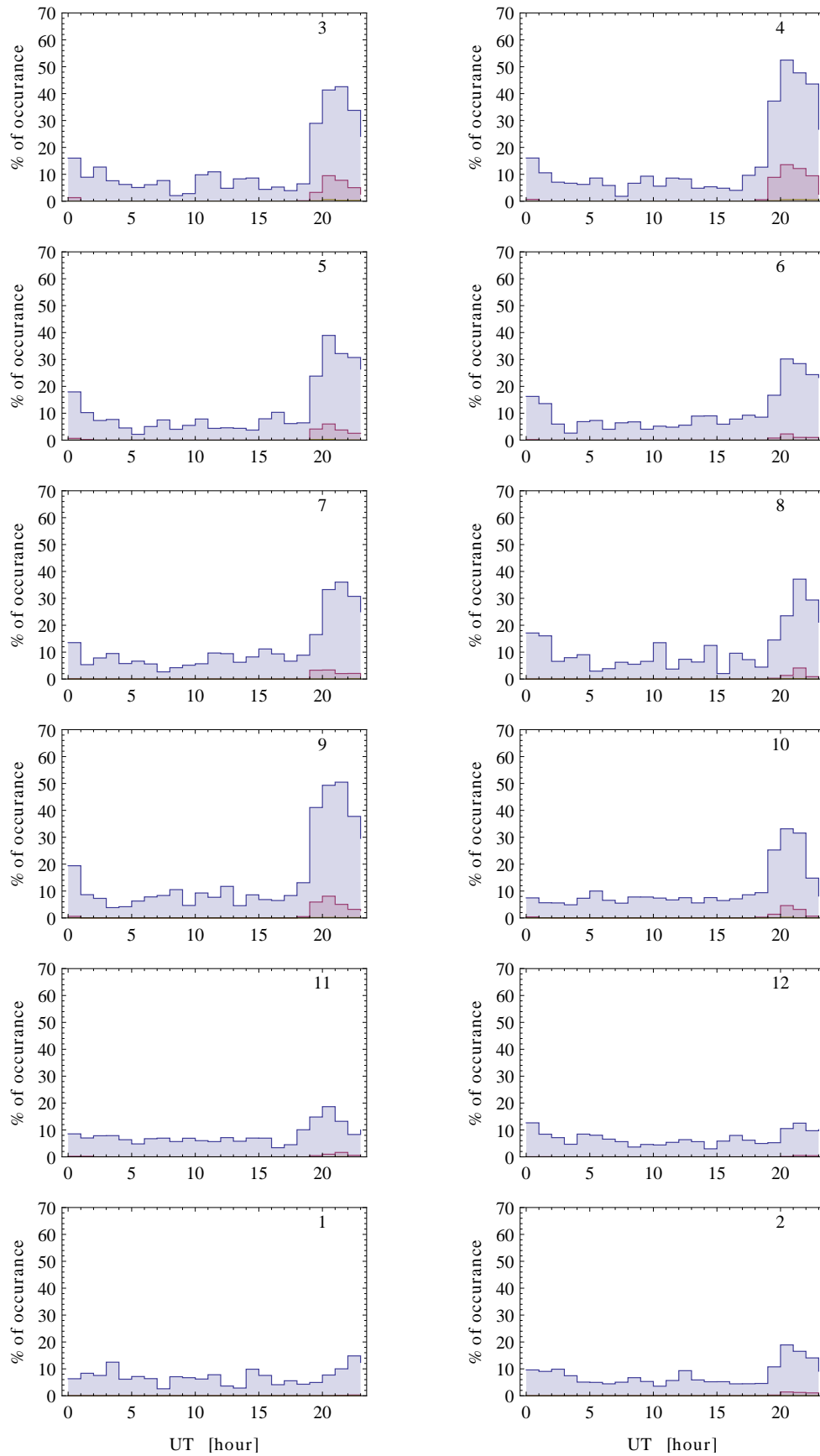


Figure 5.7: Percentage of occurrence of S_4 for all three thresholds presented with different colors (light blue \rightarrow I, red \rightarrow II and brown \rightarrow III) throughout the whole day. For description of details in the figure, please see text.

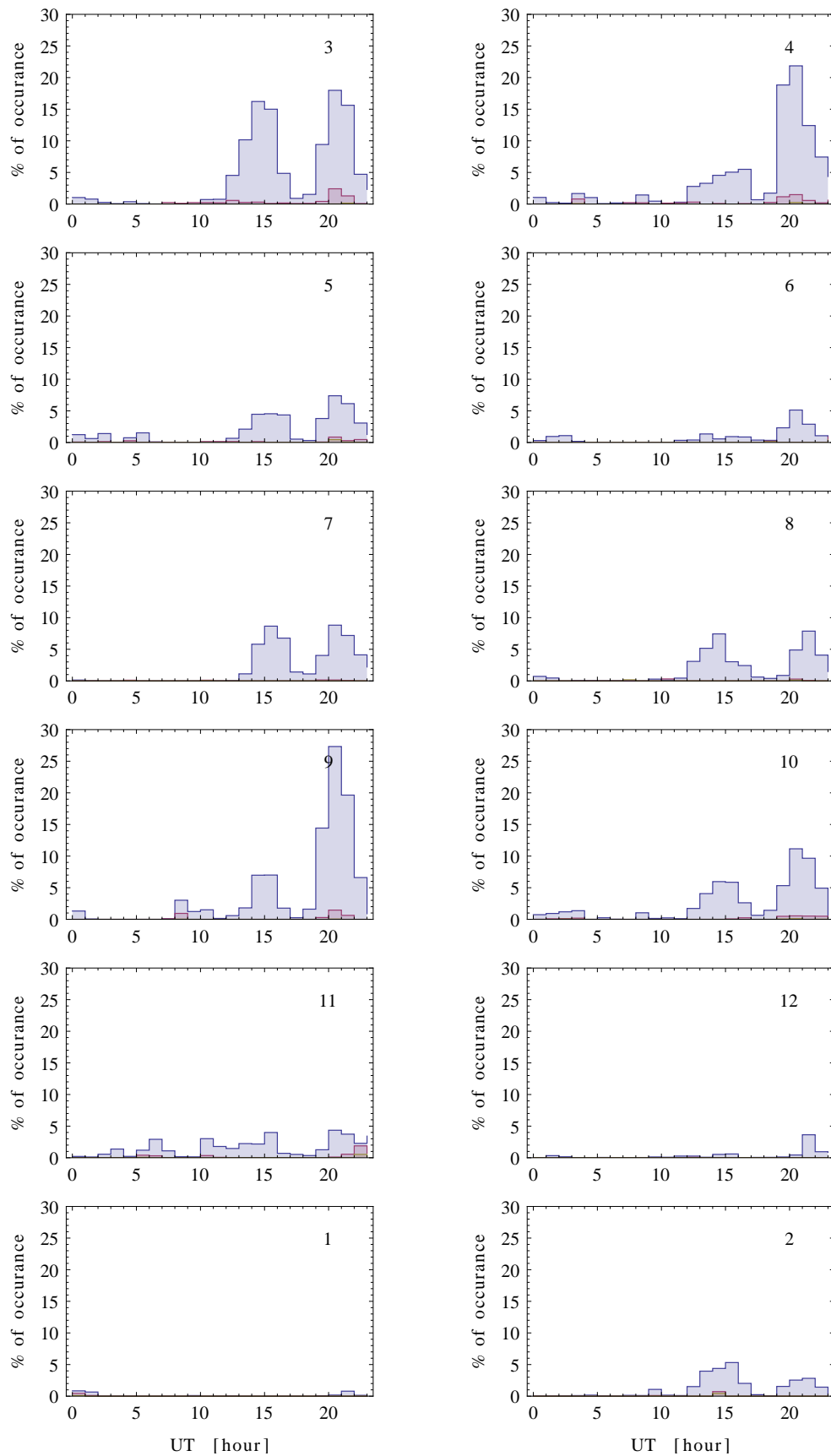


Figure 5.8: Percentage of occurrence of σ_ϕ for all three thresholds presented with different colors (light blue \mapsto I, red \mapsto II and brown \mapsto III) throughout the whole day. For description of details in the figure, please see text.

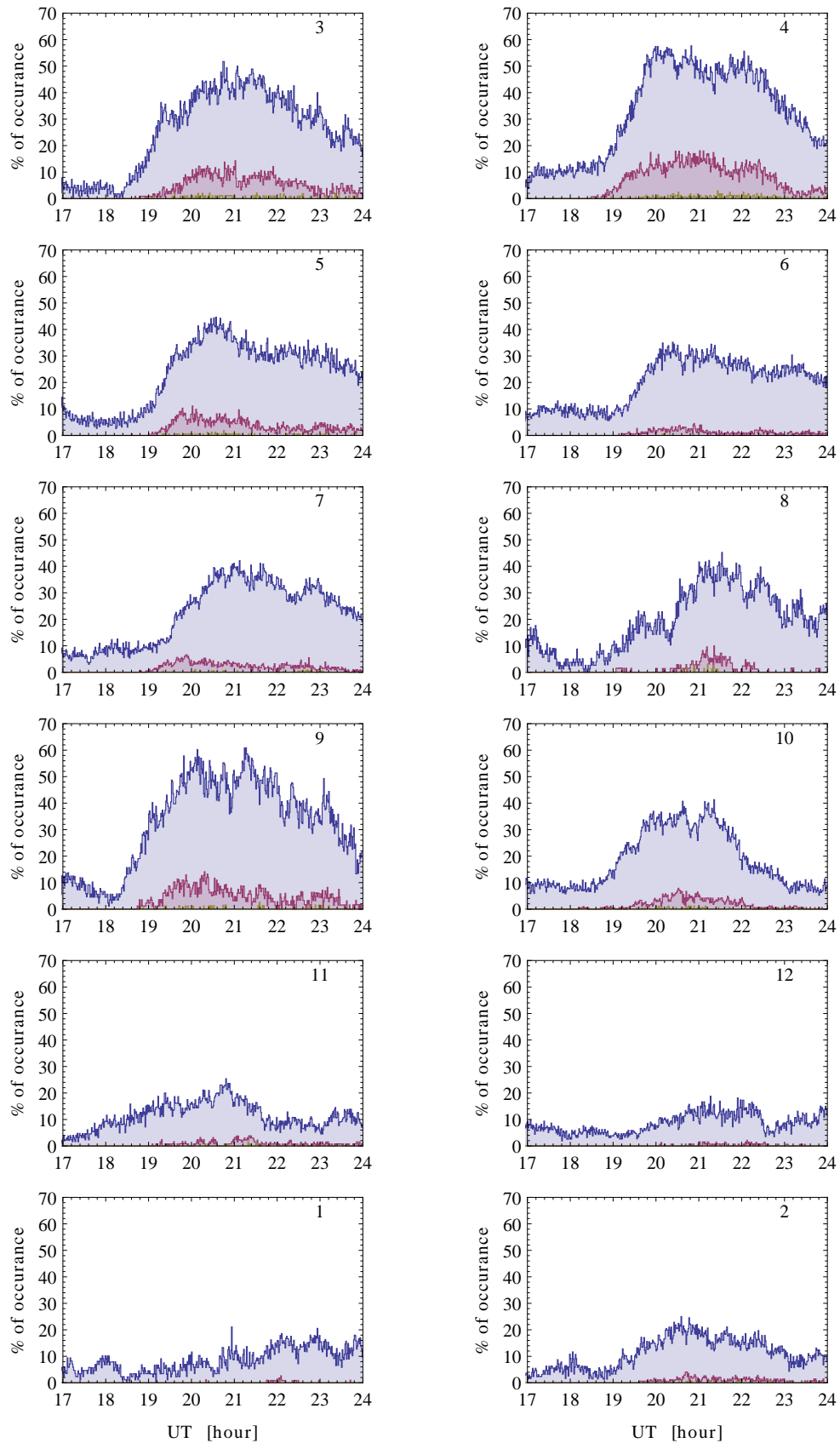


Figure 5.9: Percentage of occurrence of S_4 for all three thresholds presented with different colors (light blue \rightarrow I, red \rightarrow II and brown \rightarrow III) between 17:00 and 00:00 UT hours. For description of details in the figure, please see text.

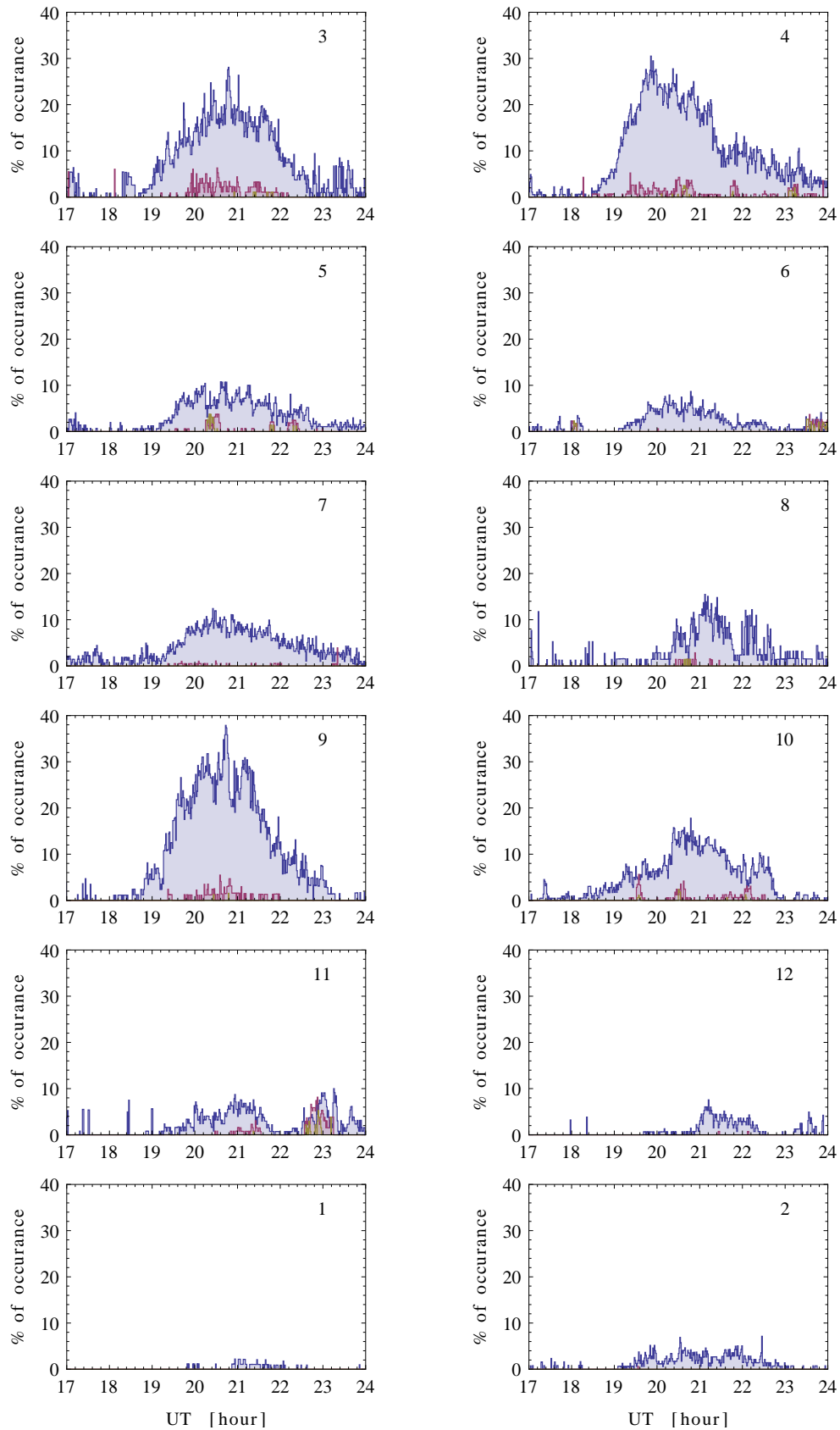


Figure 5.10: Percentage of occurrence of σ_ϕ for all three thresholds presented with different colors (light blue \mapsto I, red \mapsto II and brown \mapsto III) between 17:00 and 00:00 UT hours. For description of details in the figure, please see text.

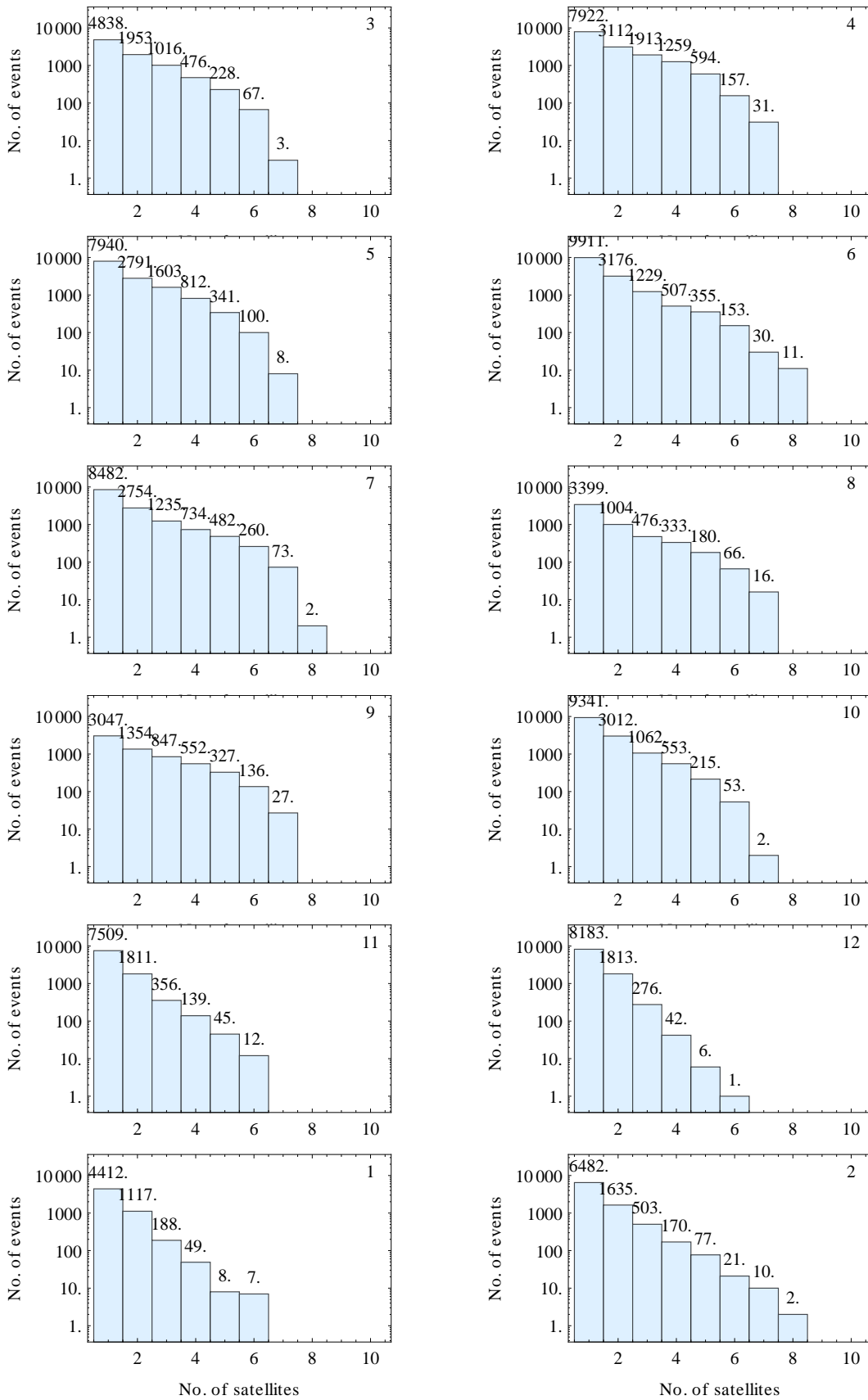


Figure 5.11: Histograms presenting the number of satellites observing S_4 for threshold I within one month for more than one minute. Each month is denoted with number (i.e. 3 \mapsto March 2004, 4 \mapsto April 2004, 5 \mapsto May 2004, 6 \mapsto June 2004, 7 \mapsto July 2004, 8 \mapsto August 2004, 9 \mapsto September 2004, 10 \mapsto October 2004, 11 \mapsto November 2004, 12 \mapsto December 2004, 1 \mapsto January 2005 and 2 \mapsto February 2005).

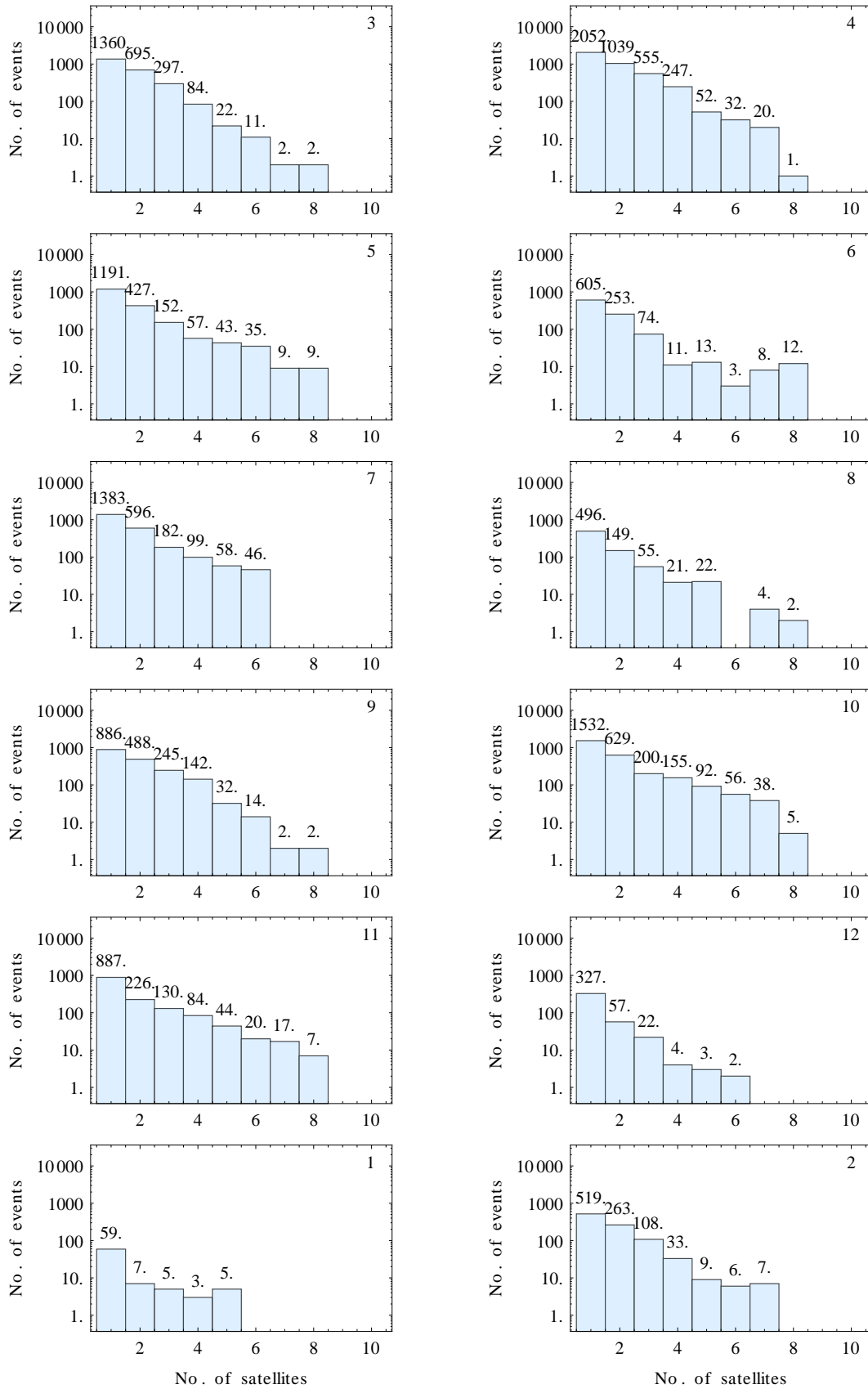


Figure 5.12: Histograms presenting the number of satellites observing σ_ϕ for threshold I within one month for more than one minute. Each month is denoted with number (i.e. 3 \mapsto March 2004, 4 \mapsto April 2004, 5 \mapsto May 2004, 6 \mapsto June 2004, 7 \mapsto July 2004, 8 \mapsto August 2004, 9 \mapsto September 2004, 10 \mapsto October 2004, 11 \mapsto November 2004, 12 \mapsto December 2004, 1 \mapsto January 2005 and 2 \mapsto February 2005).

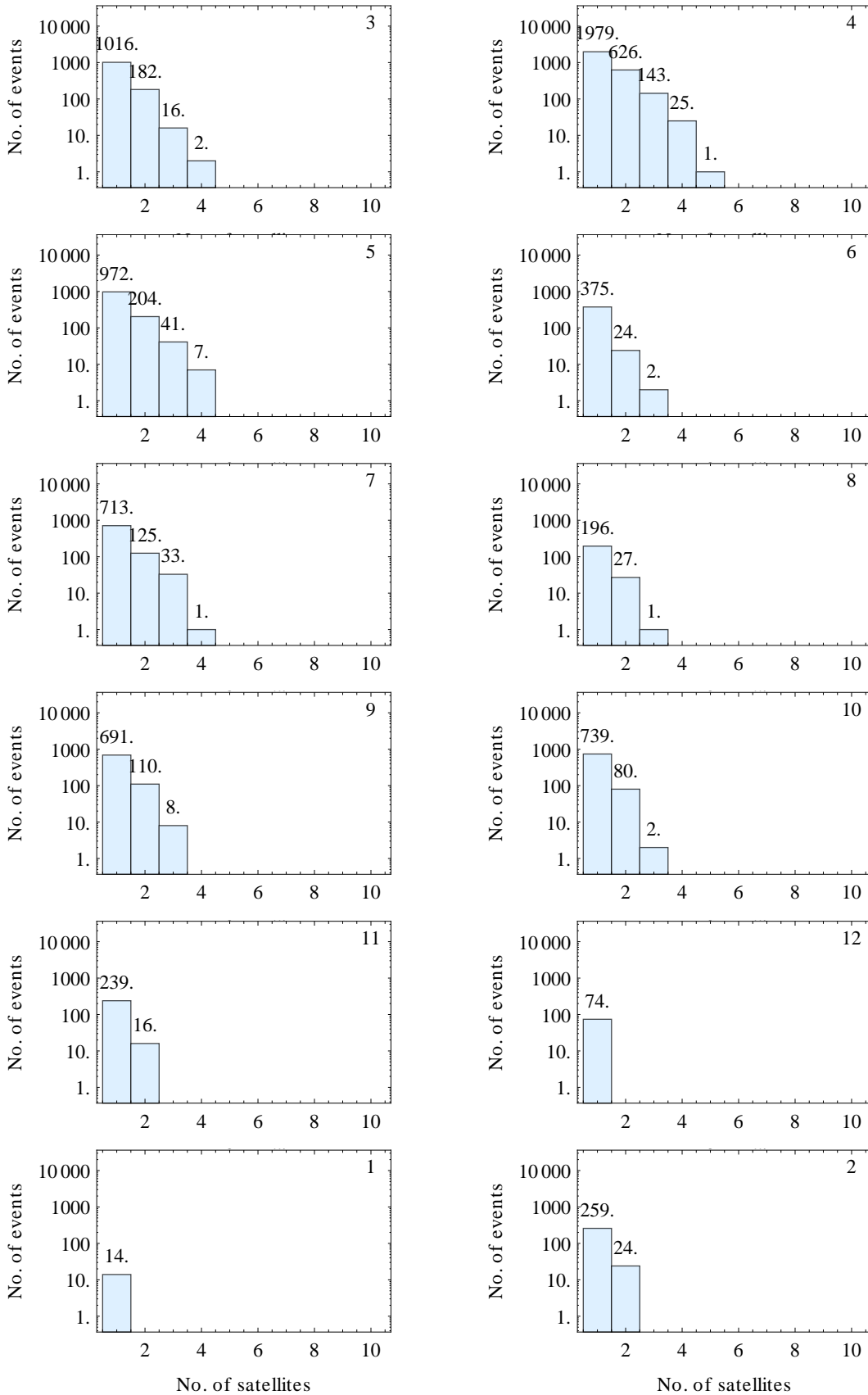


Figure 5.13: Histograms presenting the number of satellites observing S_4 for threshold II within one month for more than one minute. Each month is denoted with number (i.e. 3 \mapsto March 2004, 4 \mapsto April 2004, 5 \mapsto May 2004, 6 \mapsto June 2004, 7 \mapsto July 2004, 8 \mapsto August 2004, 9 \mapsto September 2004, 10 \mapsto October 2004, 11 \mapsto November 2004, 12 \mapsto December 2004, 1 \mapsto January 2005 and 2 \mapsto February 2005).

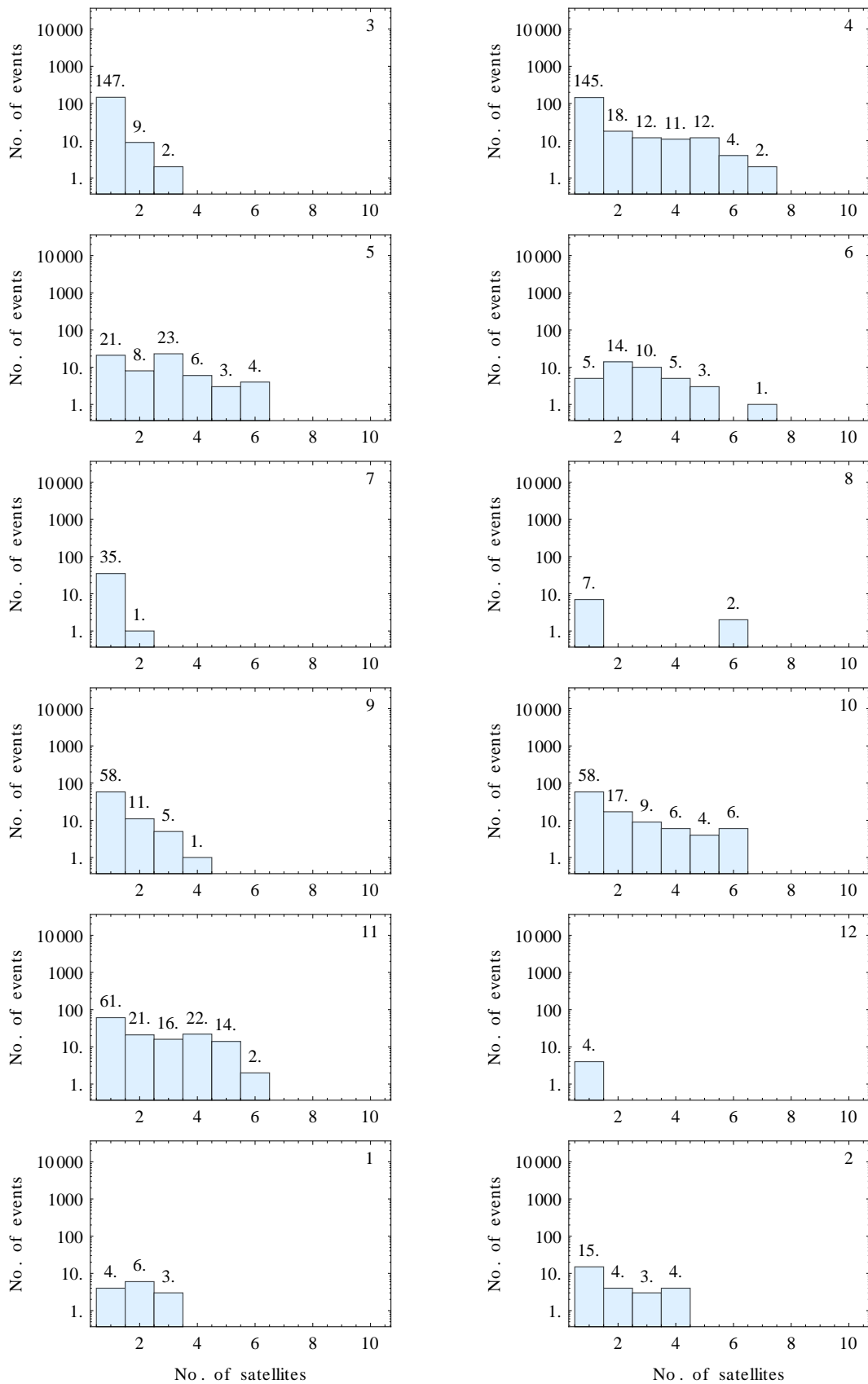


Figure 5.14: Histograms presenting the number of satellites observing σ_ϕ for threshold II within one month for more than one minute. Each month is denoted with number (i.e. 3 \mapsto March 2004, 4 \mapsto April 2004, 5 \mapsto May 2004, 6 \mapsto June 2004, 7 \mapsto July 2004, 8 \mapsto August 2004, 9 \mapsto September 2004, 10 \mapsto October 2004, 11 \mapsto November 2004, 12 \mapsto December 2004, 1 \mapsto January 2005 and 2 \mapsto February 2005).

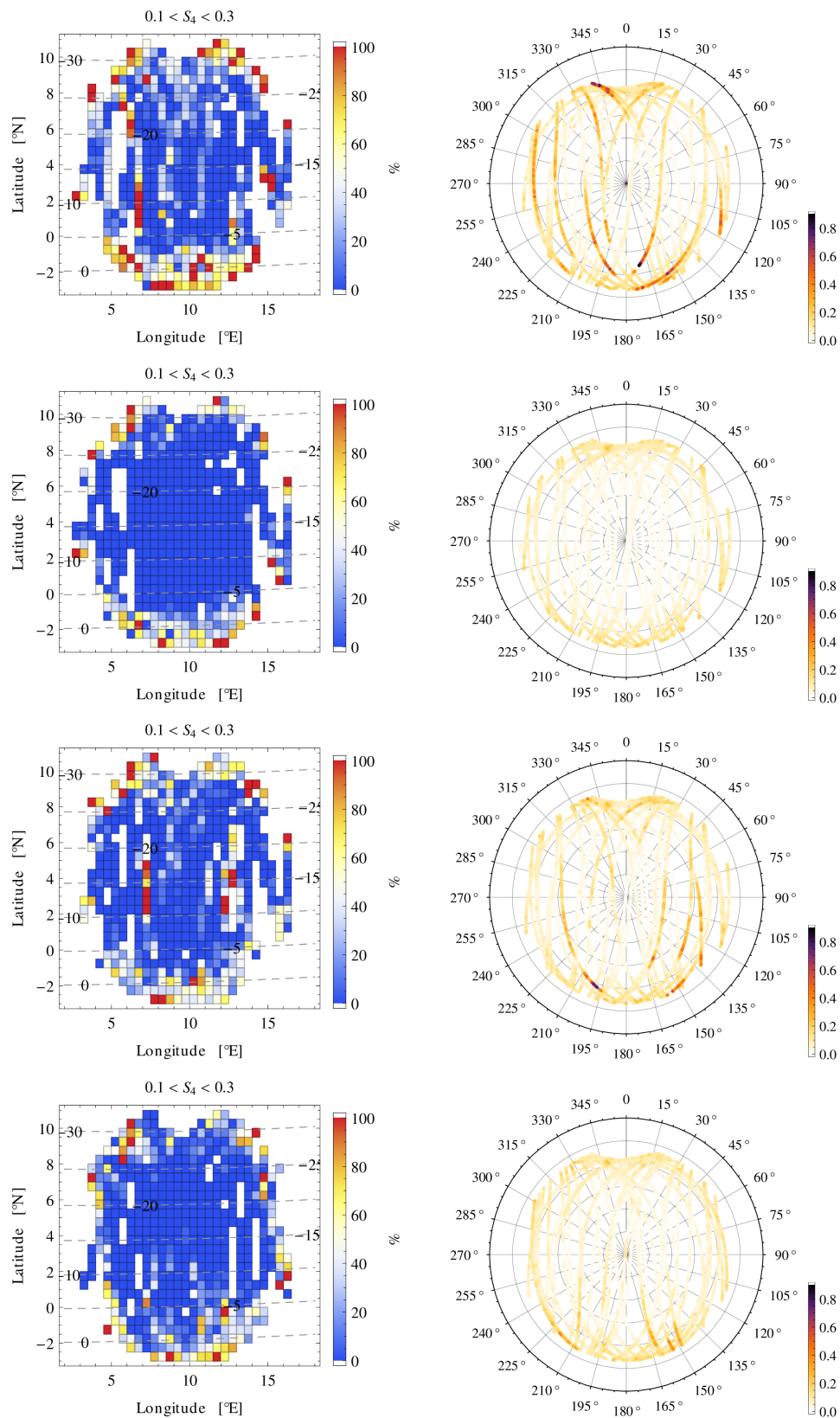


Figure 5.15: Left column – geographical distribution of the percentage of occurrence of S_4 on (from top to bottom) 4 April 2004, 15 June 2004, 29 September 2004 and 19 December 2004 for threshold I. Right column – corresponding sky-plots presenting S_4 for all satellites in view over Douala, Cameroon.

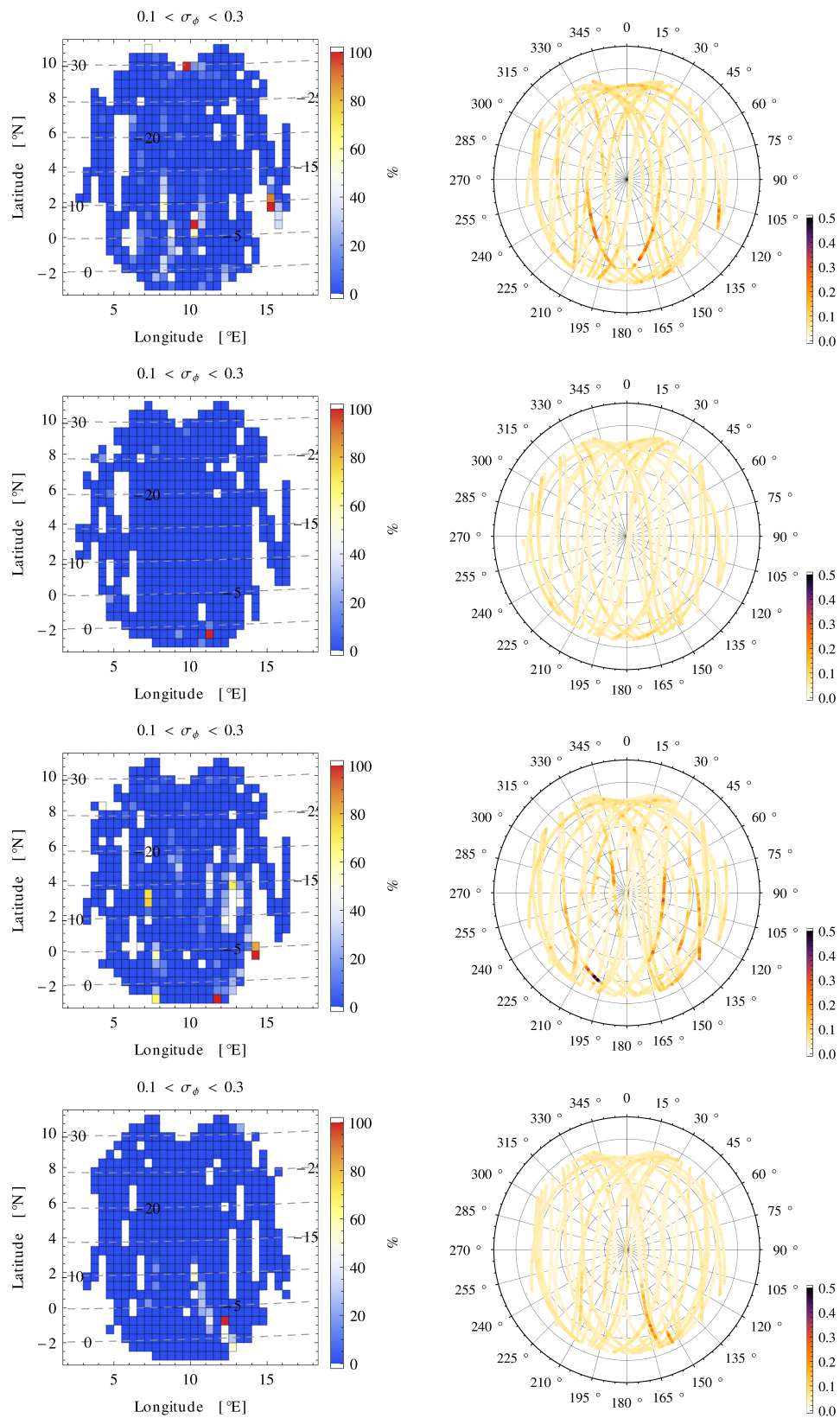


Figure 5.16: Left column – geographical distribution of the percentage of occurrence of σ_ϕ on (from top to bottom) 4 April 2004, 15 June 2004, 29 September 2004 and 19 December 2004 for threshold I. Right column – corresponding sky-plots presenting σ_ϕ for all satellites in view over Douala, Cameroon.

The use of GPS in the Pierre Auger Observatory

Contents

6.1 Introduction	117
6.1.1 The Pierre Auger Observatory	118
6.2 Topography of the SD array	119
6.2.1 Difference to the digital elevation map	120
6.2.2 Array test with different GPS position acquisition mode	122
6.2.2.1 Positions and periodicity	125
6.2.2.2 Origin of fluctuations	128
6.2.2.3 Position spread	129
6.2.2.4 Error of the mean position	130
6.2.2.5 Systematics	133
6.2.2.6 Comparison with survey database	134
6.2.3 Positions of SD Stations: Dilution of Precision Corrections	137
6.2.3.1 Weighted means	141
6.3 Conclusions	143

6.1 Introduction

Besides numerous GPS applications in atmospheric science (which were presented in previous chapters), GPS also plays important role in other fields. One of those is precise-timing of cosmic ray arrivals at the surface detectors (SD) in Pierre Auger Observatory. Unfortunately, in the Pierre Auger Observatory they use GPS only for timing of cosmic ray arrivals, but for the positions of each surface detector station they rely on geodetic surveys. The motivation behind this was to reduce time jitter from nominal >10 ns in navigate mode to <10 ns in position-hold mode. As a result bad quality surveying translated into large absolute offsets between the SD station timing. In this study we wanted to mitigate this situation by revisiting and correcting the station positions through several different methods described below.

Results presented and discussed in this chapter, were published in internal notes of the Pierre Auger Collaboration [151–153] and will be published in technical articles related to the reconstruction of events from the surface detector.

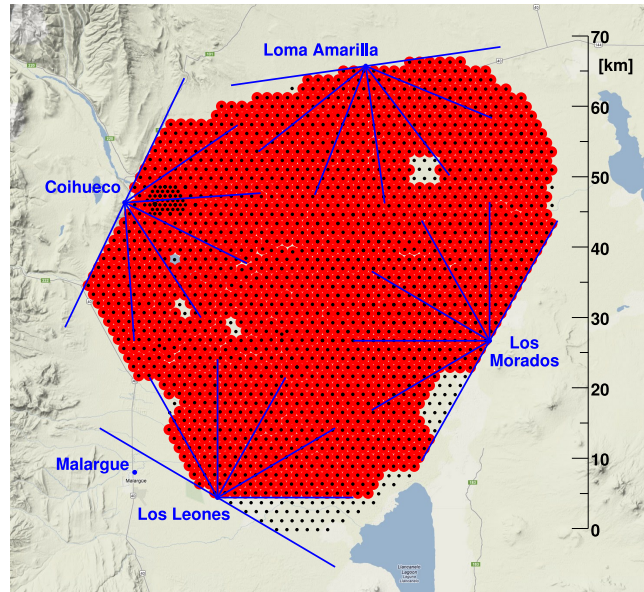


Figure 6.1: Location and structure of the Pierre Auger Observatory. Black dots show all theoretical positions of surface detector stations where the active ones (in the year 2012) are indicated with red circles, blue lines indicate the field of view of the fluorescence telescopes, located in four buildings on the perimeter of the surface detector (names marked in blue color).

6.1.1 The Pierre Auger Observatory

The Pierre Auger Observatory is the largest operating cosmic ray observatory ever built, located in “Pampa Amarilla” site ($35.1^\circ - 35.5^\circ$ S, $69.0^\circ - 69.9^\circ$, and 1300–1600 m above sea level), close to Malargue, Province of Mendoza, Argentina (Fig. 6.1) [154]. It has been built for measuring flux, arrival direction distribution and mass composition of cosmic rays from 10^{18} eV to very highest energies with high statistical significance. Most of cosmic ray particles interact with atoms in the upper atmosphere in a process known as an *extensive air shower*, where the energy of the cosmic ray goes into the production of other particles such as pions and kaons [155], which quickly decay to muons and electrons, producing a shower of “secondary cosmic rays”, reaching the surface of the Earth where they can be detected using detectors such as for instance Pierre Auger Observatory [155]. The development of the Observatory started in 1992, with a series of workshops, and construction was completed in the end of 2008, while data collection started already on a growing detector array at the beginning of 2004. The structure of the detector is shown in Fig. 6.1, where one can see that it consists of 1660 surface stations – water Cherenkov tanks and their associated electronics – arranged on a triangular grid, with the sides of the triangles being 1.5 km, and the grid covering an area of 3000 km^2 . The array of Cherenkov tanks is known as the surface detector (SD), while the optical forms the fluorescence detector (FD) which contains six telescopes designed to detect air-fluorescence light [154, 156, 157].

Reconstruction of primary cosmic ray properties from measured extensive air showers requires accurate relative timing, therefore both detectors (SD and FD) include circuitry for accurate time-tagging of signals detected by PMTs (see Table B.2 for specification of PMTs–

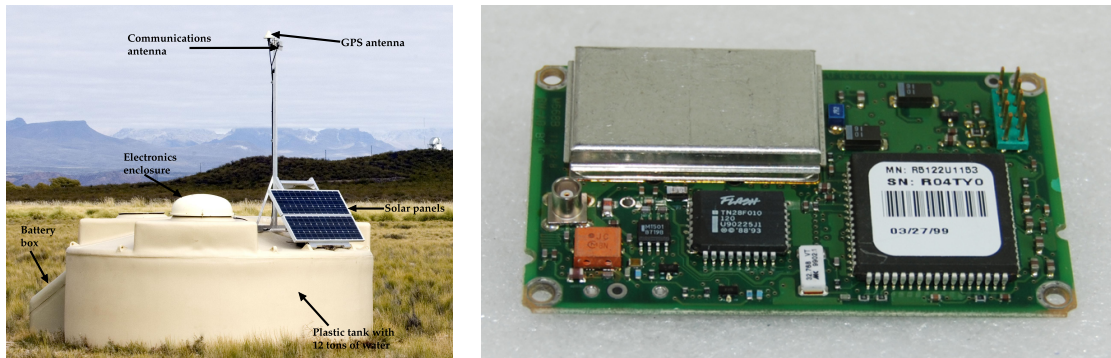


Figure 6.2: The Pierre Auger Observatory surface detector, with marked components (left), motherboard of GPS receiver Oncore UT+ (right).

denoted as PMT1 and PMT2). This circuitry is based from a commercial GPS receiver (Motorola Oncore UT+), which is mounted as a daughter-board to each system [157]. In both SD and FD stations, individual triggers are time-tagged using the 1 pulse-per-second (1 PPS) output of the GPS clock together with a serial readout correction term that allows for precision determination of the offset relative to the true GPS second for each pulse out [156]. On the left side in Fig. 6.2 the water-Cherenkov detector with marked major components is presented, while on the right side motherboard of GPS receiver is shown. The SD is self-contained, where the needed power for PMTs and the electronics is provided by a solar power system (providing 10 W of power on average). The electronics package consists of a processor, GPS receiver, radio transceiver and power controller [154]. Each Cherenkov detector is a rotationally moulded polyethylene tank, with 3.6 m in diameter and 1.55 m in high, filled with 12 tons of high purity water [154, 157]. More complete description of the Pierre Auger Observatory can be found in [154].

The Motorola UT+ Oncore GPS receiver is a L1 frequency C/A code receiver which has an eight parallel channel design capable of tracking eight satellites simultaneously [158] and is designed specifically for precise timing applications. Some technical characteristics of the GPS receiver are provided in Table B.3. Due to the fact that SD requires online timing accuracy of $< 1 \mu\text{s}$ for triggering an event, the GPS units on tanks are fixed to position-hold mode, in which the output accuracy of 1 PPS is 50 ns [158]. The position of the antenna in this mode must be determined by a site survey or by averaging GPS position fixes. To latch the time of an event as well as the time of each 1 PPS, the SD uses a 100 MHz clock (< 10 ppm precision) [156, 157]. The SD electronics continually calibrates the clock to $1 \mu\text{s}$ over the full second range by measuring the true frequency and correcting the tagged event times that are transmitted for triggering. In addition, it records the 40 MHz system clock, and the GPS corrections necessary for later reconstruction [156].

6.2 Topography of the SD array

Besides the accurate relative timing of triggered air showers in SD stations also other details such as location, orientation in space, tilt, roughness and topography of the terrain are important properties that enter many data analysis efforts done within the Auger collaboration. For example, in the analysis of the sky coverage for large energies [159] the geographical lat-

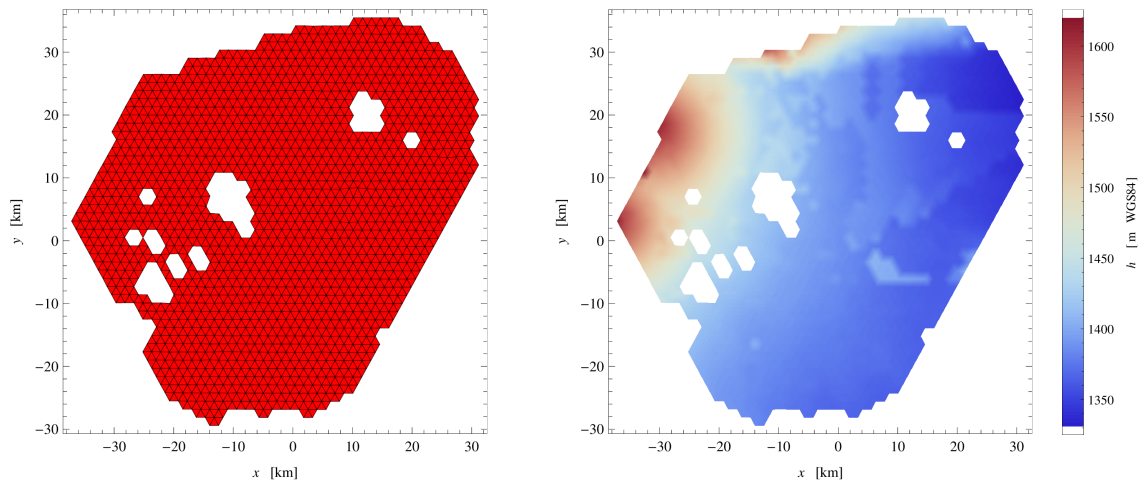


Figure 6.3: 2D layout of the SD unit triangles in array–local Cartesian coordinates (left) and color–coded WGS84 altitude (height above the ellipsoid) of the SD stations in UTM easting/northing coordinates (right).

itude of the detector is used in the calculation of the observatory’s relative exposure and its dependence on. In the same calculation the zenith–angle acceptance, $\cos \theta$, indirectly uses the notion of the local vertical. The same assumption is made in the expression [160] for an effective area of the detector (i.e. its differential area term). It was therefore instructional to look into the topographic details of the SD array in order to search for any signs of systematical errors. The performed analysis was concentrated in the properties of unit triangles that compose the SD array and the height (altitude, above sea level) of the SD stations.

In Fig. 6.3 (left) the SD unit triangles are shown in 2D projection (ignoring the z component) of the array–local Cartesian coordinate system. The SD station positions and their neighborhood association is taken from the *Auger Station List Manager* configuration as of January 2009. Fig. 6.3 does not show any irregularities in the nearest–neighbor associations and the triangles seems to follow the designed layout of the equilateral triangular grid. On the right in Fig. 6.3, the WGS84 altitude (height above the ellipsoid) is given in color coding where the x and y coordinates are in UTM easting and northing, respectively. One can see the Andes ridge building up in the western and north–western direction. While the color looks fairly smooth, some local structure can be observed, at least in the blue region of the array. However, looking only at the absolute values of the station heights it is hard to say whether the structure is caused by stations following the local terrain or due to some systematical effects in station position measurements.

6.2.1 Difference to the digital elevation map

To find out whether the structures observed in altitude map in Fig. 6.3 (right) are errors in altitude or just regular topographical features, the comparison was performed with the digital elevation models from the Shuttle Radar Topography Mission (SRTM). The topographic maps were recorded by flying a specially modified interferometric radar system on–board the Space Shuttle Endeavor during an 11–day STS–99 mission in February 2000. The horizontal resolution of the available maps is 90 m and for the purpose of the analysis the SRTM–

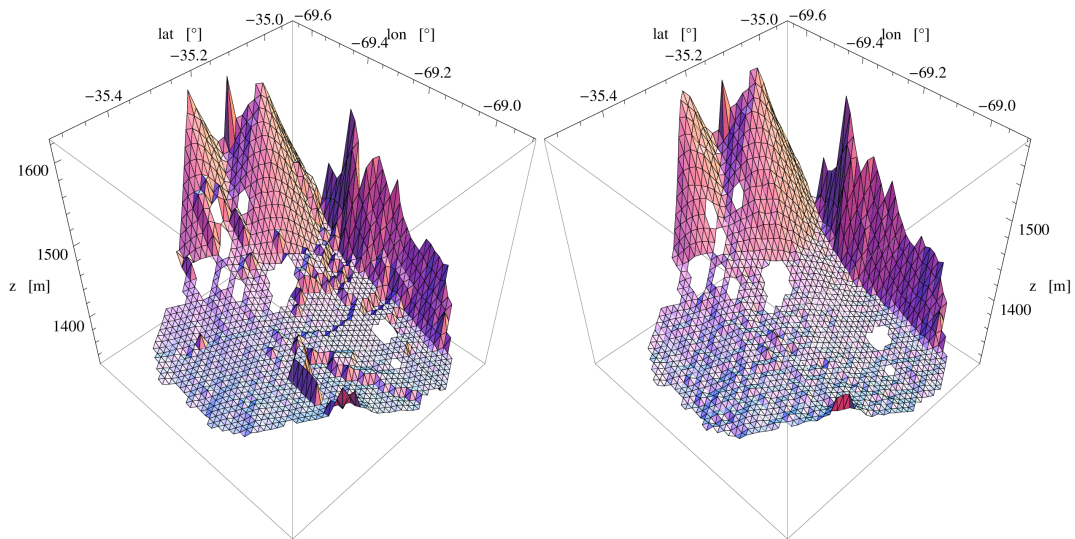


Figure 6.4: 3D layout of the SD unit triangles from the Auger database (left) and the corresponding elevations from the digital elevation model [161] (right) in geographic coordinates.

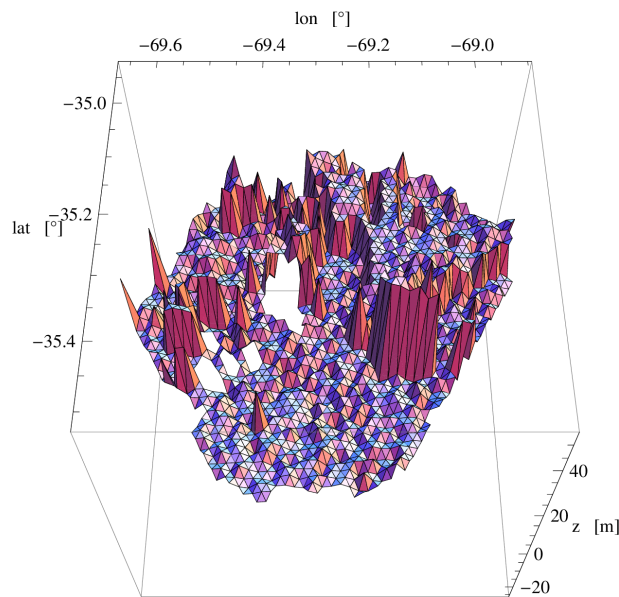


Figure 6.5: The 3D difference between the station elevations from the Auger database and the digital elevation model.

23–19 and SRTM–23–20 map quadrants covering much more than just the Auger site were used. When a specific elevation was needed in some geographic location, the neighbouring map points were used in a simple interpolation scheme. In Fig. 6.4 two plots are shown: on the left the 3D layout of the station positions and unit triangles are given according to the elevation entries in the Auger database; on the right the (interpolated) elevation obtained from the digital elevation models, evaluated in the horizontal position of the stations, is shown. The striking difference in smoothness of the two maps is immediately obvious. It is almost

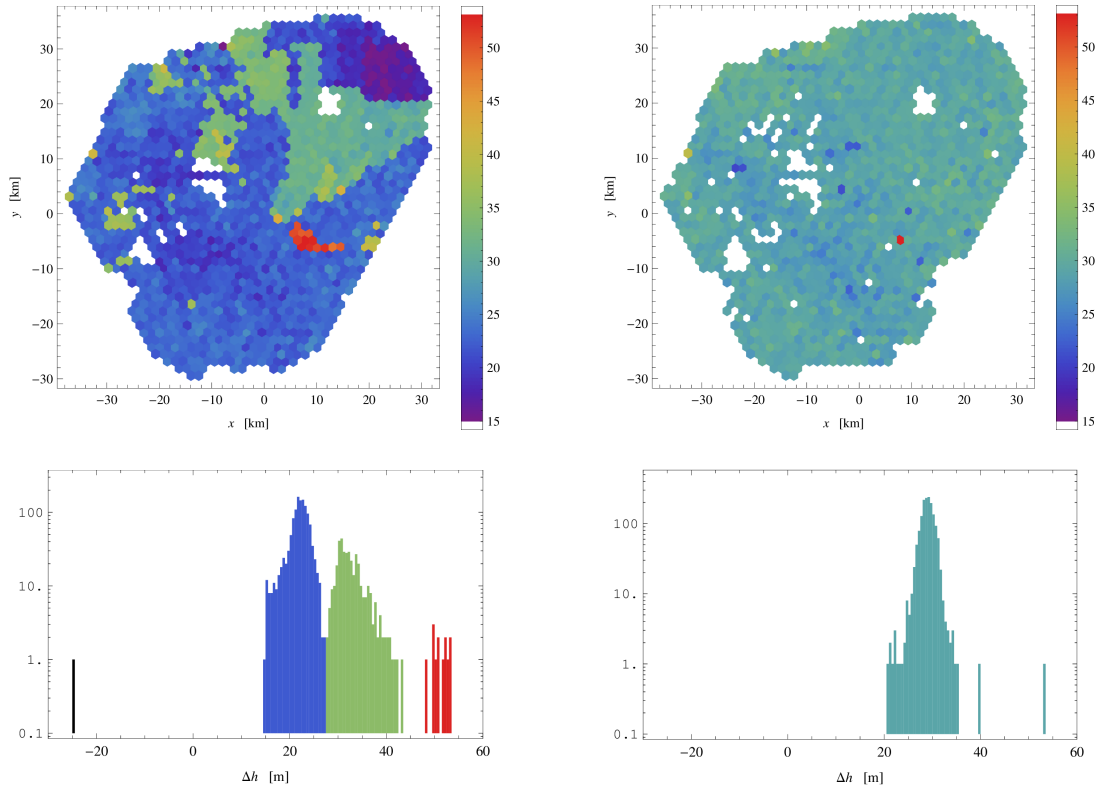


Figure 6.6: The difference between the station elevations and the digital model map in color code (top) and the corresponding histogram (bottom), in the Auger database (left) and after the GPS measurement campaign (right). In the right plot the stations with GPS receivers still running in position hold mode are removed, i.e. resulting in more holes than in the left plot, see Section 6.2.2.

impossible that the ridge structure that runs over the middle of the array is a result of the local terrain features. The difference between the two maps in 3D view is shown in Fig. 6.5, while in Fig. 6.6, difference is shown with a color-coded 2D plot. It seems that while more than half of the array agrees with the digital elevation map, there is a large class of stations that seem to have constant offset from the terrain. Three distinct groups of stations are evident. The majority of stations (shades of blue) are about 20 m above the digital elevation model. This constant offset difference can probably be simply explained by the fact that the SRTM mission is using a different ellipsoid or sea level reference. There is another quite large sample of stations where the difference is reaching up to ~ 40 m (green shades). The third group of ~ 13 stations, presented in orange–red shadows, has the difference around ~ 50 m.

6.2.2 Array test with different GPS position acquisition mode

Because the left side of Fig. 6.6 gives solid evidence that the positions of the stations had to be revisited, therefore array test was made in February 2009 for a short time (around one day) where the GPS units were set in navigate mode. In this way the positions were calculated using at least four (or more) locked satellites at the same time, but with the consequence of a slightly degraded timing accuracy. The position data gathered during this test were then

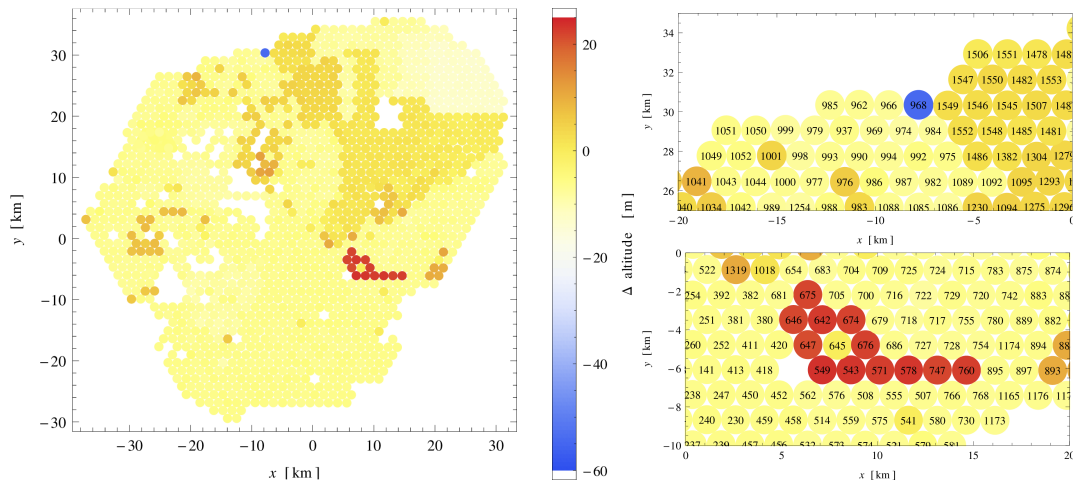


Figure 6.7: The difference between the elevation values from database and the navigate mode run, this time with a lighter color coding (left). x and y values are the 2D coordinates of the PampaAmarilla coordinate system. A larger view of the two interesting parts of the array, including the station ID numbers (right): close to Loma Amarilla (top) and close to Los Morados (bottom).

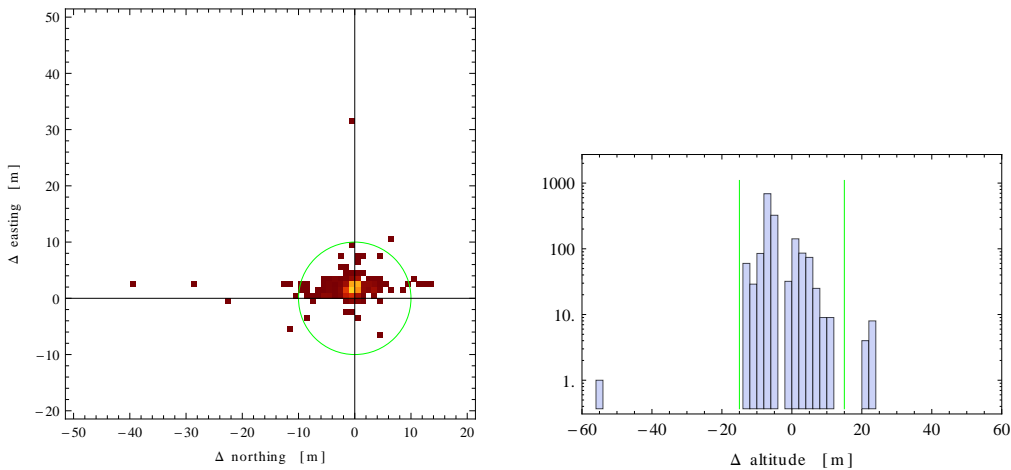


Figure 6.8: 2D (horizontal) differences between the database entries and the navigate mode run. The green circle denotes a radius of 10 m (left). The same for elevation difference with green-indicated bounds of ± 15 m outside (right).

compared to those in the database. On the right side of the Fig. 6.6 the same information is shown as on the left side, but this time with the elevation data obtained from the run in position navigate mode. The difference map appears much more uniform and is centered around ~ 30 m above the digital elevation model. The outliers at 40 m and 53 m are stations which could not be persuaded to reboot and change their position acquisition mode. The right side of the Fig. 6.6 gives solid evidence that the positions of the stations in the database have to be revisited. Nevertheless, solely from the comparison to the digital elevation model it is not clear what the absolute position are exactly.

In Fig. 6.7 (left) the difference between the database elevation and the navigation mode

137

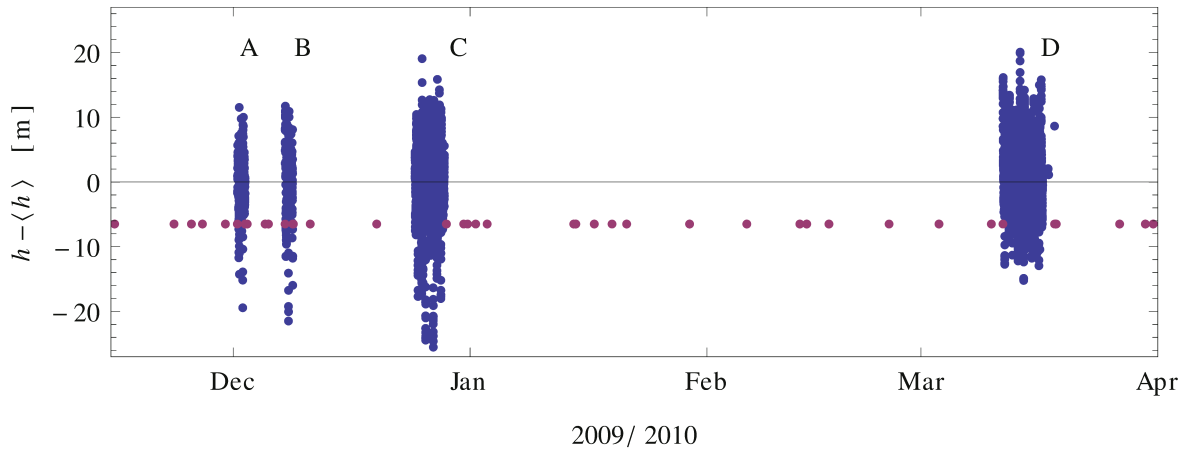


Figure 6.9: Navigate mode measurement campaigns A, B and C in December 2009, and D in March 2010 as extracted from the Motorola UT+ log files. Blue points show the fluctuations of height h around the mean $\langle h \rangle$ for station with ID 137. Red points correspond to the Central Data Acquisition System (CDAS) initialization values taken from the survey database and sent to the station during the regular operation in the position–hold mode.

run is shown. It is clear that the rough structure from the digital elevation model plots is repeated also here. The largest deviations are coming from a single station with ID 968 close to the Loma Amarilla FD site and a larger group of stations in front of the Los Morados FD site (see right panels in Fig. 6.7). Apart from these excessive deviations is also a large plateau of orange–brown stations of irregular shape that stretches between the Loma Amarilla and the Los Morados sites in the north–eastern part of the array. On the left in Fig. 6.8 a histogram of the horizontal (2D) deviations is shown where the x and y coordinates are given in the PampaAmarilla¹ coordinate system. Most of the horizontal deviations are within the 10 m radius (green circle) while there are some outliers with differences of up to 40 m. In Fig. 6.8 (right) a histogram of the elevations is given for the same two data sets (positions from database and position obtained with navigation mode). Again, most of the database station entries lie within the ± 15 m of the navigation mode measurement but there is one with a relative elevation of -60 m and several with differences of up to 24 m. Performed analysis showed discrepancies, from which we concluded that some of the station positions in the survey database should be updated with renewed surveying information. However, because this analysis was made on only one measurement campaign, the decision was made that more campaigns should be performed. Therefore additional navigation mode campaigns were performed in December 2009 and March 2010. Fig. 6.9 illustrates the extend of the measurements by showing the obtained height of the station with ID 137 (blue points). Three campaigns (A, B: 2 days and C: 4 days) can be seen in December 2009 and a longer run in March 2010 (D: 6 days). The positions sent by Central Data Acquisition System (CDAS) during the regular operation in the position–hold mode can also be seen (red points). All other stations show similar behavior during this time period.

¹which is a Cartesian coordinate system with an origin in the middle of the SD array and z-axis as local vertical in this point

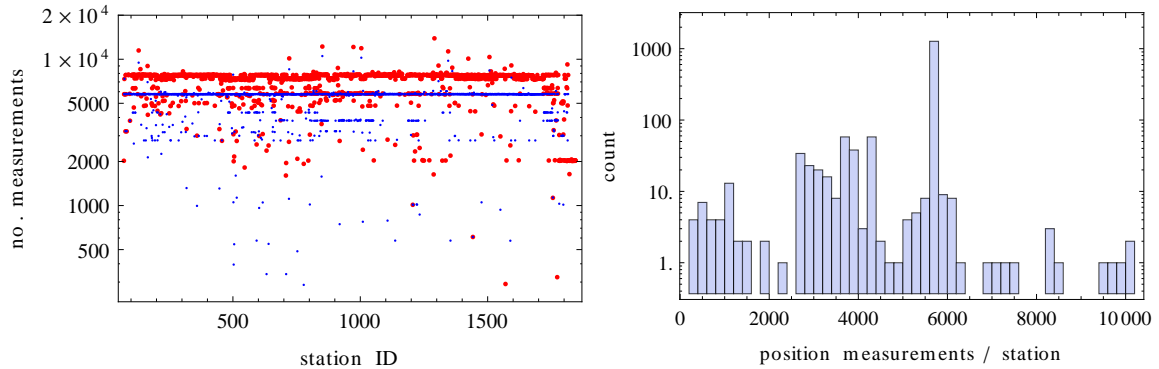


Figure 6.10: Distribution of total number of position measurements per station for all campaigns A–D (left). Total number of position measurements by station ID (right).

In Fig. 6.10 a total number of position measurements by station ID and a distribution of number of position measurements is shown for all the campaigns A–D. In this time period most of the stations delivered from 5700 to 5775 position measurements. In Fig. 6.11 distributions of time differences between consecutive GPS position measurements, as found in the receiver log files, is presented for several randomly chosen stations. From the peaks it is clear that most of the time, stations were polled in intervals of 150 or 300 s (2.5 or 5 min) and that the small remainder of the time differences is fairly evenly distributed between 0 and 400 s (6.7 min).

6.2.2.1 Positions and periodicity

With $\langle n \rangle$, $\langle e \rangle$, and $\langle h \rangle$ we denote the mean northing, easting, and height of the station, respectively, and this means are taken over all four measurement campaigns A–D. In Fig. 6.12 fluctuations of the height around its mean, $h - \langle h \rangle$, are shown for a sample of 15 randomly selected stations in the measurement campaign C (24 to 29 December 2009). Similar plots could be presented also for northing and easting, but they are not much different in type, maybe with a slightly smaller absolute variation window of only ± 10 m. What we notice immediately is that the ripple patterns follow the same time structure in all of the stations. Therefore, the variations in position reconstructions are governed by collective fluctuations of the whole GPS acquisition system and not by some effect occurring locally in a GPS unit. This is even more clearly seen from Fig. 6.13 where all stations are plotted in the same graph with different colors. It seems that also the small details of the fluctuations are common to all stations with only small deviations between them. Furthermore, the common pattern seems to be repeating itself also on a daily basis, as can be seen in Fig. 6.14. In Fig. 6.15 the same data is plotted in the easting–northing plane, revealing that the values away from the mean values are repeating almost along the same paths every day. This behaviour is connected to GPS satellite constellation geometry.

GPS satellites are placed in the medium Earth orbits at an altitude of approximately 20 200 km which was chosen so that the satellites make *two* complete rounds during *one* sidereal day. Currently there are 31 satellites in operation [162] placed into 6 orbits [163] which are fixed in the celestial frame and tilted with 55° inclination relative to the Earth's equator. Originally, the design envisaged 4 satellites per orbit but with latter additions some

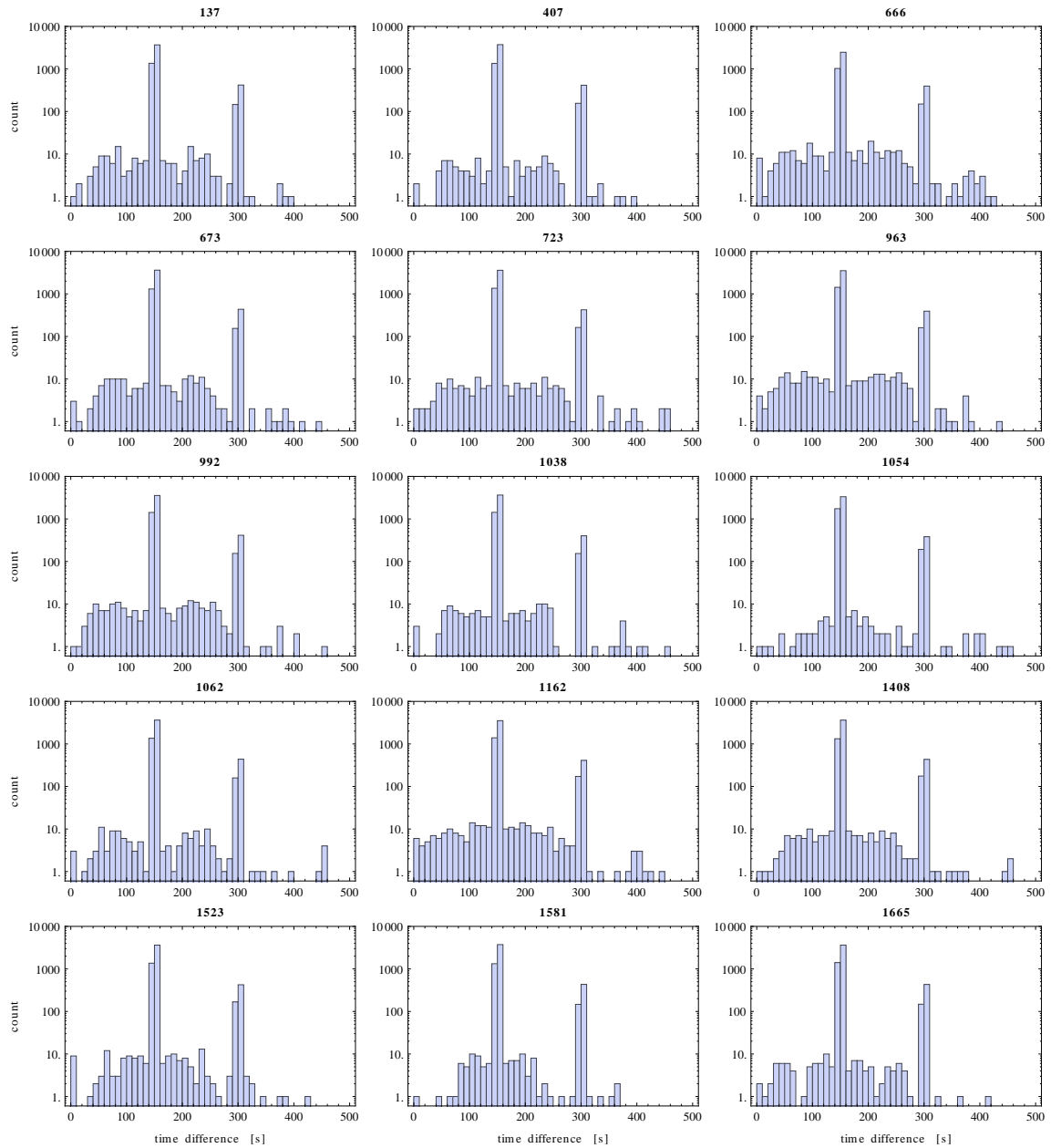


Figure 6.11: Distribution of time differences between consecutive GPS position measurements for all campaigns A–D for several randomly selected stations.

of the orbits are populated more densely. In this geometry the pattern of the satellite positions on the sky is only slowly changing and the changing is due to the difference between the Earth and sidereal day ($\sim 1^\circ/\text{day}$ or $4\text{ min}/\text{day}$). In consecutive days we can thus expect fairly similar appearance of the particular satellite twice a day (e.g. see Fig. 6.16 where an example is given for the positions of GPS satellites above Nova Gorica). For low and medium latitudes, the transition time of the satellites on the sky can be small when they only barely peek above the horizon or can be as large as almost a half of the orbiting time (6 h) but is typically only several hours.

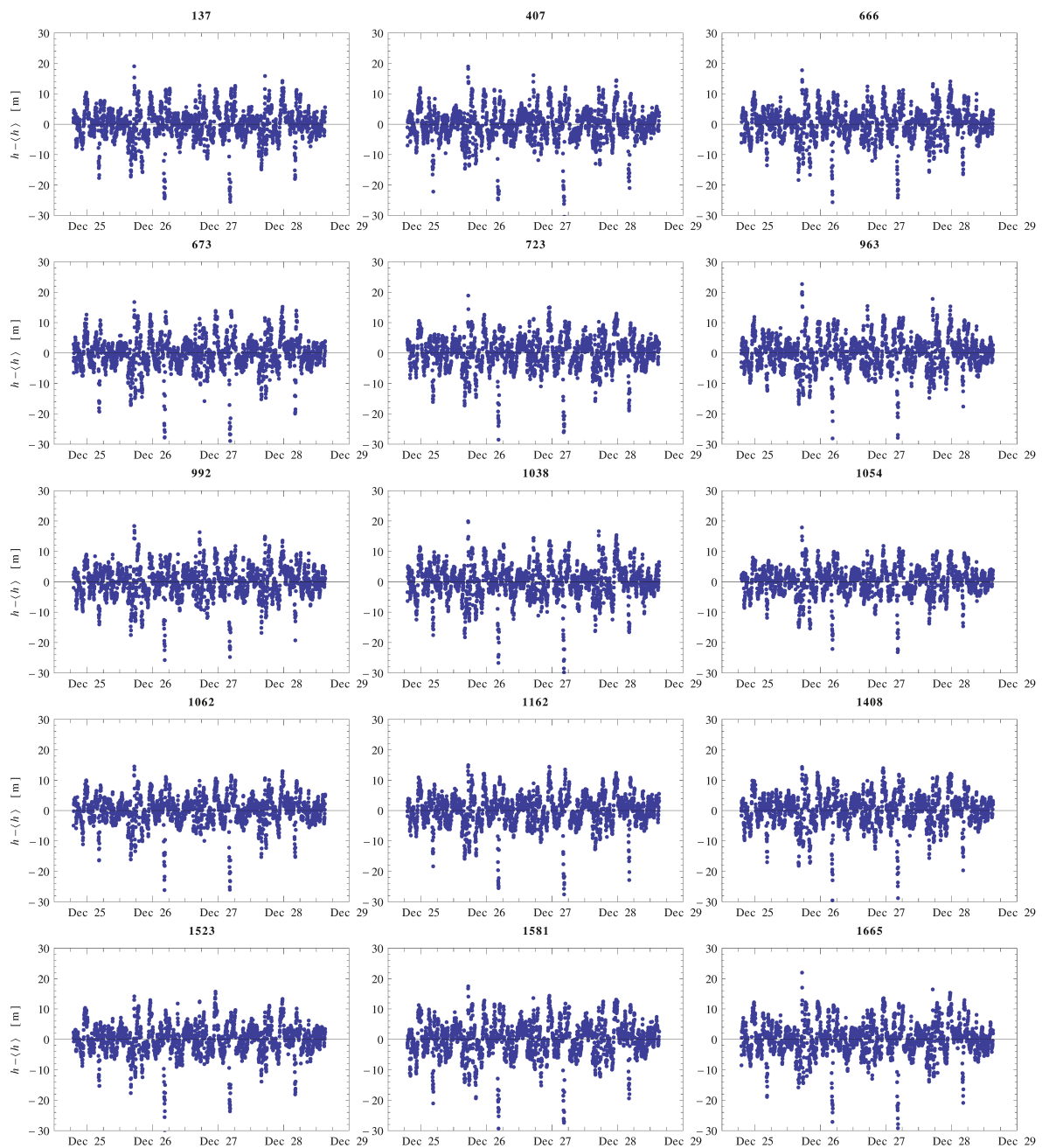


Figure 6.12: Fluctuations of height h around the mean $\langle h \rangle$ between the 24 and the 29 December 2009 (C) for several randomly selected stations.

Plotting the height fluctuations, Fig. 6.14–left (the same holds also for northing and easting of the data), with the time scale wrapped around with a UTC-day modulo (Fig. 6.14–right) these patterns, resulting from the repeated positions of the satellites on the sky, can be observed even more explicitly.

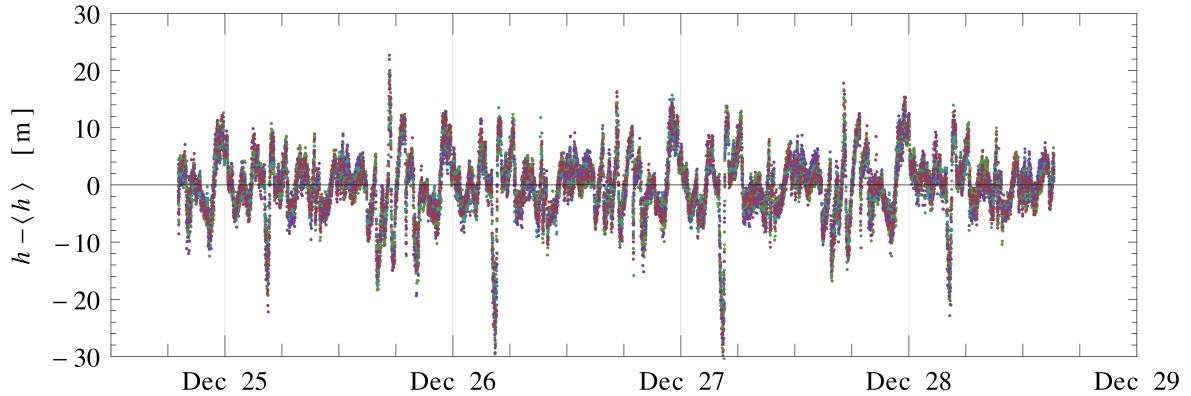


Figure 6.13: Fluctuations of height h around the mean $\langle h \rangle$ between the 24 and the 29 December 2009 (C) for all 15 randomly selected stations from Fig. 6.12 plotted on the same graph (different colors for different stations).

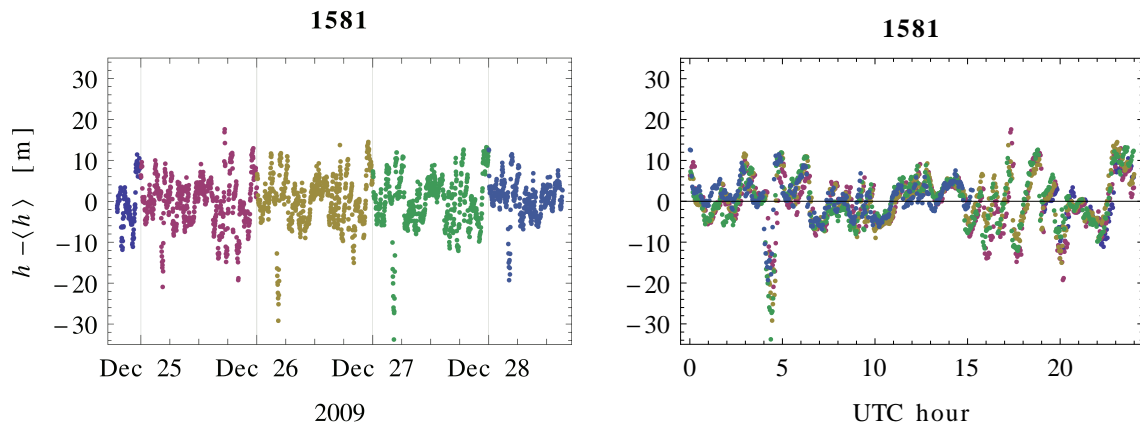


Figure 6.14: Fluctuations of height h around the mean $\langle h \rangle$ between the 24 and the 29 December 2009 (campaign C) for the station with ID 1581 with color-coded days (left), and the same data but with a UTC-day wrapped time axis in UTC hours (right) in order to expose more clearly the obvious repeating of the drift patterns in each of the days. The consecutive shifts come from the difference of the solar and sidereal time (~ 4 min/day).

6.2.2.2 Origin of fluctuations

Based on this plots we can safely state that the large structure of fluctuations of the SD station positions is a consequence of an interplay between the satellite positions and ionospheric and tropospheric delays (in this respect atmospheric pressure is a second order effect). Namely, the delays enter directly into the GPS–receiver position reconstruction. Note that in the position–navigation mode of operation, the position of a station is not fixed, but is calculated from the timings of signals from all visible satellites. The method is fitting four parameters: three components of the station position in space, and the local absolute time (four in total). Thus, the minimal number of satellites for this type of operation is four, but the accuracy of the position estimate increases with the number of available satellites above

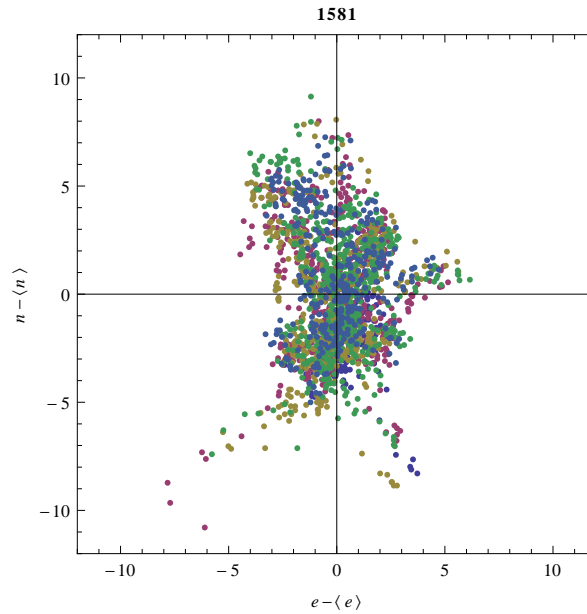


Figure 6.15: Correlation between easting, $e - \langle e \rangle$, and northing, $n - \langle n \rangle$, during the 24 and 29 December 2009 (campaign C) for the station with ID 1581. Color coding corresponds to the different days (in UTC time).

this lower limit. The currently deployed constellation of GPS satellites is such that the number of visible satellites for the lower and medium latitudes is between 5 and 12 with mean close to 8 [1]. Nevertheless, not all satellites in the line of sight might be usable, especially not when they are too close to the horizon. In this case the ionosphere and troposphere-induced delays can render satellite's signal untrackable for the timing acquisition. Since the line of sight towards a particular satellite is moving through the ionospheric irregularities and the variation of the tropospheric index of refraction is bending the signal trajectory, the relative delays of signals from different satellites will induce systematic errors on the local position and time estimates.

6.2.2.3 Position spread

For all measurement campaigns A–D the standard deviations σ_n , σ_e , and σ_h of station positions, averaged over all stations was found to be 249, 154, and 494 cm for northing, easting and height, respectively. The distribution of the deviations over all stations can be seen in Fig. 6.17. The distributions are fairly narrow, which is not so surprising due to the fact that the individual acquisitions of the station positions behave in such a collective manner. Taking any single position measurement at face value would thus bring us close to the “true” position within a order of several meters. Nevertheless, with roughly 5000 measurements per station we can probably trust the mean of the positions to a larger degree.

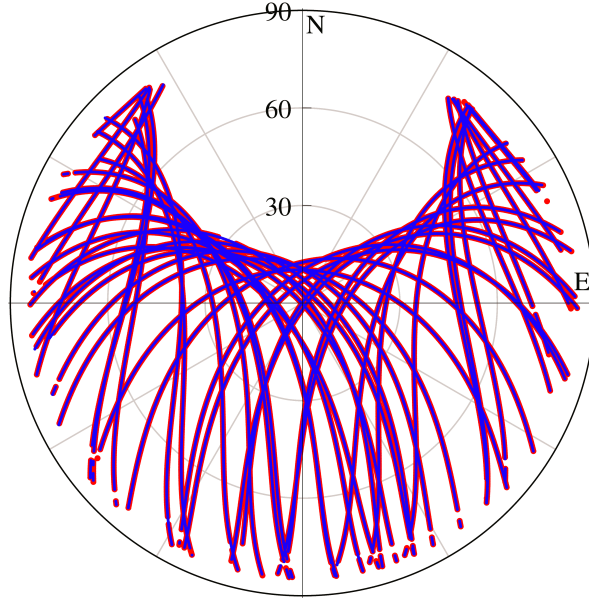


Figure 6.16: Trajectories of all visible GPS satellites (in zenith and azimuthal angles in a polar diagram) above Nova Gorica, for two consecutive days, 13 (larger red dots) and 14 (smaller blue dots) February 2011. Note that between these two days the travel pattern almost did not change. The exclusion zone towards the North (the GPS receiver in Nova Gorica is at 45.94°N , 13.64°E geographical location) is due to the 55° tilt of the GPS orbits, i.e. satellites do not fly over the North/South caps. In Malargüe the Southern exclusion zone should be smaller, with distance to the zenith point more like $\sim 25^\circ$ (and not $\sim 12^\circ$ like in Nova Gorica).

6.2.2.4 Error of the mean position

Having some observable x and its N (equivalent) measurements x_i we can define an estimate of the mean as

$$\langle x \rangle = \frac{1}{N} \sum_i x_i, \quad (6.1)$$

and its unbiased estimate for the standard deviation σ_x (or variance σ_x^2) as

$$\sigma_x^2 = \frac{1}{N-1} \sum_i (x_i - \langle x \rangle)^2. \quad (6.2)$$

In the case when x_i are independent variates that are taken from the underlying distribution in a truly random fashion, the distributions of partial sums (like in Eq. (6.1)) are in turn convolutions of the original distributions [164]. If x_i are following the normal distribution we can thus say that the variance $\sigma_{N\langle x \rangle}^2$ scales as $N\sigma_x^2$ leading us to the error of the mean,

$$\sigma_{\langle x \rangle} = \frac{\sigma_x}{\sqrt{N}}. \quad (6.3)$$

Note that in our case $\sqrt{5000} \approx 70$. Unfortunately, this holds only in the case of truly independent measurements. From the time series of the station positions it is clear that the data is not randomly sampled from some distribution but instead, a fairly large correlation exists

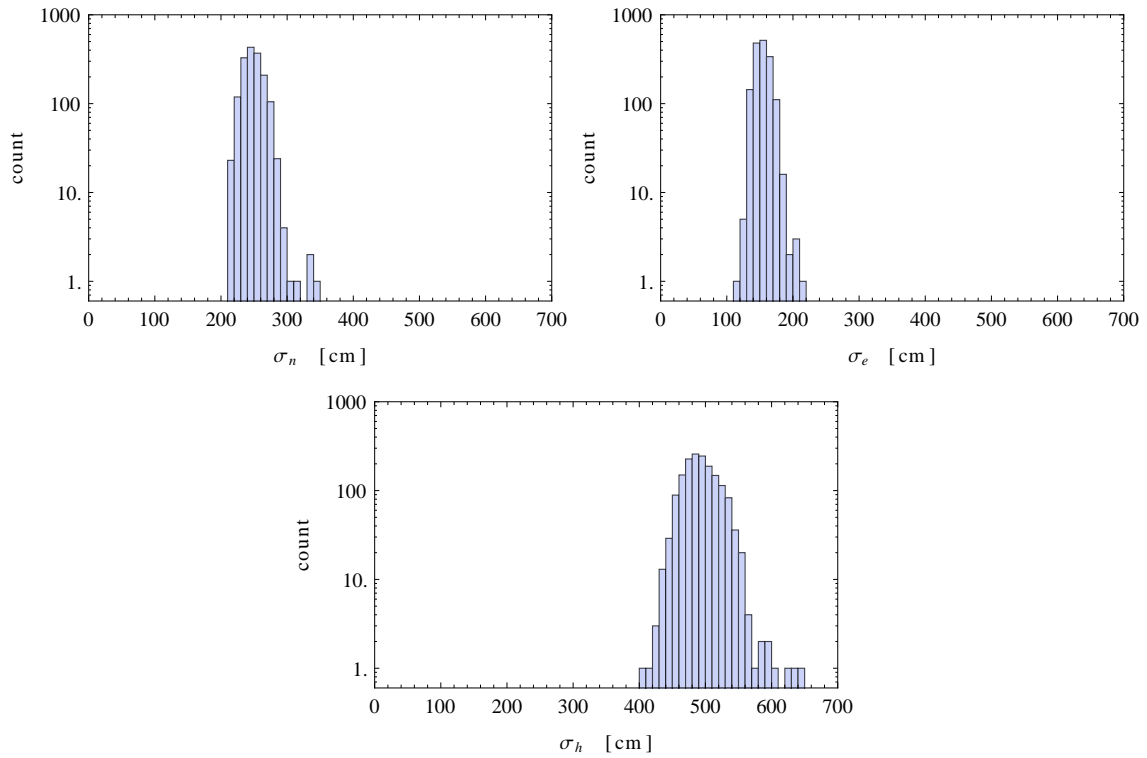


Figure 6.17: Distributions of northing, easting, and height related standard deviations σ_n , σ_e and σ_h over the stations. The average standard deviations taken over all the stations are 249, 154, and 494 cm, respectively.

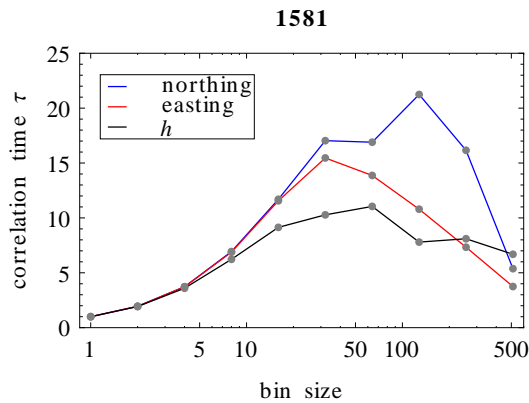


Figure 6.18: Correlation time τ in the case of a station with ID 1581.

between the consecutive measurements of the northing, easting, and height variables. Our data sample is thus not represented by N independent measurements but due to correlations contains effectively τ times smaller number of independent measurements, where τ is the *correlation time* (or *sampling correlation* since we do not have strictly periodic sampling of the positions). Judging from the rough time scale of the fluctuations in Fig. 6.14 we can estimate that the GPS correlation time is of the order of 1 hour. With the most frequent station sam-

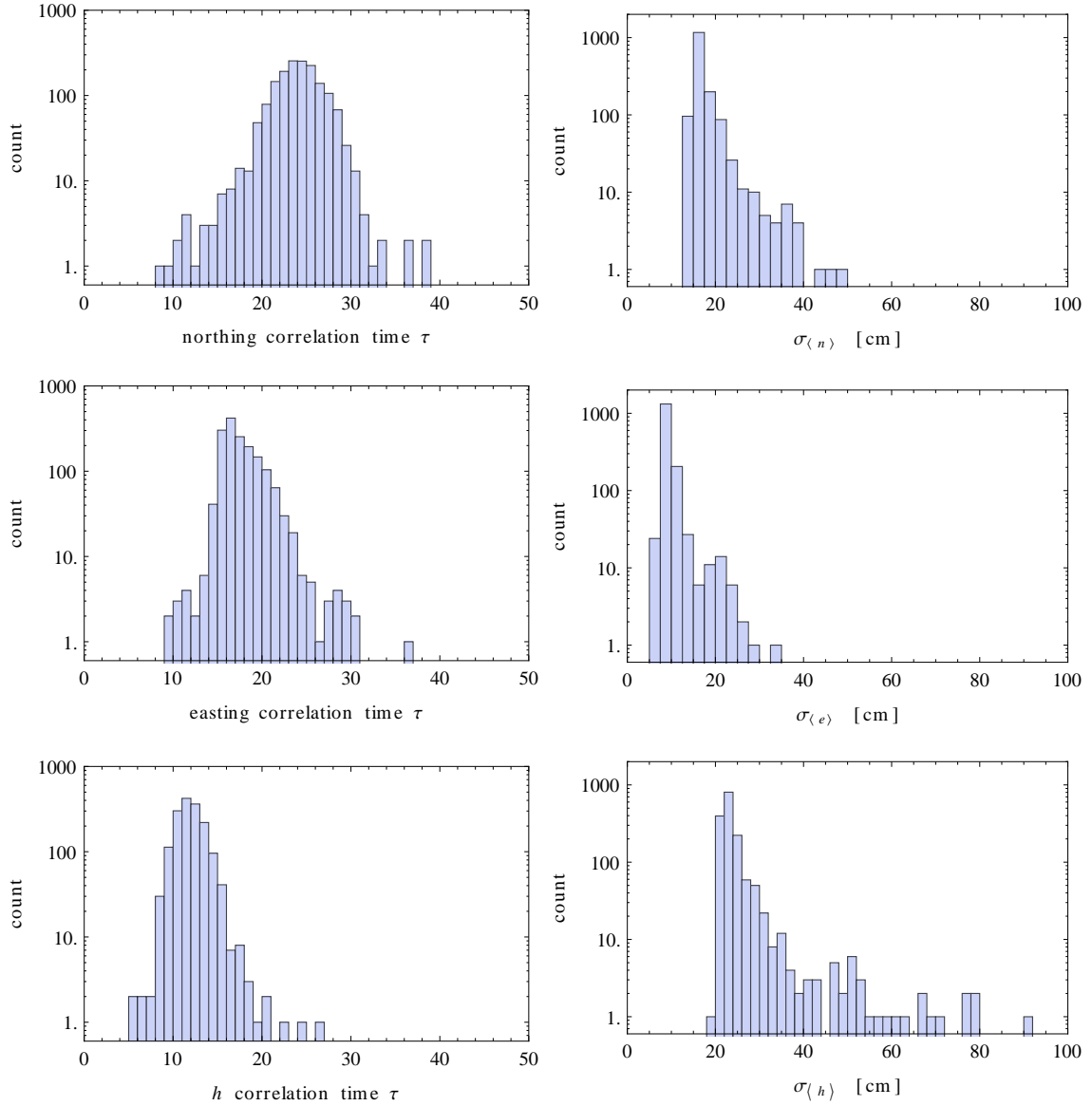


Figure 6.19: Distribution of northing, easting and height correlation time (left) and spread of the mean $\sigma_{\langle n \rangle}$, $\sigma_{\langle e \rangle}$, and $\sigma_{\langle h \rangle}$ (right) among the stations.

pling times between 150 s and 300 s (see Fig. 6.11) this gives us sampling correlation time τ of the order of several 10.

In the presence of the correlations the error of the mean is written instead [165,166] as

$$\sigma_{\langle x \rangle} = \frac{\sigma_x}{\sqrt{N/\tau}}. \quad (6.4)$$

More accurately, the correlation time τ can be estimated, for example, with binning of the original data set and observation of the scaling of the variance of the bin means, $\sigma_x^2(b)$, with

the binning size b by constructing an intermediate estimate

$$\tau(b) = b \frac{\sigma_x^2(b)}{\sigma_x^2}. \quad (6.5)$$

An evolution of such an estimator for our position data for station with ID 1581 and binning progression in powers of 2 is shown in Fig. 6.18. The lower bound for the correlation time τ is then obtained by [167, 168]

$$\tau = \max_b \tau(b). \quad (6.6)$$

For finite size data samples the absolute maximum \max_b is replaced with \max'_b where the prime is implying that the maximum is taken over all possible values of binning b except maybe for the last few largest possibilities which result in calculation of a variance estimate on a small data set of only several values and can thus produce misleadingly large values. Nevertheless, excluding the large bin sizes, the $\tau(b)$ develops a clear maximum which seems to be slightly larger for northing and easting than for height. In Fig. 6.19 the distributions for correlation times τ_n , τ_e , and τ_h , and distributions of related mean errors $\sigma_{\langle n \rangle}$, $\sigma_{\langle e \rangle}$, and $\sigma_{\langle h \rangle}$ are shown for all stations. The correlation time τ_h seems to be smaller than τ_n and τ_e , nevertheless, due to the larger spread of the height fluctuations the resulting error of the height mean $\sigma_{\langle h \rangle}$ is larger or comparable to the $\sigma_{\langle e \rangle}$ or $\sigma_{\langle n \rangle}$. Note that, for comparison using $\tau \approx 15$, now we get “only” $\sqrt{5000/15} \approx 20$.

The final conclusion is that with the current GPS measurement campaigns we can estimate the positions of stations to the accuracy of several 10 cm (excluding systematical errors).

6.2.2.5 Systematics

Unfortunately, establishing correlation times between position measurement close in time tells us nothing about the behavior of the positions on the larger time scales. Having four measurement campaigns, well separated in time, we can check for the systematical differences of the station positions between these periods. In Fig. 6.20 systematical differences in horizontal part of the mean positions are shown for consecutive measurement campaigns B–A, C–B, and D–C, but only for stations that have at least 100 position measurements available in both of the consecutive campaigns. We can see that between the periods, the acquired station positions are fairly collectively moving around on the scale of the order of 50 cm in horizontal direction. Note that the last two campaigns, C and D, lasted relatively longer in time than the first two, A and B, which might explain the slightly larger spread in the last panel for D–C. In Fig. 6.21 the same is shown also for the vertical component. From the time succession of the campaigns we can observe that while the spread has stayed the same between A–C, the acquired mean height of the stations was systematically increasing throughout all of the time periods. What is remarkable is the last panel, showing the acquired height differences have split into two populations, a smaller one gaining around 1 m more in height than the larger one. Expecting only whole-array collective movement of the acquired positions since the array is flat enough to enable the same satellite viewing conditions to every station, this is really an interesting feature. Plotting the difference in acquired mean height of stations on the array map, Fig. 6.22, and comparing it to the satellite image of the region, we can see that the smaller population of the stations that gained more in height is localized to the Atuel riverbed and the El Sosnado corner.

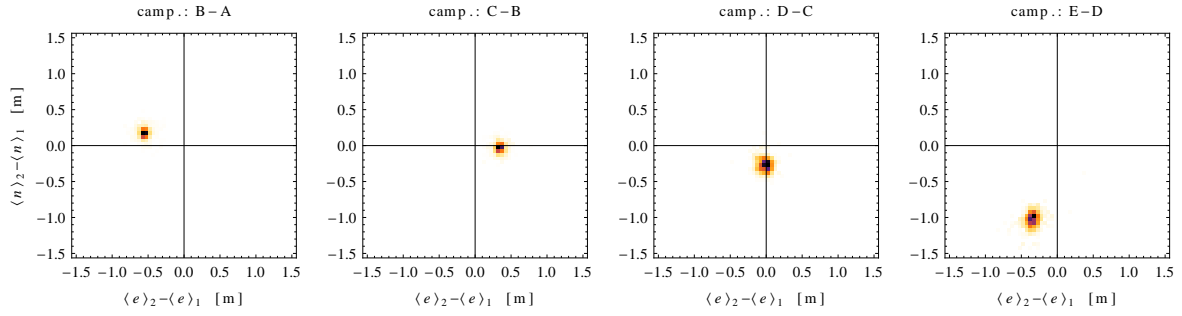


Figure 6.20: Systematic difference of the horizontal part of the position means of the stations, $\langle e \rangle_2 - \langle e \rangle_1$ and $\langle n \rangle_2 - \langle n \rangle_1$, where the indices refer to the consecutive measurement campaigns resulting in plots for the difference between the campaigns B–A, C–B, and D–C.

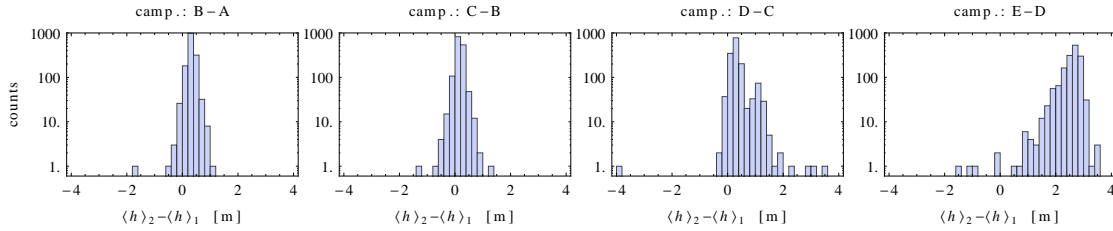


Figure 6.21: Systematic difference of the mean vertical position of the stations, $\langle h \rangle_2 - \langle h \rangle_1$, where the indices refer to the consecutive measurement campaigns resulting in plots for the difference between the campaigns B–A, C–B, and D–C.

Note that right between the measurement campaigns C and D, on the 27 February 2009, whit a magnitude 8.8 on the moment magnitude scale (M_w) earthquake struck near Concepción in Chile which reportedly caused surface movements on the order of meters (on centimeter scale even as far as Buenos Aires and Rio de Janeiro). While errors of the mean positions within each of the campaigns are small enough to detect such changes, the systematic differences show us that for distances smaller than 1 or 0.5 m we really cannot pass judgment. Nevertheless, the observed height differences at the Atuel riverbed are on the detectable edge and have a distinct clustering pattern. On the other hand, under earthquake induced earth liquefaction, we would probably expect sinking and not like our case, where stations have apparently higher positions after the incident.

6.2.2.6 Comparison with survey database

As already mentioned, in the usual mode of CDAS operation, upon initialization the stations are supplied with fixed positions from the survey database. These positions appear also in the log files. For each station we denote by $(n_{pms}, e_{pms}, h_{pms})$ a triple of position coordinates that occur most frequently in the log files for years 2009 and 2010. These coordinates should in principle correspond to the station entries in the Auger database. In Fig. 6.23 a 2D plot is showing the mean of the northing and easting, $\langle n \rangle$ and $\langle e \rangle$, from the measurement campaigns A–D relative to the database coordinates n_{pms} and e_{pms} . It is clear that most of the stations lie within 1000 cm (10 m) of the Auger database positions. In Fig. 6.24 the distri-

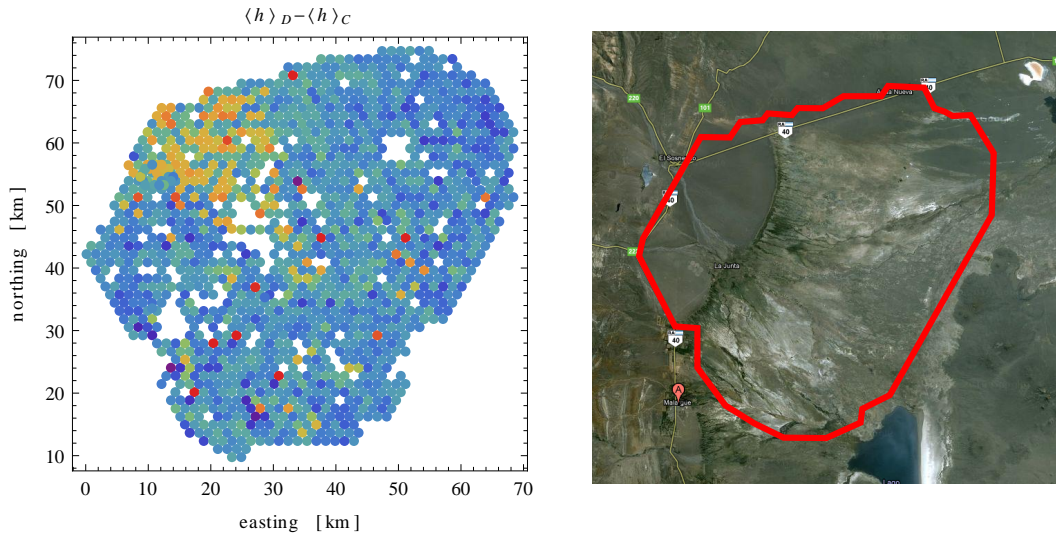


Figure 6.22: Systematic difference of the mean vertical position of the stations, $\langle h \rangle_D - \langle h \rangle_C$, for the campaigns D-C (left). Outline of the SD array in the same scale, superimposed on the satellite image map, and given for easier identification of the elevated stations above (left).

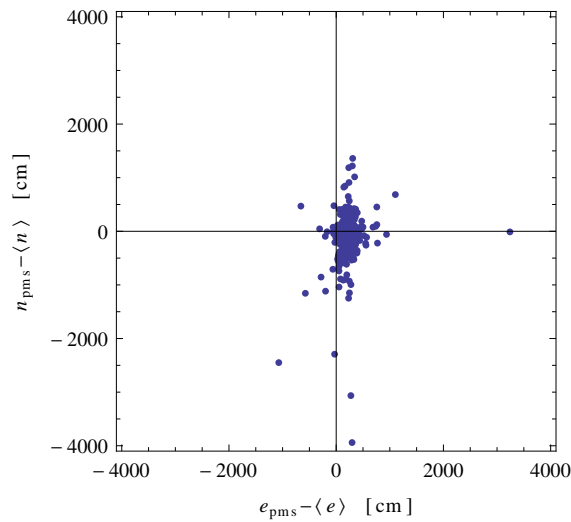


Figure 6.23: Mean of the northing and easting positions, $\langle n \rangle$ and $\langle e \rangle$, from the campaigns A-D relative to the most frequent positions, n_{pms} and e_{pms} , from the log files for years 2009 and 2010.

butions of differences $n_{pms} - \langle n \rangle$, $e_{pms} - \langle e \rangle$, and $h_{pms} - \langle h \rangle$ is shown over all the stations. For northing and easting the differences are well contained within the ± 15 m with a slight shift of the mean of easting $e_{pms} - \langle e \rangle$ distribution towards ~ 2 m. The height differences $h_{pms} - \langle h \rangle$ also seem to be mostly contained within ± 15 m, except that the distribution here is fairly broader, features a spurious gap in the middle, and that there is a distinct outlier population with $h_{pms} - \langle h \rangle > 15$ m.

The height differences are further visualized in Fig. 6.25 where a map of the SD array

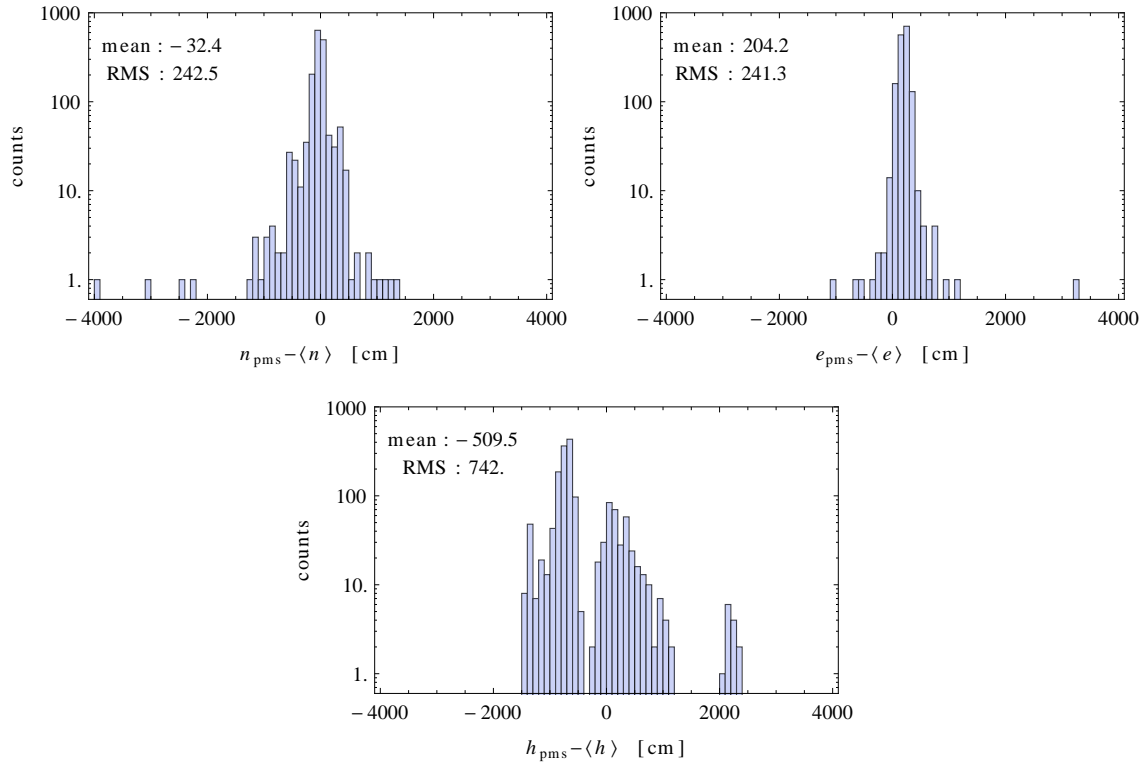


Figure 6.24: Distribution of differences $n_{\text{pms}} - \langle n \rangle$, $e_{\text{pms}} - \langle e \rangle$, and $h_{\text{pms}} - \langle h \rangle$ over the stations.

is populated with circles at the station positions, with circle radius following the absolute magnitude of the height difference. The stations with the height difference within the ± 5 m are colored green, the stations on the negative and positive side of this range are shown in red and blue, respectively. The stations with the largest height differences are in the blue “island” in the middle eastern region and the north-eastern corner of elevated (in Auger database) stations. There is also one excessive outlier close to the northern road. Looking at the whole SD array, on average the Auger database values seem to be too high in almost all places except in the connected area (green) north and west of Los Morados. Similar plot can be made also for the horizontal shifts of the survey positions relative to the obtained mean GPS positions. In Fig. 6.26 such a map is shown where the arrows are pointing in the direction of the shifts and the arrow sizes are proportional to the square-root of the shift magnitudes in order to emphasize the small shifts whose directions would otherwise not be visualized at all. What is remarkable is the apparent alignment of the shifts in preferred directions, mostly along the triangular grid axes, and clumping into domains of the same orientation. Comparing with the apparent groups in the previous Fig. 6.25 where similar segmentation can also be observed, we can conclude that the groups must most probably correspond to the surveying of large number of stations that were done at the same time.

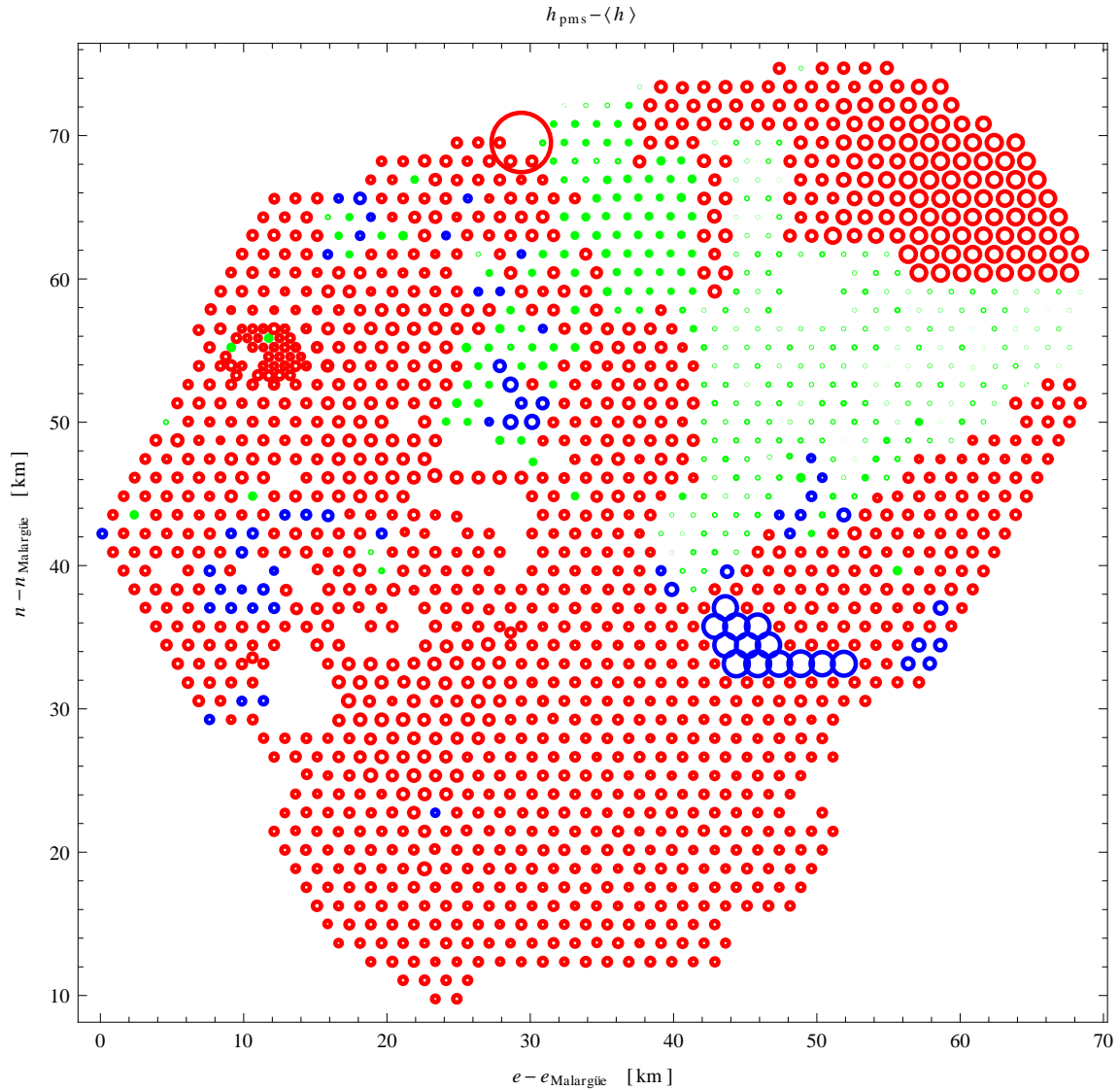


Figure 6.25: Map of height differences $h_{\text{pms}} - \langle h \rangle$. Size of a circle is proportional to the absolute difference where for the touching circles this amounts to 20 m. Stations with $h_{\text{pms}} - \langle h \rangle \leq -5$ m are shown in red color and stations with $h_{\text{pms}} - \langle h \rangle > 5$ m in blue color. The rest is depicted in green. The horizontal positions of the stations are easting and northing subtracted by the corresponding values for the Malargüe coordinate system origin.

6.2.3 Positions of SD Stations: Dilution of Precision Corrections

In order to reduce the fluctuations we attempt to weight the mean positions with the dilution of precision (DOP) quantifier. In this analysis we will add the data from an additional, fifth measurement campaign [151] that lasted roughly from 10 Feb 2012 until 16 Feb 2012. In Fig. 6.28 the number of received measurements is shown per each station ID for the previous four campaigns (blue) and the total after the last campaign (red). On average we have almost 8000 measurements for each station, but the data is slightly correlated [152]. Here we are

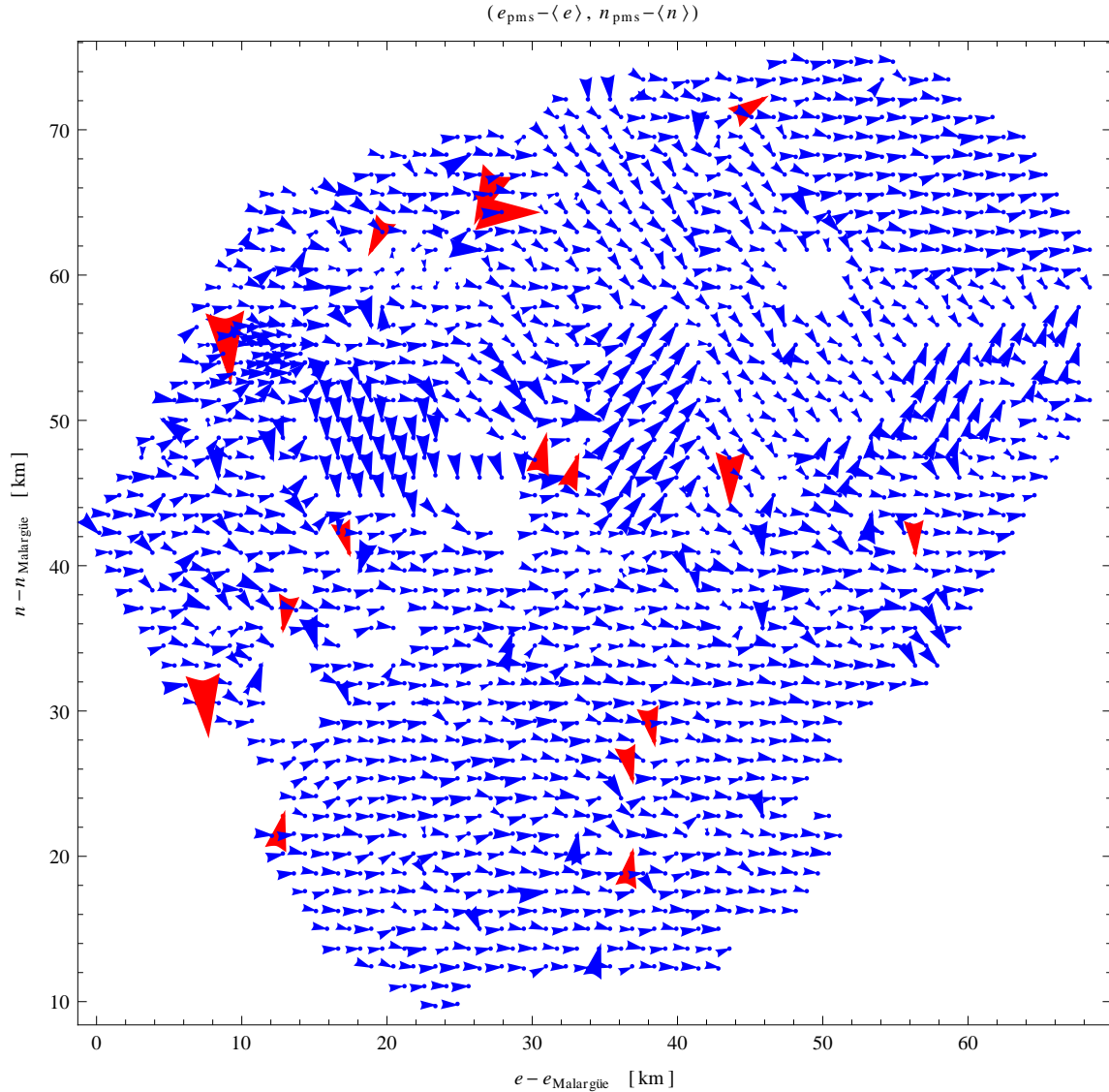


Figure 6.26: Map of horizontal differences $(e_{\text{pms}} - \langle e \rangle, n_{\text{pms}} - \langle n \rangle)$. Size of an arrow is proportional to the square-root of the shift (in order to emphasize small deviations) where the largest arrows correspond to ~ 20 m of horizontal distance. Stations with shifts larger than 10 m are shown in red color and the rest is depicted in blue. The horizontal positions of the stations are easting and northing subtracted by the corresponding values for the Malargüe coordinate system origin. Note the locally ordered structure of shifts that are probably related to the surveying campaigns.

attempting to make at least the first order correction of the measured data, the correction that can be ascribed to the accuracy of the GPS for particular satellite geometry.

The relative position of the satellites in the sky can influence the position estimates and fitting procedure employed by the GPS firmware. Schematically, the position and time fit method relies on calculation of the intersections of spheres, each with its center placed at the current position of the satellite (see Fig. 6.29). In case of well separated satellites, the spheres

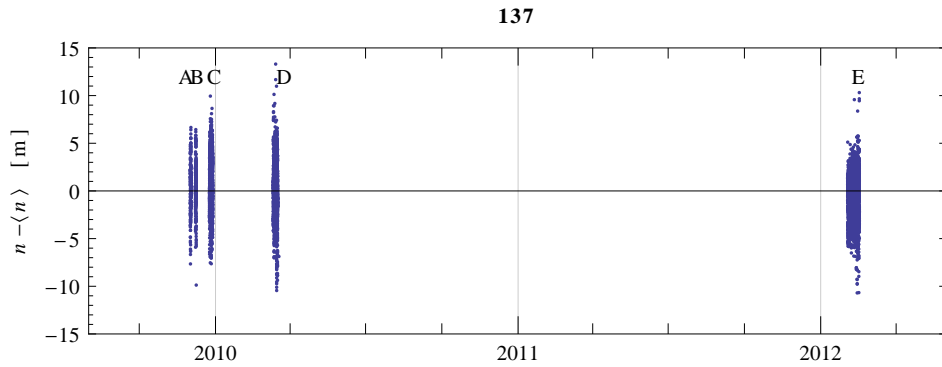


Figure 6.27: Time-line of the five measurement campaigns A–E, illustrated with the changing of the northing component n of station with ID 137.

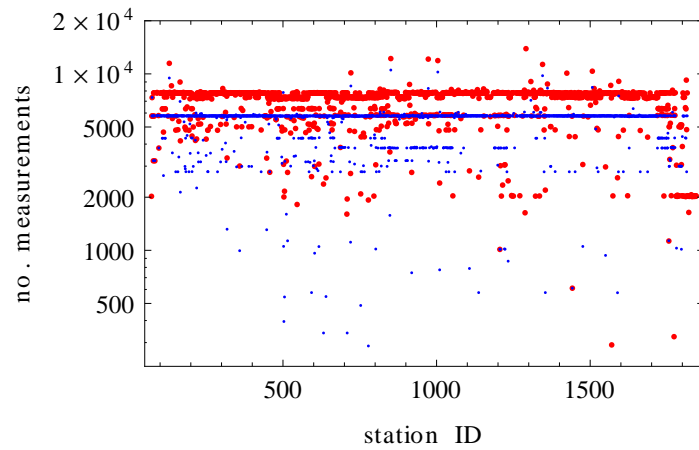


Figure 6.28: Number of available position measurements per each station ID. In blue numbers for previous four measurement campaigns A–D and in red numbers for all five campaigns A–E.

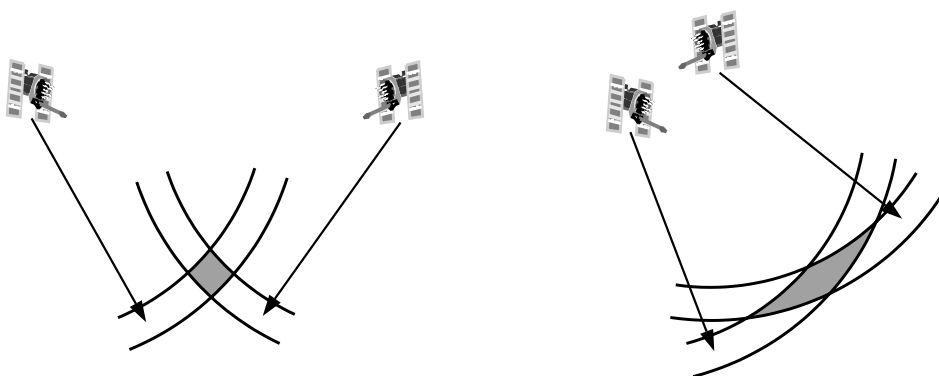


Figure 6.29: Illustration of the origin of dilution of precision (DOP). *Left*: Good constellation of tracked satellites. *Right*: Bad constellation with close-by satellite directions, effectively reducing the number of degrees of freedom. Image taken from [60].

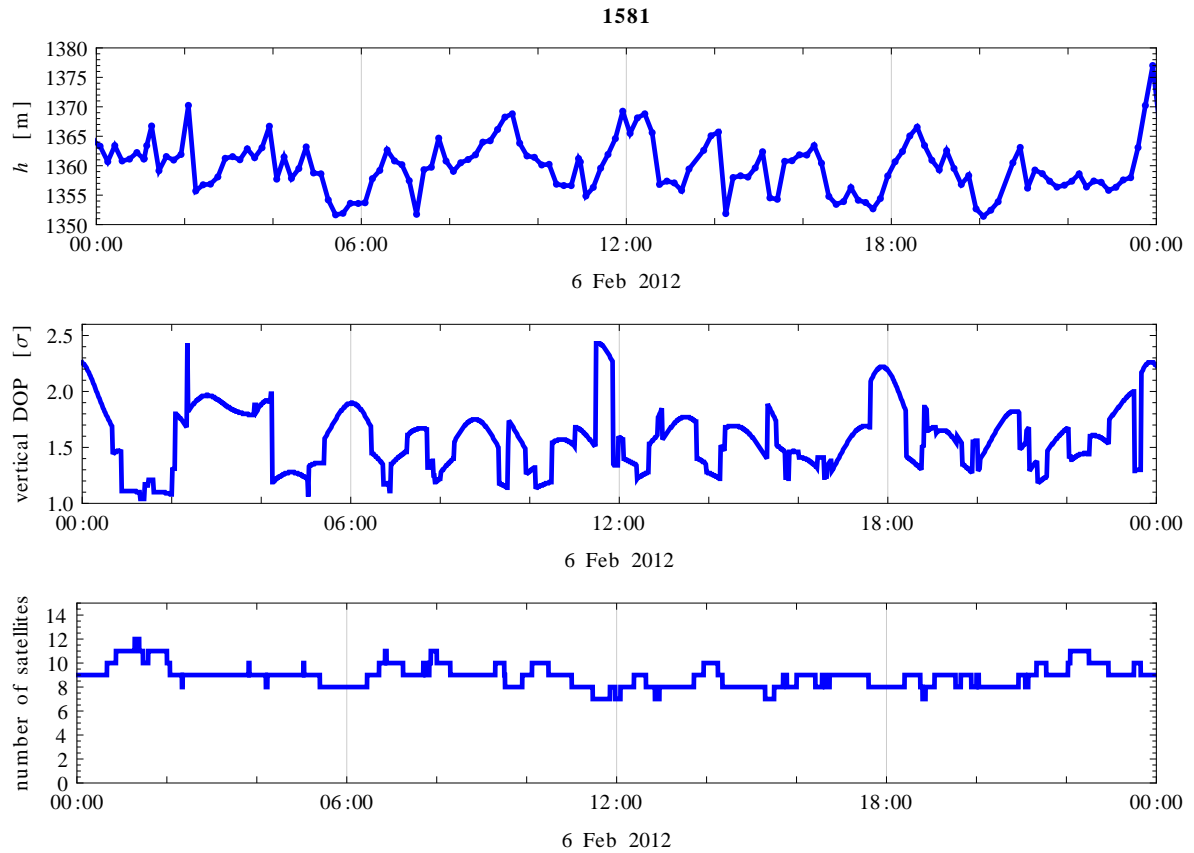


Figure 6.30: Measurement of height h for station with ID 1581 during one whole day (6 Feb 2012) of the last measurement campaign E (top). Vertical dilution of precision (VDOP) in units of pseudo-range error σ for the same time period (middle). Number of observed GPS satellites during this time period (bottom).

intersect in narrowly bounded regions, yielding accurate estimates of the GPS position (left panel of Fig. 6.29). But when there is a decrease of visible satellites² and when satellites are placed relatively close in the sky, effectively reducing the “lever arm”, the solution can have a large uncertainty. In such cases we can assume the GPS position can become more sensitive to other disturbing effects like the ionospheric scintillations, multi-path effects or even tropospheric signal delays. For this reason we have decided to estimate the influence of the geometry of satellites on the means of station positions. In the GPS technical field, the geometrical degradation of the position estimates is usually known as the dilution of precision (DOP) [169] and here we give a brief formal description of the process.

The covariance matrix of geometry estimate

$$\vec{g} = (n, e, h, t), \quad (6.7)$$

with northing n , easting e , height h (WGS84), and time t , can be expressed as

$$C_{\vec{g}} = D\sigma^2, \quad (6.8)$$

²in last few years this is not such an important effect since the GPS constellation is more than fully occupied

where σ is the standard deviation of the pseudorange measurement/modeling, and the elements of matrix D are only a function of receiver–satellite geometry [1, 169]. Horizontal and vertical dilution of precision (HDOP and VDOP) are expressed as relative to the total error of the pseudorange measurement,

$$d^H = \text{HDOP} = \frac{\sqrt{\sigma_e^2 + \sigma_h^2}}{\sigma} = \sqrt{D_{11} + D_{22}}, \quad (6.9)$$

$$d^V = \text{VDOP} = \frac{\sigma_h}{\sigma} = \sqrt{D_{33}}. \quad (6.10)$$

In Fig. 6.30–top an example of the position measurement is shown for a time period of 24 hours (station with an ID 1581, 6 Feb 2012). In the middle a corresponding vertical DOP (VDOP) is shown, typically spanning a range between unity and 2.5. In the bottom panel we can see that the dilution of precision is mostly due to the geometry of the satellite positions and not so much due to the reduction of the visible satellites since the number of tracked satellites is most of the time well above 8. Some professional GPS units can provide on–line information about the current values of all DOP variables. For our purpose, we will attempt to take DOP values into account *post festum*, using planning software developed by Trimble, the manufacturer of GPS units and GPS related circuits [170].

6.2.3.1 Weighted means

To estimate the mean position \bar{x} we can combine the measurements x_i with individual errors σ_i into a likelihood

$$\mathcal{L} = \prod_i \mathcal{L}_i = \prod_i \mathcal{N}(x_i - \bar{x}, \sigma_i), \quad (6.11)$$

where the normal distribution \mathcal{N} is written as

$$\mathcal{N}(x - \bar{x}, \sigma) = \frac{1}{\sigma\sqrt{2\pi}} \exp\left[-\frac{(x - \bar{x})^2}{2\sigma^2}\right]. \quad (6.12)$$

Introducing log–likelihood $\ell = \ln \mathcal{L} = \sum_i \ell_i$, the condition for maximum log–likelihood,

$$\frac{\partial \ell}{\partial \bar{x}} \equiv 0, \quad (6.13)$$

will provide us with an expression for an optimal mean

$$\bar{x} = \frac{\sum_i w_i x_i}{\sum_i w_i} \quad \text{iff} \quad w_i = \frac{1}{\sigma_i^2}. \quad (6.14)$$

In case of the coordinate components of the position, northing n , easting e , and height h , we thus obtain

$$\bar{n} = \frac{\sum_i w_i^H n_i}{\sum_i w_i^H}, \quad \bar{e} = \frac{\sum_i w_i^H e_i}{\sum_i w_i^H}, \quad \bar{h} = \frac{\sum_i w_i^V h_i}{\sum_i w_i^V} \quad (6.15)$$

where

$$w_i^H = \frac{1}{(d_i^H)^2} \quad \text{and} \quad w_i^V = \frac{1}{(d_i^V)^2}. \quad (6.16)$$

It is thus optimal to combine all position measurements, weighting the importance of some particular measurement by the squared inverse of the corresponding DOP value. In this way

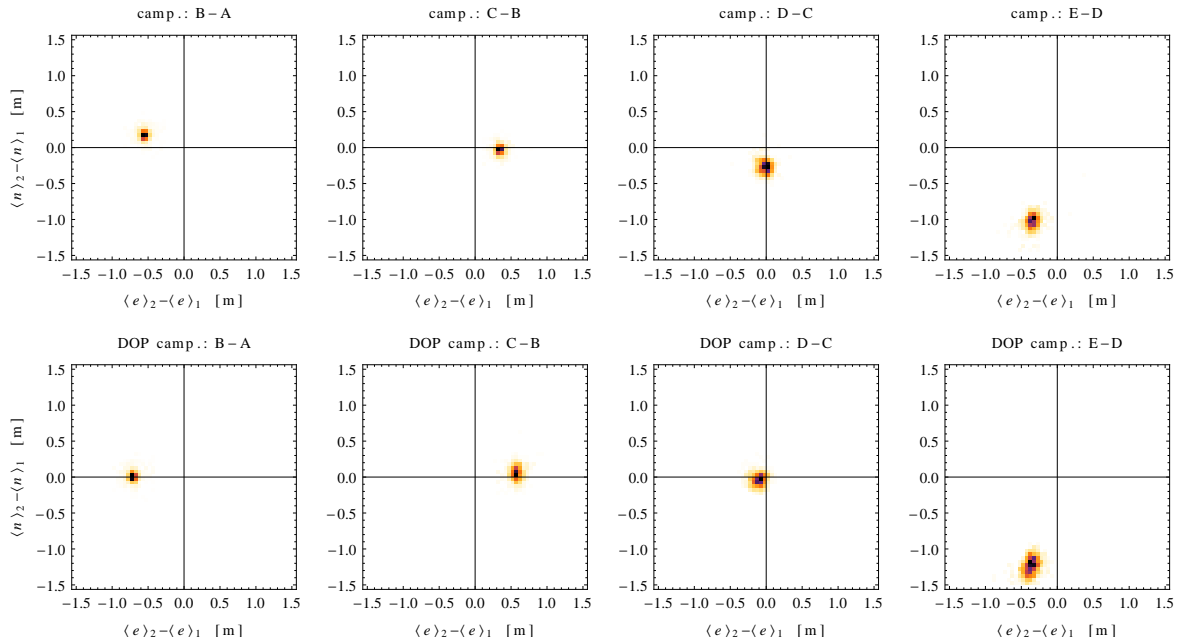


Figure 6.31: Difference between all station means for horizontal positions (n and e) for two consequent measurement-campaign pairs, using normal, unweighted averaging (top). The weighted means are the weights depend on instantaneous values of the HDOP parameter (bottom).

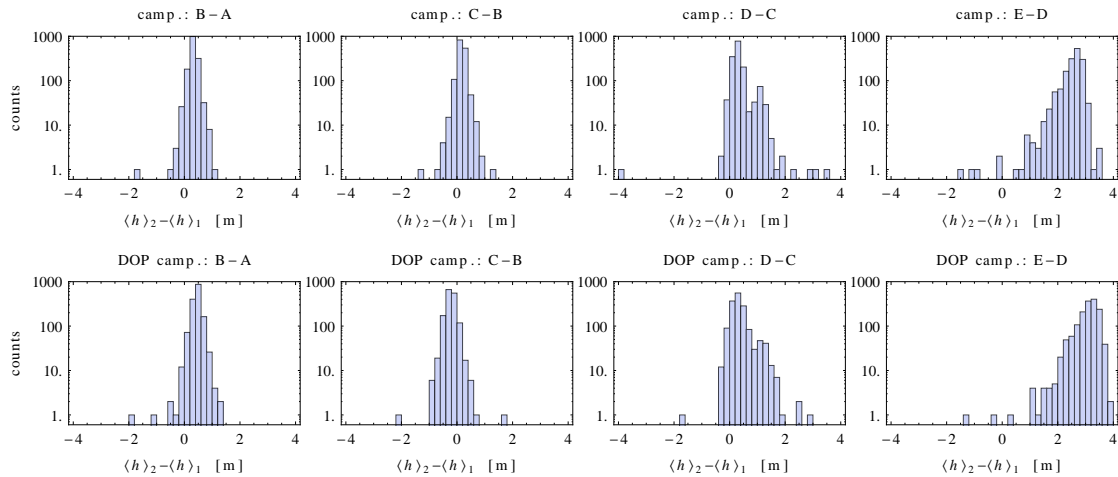


Figure 6.32: Difference between all station means of vertical positions (h) for two consequent measurement-campaign pairs, using normal, unweighted averaging (top). The same, but this time with the weighted means where the weights depend on instantaneous values of the VDOP parameter (bottom).

the measurement point that showed large dilution of precision will be taken into account with lesser weight than those measurement points that had DOP values close to unity.

In Figs. 6.31 and 6.32 we can see the average positions of the stations, calculated only

within each of the measurement campaign and compared between two consecutive periods. The averages are calculated with the usual mean (top row of figures) and with the expression for a DOP weighted means from Eq. (6.15). As can be seen from the plots for the horizontal components, the intra-campaign differences stay at approximately the same level, slightly reducing them in one of the directions while slightly increasing the other direction. Overall we can claim that the DOP corrections did not have a tremendous effect on the obtained positions and that the main contribution has to come from other effects, most probably acting on larger time scales and being correlated with seasons.

6.3 Conclusions

In order to increase the timing resolution, the on-board GPS units on the SD stations are by default initialized into position-hold mode, where the fixed positions were obtained by the geodetic field surveys. However, in the second half of the year 2009 it became clear that there are quite unusual structures appearing in the height of the SD stations.

The investigation into the topographical properties of the SD array was performed and presented with the difference to the digital elevation map and array test with different GPS position acquisition mode, where positions and periodicity, origin of fluctuations and finally comparison with survey database was investigated. Landscape morphology was still a strong candidate for the apparent ridges but after the comparison with the digital elevation maps it was revealed that, at least in digital elevation maps, there are no corresponding topographical features present. Based on this findings the on-board GPS units of the whole SD array were in early December 2009 switched for approximately 2 days into the navigation mode (instead of the usual position-hold mode). The analysis of the survey database positions showed that relative to the position from the measurement campaign A we have 27 stations in the survey database with horizontal distances above 10 m and/or vertical differences larger than ± 15 m. Later several more measurement campaigns were initiated, through which we can conclude that an improvement in the position information of SD stations is needed in order to reduce the systematical effects of the difference between the assumed and the true positions on the reconstruction of the shower data. In order to reduce the fluctuations we attempted to weight the mean positions, obtained with the five dedicated campaigns, with the dilution of precision quantifier, however the results showed that the inter-campaign positions were dominated by other, possible seasonal effects.

Conclusions and Future work

7.1 Conclusions

The uses of ground based GPS receivers in atmospheric science at the University of Nova Gorica, from the ionosphere to meteorology and into the cosmic ray field, were investigated and presented in this dissertation. The theory of the GPS system and its potentials in atmospheric research at the University of Nova Gorica were discussed in detail and demonstrated with different experiments. During the PhD research, two dedicated GPS units were successfully deployed. The two units are currently recording not only data needed for water vapor estimation but also for monitoring ionospheric conditions and their effects on GPS signals.

A significant amount of work was put into the investigation of the capabilities of the GPS system for the remote sensing of water vapor in the SW part of Slovenia, and this research was divided into two major parts. In the first part, development of a local T_m model was performed, using a simple linear regression model and an extended linear method. Different T_m parametrizations were estimated using data from a ground based meteorological station in Ljubljana, and compared to the T_m values obtained from co-located radiosonde measurements. For each of the parametrizations, the comparison to the radiosonde data and subsequent error analysis was performed separately using the well known Bevis *et al.* (1992) equation. The results showed little discrepancies leading to the conclusion that our new local T_m models are valid not only for the Ljubljana region but also for Nova Gorica.

Research continued with the estimation of wet delay using GPS data and GIPSY software. Since this was the first time such a study was performed at the University of Nova Gorica, different strategies were tested and presented. Due to the fact that the two GPS monitors deployed by the UNG became operational in the later stages of this dissertation, first, the estimation of wet delay and further calculations of IWV were performed using the data from the GPS monitor in Ljubljana. This provided not only a long-term data set (7 years) but also the best possible statistical comparison between IWV from GPS delay and IWV obtained using co-located radiosonde profiles. As a final result, obtained IWV was then compared using UNG monitors. Based on the results presented in Chapter 3, the conclusion can be drawn that an operational GPS water vapor system can be fully implemented at the University of Nova Gorica in the near future, which might be of great benefit not only for numerical weather prediction but also for the investigations of water vapor influence on a local scale, which is useful in the determination of the likelihood of the onset of floods or severe droughts (very important for the Primorska region).

To extensively validate the measured water vapor content, an additional remote sensing tool was used: Raman lidar. However, due to the current configuration of the system, which does not enable sufficient measurable range for reliable estimation of IWV, the analysis was not performed and only water vapor mixing ratio profiles were calculated and presented.

Atmospheric science is not the only research area at the University of Nova Gorica, where GPS techniques are being used. The Astroparticle physics group, which frequently collaborates with the Centre for atmospheric research, is involved in the Pierre Auger Observatory, where the primary use of the GPS is for the precise-timing of cosmic ray arrivals. As a result of this collaboration between the two groups, a precision study was performed in the scope of this thesis and is presented in its final chapter. Based on the results of the performed analysis an improvement in the position information of the SD stations is needed in order to reduce the systematical effects of the difference between the assumed and the true position. There are two possible strategies for improvement. One is to switch the whole array into the normal navigate mode, as was done for a short time for the purposes of this study. Nevertheless, as can be seen from the time series of the obtained measurements, this would introduce another source of semi-deterministic disturbances and is maybe not worth the risk without a full analysis of the consequences. The second option is to keep the array running in the position-hold mode but to update the survey database with the mean positions obtained from the GPS measurement campaigns, and maybe repeat these measurements at regular intervals to check for seasonal and sidereal effects, antenna degradation, GPS unit malfunction, and to check for the statistical consistency of historical and present position data.

7.2 Future work

Although preliminary results from the GPS monitors deployed by the University of Nova Gorica were in good agreement with the data of the GPS monitor stationed in Ljubljana, there are several remaining issues to be resolved in the future. One of them is the development of a dedicated software algorithm with which the direct estimation of the dry delay would be possible using ground based meteorological stations that could be subsequently inserted into the GPS processing scheme with the GIPSY-OASIS II (or some other) software on a daily basis. Although this would not be performed in real-time, one would still be able to process all available data in near-real time (data latency <6 hours).

In order to perform co-located water vapor measurements using a Raman lidar and GPS monitor, re-location of the GPS monitor stationed in Rožna Dolina to Otlica Observatory is necessary. In that way one would be able to perform not only co-located measurements but also measurements of differential water vapor content between Otlica and Ajdovščina (where the second monitor is located). Deployment of several similar GPS monitors within the region would provide an additional capability for obtaining not only temporal information on water vapor but also spatial information, i.e. water vapor maps.

There are two possible ways of increasing the range of the Raman lidar system [89]: one is to acquire a new laser with higher pulse energy; the other is to build a new telescope which would provide a larger light flux to the spectroscopic filter. Both upgrades could be done simultaneously. For absolute calibration, not only of GPS-IWV but also of Raman lidar mixing ratio profiles, instillation of a dedicated water vapor radiometer such as MIAWARA-C is needed. MIAWARA-C is a 22 GHz water vapor spectroradiometer which was specifically designed for profile measurement campaigns. One of the major advantages of this system is that it can be operated as a standalone instrument as it maintains its own weather station and has an internal calibration scheme that does not rely on other

systems [171].

Even though the two GPS receivers used in the scope of this thesis were used only for estimating water vapor information along the line of sight, they can also be used for ionospheric research, especially for local response on geomagnetic disturbances in the Alpine-Adriatic region and for monitoring travelling ionospheric disturbances. Furthermore, because the two monitors have been in operational use since the end 2011, a similar long term analysis can be performed as in the case presented in this thesis using the data from a similar system located in Douala, Cameroon (Chapter 5).

Bibliography

- [1] P. Misra and P. Enge, *Global Positioning System: Signals, Measurement, and Performance*, (Second Edition, Ganga-Jamuna Press, 2006).
- [2] E.D. Kaplan and C.J. Hegarty, *Understanding GPS: Principles and Applications*, (Second Edition, Artech House Inc., 2006).
- [3] M. Bevis, S. Businger, T.A. Herring, C. Rocken, R.A. Anthes and R. Ware, *GPS Meteorology: Remote Sensing of Atmospheric Water Vapor Using the Global Positioning System*, *Journal of Geophysical Research* **97** (1992) 787–801, doi:10.1029/92JD01517.
- [4] A. El-Rabbany, *Introduction to GPS: the Global Positioning System*, Artech House, Boston, 2002.
- [5] C.J. Hegarty and E. Chatre, *Evolution of the Global Navigation Satellite System (GNSS)*, *Proceedings of the IEEE* **96** (2008) 1902–1917, doi:10.1109/JPROC.2008.2006090.
- [6] *Satellite navigation, Galileo: Satellite launches*, available at: http://ec.europa.eu/enterprise/policies/satnav/galileo/satellite-launches/index_en.htm, accessed on 1 March 2013.
- [7] R.G. Fleagle and J.A. Businger, *An Introduction to Atmospheric Physics*, (Second Edition, Academic Press, Inc., New York, 1981).
- [8] J.B. Campbell and R.H. Wynne, *Introduction to Remote Sensing*, (Fifth Edition, The Guilford Press 2011).
- [9] A.H. Dodson, P.J. Shardlow, L.C.M. Hubbard, G. Elgered and P.O.J. Jarelmark, *Wet tropospheric effects on precise relative GPS height determination*, *Journal of Geodesy*, **70** (1996) 188–202.
- [10] J.L. Awange, *Environmental Monitoring using GNSS*, (Springer-Verlag, Berlin, Germany, 2012).
- [11] Institute for Scientific Research, Boston College, *Space Weather Effects on GPS and WASS*, available at: <http://www.bc.edu/research/isr/spaceweathereffects.html>, accessed on 19 August 2011.
- [12] A. Coster, J. Foster and P. Erickson, *Space Weather*, GPS World, electronic edition, available at: <http://www.gpsworld.com/gps/space-weather-804>, accessed on 19 August 2011.
- [13] P.M. Kintner Jr., *A Beginners Guide to Space Weather and GPS*, electronic edition, available at: http://gps.ece.cornell.edu/SpaceWeatherIntro_update_2-20-08_ed, accessed on 19 August 2011.
- [14] J. Aarons, E. Whitney and R.S. Allen, *Global Morphology of Ionospheric Scintillations*, *Proceedings of the IEEE* **59** (1971) 159–172.
- [15] S. Datta-Barua, P.H. Doherty, T. Dehel and J.A. Klobuchar, *Ionospheric Scintillation Effects on Single and Dual Frequency GPS Positioning*, *Proceedings of the 16th International Technical Meeting of the Satellite Division of The Institute of Navigation, (ION GPS/GNSS 2003)*, Portland, OR, September 2003, 336–346.

- [16] S. Basu, K.M. Groves, Su. Basu and P.J. Sultan, *Specification and forecasting of scintillations in communication/navigation links: current status and future plans*, *Journal of Atmospheric and Solar-Terrestrial Physics* **64** (2002) 1745–1754, doi:10.1016/S1364-6826(02)00124-4.
- [17] P. Cannon *et al.*, *Extreme space weather: impacts on engineered systems and infrastructure*, (Royal Academy of Engineering, London, 2013).
- [18] F. Kleijer, *Troposphere Modeling and Filtering for Precise GPS Leveling*, (Netherlands Geodetic Commission, Delft, The Netherlands, 2004).
- [19] W.P. Elliot and D.J. Gaffen, *On the Utility of Radiosonde Humidity Archives for Climate Studies*, *Bulletin of the American Meteorological Society* **72** (1991) 1507–1520, doi:10.1175/1520-0477(1991)072;1507:OTUORH;2.0.CO;2.
- [20] D.N. Whiteman, S.H. Melfi and R.A. Ferrare, *Raman lidar system for the measurement of water vapor and aerosols in the Earth's atmosphere*, *Applied Optics* **31** (1992) 3068–3082, doi:10.1364/AO.31.003068.
- [21] M. Adam, *Development of lidar techniques to estimate atmospheric optical properties*, Ph.D. Thesis, Johns Hopkins University, United States of America, (2005).
- [22] V.A. Kovalev and W.E. Eichenger, *Elastic Lidar, Theory, Practice, and Analysis Methods*, (John Wiley & Sons, Inc., New York, 2004).
- [23] D.N. Whiteman, *Examination of the Traditional Raman Lidar Technique. I. Evaluating the Temperature-Dependent Lidar Equations*, *Applied Optics*, **42(15)** (2003) 2571–2592, doi:10.1364/AO.42.002571.
- [24] Y.B. Kumar, *Development of LIDAR techniques for environmental remote sensing*, *International Journal of Engineering Science and Technology* **2** (2010) 5872–5881.
- [25] A. Jursa, *Handbook of Geophysics and the Space Environment*, (National Technical Information Services Document, Accession No. ADA 167000, 1985).
- [26] K. Davies, *Ionospheric radio propagation*, (United States Department of Commerce, National Bureau of Standards Monograph 80, 1965).
- [27] S. Jen, G.P. Feng and S. Gleason, *Remote sensing using GNSS signals: Current status and future directions*, *Advances in Space Research* **47** (2011) 1645–1653, doi:10.1016/j.asr.2011.01.036.
- [28] M. Bevis, S. Businger, S. Chiswell, T.A. Herring, R.A. Anthes, C. Rocken, R.H. Ware *GPS meteorology: Mapping zenith wet delays onto precipitable water*, *Journal of Applied Meteorology and Climatology* **33** (1994) 379–386. doi:10.1175/1520-0450(1994)033;0379:GMMZWD;2.0.CO;2.
- [29] R. Ware *et al.*, *GPS Sounding of the Atmosphere from Low Earth Orbit: Preliminary Results* *Bulletin of the American Meteorological Society* **77** (1996) 19–40. doi:10.1175/1520-0477(1996)077;0019:GSOTAF;2.0.CO;2.
- [30] T.P. Yunck, *An Overview of Atmospheric Radio Occultation*, *Journal of Global Positioning Systems* **1** (2002) 58–60.
- [31] W.G. Melbourne, E.S. Davis, C.B. Duncan, G.A. Hajj, K.R. Hardy, E.R. Kursinski, T.K. Meehan, L.E. Young and T.P. Yunck, *The application of spaceborne GPS to atmospheric*

- limb sounding and global change monitoring*, (JPL Publication 94-18, Jet Propulsion Laboratory, California Institute of Technology, Pasadena, 147 pp., 1994).
- [32] GFZ German Research Centre for Geosciences, *The CHAMP Mission*, available at: <http://op.gfz-potsdam.de/champ/>, accessed on 1 March 2013.
- [33] European Organisation for the Exploitation of Meteorological Satellites (EUMETSAT), available at: <http://www.eumetsat.int/Home/index.htm>, accessed on 1 March 2013.
- [34] C. Rocken, T. Van Hove, J. Johnson, F. Solheim, R. Ware, M. Bevis, S. Chiswell and S. Businger, *GPS/STORM - GPS Sensing of Atmospheric Water Vapor for Meteorology*, *Journal of Atmospheric Oceanic Technology* **12** (1995) 468–478, doi:10.1175/1520-0426(1995)012<3C0468:GSOAWV>3E2.0.CO;2.
- [35] C. Rocken, R. Ware, T. Van Hove, F. Solheim, C. Alber, J. Johnson, M. Bevis and S. Businger, *Sensing atmospheric water vapor with the global positioning system*, *Geophysical Research Letters*, **20(20)** (1993) 2631–2634, doi:10.1029/93GL02935.
- [36] S. Businger *et al.*, *The promise of GPS in atmospheric monitoring* *Bulletin of the American Meteorological Society* **77** (1996) 5–18.
- [37] S.I. Gutman, R.B. Chadwick, D.E. Wolfe, A.M. Simon, T. Van Hove and C. Rocken, *Toward an operational water vapor remote sensing system using GPS* *FSL Forum*, September 1994, pp.13–19, available at: http://www.arm.gov/publications/proceedings/conf04/extended_abs/gutman_si.pdf.
- [38] D.E. Wolfe, S.I. Gutman *Developing an Operational, Surface-Based, GPS, Water Vapor Observing System for NOAA: Network Design and Results* *Journal of Applied Meteorology and Climatology*, **17** (2000) 426–440.
- [39] The International GNSS Service (IGS), Formerly the International GPS Service, <http://igscb.jpl.nasa.gov/>.
- [40] J.M. Dow, R.E. Neilan and C. Rizos, *The International GNSS Service in a changing landscape of Global Navigation Satellite Systems* *Journal of Geodesy* **83(7)** (2009) 191–198, doi:10.1007/s00190-008-0300-3.
- [41] G. Elgered, *Ground-based GPS networks for remote sensing of the atmospheric water vapour content: a review*, 7th Study Conference on BALTEX June 1014, 2013, Borgholm, Island of Oland, Sweden, pp. 12–13, available at: http://publications.lib.chalmers.se/records/fulltext/178098/local_178098.pdf.
- [42] H. Van der Marel, *COST-716 demonstration project for the near real-time estimation of integrated water vapour from GPS*, *Physics and Chemistry of the Earth, Parts A/B/C*, **29** (2004) 187–199, doi:10.1016/j.pce.2004.01.001.
- [43] G. Elgered, H.P. Plag, H. van der Marel, S. Barlag and J. Nash, *COST Action 716-Exploitation of ground-based GPS for operational numerical weather prediction and climate applications*, final report. Luxembourg: Office for Official Publications of the European of the European Communities, 2005. ISBN 92-898-00127-7.
- [44] M. Hantel, *Editorial: Scientific results of the European NEWBALTIC project*, *Meteorology and Atmospheric Physics* **77** (2001) 1–7, doi:10.1007/s007030170013.
- [45] J. Haase *et al.*, *The contributions of the MAGIC project to the COST 716 objectives of assessing the operational potential of ground-based GPS meteorology on an international scale*, *Physics and Chemistry of the Earth Part A: Solid Earth and Geodesy* **26** (2001) 433–437.

- [46] A.H. Dodson, H.C. Backer, B. Burki, G. Elgered, A. Rius and M. Rothacher, *The WAVEFRONT project on ground-based GPS water vapour estimation*, GNSS98 conference proceedings, 1998.
- [47] E-GVAP, The EUMETNET EIG GNSS water vapour programme, *Proposal for the second EUMETNET GNSS Water Vapour Programme (E-GVAP-II)*, available at: <http://egvap.dmi.dk/E-GVAP-II-proposal.pdf>.
- [48] E-GVAP, The EUMETNET EIG GNSS water vapour programme, <http://egvap.dmi.dk/>.
- [49] N. Bergeot, C. Bruyninx, P. Defraigne, S. Piereaux, J. Legrand, E. Pottiaux and Q. Baire, *Impact of the Halloween 2003 ionospheric storm on kinematic GPS positioning in Europe*, *GPS Solutions* **15**(2) (2011) 171–180, doi:10.1007/s10291-010-0181-9.
- [50] N. D'Agostino and G. Selvaggi, *Crustal motion along the Eurasia-Nubia plate boundary in the Calabrian Arc and Sicily and active extension in the Messina Straits from GPS measurements*, *Journal of Geophysical Research* **109**(B11) (2004) , doi:10.1029/2004JB002998.
- [51] H.C. Baker, A.H. Dodson, N.T. Penna, M. Higgins, D. Offiler, *Ground-based GPS water vapour estimation: potential for meteorological forecasting*, *Journal of Atmospheric and Solar–Terrestrial Physics*, **63** (2001) 1305–1314, doi:10.1016/S1364-6826(00)00249-2.
- [52] United States Naval Observatory (USNO), Block II satellite information, available at: <ftp://tycho.usno.navy.mil/pub/gps/gpsb2.txt>, accessed on 10 June 2013.
- [53] Z. Bai, *Near–Real–Time GPS Sensing of Atmospheric Water Vapour*, Ph.D. Thesis, Queensland University of Technology, Australia (2004).
- [54] G. Xu, *GPS–Theory, Algorithms and Applications*, (Second Edition, Springer-Verlag, Berlin, New York, 2007).
- [55] M.S. Grewal, L.R Weill and A.P Andrews, *Global Positioning Systems, Inertial navigation and integration*, (Second Edition, John Wiley & Sons, Inc., New Jersey, 2007).
- [56] A. Gore, *New Global Positioning System Modernization Initiative*, The White House, Office of the Vice President, Public Announcement on the Global Positioning System. Washington, DC, January 25, 1999.
- [57] GPS.gov, *Official U.S. Government information about the Global Positioning System (GPS) and related topics*, available at: <http://www.gps.gov/systems/gps/>, accessed on 10 June 2013.
- [58] GPS World, *Lockheed Martin Team Completes Delta Preliminary Design for Next GPS III Satellite Capabilities*, available at: <http://www.gpsworld.com/>, accessed on 10 June 2013.
- [59] Lockheed Martin International, available at: <http://www.lockheedmartin.com/>, accessed on 10 June 2013.
- [60] A. El-Rabbany, *Introduction to GPS: the Global Positioning System*, (Artech House Inc., United States of America, 2002).
- [61] A. Komjathy, *Global Ionospheric Total Electron Content Mapping Using the Global Positioning System*, Ph.D. Thesis, University of New Brunswick, Canada, (1997).
- [62] B.W. Parkinson, J.J Spilker Jr., P. Axelrad and P. Enge, *Global Positioning System: Theory and Applications Volume I*, (American Institute of Aeronautics and Astronautics, Inc., 2002).

- [63] R.D. Fontana, W. Cheung, P.M. Novak and T.A. Stansell, *The New L2 Civil Signal*, Proceedings of the 14th International Technical Meeting of the Satellite Division of The Institute of Navigation (ION GPS 2001), Salt Lake City, UT, September 2001, pp. 617–631, available at: <http://navcen.uscg.gov/>.
- [64] S.U. Qaisar and A.G. Dempster, *Assessment of the GPS L2C Code Structure for Efficient Signal Acquisition*, Aerospace and Electronic Systems, IEEE Transactions on **48** (2012) 1889–1902, doi:10.1109/TAES.2012.6237568.
- [65] IS-GPS-200D Global Positioning System Interface Specification, 7 March 2006, available at: <http://www.gps.gov/>.
- [66] B.C. Barker, J.W. Betz, J.E. Clark, J.T. Correia, J.T. Gillis, S. Lazar, K.A. Rehborn and J.R. Straton, *Overview of the GPS M Code Signal*, Proceedings of the 2000 National Technical Meeting of The Institute of Navigation, Anaheim, CA, January 2000, pp. 542–549, available at: <http://www.mitre.org/>.
- [67] G.X. Gao *et al.*, *Modernization Milestone—Observing the First GPS Satellite with an L5 Payload Inside GNSS*, **May/June** (2009) 30–36, available at: <http://www.insidegnss.com/auto/mayjune09-gao.pdf>
- [68] A.J. Van Dierendonck and C. Hegarty, *The New L5 Civil GPS Signal*, GPS World **11** (2000) 64–72.
- [69] J.W. Betz *et al.*, *Description of the L1C Signal* Proceedings of the 19th International Technical Meeting of the Satellite Division of The Institute of Navigation (ION GNSS 2006), Fort Worth, TX, September 2006, pp. 2080–2091, available at: <http://www.mitre.org/>.
- [70] T. Stansell, K. Hudnut and R. Keegan, *Future Wave: L1C Signal Performance and Receiver Design*, GPS World, **41** (2011) 30–36 (cover article), available at: <http://www.gpsworld.com/>.
- [71] J.W. Betz *et al.*, *Enhancing the Future of Civil GPS: Overview of the L1C Signal*, Inside GNSS (2007) 42–49, available at: http://www.insidegnss.com/auto/igm_042-049.pdf
- [72] M. Ge, G. Gendt, M. Rothacher, C. Shi and J. Liu, *Resolution of GPS carrier-phase ambiguities in Precise Point Positioning (PPP) with daily observations*, Journal of Geodesy, **82**(7) (2008) 389–399, doi:10.1007/s00190-007-0208-3.
- [73] C.A. Ogaja, *Applied GPS for engineers and project managers*, (American Society of Civil Engineers, 2011).
- [74] C. Rizos, V. Janssen, C. Roberts and T. Grinter, *Precise Point Positioning: Is the Era of Differential GNSS Positioning Drawing to an End?*, Proceedings of FIG Working Week 2012, 6–10 May 2012, Rome, Italy (2012), available at: http://www.gmat.unsw.edu.au/snap/publications/rizos_etal2012a.pdf.
- [75] J.F. Zumberge, M.B. Heflin, D.C. Jefferson, M.M. Watkins, and F.H. Webb, *Precise point positioning for the efficient and robust analysis of GPS data from large networks*, Journal of Geophysical Research: Solid Earth **102**(B3) (1997) 5005–5017, doi:10.1029/96JB03860.
- [76] C.O. Andrei, D. Salazar and R. Chen, *Performance Analysis of the Precise Point Positioning technique at BUCU IGS Station*, RevCAD—Journal of Geodesy and Cadastre **10** (2010) 9–20.


- [77] Y. Gao, *Precise Point Positioning and Its Challenges, Aided-GNSS and Signal Tracking*, *Inside GNSS* **1(8)** (2006) 16–18, available at: <http://www.insidegnss.com/auto/NovDec06GNSSolutions.pdf>
- [78] J. Sanz Subirana, J.M. Juan Zornoza and M. Hernandez-Pajares, *Carrier Phase Wind-up Effect*, http://www.navipedia.net/index.php/Carrier_Phase_Wind-up_Effect
- [79] J. Wu, S. Wu, G. Hajj, W. Bertiguer and S. Lichten, *Effects of Antenna Orientation on GPS Carrier Phase Measurements*, *Manuscripta Geodaetica*, **18(2)** (1993) 91–98.
- [80] G. Beutler, H. Bock, R. Dach, P. Fridez, A. Gäde, U. Hugentobler, A. Jäggi, M. Meindl, L. Mervart, L. Prange, S. Schaer, T. Springer, C. Urschl, P. Walser, *Bernese GPS Software Version 5.0*, (Astronomical Institute of the University of Bern, Stämpfli Publications, 2011), available at: <http://www.bernese.unibe.ch/>
- [81] L. Urquhart, *Atmospheric Pressure Loading and its Effects on Precise Point Positioning*, Proceedings of the 22nd International Technical Meeting of The Satellite Division of the Institute of Navigation (ION GNSS 2009), Savannah, GA, September 2009, pp. 658–667.
- [82] Atmospheric Pressure Loading Service, <http://gemini.gsfc.nasa.gov/aplo/>.
- [83] GSV4004B, *GPS Ionospheric Scintillation & TEC Monitor, (GISTM)*, User's manual, August 2007.
- [84] M.T.A.H. Muella, E.R. de Paula, I.J. Kantor, I.S. Batista, J.H.A. Sobral, M.A. Abdu, P.M. Kintner, K.M. Groves and P.F. Smorigo, *GPS L-band scintillations and ionospheric irregularity zonal drifts inferred at equatorial and low-latitude regions*, *Journal of Atmospheric and Solar-Terrestrial Physics* **70** (2008) 1261–1272, doi:10.1016/j.jastp.2008.03.013.
- [85] Slovenian Environmental Agency, *Atlas Okolja (Environmental Atlas of Slovenia)*, available at: <http://gis.arso.gov.si/atlasokolja/>, accessed on 4 August 2011.
- [86] C.S. Carrano, *GPS SCINDA: A real time GPS data acquisition and ionospheric analysis system for SCINDA, AFRL VS TR 2007 0000*.
- [87] Centre for Atmospheric Research, University of Nova Gorica, available at: <http://www.ung.si/en/research/atmospheric-research/otlica/lidar-otlica/>, accessed on 7 November 2012.
- [88] C. Weitkamp, *Lidar: range-resolved optical remote sensing of the atmosphere*, (Springer Science+Business Media Inc, New York, 2005).
- [89] F. Gao, *Study of Processes in Atmospheric Boundary Layer over Land-Sea Transition Interface Using Scanning Lidar*, Ph.D. Thesis, University of Nova Gorica, Slovenia (2012).
- [90] K. Saha, *The Earth's Atmosphere: Its Physics and Dynamics*, (Springer-Verlag, Berlin, Germany, 2008).
- [91] M.C. Kelley, *The Earth's Ionosphere: Plasma physics and electrodynamics*, (Second Edition, Academic Press, Inc., New York, 2009).
- [92] P. Pavlovčič, *Vpliv troposphere na GPS opazovanja*, master dissertation, University of Ljubljana, Slovenia (2000).
- [93] R.W. Schunk and A.F. Nagy, *Ionosphere: Physics, plasma physics and chemistry*, (Cambridge University Press, 2000).

- [94] R.G. Fleagle and J.A. Businger, *An Introduction to atmospheric physics*, (Second Edition, International Geophysics Series, Volume 25, Academic Press, Inc., New York, 1980).
- [95] J.H. Seinfeld and S.N. Pandis, *Atmospheric chemistry and physics : from air pollution to climate change*, (Second Edition, Willey & Sons, Inc., New Jersey, 2006).
- [96] J.M. Wallace and P.V. Hobbs, *Atmospheric science: an introductory survey*, (Second Edition, Elsevier Inc., Amsterdam, Netherlands, 2005).
- [97] *Earth's CO₂ Home Page*, available at: <http://co2now.org/>
- [98] World Meteorological Organization (WMO), *Greenhouse Gas Concentrations Continue Climbing*, available at: https://www.wmo.int/pages/mediacentre/press_releases/pr_934_en.html
- [99] C.N. Hewitt and A.V. Jackson, *Handbook of Atmospheric Science, Principles and Applications*, (Blackwell Science Ltd., United Kingdom, 2003).
- [100] A.A. Tsonis, *An Introduction to Atmospheric Thermodynamics*, (Second Edition, Cambridge University Press, United Kingdom, 2007).
- [101] F. Gao, S. Stanič, T.Y. He and D.X. Hua, *Ultraviolet scanning Raman lidar with fast telescope for measurements of water vapor and aerosols in lower atmosphere*, Proc. SPIE 8379, Laser Radar Technology and Applications XVII, 837916 (May 1, 2012); doi:10.1117/12.918346.
- [102] WMO *Guide to Meteorological Instruments and Methods of Observation*, <http://www.wmo.int/pages/prog/www/IMOP/publications/CIMO-Guide/CIMO%20Guide%207th%20Edition,%202008/Part%20I/Chapter%204>, WMO-No. 8 (7th ed.), Annex 4.B, 6 August 2008.
- [103] T.F. Tascione, *Introduction to the space environment*, (Second Edition, Krieger Publishing Company, Florida, 1994).
- [104] A. de Oliveira Moraes and W.J. Perrella, *Performance evaluation of GPS receiver under equatorial scintillation*, Journal of Aerospace Technology and Management **1** (2009) 193–199.
- [105] P.M. Kintner, B.M. Ledvina, and E.R. de Paula, *GPS and ionospheric scintillations*, Space Weather **5** (2007) S09003, doi:10.1029/2006SW000260.
- [106] A.W. Wernik, L. Alfonsi and M. Materrasi, *Ionospheric irregularities, scintillation and its effect on systems*, Acta Geophysica Polonica **52** (2004) 237–249.
- [107] S. Basu and S. Basu, *Equatorial scintillations—a review*, Journal of Atmospheric and Terrestrial Physics **43** (1981) 473–489, doi:10.1016/0021-9169(81)90110-0.
- [108] M.T.A.H. Muella, E.R. de Paula, I.J. Kantor, I.S. Batista, J.H.A. Sobral, M.A. Abdu, P.M. Kintner, K.M. Groves and P.F. Smorigo, *GPS L-band scintillations and ionospheric irregularity zonal drifts inferred at equatorial and low-latitude regions*, Journal of Atmospheric and Solar–Terrestrial Physics **70** (2008) 1261–1272, doi:10.1016/j.jastp.2008.03.013.
- [109] A.J. Van Dierendock, J. Klobuchar and Q. Hua, *Ionospheric Scintillation Monitoring Using Commercial Single Frequency C/A Code Receivers*, ION GPS-93 proceedings: 6th international technical meeting of the satellite division of the Institute of Navigation, Institute of Navigation, Salt Lake City, Utah (1993) 1333–1342.

- [110] M. Abdullah, A.F.M. Zain, Y.H. Ho and S. Abdullah, *TEC and Scintillation Study of Equatorial Ionosphere: A Month Campaign over Sipitang and Parit Stations, Malaysia*, American Journal of Engineering and Applied Sciences **2** (2009) 44–49, doi:10.3844/ajeassp.2009.44.49
- [111] J. Aarons, *Equatorial Scintillations: A Review*, IEEE Transactions on Antennas and Propagation **25** (1977) 729–736, doi: 10.1109/TAP.1977.1141649.
- [112] M.A. Cervera, and R.M. Thomas, *Latitudinal and temporal variation of equatorial ionospheric irregularities determined from GPS scintillation observations*, Annales Geophysicae **24** (2006) 3329–3341.
- [113] J.R. Koster, *Equatorial scintillation*, Planetary and Space Science **20** (1972) 1999–2014.
- [114] A. Coster and T. Tsuguwa, *The Impact of Traveling Ionospheric Disturbances on Global Navigation Satellite System Services*, Proceeding of XXVIIIth General Assembly of the International Union of Radio Science, United States of America (2008).
- [115] M. Rieger and R. Leitinger, *The effect of traveling ionospheric disturbances (TIDs) on GNSS user Systems*, Proceeding of XXVIIth General Assembly of the International Union of Radio Science, Netherlands (2002).
- [116] Minority Serving Institution Partnership Development Program, *Northern Lights: Earth Activity*, available at: <http://www.spacegrant.montana.edu/msiproject/earthactivity.html>, accessed on 12 September 2012.
- [117] R.D. Hunsucker and J.K. Hargreaves, *The high-latitude ionosphere and its effects on radio propagation*, (Cambridge University Press, United Kingdom, 2003).
- [118] *Electronic Warfare and Radar Systems Engineering Handbook*, available at: <http://www.rfcafe.com/references/electrical/ew-radar-handbook/electro-optics.htm>, accessed on 25 December 2012.
- [119] K.C. Yeh and Chao-Han Liu, *Radio Wave Scintillations in the Ionosphere*, Proceedings of the IEEE **70** (1982) 324–360, doi:10.1109/PROC.1982.12313.
- [120] J. Aarons, *Global Morphology of Ionospheric Scintillations*, Proceedings of IEEE **59** (1982) 159–172, doi:10.1109/PROC.1971.8122.
- [121] J. Aarons, J.P. Mullen and H.E. Whitney, *UHF scintillation activity over polar latitudes*, Geophysical Research Letters **8** (1981) 277–280, doi:10.1029/GL008i003p00277.
- [122] S.C. Mushini, P.T. Jayachandran, R.B. Langley, J.W. MacDougall and D. Pokhotelov, *Improved amplitude- and phase-scintillation indices derived from wavelet detrended high-latitude GPS data*, GPS Solution **16** (363–373) 2012, doi:10.1007/s10291-011-0238-4.
- [123] J. Zhang, *Investigations into the Estimation of Residual Tropospheric Delays in a GPS Network*, master dissertation, The University of Calgary, Canada, (1999).
- [124] S.M. Shrestha, *Investigations into the Estimation of Tropospheric Delay and Wet Refractivity Using GPS Measurements*, master dissertation, The University of Calgary, Canada (2003).
- [125] V.B. Mendes, *Modeling the neutral-atmospheric propagation delay in radiometric space techniques*, Ph.D. Thesis, Department of Geodesy and Geomatics Engineering Technical Report No. 199, University of New Brunswick, Fredericton, New Brunswick, Canada, 353 pp., (1999).

- [126] A.E. Niell, *Global mapping functions for the atmosphere delay at radio wavelengths*, Journal of Geophysical Research: Solid Earth **101** (1996) 3227–3246, doi:10.1029/95JB03048.
- [127] H. Sakadin, M.R.A. Bakar, A.R.M. Sharif, M.S.M. Noorani, A.N. Matori and A. Mohamed, *Effect of GPS Tropospheric delay Neill Mapping Function Simplification*, Malaysian Journal of Mathematical Sciences **3** (2009) 95–107.
- [128] J. Boehm and H. Schuh, *Vienna Mapping Functions in VLBI Analyses*, Geophysical Research Letters **31** (2004) L01603, doi:10.1029/2003GL018984
- [129] A.E. Niell, *Improved atmospheric mapping functions for VLBI and GPS*, Earth, Planets and Space **52** (2000) 699–702, available at: ftp://gemini.haystack.edu/pub/aen/JAOT/EPS2001_final.pdf.
- [130] J. Boehm and H. Schuh, *Vienna Mapping Functions in VLBI Analyses*, IVS 2004 General Meeting Proceedings, pp.277–281, available at: <ftp://ivscc.gsfc.nasa.gov/pub/general-meeting/2004/pdf/boehm1.pdf>.
- [131] J. Boehm, B. Werl, and H. Schuh (2006), *Troposphere mapping functions for GPS and very long baseline interferometry from European Centre for Medium-Range Weather Forecasts operational analysis data*, Journal of Geophysical Research **111** (2006) B02406, doi:10.1029/2005JB003629.
- [132] R.M. Measures, *Laser remote chemical analysis*, (John Willey & Sons Inc., New York, 1988).
- [133] D.A. Long, *The Raman Effect: a unified treatment of the theory of Raman scattering by molecules*, (John Wiley & Sons, Inc., Chichester, England, 2002).
- [134] T. Gregorius, *GIPSY-OASIS II: How it works...*, (California Institute of Technology, United States of America, 1996).
- [135] S.P. Alexander, *Studies of the lower troposphere*, Ph.D. Thesis, University of Adelaide, Australia, (2004).
- [136] Jet Propulsion Laboratory, *GIPSY-OASIS, GNSS-Infer Positionin System and Orbit Analysis Simulation Software*, available at: <https://gipsy-oasis.jpl.nasa.gov/index.php?page=data>, accessed on 26 November 2012.
- [137] G. Petit and B. Luzum, *IERS conventions 2010*, IERS Technical Note No. 36, available at <http://www.iers.org/IERS/EN/Publications/TechnicalNotes/tn36.html>
- [138] F. Lyard, F. Lefevre, T. Letellier, and O. Francis, *Modelling the global ocean tides: modern insights from FES2004*, Ocean Dynamics **56** (2006) 394–415, doi:10.1007/s10236-006-0086-x.
- [139] *GIPSY-OASIS II version 6.1.2, manual pages*
- [140] W. Bertiger, S.D. Desai, B. Haines, N. Harvey, A.W. Moore, S. Owen and J.P. Weiss, *Single receiver phase ambiguity resolution with GPS data*, Journal of Geodesy, **84**(5) (2010) 327–337, doi:10.1007/s00190-010-0371-9.
- [141] J. Duan, M. Bevis, P. Fang, Y. Bock, S. Chiswell, S. Businger, C. Rocken, F. Solheim, T. van Hove, R. Ware, S. McClucky, T.A. Herring and R.W. King, *GPS Meteorology: Direct Estimation of the Absolute Value of Precipitable Water*, Journal of Applied Meteorology **35** (1995) 830–838, doi:10.1175/1520-0450(1996)035<3C0830:GMDEOT>3E2.0.CO;2

- [142] S. Heise, G. Dick, G. Gendt, T. Schmidt and J. Wickert, *Integrated water vapour from IGS ground-based GPS observations: initial results from a global 5-minute data set*, *Annales Geophysicae* **27** (2009) 2851–2859, doi:10.5194/angeo-27-2851-2009.
- [143] M. Schmidt and H. Lipson, *Distilling Free-Form Natural Laws from Experimental Data*, *Science*, **324(5923)** (2009) 81–85.
- [144] C. Bruyninx, *The EUREF Permanent Network: a multi-disciplinary network serving surveyors as well as scientists*, *GeoInformatics* **7** (2004) 32–35.
- [145] Republic of Slovenia, Ministry of Infrastructure and spatial planning, available at: <http://www.gu.gov.si/si/storitve/>, accessed on 1 March 2013.
- [146] L.F. Sapucci, L.A.T. Machado, R.B. da Silveira, G. Fisch, J.F.G. Monico, *Analysis of Relative Humidity Sensors at the WMO Radiosonde Intercomparison Experiment in Brazil*, *Journal of Atmospheric and Oceanic Technology*, **22** (2005) 664–678, doi:10.1175/JTECH1754.1.
- [147] A. Sušnik and B. Forte, *Ionospheric scintillation activity measured in the African sector*, General Assembly and Scientific Symposium, 2011 XXXth URSI, pp.1–3, 13–20 August 2011, Istanbul, Turkey, doi:10.1109/URSIGASS.2011.6050919.
- [148] A. Sušnik and B. Forte, *Ionospheric scintillation activity measured in the African region by means of GNSS signals*, V: European Geoscience Union, General Assembly 2011, Vienna, Austria, 03–08 April 2011, (Geophysical research abstracts, vol. 13)
- [149] National Geophysical Data Center (NOAA), *Compute Earth's Magnetic Field Values*, available at: <http://www.ngdc.noaa.gov/geomag/magfield.shtml>, accessed on 7 May 2012.
- [150] B. Deng, J. Huang, W. Liu, J. Xu and L. Huang, *GPS scintillation and TEC depletion near the northern crest of equatorial anomaly over South China*, *Advances in Space Research* **51** (2013) 356–365, doi:10.1016/j.asr.2012.09.008.
- [151] D. Veberič, R. Sato and A. Sušnik, *Update on Positions of SD Stations*, Auger Malargüe Meeting, March 2012.
- [152] D. Veberič, R. Sato and A. Sušnik, *Positions of SD Stations as Acquired by On-board GPS Units*, Pierre Auger Collaboration Internal Note, GAP-2011-094.
- [153] D. Veberič, R. Sato and A. Sušnik, *Position of SD stations : dilution of precision corrections*, Pierre Auger Collaboration Internal Note, GAP-2012-052.
- [154] K. Loudec, *Atmospheric aerosols at the Pierre Auger Observatory: characterization and effect on the energy estimation for ultra-high energy cosmic rays*, Ph. D. Thesis, University Paris Sud–Paris XI, France (2011).
- [155] Urban Sputnik, *Interactive Cosmology, Cosmic Rays*, available at: <http://urbansputnik.com/Cosmic-Rays>, accessed on 14 January 2013.
- [156] P. Allison, J. Bellido, X. Bertou, C.E. Covault, B.E. Fick, H. Gemmeke, M. Kleifges, M. Mostafa, A. Menshikov, F. Meyer, C. Pryke, P. Sommers, E. Vanderpan, F. Vernotte and L. Wiencke for the Auger Collaboration, *Timing Calibration and Synchronization of Surface and Fluorescence Detectors of the Pierre Auger Observatory*, 29th International Cosmic Ray Conference Pune (2005) 101–104.

- [157] T. Suomijärvi for the Pierre Auger Collaboration, *Performance of the Pierre Auger Observatory Surface Detector*, Proceedings of the 30th International Cosmic Ray Conference, Mexico City, Mexico 4 (2008) 311–314.
- [158] Motorola GPS Products, *Oncore User's Guide*, Revision 3.2, 1998, available at: <http://www.uadrones.net/systems/research/1998/06.htm>
- [159] P. Sommers, *Cosmic ray anisotropy analysis with a full-sky observatory*, *Astroparticle Physics* 14 (2001) 271–286, doi:10.1016/S0927-6505(00)00130-4.
- [160] F. Salamida and S. Petrera, *An End-to-end Calculation of the Auger Hybrid Exposure*, Pierre Auger Collaboration Internal Note, GAP-2007-002.
- [161] Shuttle Radar Topography Mission (SRTM), available at: <http://www.jpl.nasa.gov/srtm/>
- [162] Daily updates of the *Current GPS Constellation*, U.S. Naval Observatory, available at: <http://tycho.usno.navy.mil/gpscurre.html>.
- [163] Visualization of placement of GPS satellites into orbits, available at: <http://www.colorado.edu/geography/gcraft/notes/gps/gif/oplanes.gif>.
- [164] D.S. Wilks, *Statistical methods in the atmospheric sciences*, (Third Edition, Elsevier Inc., Amsterdam, Netherlands, 2011).
- [165] H.G. Evertz, *The loop algorithm*, *Advances in Physics* 52 (2003) 1–66, doi:10.1080/0001873021000049195.
- [166] C.K. Yang and D.H. Robinson, *Understanding and Learning Statistics by Computer*, Computer Sciences vol. 4, (World Scientific, 1986).
- [167] K. Binder, *Monte Carlo Methods in Statistical Physics*, (Second Edition, Springer, Berlin, 1986); K. Binder, *Application of the Monte Carlo Method in Statistical Physics*, (Second Edition, Springer, Berlin, 1987); K. Binder and D.W. Heermann, *Monte Carlo Simulation in Statistical Physics*, (Springer, Berlin, 1986).
- [168] D.P. Landau and K. Binder, *A Guide to Monte Carlo Simulations in Statistical Physics*, (Cambridge University Press, 2000).
- [169] R.B. Langley, available at: *Dilution of Precision*, GPS World, May (1999) 52.
- [170]  Trimble Planning Software, <http://www.trimble.com/planningsoftware.ts.asp>.
- [171] C. Straub, A. Murk and N. Kämpfer, *MIAWARA-C, a new ground based water vapor radiometer for measurement campaigns*, *Atmospheric Measurement Techniques* 3 (2010) 1–15, doi:10.5194/amtd-3-2389-2010.
- [172] *How to upload station data*, available at: <http://magicgnss.gmv.com/wordpress/?p=274>, accessed on 26 November 2012.
- [173] K.M. Larson, *RINEX: The Receiver Independent Exchange Format Version 2.10*, available at: <http://spot.colorado.edu/~kristine/rinex210.txt>, accessed on 26 November 2012.

Atmospheric properties

Height [km]	Pressure [hPa]	Temperature [K]	Density [g/m ³]	Moist Stratosphere [g/m ³]	Dry Stratosphere [g/m ³]
0	1.013×10^3	288	1.225×10^3	5.9	5.9
1	8.98×10^2	282	1.112×10^3	4.2	4.2
2	7.950×10^2	275	1.007×10^3	2.9	2.9
3	7.012×10^2	269	9.093×10^2	1.8	1.8
4	6.166×10^2	262	8.194×10^2	1.1	1.1
5	5.405×10^2	256	7.364×10^2	6.4×10^{-1}	6.4×10^{-1}
6	4.722×10^2	249	6.601×10^2	3.8×10^{-1}	3.8×10^{-1}
7	4.111×10^2	243	5.900×10^2	2.1×10^{-1}	2.1×10^{-1}
8	3.565×10^2	236	5.258×10^2	1.2×10^{-1}	1.2×10^{-1}
9	3.080×10^2	230	4.671×10^2	4.6×10^{-2}	4.6×10^{-2}
10	2.650×10^2	223	4.135×10^2	1.8×10^{-2}	1.8×10^{-2}
11	2.270×10^2	217	3.648×10^2	8.2×10^{-3}	8.2×10^{-3}
12	1.940×10^2	217	3.119×10^2	3.7×10^{-3}	3.7×10^{-3}
13	1.658×10^2	217	2.666×10^2	1.8×10^{-3}	1.8×10^{-3}
14	1.417×10^2	217	2.279×10^2	8.4×10^{-4}	8.4×10^{-4}
15	1.211×10^2	217	1.948×10^2	7.2×10^{-4}	7.2×10^{-4}
16	1.035×10^2	217	1.665×10^2	5.5×10^{-4}	3.3×10^{-4}
17	8.850×10^1	217	1.423×10^2	4.7×10^{-4}	2.8×10^{-4}
18	7.565×10^1	217	1.217×10^2	4.0×10^{-4}	2.4×10^{-4}
19	6.467×10^1	217	1.040×10^2	4.1×10^{-4}	2.1×10^{-4}
20	5.529×10^1	217	8.891×10^1	4.0×10^{-4}	1.8×10^{-4}
21	4.729×10^1	218	7.572×10^1	4.4×10^{-4}	1.5×10^{-4}
22	4.048×10^1	219	6.450×10^1	4.6×10^{-4}	1.3×10^{-4}
23	3.467×10^1	220	5.501×10^1	5.2×10^{-4}	1.1×10^{-4}
24	2.972×10^1	221	4.694×10^1	5.4×10^{-4}	9.4×10^{-5}
25	2.549×10^1	222	4.008×10^1	6.1×10^{-4}	8.0×10^{-5}
30	1.197×10^1	227	1.841×10^1	3.2×10^{-4}	3.7×10^{-5}
35	5.746	237	8.463	1.3×10^{-4}	1.7×10^{-5}
40	2.871	253	3.996	4.8×10^{-5}	7.9×10^{-6}
45	1.491	264	1.966	2.2×10^{-5}	3.9×10^{-6}
50	7.978×10^{-1}	271	1.027	7.8×10^{-6}	2.1×10^{-6}
70	5.220×10^{-2}	220	8.283×10^{-2}	1.2×10^{-7}	1.8×10^{-7}
100	3.008×10^1	210	4.990×10^{-4}	3.0×10^{-4}	1.0×10^{-9}

Table A.1: Temperature, pressure and density (dry air and water vapor) variations with height according to U.S. Standard Atmosphere, 1976 [95].

Detection systems and their technical details

B.1 GPS monitors at University of Nova Gorica

Radio frequency	
3 dB pass band (typical)	L1 : 1575.42 ± 13 MHz L2: 1227.60 ± 13 MHz
out-of-band rejection (typical)	>40 dBc
gain at zenith ($\alpha = 90^\circ$) (min)	L1 : +7.7 dBic L2: +4.7 dBic
gain roll-off (zenith to horizon)	L1 : 15.2 dB L2: 18 dB
L1/L2 LNA gain (typical)	31/33 ± 2 dB
polarization	right-hand circular
noise-figure (typical)	3.0 dB
nominal impedance	50 Ω
VSWR	≤1.5 : 1
Power	
input voltage	2.5 to 24 VDC
current (typical)	35 mA
Physical	
diameter	308 mm
weight	4.1 kg
Environmental	
maximum altitude	9 km
operating temperature	−55° to +85°
storage temperature	−55° to +85°
design standards	D0-160D
	DO228
	MIL-C-5541
	MIL-E-5541
	MIL-I-45208A
	MIL-STD-810
	SO-C144
	SAE J1455

Table B.1: General specification parameters of NovAtel antenna (model ANT-C2GA-TW-N) [83].

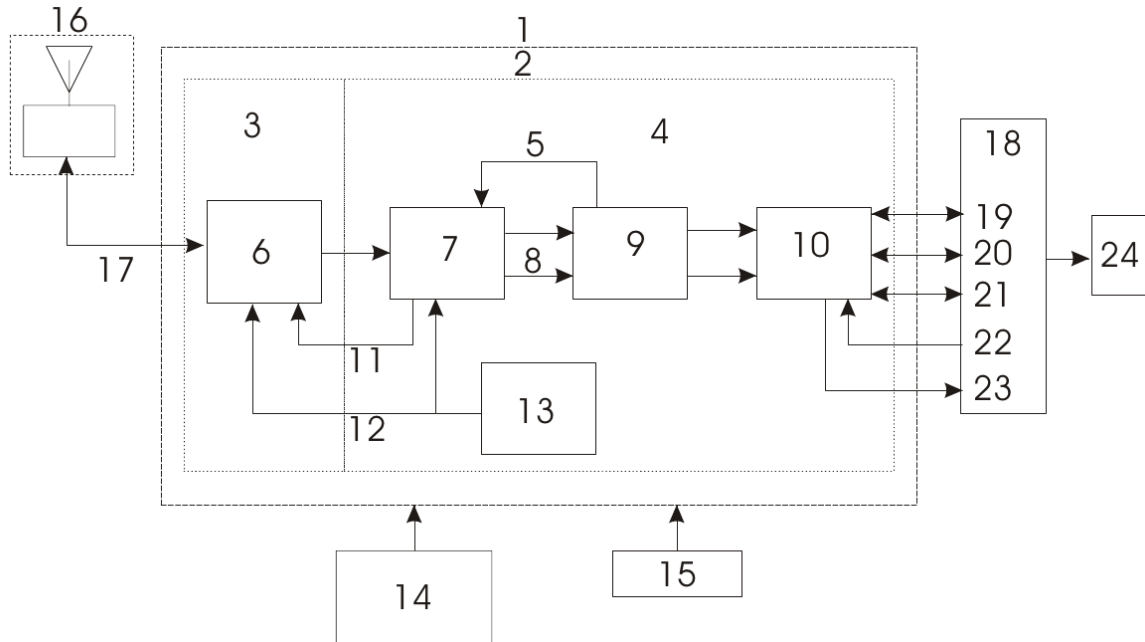


Figure B.1: GPS receiver system functional diagram. 1–enclosure; 2–GPSCard; 3–RF section; 4–digital section; 5–controls; 6–RF-IF sections; 7–signal processor; 8–clock; 9–22-BIT CPU; 10–system I/O; 11–AGC; 12–clock; 13–VCTCXO; 14–optional LNA power; 15–power supply; 17–RF and power; 18–data and signal processing; 19–COM1; 20–COM2; 21–COM3; 22–input timing signal; 23–output timing signal; 24–USB communication [83].

B.2 Raman lidar at Otlica Observatory

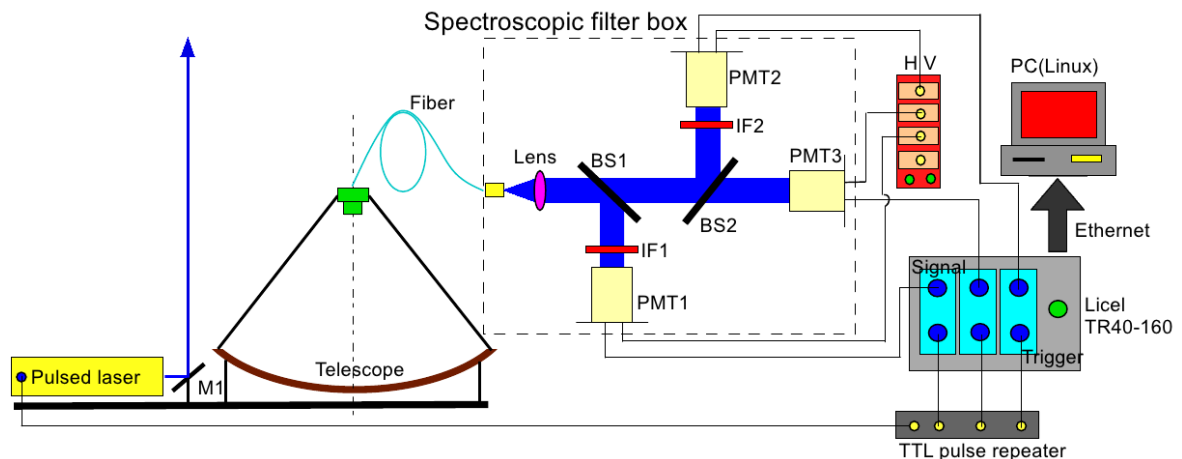


Figure B.2: Raman lidar setup at Otlica Observatory. M1–mirror; BS1, BS2–beam splitter; IF–Interference filter; PMT–photomultiplier tube; HV–high voltage power supply [89].

Transmitter	Nd:YAG laser
Wavelength	354.7 nm
Pulse energy	100 mJ
Repetition rate	20 Hz
Receiver optics	Parabolic mirror
Effective diameter	585.7 mm
Fiber core diameter	1000 μm
Fiber's acceptance	25.4°
Detectors	Hamamatsu PMT
PMT 1 and 2	
Type	H1949-50
Quantum efficiency	23%
Gain	2.07×10^6
High voltage	3000 V
PMT 3	
Type	H2341-50
Quantum efficiency	20%
Gain	2.5×10^6
High voltage	3500 V
Transient recorder	TR40-160
Wavelength channels	3
Range resolution	3.75 m
Sampling rate in Analog	40 MSPS
Max. count rate in Photon	250 MHz

Table B.2: Specification parameters of the Raman lidar system [89].

B.3 GPS Auger Motorola Oncore UT+ specifications

General Characteristics	
Receiver Architecture	8 parallel channels L1: 1575.42 MHz C/A code (1.023 MHz chip rate) Code plus carrier tracing (carrier aided tracking)
Tracking Capability	8 simultaneous SV
Performance Characteristics	
Acquisition Time (Time To First Fix-TTFF)	<20 s typical TTFF-hot (with current almanac, position, time and ephemeris) <50 s typical TTFF-warm (with current almanac, position and time) <300 s typical TTFF-cold
(Tested at -30 to $+80^{\circ}\text{C}$)	<1.0 s internal reacquisition (typical)
Positioning Accuracy	100 m 2dRMS with SA as per DoD specifications less than 25 m SEP whiteout SA time RAIM algorithm
Timing Accuracy (1 PPS)	<130 ns (1 sigma) with SA on in position hold mode, <50 ns (1 sigma) with SA on
Antenna	active micro strip patch antenna module powered by receiver module (5 to 80 mA at 5 V)
Datum	WGS-84
Serial Communication	
Output Messages	latitude, longitude, height, velocity, time software selectable output rate (continuous or poll) TTL interface (0 to 5 V)
Physical Characteristics	
dimensions	$50.8 \times 82.6 \times 16.3$ mm
weight	51 g

Table B.3: Oncore technical characteristics for UT model [158].

RINEX data format

Daily and hourly files:

ssssdddf.yyt

t: file type: t = **O** for observations files, t = **d** for Hatanaka files

yy: two-digit year

f: file sequence number / character within day

daily file: f = **0**

hourly files:

f = **a**: 1st hour 00h–01h; f = **b**: 2nd hour 01h–02h; ...

f = **x**: 24th hour 23h–24h

ddd: day of the year

ssss 4-character station name

15-min files:

ssssdddfmm.yyt

mm: starting minute within the hour (**00, 15, 30, 45**)

Figure C.1: Standard naming convention for RINEX data files [172, 173]

RINEX stands for the “**R**eciever **I**ndependent **E**xchange **F**ormat” and has been developed by the Astronomical Institute of the University of Berne for the purpose of easy exchange of the GPS data that were collected during the large European GPS campaign called EUREF 89, which involved more than 60 GPS receivers of 4 different manufacturers [173]. It is a standardized format of the GPS data that allows easy management of the data generated by the receiver and processing them with a large number of application in various scientific fields, from geology to atmospheric science. One of the key features of RINEX file is the name of the file (see Fig. C.1). From Fig. C.1 one can see that they can be daily, hourly or 15-minute files.

Currently there are 6 ASCII file types, from which so-called Observation Data File is needed in GIPSY-OASIS analysis. The observation data file is divided in header section and data section (see below for example of part of the observation file for ZOUF receiver). In header section all global information for the entire file are located, such as types of observations (in case of provided example there are L1, L2, C1, P2, P1), approximate X,Y,Z coordinates in WGS-84 format, to which satellite system the data are referring (in example below this was G where G stands for GPS satellite system), the time of the first observation being recorder and in some cases also the end time [135, 173].

The data or body section of the file is in epoch format with multiple lines of observations. The number of lines in one epoch is equal to the number of satellites being tracked at that moment. From left to right, an epoch line specifies the year (two digits), month, day, hour, minute and second of the observation in Universal Time (UT). After the time specification follows the number which indicates if everything is "OK" with data. For instance "O" means that everything is OK with data in that epoch, "1" stands for power failure between previous and current epoch and ">1" is event flag [135,173]. After that number the number of satellites observables is recorded and last the PRN number of satellites is listed. Below this line the lines with measurements of carrier and pseudorange data follows [135].

```

2.10          OBSERVATION DATA   G (GPS)          RINEX VERSION / TYPE
HEADER CHANGED BY EPN CB ON 2011-08-05          COMMENT
TO BE CONFORM WITH THE INFORMATION IN          COMMENT
ftp://epncb.oma.be/pub/station/log/zouf.log      COMMENT
teqc 2003Sep15                20050102 04:00:04UTCPGM / RUN BY / DATE
Linux 2.0.36|Pentium II|gcc -static|Linux|486/DX+  COMMENT
teqc 2003Sep15      OGS/CRS          20050102 03:40:25UTCCOMMENT
BIT 2 OF LLI FLAGS DATA COLLECTED UNDER A/S CONDITION  COMMENT
U-file data mode 7: pseudorange smoothing not applied  COMMENT
ZOUF          MARKER NAME
12763M001     MARKER NUMBER
David Zuliani OGS/CRS          OBSERVER / AGENCY
20305        ASHTECH UZ-12      CN00      REC # / TYPE / VERS
20415        ASH701945C_M      SCIT      ANT # / TYPE
  4282710.1618  986659.2995  4609469.7059  APPROX POSITION XYZ
    0.0083      0.0000      0.0000  ANTENNA: DELTA H/E/N
      1      1  WAVELENGTH FACT L1/2
      5  L1  L2  C1  P2  P1  # / TYPES OF OBSERV
    30.0000  INTERVAL
Forced Modulo Decimation to 30 seconds  COMMENT
Version: Version:  COMMENT
Project: A30541512220GSZOUF_SITE_----  COMMENT
SNR is mapped to RINEX snr flag value [0-9]  COMMENT
  L1 & L2:  2-19 dBHz = 1, 20-27 dBHz = 2, 28-31 dBHz = 3  COMMENT
           32-35 dBHz = 4, 36-38 dBHz = 5, 39-41 dBHz = 6  COMMENT
           42-44 dBHz = 7, 45-48 dBHz = 8, >= 49 dBHz = 9  COMMENT
Forced Modulo Decimation to 30 seconds  COMMENT
  2005      1      1      0      0  30.0000000      GPS      TIME OF FIRST OBS
                                           END OF HEADER
05  1  1  0  0  30.0000000  0  9G13G 4G20G24G10G23G 8G27G17
27179794.53249  23517733.57859  20395532.5594  20395534.504  20395533.0594
32136967.42849  27379595.75148  21338685.4004  21338689.038  21338685.9194
48454542.87547  40092553.23945  24444028.3594  24444031.046  24444027.4394
32353163.94349  27550288.56948  21380231.7144  21380235.385  21380231.9464
50613753.20847  41778088.35045  24855044.3724  24855044.744  24855044.1274
34383505.25949  29129765.22948  21766674.3834  21766674.303  21766674.2884
42572646.07748  35509501.03947  23324864.8464  23324869.080  23324863.8714
33507323.25349  28445768.81748  21599356.9084  21599359.718  21599357.0404
47571234.99348  39403658.42445  24275761.1574  24275762.971  24275759.7604
05  1  1  0  1  0.0000000  0  9G13G 4G20G24G10G23G 8G27G17
27208760.55749  23540304.50649  20401044.618  20401046.636  20401045.007
32178811.40049  27412201.44648  21346647.457  21346651.068  21346647.946
48556741.33147  40172188.38345  24463475.786  24463477.981  24463475.677
32372956.86449  27565711.61148  21383997.810  21384001.207  21383998.021
50511048.07747  41698058.41445  24835500.074  24835500.650  24835499.476

```


34457424.04549	29187364.27148	21780740.893	21780740.503	21780740.635
42463734.00948	35424634.48947	23304139.944	23304143.702	23304140.035
33441042.66649	28394121.62148	21586744.289	21586747.024	21586744.335
47475697.58848	39329213.65145	24257580.233	24257583.199	24257579.848

